THEORETICAL ANALYSIS OF A DOWNER REACTOR AND RISER REGENERATOR INTEGRATED SYSTEM IN FCC PROCESS

Anon Chuachuensuk[1], Jesse Zhu[2], Amornchai Arpornwichanop[1,3*]

[1] Department of Chemical Engineering, Faculty of Engineering, Chulalongkorn University, Bangkok 10330, Thailand
[2] Department of Chemical and Biochemical Engineering, The University of Western Ontario, London, Ontario, N6A 5B9 Canada
[3] Computational Process Engineering, Chulalongkorn University, Bangkok, 10330 Thailand

[*] Author for correspondence; E-Mail: Amornchai.a@chula.ac.th, Tel. +66 2218 6878, Fax. +66 2218 6877

Abstract: A fluid catalytic cracking (FCC) unit plays an increasing role in the petroleum and petrochemical industries. A conventional FCC comprises of a riser reactor and a turbulent bed regenerator. Different technologies have been developed to improve its operation and performance. A concurrent down-flow reactor (the so-called downer) has been considered to be a promising reactor because it has several pros, compared to a riser reactor, such as less gas and solids back-mixing, more uniform flow structure and narrower solids residence time distribution. Both experimental and simulated results suggest that using the downer as a reactor in a fluid catalytic cracking process can improve yield and selectivity of the desired products. However, few studies focused on the accompanying regenerator have been reported. Shortcomings of the conventional regenerator, such as high solids inventory and long residence time, lead to the development of a concurrent up-flow regenerator (the riser) that operates in fast fluidization regime having advantages of high heat and mass transfers, low catalyst inventory and high throughput. This study carries out an analysis of a downer reactor and a riser regenerator in an FCC process. Simulation of the FCC process is performed using a one-dimensional model of hydrodynamic and kinetics of cracking and burning reactions. The obtained results provide useful information about the operation of a downer reactor with a riser regenerator, which can be used for optimal design of the reactor and regenerator system in the FCC process.

1. Introduction

A fluid catalytic cracking (FCC) unit plays an increasing role in the petroleum and petrochemical industries. This unit had been used a commercial operation in 1942 [1]. It is used for modification of the hydrocarbon molecules by cracking of long chain molecules into smaller molecules which have higher demand and value. In general, FCC unit in the current generation is composed of two main units, i.e., riser reactor and turbulent bed regenerator. The profit margin obtained from this unit in combination with other requirements, such as more residual feedstock, higher product quality and environmental concern, stimulates the improvement of its operation and performance.

From the hydrodynamic point of view, it is found that the concurrent up-flow reactor (riser) provides several drawbacks compared to the concurrent down-flow reactor (downer). Flow direction of gas and solids in downer reactor is in the same direction of the gravitational force; therefore, the disadvantage of gas and solids back-mixing of the riser reactor have been reduced. This enables more uniform flow structure and narrower solids residence time distribution [2-3]. In addition, both experimental and simulated results suggest that using the downer as a reactor in a fluid catalytic cracking process can improve both yield and selectivity of the desired products [4-5]. However, the knowledge of the downer reactor in the literature usually considers only the downer itself, with a few studies that provides details about the accompanying regenerator. Shortcomings of the conventional regenerator, such as high solids inventory and long residence time, lead to the development of the regenerator. The high efficiency regenerator with turbulent fluidized bed at bottom part and the entrained fast fluidized is the effective design that allows the invention of a concurrent up-flow regenerator (the riser) that operates in fast fluidization regime having advantages of high heat and mass transfer, low catalyst inventory and high throughput [6-7]. This work carries out a theoretical analysis of an integrated system between downer reactor and riser regenerator in the FCC process. Simulation of the FCC process is performed using a one-dimensional model of hydrodynamic and kinetics of cracking and burning reactions. Obtained results provide useful information about the operation of a downer reactor with a riser regenerator, which can be used for optimal design of the reactor and regenerator system in the FCC process.

2. Process description

The process diagram of the integrated system of downer reactor and riser regenerator and its ancillary unit in fluid catalytic cracking process are shown in Figure 1. It consists of a downer reactor, a riser regenerator, a storage tank for regenerated catalyst, a quick separator, a stripper and a set of cyclones installed in a cyclone housing. The routine operation begins with the injection of the feedstock together with steam for atomization. After contacting with high-temperature regenerated catalyst flowing from the storage tank, feedstock vaporizes and moves downward with catalyst. The endothermic cracking reactions proceed while feedstock vapour is contacted with the catalyst. As a by-product of the reactions, the carbonaceous material (coke) forms on the catalyst surface causing the reduction of the catalytic activity. Therefore, a regeneration process is needed for restoring the catalyst activity. Moreover, this process provides heat for vaporization of the feedstock and endothermic cracking reactions that occur in the reactor.

At the exit of downer reactor, spent catalyst and gaseous products including cracked and un-cracked feedstock are separated using a quick separator. Due to the fact that the desired product of the cracking reactions is gasoline which is an intermediate substance, the fast separation is required. A quick separator is used for separation of the gaseous products and spent catalyst because the separation resident time is less than that of cyclones. The products are sent to a main fractionator for separation (not shown here) and the spent catalyst falls into the stripper where steam is used to remove the entrained products. Then, spent catalyst and air are fed together at the bottom of the riser for starting the regeneration process. Coke is oxidized with oxygen in air to form CO, CO_2 and H_2O inside the regenerator. Flue gas and regenerated catalyst are separated by a set of cyclones installed in the cyclone housing. A portion of regenerated catalyst are recycled back to the bottom of the riser regenerator to maintain heat balance of the regeneration process and the rest is stored in the storage tank before feeding to the downer reactor.

3. Mathematical model

All equations together with the parameters and initial conditions are solved by Euler's method to obtain the variations of the species concentration and temperature profile along the length of the reactor and the regenerator. The important equations are shown in the following section.

3.1 Downer Reactor

3.1.1 Hydrodynamic model

The momentum conservation equations are:

Gas phase:

$$\frac{d(\bar{\varepsilon}_{g,rxt}\rho_{g,rxt}\bar{V}^2_{g,rxt})}{dz_{rxt}} = -\frac{dP_{rxt}}{dz_{rxt}} - F_{D,rxt} - F_{fg,rxt} + \bar{\varepsilon}_{g,rxt}\rho_{g,rxt}g \tag{1}$$

Solid phase:

$$\frac{d(\bar{\varepsilon}_{s,rxt}\rho_s\bar{V}^2_{s,rxt})}{dz_{rxt}} = F_{D,rxt} - F_{fs,rxt} + \bar{\varepsilon}_{s,rxt}(\rho_s - \rho_{g,rxt})g \tag{2}$$

3.1.2 Mass balance

Mass fractions of each lump is calculated based on the four lumps reaction scheme and can be expressed as:

$$\frac{dy_{i,rxt}}{dz_{rxt}} = \frac{\rho_s\bar{\varepsilon}_{s,rxt}A_{rxt}\phi_s}{F_{g,rxt}} r_{i,rxt}\,, \quad i = go, gl, gs, \text{and } ck \tag{3}$$

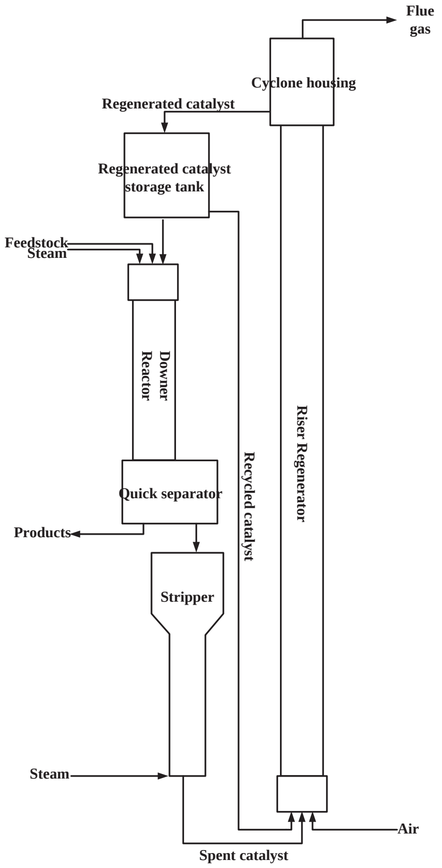

Figure 1. Schematic diagram of a downer reactor and riser regenerator integrated system.

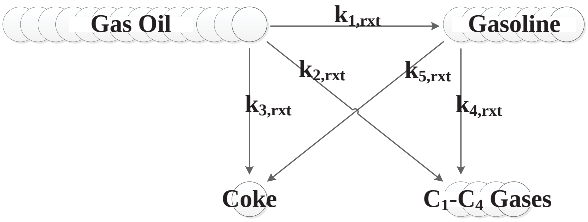

Figure 2. Four-lump reactions scheme.

The kinetics of cracking reactions used in this simulation are obtained from [8]. The cracking of gas oil is considered to be the second order reaction with respect to the gas oil concentration (or fraction of gas oil) while the cracking reactions of other species are the first order reactions. The reactions scheme is shown in Figure 2. Gas oil is cracked to gasoline, C_1-C_4 gases and coke. The gasoline can be further cracked to form C_1-C_4 gases and coke. The rates of cracking reactions and the rate constants are shown below:

$$r_{go,rxt} = -\left(k_{1,rxt} + k_{2,rxt} + k_{3,rxt}\right)y^2_{go,rxt} \tag{4}$$

$$r_{gl,rxt} = k_{1,rxt}y^2_{go,rxt} - k_{4,rxt}y_{gl,rxt} - k_{5,rxt}y_{gl,rxt} \tag{5}$$

$$r_{gs,rxt} = k_{2,rxt}y^2_{go,rxt} + k_{4,rxt}y_{gl,rxt} \tag{6}$$

$$r_{ck,rxt} = k_{3,rxt}y^2_{go,rxt} + k_{5,rxt}y_{gl,rxt} \tag{7}$$

3.1.3 Energy balance

The variations of catalyst and gas temperature along the length of the reactor can be derived as:

Solid phase:

$$\frac{dT_{s,rxt}}{dz_{rxt}} = \frac{A_{rxt} h_{p,rxt} A_{p,rxt}}{F_{s,rxt} C_{p,s}} \left(T_{g,rxt} - T_{s,rxt} \right) \tag{8}$$

Gas phase:

$$\frac{dT_{g,rxt}}{dz} = \frac{A_{rxt}}{F_{g,rxt} C_{p,g,rxt}} \Big[h_{p,rxt} A_{p,rxt} \left(T_{s,rxt} - T_{g,rxt} \right) + \rho_s \bar{\varepsilon}_{s,rxt} Q_{react,rxt} \Big] \tag{9}$$

3.2 Riser regenerator

3.2.1 Hydrodynamic model

Hydrodynamic model of the riser reactor is similar to that of the downer and some equations are identical to the downer model.

The momentum conservation equations are:

Gas phase:

$$\frac{d(\bar{\varepsilon}_{g,reg} \rho_{g,reg} \bar{V}_{g,reg}^2)}{dz_{reg}} = -\frac{dP_{reg}}{dz_{reg}} - F_{D,reg} - F_{fg,reg} - \bar{\varepsilon}_{g,reg} \rho_{g,reg} g \tag{10}$$

Solid phase:

$$\frac{d(\bar{\varepsilon}_{s,reg} \rho_s \bar{V}_{s,reg}^2)}{dz_{reg}} = F_{D,reg} - F_{fs,reg} - \bar{\varepsilon}_{s,reg} (\rho_s - \rho_{g,reg}) g \tag{11}$$

3.2.2 Mass balance

The main objective of the regeneration process is to recover the cracking activity of the FCC catalyst caused by the deposition of coke. Generally, coke is considered to be composed of carbon and hydrogen atoms at a different ratio. This ratio is obtained by a laboratory determination and found that H/C ratio in coke ranges from 0.5 to 1.0 [9]. The mass balance along the length of the regenerator can be expressed as;

Carbon:

$$\frac{dC_{\mathrm{C,reg}}}{dz_{reg}} = \frac{-r_{\mathrm{C,reg}} \rho_s (1 - \bar{\varepsilon}_{g,reg})}{G_{s,reg}} \tag{12}$$

Hydrogen:

$$\frac{dC_{\mathrm{H,reg}}}{dz_{reg}} = \frac{-r_{\mathrm{H,reg}} \rho_s (1 - \bar{\varepsilon}_{g,reg})}{G_{s,reg}} \tag{13}$$

Oxygen:

$$\frac{dC_{\mathrm{O_2},reg}}{dz_{reg}} = \frac{-(r_{\mathrm{C,reg}}/12 + r_{\mathrm{H,reg}}/4) \rho_s (1 - \bar{\varepsilon}_{g,reg})}{U_{g,reg}} \tag{14}$$

The regeneration reaction is the burning reaction of coke with oxygen in air. In this work, we assume that the regeneration is in complete combustion mode; therefore, there is no carbon monoxide in the flue gas. The burning reaction can be expressed as:

$$\mathrm{CH}_{12\alpha} + \left(1 + 3\alpha\right)\mathrm{O}_2 \longrightarrow \mathrm{CO}_2 + 6\alpha \mathrm{H}_2\mathrm{O} \tag{15}$$

In this study, the regeneration process is considered as carbon burning and hydrogen burning. The rates of reactions are given as [10]:

$$-r_{\mathrm{C,reg}} = k_{\mathrm{C,reg}} \, p_{\mathrm{O_2},reg} C_{\mathrm{C,reg}} \tag{16}$$

$$-r_{\mathrm{H},reg} = k_{\mathrm{H},reg} \, p_{\mathrm{O_2},reg} C_{\mathrm{H,reg}} \tag{17}$$

Table 1: Product yields of downer reactor from experimental and predicted data

Lumps	Yield (wt%)		Deviation
	Experiment	Model	(%)
C_1-C_4 Gases	29.5	29.13	-1.25
Gasoline	48.50	49.96	3.01
Coke	2.0	0.93	-53.5

3.2.3 Energy balance

In this work, we assume that the temperature of the catalyst and gas in the regenerator are in thermal equilibrium so the temperature variation along the regenerator length can be expressed as shown below:

$$\frac{dT_{reg}}{dz_{reg}} = \frac{\rho_s (1 - \bar{\varepsilon}_{g,reg})(r_{\mathrm{C,reg}} \Delta H_{C,reg} + r_{\mathrm{H,reg}} \Delta H_{\mathrm{H,reg}})}{U_{g,reg} \rho_{g,reg} C_{p,g,reg} + G_{s,reg} C_{p,s}} \tag{18}$$

4. Simulation results and discussion

4.1 Model validation

Predicted data of the downer reactor is compared with the experimental data available in the literature. The comparison of product yields obtained from experiment and model of downer reactor at the catalyst/oil ratio of 20 and 80% conversion are shown in Table 1. It can be seen that the simulation data obtained by the model prediction is very close to the experimental data obtained from [4]. This shows the validity of the model prediction.

It is noted that the model for the riser regenerator used in the simulation is obtained from [7].

4.2 Operation of the integrated system

The product distributions are shown in Figure 3. The simulation results indicate that gas oil reduces along the length of the downer reactor while the products containing C_1-C_4 gases, gasoline and coke increase. However, coke yield is almost constant since downer reactor provides a small coke yield. In this work, we process the feedstock with high Conradson Carbon Residue (CCR) and also assume that all CCR is converted to be coke deposited on the catalyst surface, for the sake of heat balance of the system. The value of CCR used is 4.0 wt%. Although, low coke yield is preferable for the prevention of losing valuable products, coke is useful towards the heat aspect. Coke is used for maintaining heat balance of the system since coke burning reaction is the source of heat needed in the reactor.

The operation of the accompanying riser regenerator is shown in Figure 4. It is clearly seen that coke on the catalyst surface is removed efficiently. The heat obtained from coke burning raises the temperature of the regenerator up and this amount of heat is adequate for providing to the downer reactor and thus, the heat balance of the system is maintained.

4.3 Effect of the Conradson Carbon Residue

The effect of CCR on the operation of the integrated system in an aspect of heat balance is shown

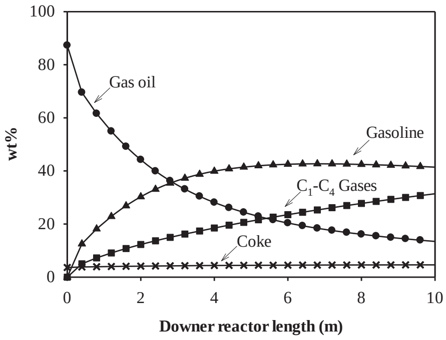

Figure 3. Mass fraction of the species along the downer reactor.

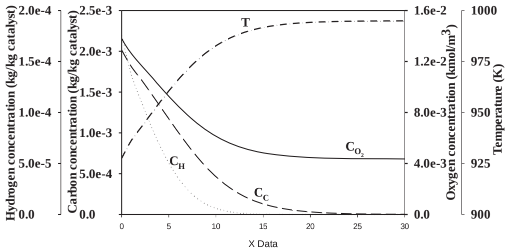

Figure 4. The species concentration and temperature variation along the length of the riser regenerator.

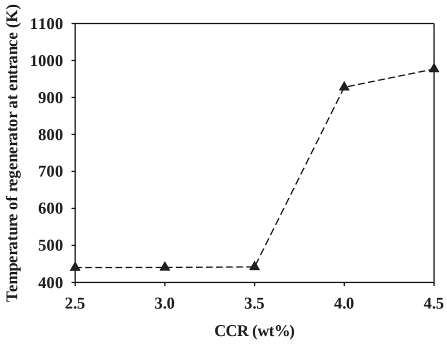

Figure 5. Effect of CCR on inlet temperature of the riser regenerator.

in Figure 5. The results reveal that at the point below 4.0 wt.% of CCR, the inlet temperature of the riser regenerator decreases. This is not the preferable condition for the burning reaction because regenerator can proceed effectively at temperature above 800 K. [11]. Therefore, the burning reaction scarcely occurs and the heat balance is not maintained. This causes the failure in operation of the FCC integrated system.

4. Conclusions

This work presents the theoretical analysis of an integrated system between a downer reactor and riser regenerator using the simulation study. The model used consists of the hydrodynamic model and reactions kinetics of both downer reactor and riser regenerator. The simulation results showed that coke yield obtained from downer reactor is low which in turn is not enough to maintain heat balance of the integrated system. Therefore, the downer reactor needs the residual feed with more CCR as a feedstock for maintaining heat balance and operation of the system. The results can be used for optimal design of the integrated system between a downer reactor and a riser regenerator in FCC processes.

Acknowledgements

Support from the 90th Anniversary of Chulalongkorn University Fund (Ratchadaphi seksomphot Endowment Fund) and PhD Scholarship for research aboard is gratefully acknowledged.

Nomenclatures

A	cross-sectional area (m^2)
A_p	effective interface heat transfer area per unit volume between the catalyst and gas phases (m^2/m^3)
C	species concentration (kmol/m^3), (kg/kg catalyst)
F_D	drag force between gas and particle (N)
F_{fg}	friction force between gas and wall (N)
F_{fs}	friction force between solid and wall (N)
g	acceleration due to gravity (m/s^2)
gl	lump of gasoline
go	lump of gas oil
gs	lump of C_1-C_4 gases
G	flow rate (based on cross-sectional area) (kg/(m^2 s))
h_p	interface heat transfer coefficient between the catalyst and gas phases (kJ/m^2 s K)
k	reaction rate constant (1/s), (1/(kPa s))
p_{O_2}	partial pressure of oxygen (kPa)
P	pressure (kPa)
r	reaction rate (1/s), (kg/(kg catalyst s))
T	temperature (K)
$\bar{V}$	cross-sectionally averaged velocity (m/s)
y	weight fraction of species (-)
z	downer or riser length (m)

References

[1] W. Letzsch, Handbook of Petroleum Processing, Springer, Dordrecht, Netherlands (2008).
[2] J.X. Zhu, Z.Q. Yu, Y. Jin, J.R. Grace and A. Issangya, Can. J. Chem. Eng. 73 (1995) 662-677.
[3] Y. Jin, Y. Zheng and F. Wei, in: J. Grace, J. Zhu, H. de Lasa (Eds.), Circulating Fluidized Bed Technology VII, Canadian Society for Chemical Engineers, Niagara Falls, (2002), pp. 40.
[4] M.A. Abul-Hamayel, Pet. Sci. Technol. 22 (2004) 475-490.
[5] C. Wu, Y. Cheng and Y. Jin, Ind. Eng. Chem. Res. 48 (2009) 12-26.
[6] D. Bai, J.X. Zhu, Y. Jin and Z. Yu, Ind. Eng. Chem. Res. 36 (1997) 4543-4548.
[7] D. Bai, J.X. Zhu, Y. Jin and Z. Yu, Chem. Eng. J. 71 (1998) 97-109.
[8] A.A. Shaikh, E.M. Al-Mutairi and T. Ino, Ind. Eng. Chem. Res. 47 (2008) 9018-9024.
[9] P.B. Weisz and R.D. Goodwin, J. Catal. 2 (1963) 397-404.
[10] G. Wang, S. Lin, W. Mo, C. Peng and G. Yang, Ind. Eng. Chem. Process Des. Dev. 25 (1986) 626-630.
[11] A. Chuachuensuk, W. Paengjuntuek, S. Kheawhom and A. Arpornwichanop, Comput. Chem. Eng. 49 (2013) 136-145.

SYSTEMATIC DESIGN OF A HEAT INTEGRATED REACTIVE DISTILLATION FOR BIODIESEL PRODUCTION

Lida Simasatitkul[1], Rafiqul Gani[2], Amornchai Arpornwichanop[1*]

[1] Computational Process Engineering, Department of Chemical Engineering, Faculty of Engineering, Chulalongkorn University, Bangkok,10330 Thailand
[2] CAPEC, Department of Chemical & Biochemical Engineering, Technical University of Denmark, DK-2800, Lyngby, Denmark
[*] Author for correspondence; E-Mail: Amornchai.A@chula.ac.th, Tel. +66 22186999, Fax. +66 22186787

Abstract: Biodiesel is generally produced from transesterification of triglycerides in vegetable oils with methanol. Because free fatty acids in the waste cooking oil is sensitive to alkali catalyst, heterogeneous acid catalyst has been developed to overcome such the limitation. However, high pressure operation is required in order to shift the acid-catalyzed esterification. A reactive distillation has a potential to improve the conversion of reversible reactions and in addition, application of a heat integration concept to design the reactive distillation is beneficial to cost and energy savings. In this work, a systematic design methodology for the heat integrated reactive distillation for biodiesel production from waste cooking oil is developed. A heterogeneous acid catalyzed process based on a single reactive distillation is first analyzed and compared with alkali catalyzed process. A superstructure of the biodiesel process including a full set of alternatives is generated, and then it is reduced through the sequential of constraints, such as purity and properties of product mixture. A total annual cost is used as a criteria to determine the suitable configuration of the heat integrated reactive distillation and design parameters. To design the biodiesel process, it is found that water and glycerol are key components affecting a configuration of the heat integrated reactive distillation. From the developed design methodology, the suitable configurations of the heat integrated reactive distillation after screening step are a thermal coupling indirect sequence reactive distillation integrated with distillation column, a multi-effect indirect split arrangement reactive distillation, a heat integrated reactive distillation with distillation column (with heat exchanger) and a heat integrated reactive distillation with distillation column (without heat exchanger). Based on the minimization of total annual cost, the multi-effect indirect split arrangement reactive distillation shows the best alternative; the cost reduction of 22.35% is obtained, compared with a single conventional reactive distillation.

1. Introduction

Biodiesel is a renewable fuel that has been widely used as an alternative to a conventional petroleum diesel because their properties are similar. A conventional process for biodiesel production is an alkali catalyzed process that uses pure vegetable oil as raw material. However, it is highly expensive resource. Heterogeneous acid catalyzed process for biodiesel production from waste cooking oil becomes alternative option [1].

It has been known that tranesterification and esterification are reversible reactions. The application of reactive separations like a reactive distillation, instead of a conventional reactor, is probably a potential approach to improve conversion of reversible reactions [2]. Furthermore, implementation of a heat integration concept to a reactive distillaiton can reduce an overall process energy consumption, especially for a reactant and product mixture having small difference in their boiling points. In the past, a number of heat-integrated reactive distillation configurations were proposed, such as a petlyuk reactive distillation [3], a thermal coupling reactive distillation [4], an internal heat integrated reactive distillation (HiRDC) [5] and a multi-effect distillation [6].

Although the heat integration of conventional and reactive distillation columns has been studied, a limited works have focused on a systematic design of the heat-integrated reactive distillation. For example, Caballero [7] proposed a design methodology of the sequence of distillation columns and thermally-coupling distillations. Seader et al. [8] proposed the selection of distillation configuration for separation of a ternary mixtures. The criteria is based on an ease-of-separation index (ESI), however, it cannot be applied to heat integrated distillations.

This study presents a systematic design of a heat integrated reactive distillation for biodiesel production. The selection criteria for different configurations of reactive distllaiton with heat integration is also considered. In the proposed methodology, a full set of alternatives of the heat integrated reactive distillation is generated. The number of alternatives is reduced by considering a sequence of contraints, such as purity, properties of the product mixture, and total annual cost, until a feasible one is obtained.

2. Methodology

The methodology for designing a heat integrated reactive distillation is shown in Figure 1.

Step 1: Define problem

The starting point is problem definition, where the number of available renewable sources, the number of desired main products, the qualities of the main products and the performance criteria for the desired process is defined. Here, the minimization of a total annual cost is set as a target for process design.

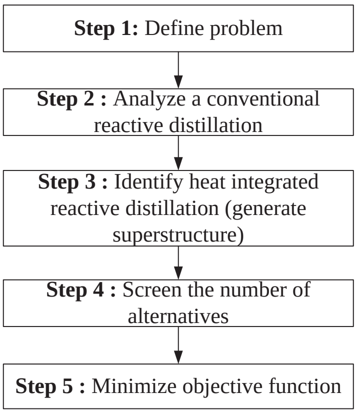

Figure 1. Design methodology of the heat integrated reactive distillation**.**

Step 2: Analyze a conventional reactive distillation

In this step, a conventional reactive distillation is analyzed in order to determine the limitation of the reactive distillation. The boiling point of all components is ranked and the boiling point ratio of adjacent components is used to find top and bottom products. If the boiling point ratio is equal to one, a solvent selection is needed.

Step 3: Identify heat integrated reactive distillation

The objective of this step is to generate a full set of heat integrated reactive distillation column.

Step 4: Screen the number of alternatives

All process design alternatives is screened through the constraints until a feasible one is obtained. This step is divided into three sub-steps. First, the number of alternatives is reduced through the easier constraints that perform by the purity of components. If high purity of non-key component is required (95%), the multi-effect indirect split arrangement reactive distillation, heat integrated reactive distillation with distillation column are eliminated. Secondly, the boiling point ratio of key components is considered. If it is higher than 1.3 but less than 1.5, a feed split multi-effect reactive distillation is a preferable option. When the boiling point ratio equals to 2, the petyuk reactive distillation is a preferable choice. Finally, the key component is taken into account. If the key component is the lightest or light component, a direct sequence thermal coupling reactive distillation is choosen as a preferable option, whereas it is light component and the heaviest component, an indirect sequence thermal coupling reactive distillation and multi-effect indirect split arrangement reactive distillation is preferable. Otherwise, a heat integrated reactive distillation with distillation column (with and without heat exchanger between the two columns) is chosen.

Step 5: Minimize objective function

The objective function, such as a total annual cost and energy consumption, is minimized in order to find a feasible one and suitable parameters, such as the number of reactive stages, the number of stripping stages, the number of rectifying stages and feed location.

3. Case study: Biodiesel production from waste cooking oil

In this case study, a biodiesel production from waste cooking oil using heterogeneous acid catalyst is studied. Trilinolein is represented as triglyceride while oleic acid is represented as free fatty acid. A reactive distillation is applied to produce the biodiesel product (methyl ester) at high pressure operation. Crude biodiesel consisting of biodiesel, methanol, glycerol and unreacted triglyceride is obtained at the bottom of the reactive distillation column while excess methanol is removed at the top of the column. A conventional reactive distillation for biodiesel production is shown in Figure 2.

To design a heat integrated reactive distillation, the proposed methodology is applied. The methodology starts with the problem definition (Step 1). Here, the minimization of a total annual cost is considered the objective function, as given in Equation 1.

$$\min TAC = \text{Operating cost} + \frac{\text{Capital cost}}{3} \qquad (1)$$

subject to process model, the product specification (purity of methyl ester from reactive distillation = 84%), purity of methanol is 99.5% , production rate and binary decision variable (a selection of type of the heat integrated reactive distillation).

At Step 2, the boiling point of all components in the biodiesel production process is ranked and then the boiling point ratio of adjacent component is computed as shown in Table 1. It is found that the ratio of boiling point of water and glycerol is the highest value; therefore, methanol and water are removed at the top of the column while other components, such as methyl oleate, glycerol, unreacted triolein, are removed at the bottom. It can be seen that the reactive distillation can separate the light product from the heavy product.

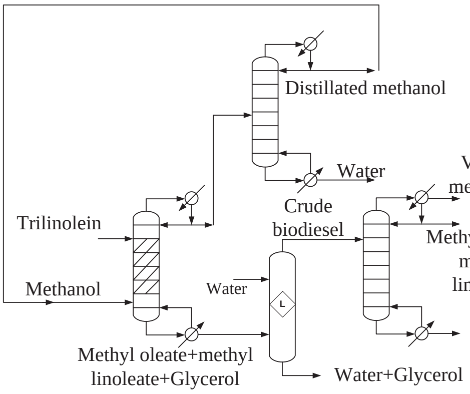

Figure 2. Conventional reactive distillation process for biodiesel production using heterogeneous acid catalyze.

Table 1: The ratio of boiling point of adjacent components

component	Ratio of boiling point
Methanol/water	1.45
Water/glycerol	2.85
Glycerol/methyl oleate	1.1
Methyl oleate/oleic acid	1.03
Oleic acid/trilinolein	1.45

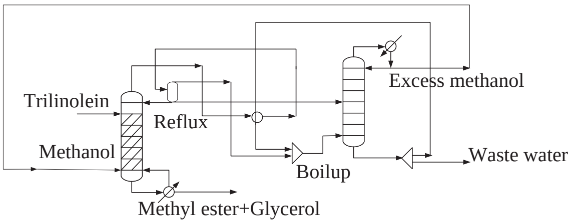

Figure 3. Multi-effect indirect split arrangement reactive distillation.

A full set of alternatives for heat integrated reactive distillation is identified (Step 3). They include HiRDC without heat exchanger, HiRDC with heat exchanger, petyuk RD, feed split multi-effect RD, HiRDC with distillation column without heat exchanger, HiRDC with distillation column with heat exchanger, thermal coupling indirect RD integrated with distillation column, thermal coupling direct sequence RD integrated with distillation column and multi-effect indirect split arrangement RD integrated with distillation column. Thus, the number of alternatives is 9.

To screen the alternatives (Step 4), the ratio of boiling point is used as criteria. Since the boiling point ratio of the key component is 2.85, the feed split multi-effect RD, HiRDC without heat exchanger, HiRDC with heat exchanger and petyuk RD are eliminated. As a result, the number of alternatives is reduced from 9 to 5. Since the key components are the light component (water) and the heavy component (glycerol), the direct sequence thermal coupling RD integrated with distillation column is eliminated.

Next, a rigorous simulation by using a process simulator is performed and the suitable process parameters, such as operating pressure, the number of reactive stages, the number of stripping stages and the number of rectifying stages are determined based on the minimization of TAC (Step 5). The most suitable configuration of the heat integrated RD is obtained at the end of this step. Details of this simulaiton step will be described in the next section.

3.1 Multi-effect indirect split arrangement reactive distillation

Mult-effect indirect sequence multi-effect RD is shown in Figure 3. Heat integration between reactive distillation and distillation columns is carried out through a heat exchanger, which acts as a condenser for the reactive distillation and as a reboiler for the distillation column.

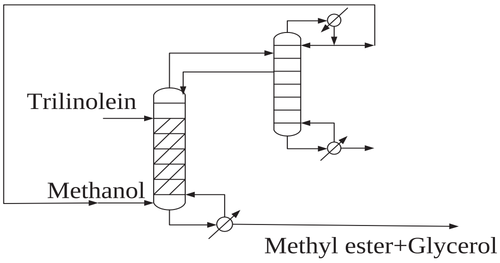

Figure 4. Indirect thermal coupling reactive distillation.

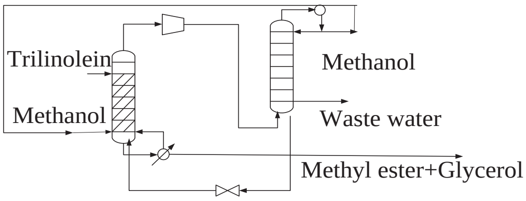

Figure 5. Heat integrated reactive distillation without heat exchanger (HiRDC without heat exchanger).

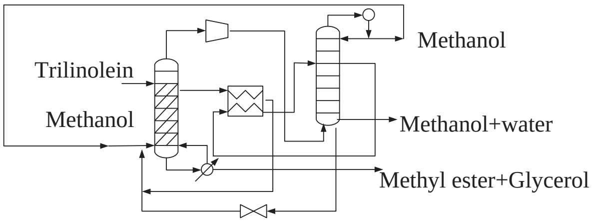

Figure 6. Heat integrated reactive distillation with heat exchanger (HiRDC with heat exchanger)

3.2 Thermal coupling indirect sequence reactive distillation

The principle of an indirect thermal coupling RD is similar to the multi-effect indirect split arrangement RD; however, there is no heat exchanger to transfer the heat (Figure 4). Thus, the number of unit operations is reduced because a condenser of the reactive distillation is eliminated.

3.3 Heat integrated reactive distillation without heat exchanger (HiRDC)

HiRDC is considered a process intensification between vapor recompression and heat integration of distillation column (assumed as rectifying section) and reactive distillation (assumed as stripping section). The liquid at the bottom of distillation column that is higher pressure is sent to reactive distillation for supplying the heat. In this case heat exchanger between reactive distillation and distillation is not installed. The configuration of heat integrated reactive distillation without heat exchanger is shown in Figure 5.

3.4 Heat integrated reactive distillation with heat exchanger

The principle of HiRDC with heat exchanger is similar to the heat integrated reactive distillation without heat exchanger; however, there are heat exchangers between rectifying section and stripping section so heat from the rectifying section can be transferred to the stripping section due to the difference of temperature between the two columns. The configuration of heat integrated reactive distillation with heat exchanger is shown in Figure 6.

4. Results and discussion

The chosen configurations of a heat integrated reactive distillation obtained after performing a screening process are shown in Table 2.

Table 2: Comparison of conventional and heat integrated reactive distillation for biodiesel production from waste cooking oil

	1	**2**	**3**	**4**	**5**
Pressure of RD column (bar)	5.5	6	6	6	6
Pressure of DC	1	1	1	23	23
Reactive stage of RD	11	3	9	8	8
Rectifying stage of RD	-	-	1	1	1
Stripping stage of RD	1	-	-	-	-
Total stage of DC	9	4	10	10	10
TAC of RD ($x10^6$\$/year)	1	1.05	1.07	1.17	1.107
TAC of distillation ($x10^5$\$/year)	5.6				
TAC of the processes ($x10^6$\$/year)	2.255	1.74	1.76	1.865	1.8
Cost saving (%)	-	22.35	21.95	17.3	20.17

Note: 1 = Conventional RD, 2 = multi-effect indirect split arrangement RD, 3 = Thermal coupling RD, 4 = HiRDC without heat exchanger, 5 = HiRDC with heat exchanger

Operating pressure for all types of the heat integrated reactive distillation is higher than a conventional RD because it is needed to increase the reboiler duty of reactive distillation and to ahieve the production rate. The results shown in Table 2 indicate that the multi-effect indirect split arrangement RD can reduce the number of unit operations because heat is transferred from the vapor stream (hot stream) of RD to the liquid stream (cold stream) of distillation. Multi-effect indirect split arrangement RD can acheive the lowest TAC. Although the other types of the heat integrated RD can reduce the TAC, compared to the conventional RD, the multi-effect indirect split arrangement RD is the most feasible one as it is operated at atmospheric pressure. The result for screening procedure is given in Table 3. At the end, the best process is found to be the multi-effect indirect split arrangement reactive distillation.

Table 3: Alternative processes obtained the screening step

Step	**Criteria**	**Number of alternatives**
1,2,3	-	11
4	Purity of waste water from distillation column	9
	Ratio of boiling point of key components	5
	Type of key components	4
5	Minimum TAC	1

5. Conclusions

In this study, a design methodology for a heat integrated reactive distillation is proposed. A full set of all possible heat integrated reactive distillations is first generated. Component purify, a boiling point ratio of adjacent components and key component are considered to screen the process alternatives. The best heat integrated reactive distillation is selected based on a minimization of a total annual cost. The proposed design methodology is demonstrated via a biodiesel production from waste cooking oil, as a case study. The results show that the multi-effect indirect split arrangement reactive distillation is the best suitable heat integrated reactive distillation for biodiesel production.

Acknowledgements

Support from the Thailand Research Fund (RGJ-PhD Program), CAPEC of Technical University of Denmark (DTU) and the Computational Process Engineering Research Group, the Special Task Force for Activating Research (STAR), Chulalongkorn University Centenary Academic Development Project is gratefully acknowledged.

References

[1] K. Jacobson, R. Gopinath, L.C. Meher and AK. Dalai, *Appl. Catal., B* **85** (2008) 86-91.

[2] B. He, *Final Report* National Institute for Advanced Transportation Technology University of Idaho (2006).

[3] F. Gomez-Castro, V. Rico-Ramirez, J. Segovia-Hernandez and S. Hernandez, *Chem. Eng. Prog.* **49** (2010) 262-269.

[4] S. Wang, H. Huang and C. Yu, *Ind. Eng. Chem. Res* **49** (2010) 750-760.

[5] SV. Mali and AK. Jana, *Sep. Purif. Technol.* **70** (2009) 136-139.

[6] H. Lee, Y. Lee, I. Chien and H. Huang, *Ind. Eng. Chem. Res.* **49** (2010) 7398-7411.

[7] JA. Caballero and IE. Grossman, *Comput. Chem. Eng.* **28** (2008) 2307-2309.

[8] WD. Seider, JD. Seader and DR. Lewin Production & Process Design Principles Wiley, New York (2004)

CHARACTERIZATIONS AND PROPERTIES OF CONSTRUCTION BRICK IN SMALL AND MICRO ENTERPRISE COMMUNITY IN CLAY BRICK MAKING GROUP SAN BUN REUNG VILLAGE, LAMPANG PROVINCE

Soravich Mulinta[1] , Sukdipown Thiansem[2]

[1]*Department of Technology ceramics, Faculty of Industrial Technology, Lampang Rajaphat University, Lampang,52100 Thailand*
[2]*Department of Industrial Chemistry, Faculty of Science, Chiang Mai University, Chiang Mai, 53000, Thailand*
* Author for correspondence*: E-mail:* Soravich_mu48@hotmail.com ,Tel +66 80 858 5538

Abstract : The objectives of this study were to characterize the properties of construction bricks made by Small and Micro Enterprise Community clay brick making group in San Bun Reung village, Lampang for designed drying technique. The characterization was analyzed by particle size, chemical, mineral and differential thermal analyses. The physical and mechanical properties were tested consisting of the moisture content, shrinkage, bulk density, microstructure, pore volume, bending strength and compressive strength. The experimental drying system of clay brick was carried out by heating up and drying temperature in the range of room temperature – 40, 40 – 50, 50 – 60 and 60 – 70 °C. The results showed that the clay brick had 25% moisture content. Drying heating up with wood fuel at 50 – 60 °C, and drying time for 21 hours were optimum conditions. The clay brick had 6.5% shrinkage value.

1. Introduction

Clay brick is the first man made artificial building material and one of the oldest building materials known. Its widespread use is mainly due to the availability of clay in most countries. Its durability and aesthetic appeal also contribute to its extensive application in both load bearing and non-load bearing structures [1]. According to their purpose they are divided into blocks for outside and inside wall, foundation cellar wall, etc [2].

In data collection of Small and Micro Enterprise Community in Clay Brick Making Group San Bun Reung Village, there is a great production of red brick, mainly perforated brick, estimated in 200,000 units/month. Brick are normally fired at temperature around 900 °C in up draft kiln type furnace, using fire wood as fuel, using firing time at 2 days. Considering only the firing stage, 23.5 tons of fired bricks waste are generated every month by the community. Quantity damage of clay brick from forming, drying and firing section respectively, as show in the table 1.

Table 1: The amount of damage caused in the processing of clay brick.

Processing	Number of Production (brick)	Damage (brick)	Percentage of damage. (%)
Forming	25,000	-	-
Drying	25,000	2,830	11.3
After firing	22,170	285	1.1
total	25,000	3,115	12.4

11.3% of damage on solar dryer at 7 -15 days were caused by warping and cracking in drying section.

Drying of the removal of water from clay brick can take place only at the surface of the brick ware by evaporation. The water on the interior of the ware must travel to the surface by seeping or wicking through interconnected pores. Both processes evaporation and seepage toward the surface are accelerated by heating. Furthermore, the rate of evaporation of water from the surface is accelerated by low surrounding humidity and by rapid air movement across the surface [3], the drying of clay brick in a constant environment (e.g. with the velocity, humidity and temperature of the drying-air constant) [4]. The basic requirements for good drying rate are high temperature of the air to provide the latent heat, and low relative humidity of the air to maintain the pressure differential and a sufficiently high velocity of the air to give turbulence and effective vapour removal [5] The literatures on drying divide a drying process into; (i) “constant rate period” with initial weight loss and major shrinkage, and (ii) :declining rate period” with successive weight loss and minor shrinkage. The shrinkage process an lead to the occurrence of the drying crack of the ceramic bodies [6].

The aim of this study to characterization and properties of construction brick in Small and Micro Enterprise Community in Clay Brick Making Group San Bun Reung Village, Lampang Province for designed drying technique. The experimental drying system and drying temperature for clay brick were dried in the range of room temperature – 40, 40 – 50, 50 – 60 and 60 – 70 °C.

2. Experimental procedure

2.1 Raw materials for forming clay brick.

The raw material used in the study are from local soures. They are pong san tong red clay in lampang province.

2.2 Characterization analysis of raw material.

Particle size of the raw material was analyzed by laser diffraction (Mastersizer S, Malvern, USA). Chemical composition of the raw material was analyzed by X-ray fluorescence (XRF, Megix Pro MUA/USEP T84005, Philips, USA). Mineralogical composition was identified by X-ray diffraction (XRD, D500, Siemens, Germany). Thermal behavior of the raw material was analyzed by Differential thermoanalysis (DTA) and thermogravimetry (TG) were simultaneously conducted in a model STA 409 EP, using powder sample screened pass through mesh no. 200. Operating condition was under a 100 ml/min flow of air with heating rate of 10°C/min.

2.3 Study of drying techniques for clay brick.

The experimental drying technique and drying temperature for clay brick were dried in the range of room temperature – 40, 40 – 50, 50 – 60 and 60 – 70 °C. using dryer cabinet as shown in figure.1

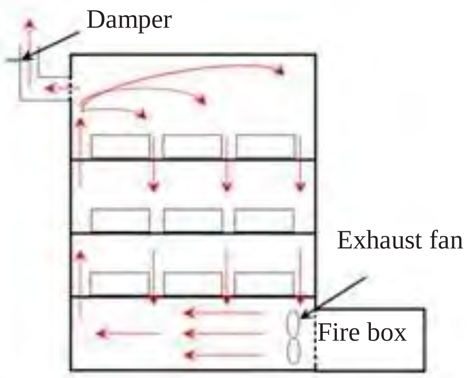

Figure 1. The dryer cabinet

2.4 Properties measurement of clay brick.

Tests to obtain linear shrinkage, water absorption, mechanical strength and compressive strength were carried out. Linear shrinkage was assessed as the difference between the diameter of the dry and fired specimens divided by the diameter of the dry specimen. Water absorption was calculated by measuring the weight of the test specimens after placing them in boiling water for 5 h.

The microstructure of the fracture surface of selected dry and fired samples were studied by scanning electron microscopy, SEM, using a JSM-5910 LV, JEOL , Japan. The pore volume was obtained by surface area analyzer, using a nitrogen absorption, in an Autosorb 1 MP Quantachrome.

3. Result and Discussion

3.1 Characterization of raw material.

Particle size of raw material was controlled by grinding and passing through a 40 mesh sieve (particles smaller than 0.42 mm.) having particle size average of 4.94 μm.

The chemical composition of raw material analyzed by X-ray fluorescence is shown in Table 1. The major components included of silicon oxide (SiO_2), aluminum oxide (Al_2O_3) and ferric oxide (Fe_2O_3). CaO, K_2O, BaO MnO, ZrO_2, TiO_2, P_2O_5, MgO, Y_2O_3 and Rb_2O were in small quantities. Raw material used for clay brick production had a large amount of ferric oxide up to 12.4wt%.

The mineralogical composition of raw material was analyzed by X-ray diffraction**.** Figure 2 shows the XRD pattern of the raw material. The predominant peaks were associated with quartz (Q), while secondary peaks identified the crystalline mineral phase of orlymanite (O) muscovite (Mu) and montmorillonite (Mo).

Thermal behavior was analyzed by Differential Thermal analysis and Thermal Gravimetric (DTA/TG) fired at 900 °C with the firing rate of 10°C /min. Figure 3 shows the DTA/TG curve of the raw material. Two endothermic peaks were identified. The first endothermic peaks A at 180 °C was due to hygroscopic water and was associated with a 3.0 % of weight loss. The second peak B at 523 °C was due to the dehydroxylation of the remaining quartz with a weight loss of 1.5%.

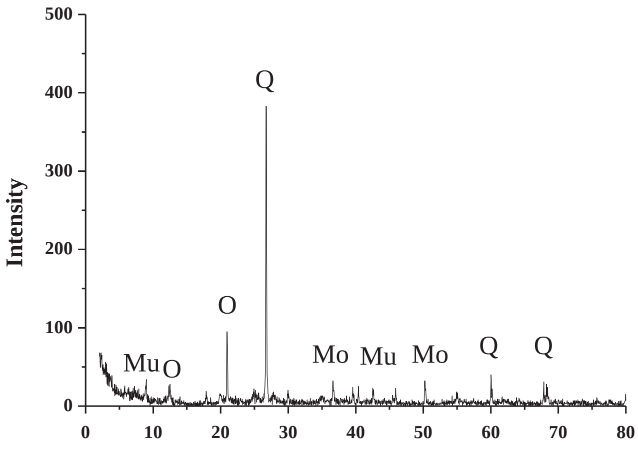

Figure 2. X-ray diffraction of the raw material. Q = Quartz; O = Orlymanite; Mu = Muscovite and Mo = Montmorillonite.

Table 1:Chemical composition of the raw material.

Element	SiO_2	Al_2O_3	Fe_2O_3	CaO	K_2O	BaO	MnO	MgO	TiO_2	P_2O_5	LOI
Chemical composition (%wt)	63.08	15.42	12.44	0.48	3.84	< 0.01	0.26	0.46	1.32	0.66	2.05

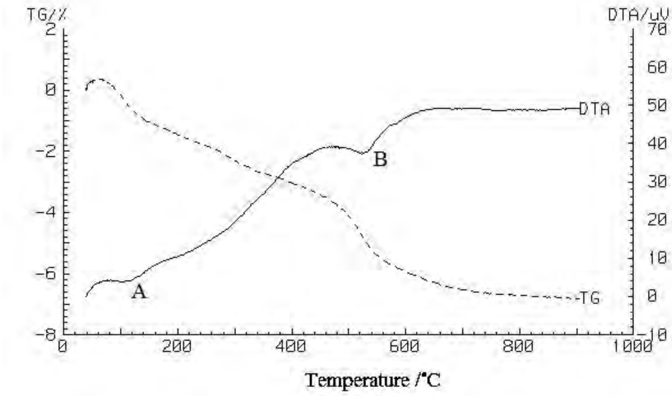

Figure 3. DTA/TG curve of the raw material.

3.2 Study of drying techniques for clay brick

The experimental drying technique of clay brick was as followed. The mixed clay dough was made by grinding. After 24 h aging, the dough was extruded into a rectangle bar (80 mm Width × 200 mm Length × 60 mm Height).

The results showed that the clay brick after forming had 25% moisture content with drying heating up with wood fuel at room temperature – 70 °C**.**

For the drying temperature at room temperature – 40°C, the first of drying, the moisture content between 25 to 15% during the induction. Clay brick was exposed to heat (sensible period) with clay bricks had higher temperature. The moisture content of 16.4% was found that the clay bricks had the slowest rate of drying, 0.44 g/h. Humidity at a critical point (critical moisture content; X_C), found the mass transfer [8]. The moisture transfer of clay material depends on the moisture content (on a dry basis) of the product The drying time was 24 h.

For the drying temperature at 40 – 50°C**,** moisture content of 13.6% was found that the clay bricks had the highest rate of drying, 0.6 g/h. Humidity at a critical point (critical moisture content; X_C) had the drying time of 23 h.

For the drying temperature at 50 – 60°C, moisture content of 14.5% was found that the clay bricks had the high rate of drying, 0.83 g/h. Humidity at a critical point (critical moisture content; X_C) had drying time of 16 h. The moisture content of between 5-14% of water under the surface of clay brick evaporation continued, and drying to equilibrium as shown in Figure 4.

The clay brick of drying temperature at 60 – 70°C**,** moisture content of 16.4% was found that the clay bricks had the highest rate of drying, 0.97 g/h. Humidity at a critical point (critical moisture content; X_C), had the drying time of 15 h end of drying. 70% of the amount of damage included cracking and warping due to high temperature drying.

Figure 5 shows linear shrinkage of the dry clay brick during dry at 50-60 °C. Clay brick with a slowly shrinking continued. When drying was completed, no damage was found in the clay brick.

The optimum temperature for drying clay brick was in range 50-60°C, due to the high drying rate, less drying temperature and not damage.

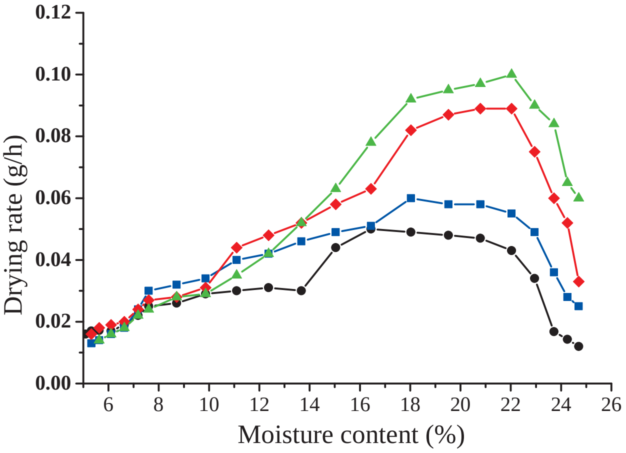

Figure 4. The moisture content on drying rate for clay brick drying.

● = < 40 – 40 ■ = 40 – 50 ◆= 50 – 60 ▲ = 60 – 70

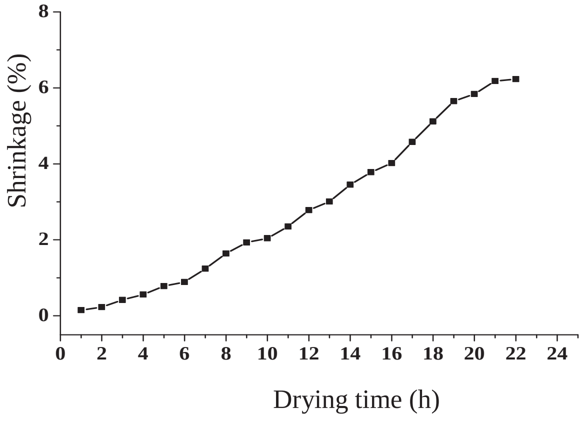

Figure 5. The moisture content on shrinkage for clay brick drying at 50 – 60 °C

3.2 Properties of clay brick.

For shrinkage of the clay brick before and after firing temperature at 900 °C, the results showed that the clay brick before firing had shrinkage of 6.5% and clay brick after firing had shrinkage of 13.5%.

For bulk density of the clay brick before and after firing temperature at 900 °C, the results showed that the clay brick before firing had bulk density of 2.93 g/cm^3 and clay brick after firing had bulk density of 3.18 g/cm^3.

For water absorption of the clay brick after firing temperature at 900 °C, the results showed that the clay brick after firing had water absorption of 12.85%.

Bending strength of the clay brick before and after firing temperature at 900 °C showed that the clay brick before firing had resistance of bending of 8.75kg/cm^2**.** The clay brick after firing had resistant of bending of 61.9 kg/cm^2**.**

Compressive strength of the clay brick before and after firing temperature at 900 °C showed that the clay brick before firing had compressive of 33.5kg/cm^2**.** The clay brick after firing had compressive of 116 kg/cm^2**.**

Table 2: Physical and mechanical properties of clay brick.

Properties	**Before firing**	**After firing**
Shrinkage(%)	6.5	13.5
Bulk density(g/cm^3)	2.93	3.18
Water absorption(%)	-	12.85
Specific surface area (m^2/g)	0.3977	0.1722
Pore volume (cc/g)	0.1050	0.0687
Bending strength (kg/cm^2)	8.75	61.95
Compressive strength (kg/cm^2)	33.5	116

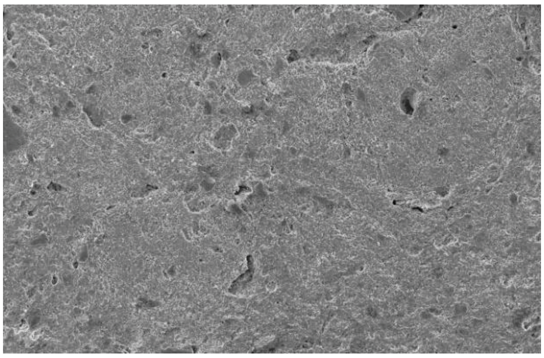

Figure 6. Microstructure of clay brick before firing

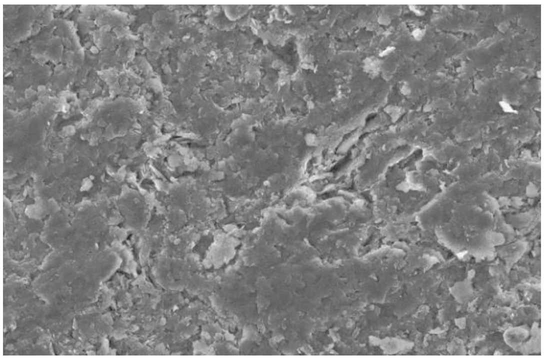

Figure 7. Microstructure of clay brick after firing

The microstructure of clay brick investigated by scanning electron microscope showed the sand and pore were consisted in the brick construction. A fracture surface with an apparently higher amount of pores is observed as shown in Figure 6. The microstructure of fired clay brick could be observed that both bodies presented a rough fractured surface with loose particle and interconnected pores as shown in Figure 7.

4. Conclusions

Clay brick drying system of clay brick was carried out by heating up and drying temperature in the range of room temperature – 40, 40 – 50, 50 – 60 and 60 – 70 °C. The results showed that the clay brick had 25% moisture content. Drying heating up with wood fuel at 50 – 60 °C, and drying time for 21 hours were optimum conditions. The clay brick had 6.5% shrinkage. The characterizations and the properties of clay bricks produced by the community fulfilled the requirements of Thai industrial standard (TIS 77-2545).

Acknowledgments

The authors would like to thank Lampang Rajaphat University for experiment and support for research.

References

[1] I Johari, RP Jaya, ZA Ahmad, BHA Bakar, S Said. *Chemical and Physical Properties of Fired-Clay Brick at Different type of Rice Husk Ash.* IPCBEE **vol.8** (2011) IACSIT Press, Singapore

[2] P.P. Budnikov, *The technology of ceramics and refractories*, MIT Press, Cambridge, MA, (1964), 5-6.

[3] JT Jone, MF Beroad. *Ceramics Industrial Processing and Testing.* Second edition. Iowa State University Press, Ames, (1993), pp. 107.

[4] RW Ford. *Ceramics Drying.* (1986) First ed. Pergamon, Oxford. 3-4.

[5] D Allen. *Pottey science*, *Materia* , *Process and Products.* (1986) Chichester, West Sussex, England : Ellis Horwood Ltd, 126 – 127.

[6] A Prapun, W Shigetaka. *Correlation between Bigot and Ratzenberger drying sensitivity indices of red clay from Ratchaburi province.* Journal of Applied Clay Science **43** (2009) 182-185.

[7] V Belessiotis, E Delyannis. *Solar Drying.* Journal of Solar Energy **85** (2011) 1665 – 169*1*

[8] C Saber, Z Fethi. *Water diffusion coefficient in clay material from drying data.* Journal of Desalination **185** (2005) 491 – 498.

Inorganic Chemistry

ASSEMBLY PROPERTIES OF AMIDOPYRROLIC ANION RECEPTORS: THEORETICAL STUDIES

Korakot Navakhun[1]*, Ranu Sawangsri[1]

[1] Department of Chemistry and Center of Excellence for Innovation in Chemistry, Faculty of Science, Ramkhamhaeng University, Huamark, Bangkapi, Bangkok 10240, Thailand

[*] E-Mail: n_korakot@ru.ac.th, Tel. +66 2 3108400, Fax. +66 2 3108401

Abstract: Assembly properties of two amidopyrrolic anion receptors, 3,4-dichloro-diphenyl-1*H*-pyrrole-2,5-dicarboxamide (L^1H) and 3,4-tetraphenyl-1*H*-pyrrole-2,5-dicarboxamide (L^2H), in the systems with fluoride, chloride, bromide and hydroxide ions have been investigated using the B3LYP/6-31G(d) level of theory. The results show that anionic induced self-assembly dimerization processes via $NH_{amide}\cdots N^{-}_{pyrrole}$ interactions were obtained in the L^1H systems with fluoride and hydroxide ions. However, in the L^1H systems with chloride and bromide ions, anion complexation processes were obtained. In the other hand, anion complexation processes were obtained in all L^2H systems with these anions.

1. Introduction

Assembly properties of anionic molecules have been interested from a numbers of researches to know these unusual processes that perform the new noncovalently link molecular architectures [1,2]. Amidopyrrolic anion receptors containing with the electron withdrawing groups such as chlorine and intro groups have been found the formation of the anionic self-assembly dimers via $NH_{amide}\cdots N^{-}_{pyrrole}$ interactions in the solid state [3,4]. In theses structures, the pyrrole groups have been deprotonated and the N^- centers were stabilized by the formation of two amide $NH\cdots N^-$ hydrogen bonds from another anions. Vice versa, another N^- atoms were stabilized in the same way from the opposite anionic pyrroles resulting to the formation of their anionic self-assembly dimers. These processes have been studied using the density functional theory (DFT) calculation methods [5-8]. In this work, two amidopyrrolic anion receptors which are 3,4-dichloro-diphenyl-1*H*-pyrrole-2,5-dicarboxamide (**L**^{1}H) and 3,4-tetraphenyl-1*H*-pyrrole-2,5-dicarboxamide (**L**^{2}H), have been investigated theoretically their anionic self-assembly properties in the systems with fluoride, chloride, bromide and hydroxide ions.

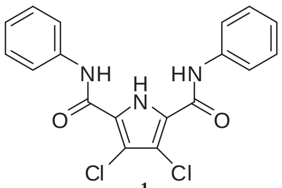

L^{1}H

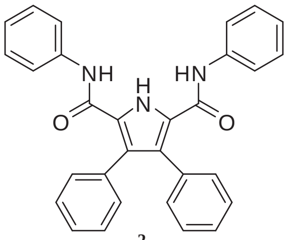

L^{2}H

2. Materials and Methods

Geometries of various species of **L**^{1}H and **L**^{2}H, their deprotonated species, fluoride, chloride, bromide and hydroxide complexes and anionic self-assembly dimer have been optimized using the density functional theory (DFT) method. The DFT calculations have been performed with the Becke's three-parameter exchange functional with the Lee–Yang–Parr correlation functional (B3LYP). All geometry optimizations have been carried out using the MO computations at the B3LYP/6-31G(d) level and single point calculations at the B3LYP/6-31G(d) level. All calculations were performed with the GAUSSIAN09 program.

Stepwise deprotonation reactions of the system in presence and absence of the fluoride, chloride, bromide and hydroxide ions (X^-) are described by the following equations.

System without X^-:

$$2\mathbf{L}H \rightleftharpoons 2\mathbf{L}^- + 2H^+ \rightleftharpoons [\mathbf{L}_2]^{2-} + 2H^+ \qquad \textbf{(1)}$$

System with X^-:

$$2\mathbf{L}H + 2TBA.X^- \rightleftharpoons 2[\mathbf{L}H.X]^- + 2TBA^+ \qquad \textbf{(2)}$$

$$2[\mathbf{L}H.X]^- + 2TBA^+ \rightleftharpoons [\mathbf{L}_2.2TBA] + 2HX \qquad \textbf{(3)}$$

3. Results and Discussion

The B3LYP/6-31G(d) optimized structures of non-deprotonated, deprotonated species and their complexes with fluoride, chloride, bromide and hydroxide ions of **L**^{1}H and **L**^{2}H are shown in Figure 1 and 2 respectively.

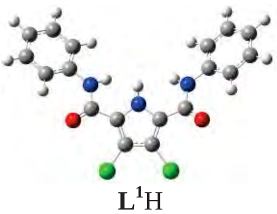

L^{1}H

L^{1-}

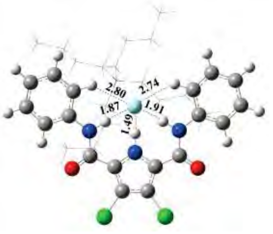

[**L**^{1}H.F]$^-$

[**L**^{1}H.Cl]$^-$

$[\mathbf{L^1}H.Br]^-$ $[\mathbf{L^1}H.OH]^-$

Figure 1. The B3LYP/6-31G(d) optimized structures of non-deprotonated, deprotonated species and their complexes with fluoride, chloride, bromide and hydroxide ions of $\mathbf{L^1}$H.

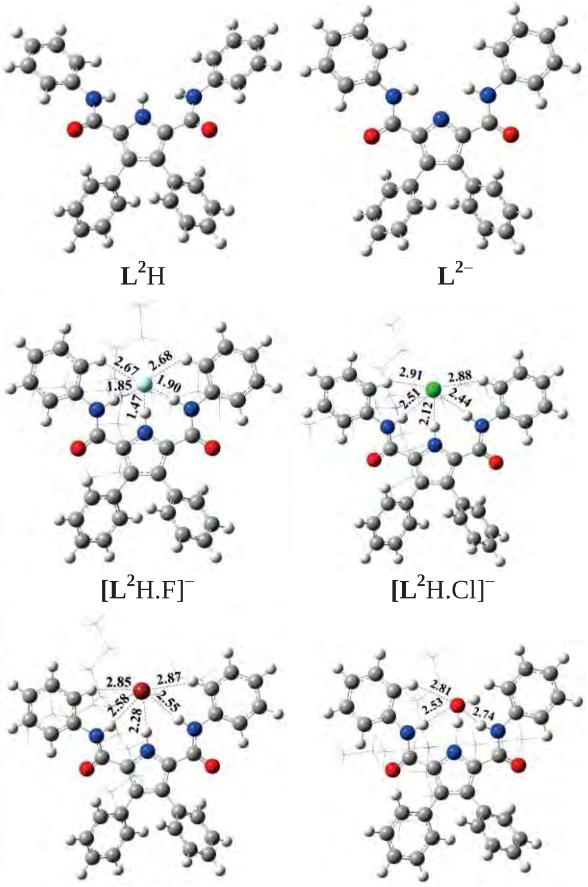

$\mathbf{L^2}$H $\mathbf{L}^{2-}$

$[\mathbf{L^2}H.F]^-$ $[\mathbf{L^2}H.Cl]^-$

$[\mathbf{L^2}H.Br]^-$ $[\mathbf{L^2}H.OH]^-$

Figure 2. The B3LYP/6-31G(d) optimized structures of non-deprotonated, deprotonated species and their complexes with fluoride, chloride, bromide and hydroxide ions of $\mathbf{L^2}$H.

The B3LYP/6-31G(d) optimized structures of $[\mathbf{L^1}_2.2TBA]$ and $[\mathbf{L^2}_2.2TBA]$ are shown in Figure 3. The relative energy profiles for self-assembly processes of the absence of anion for $\mathbf{L^1}$H and $\mathbf{L^2}$H computed at the B3LYP/6-31G(d) are shown in Figure 4. The relative energy profiles for self-assembly processes for $\mathbf{L^1}$H and $\mathbf{L^2}$H in the presence of fluoride, chloride, bromide and hydroxide ions computed at the B3LYP/6-31G(d) are shown in Figure 5, 6, 7 and 8 respectively.

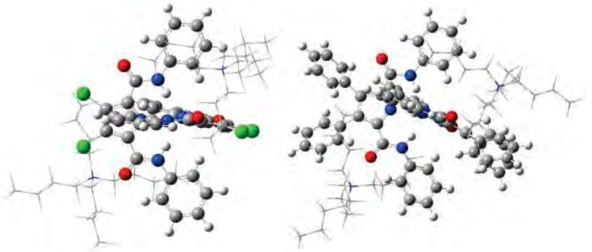

$[\mathbf{L^1}_2.2TBA]$ $[\mathbf{L^2}_2.2TBA]$

Figure 3.The B3LYP/6-31G(d) optimized structures of $[\mathbf{L^1}_2.2TBA]$ and $[\mathbf{L^2}_2.2TBA]$.

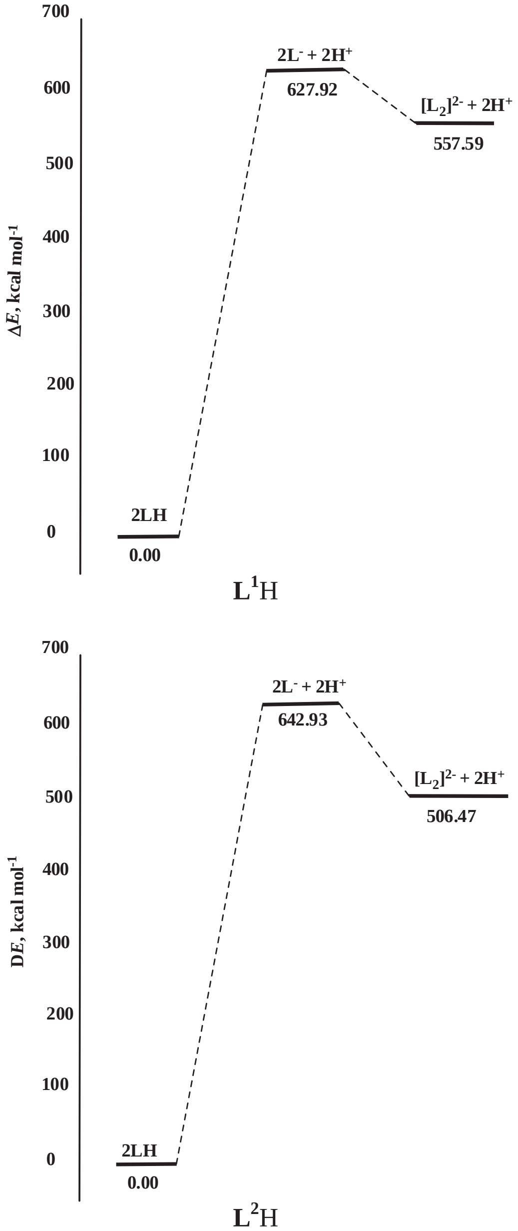

Figure 4. The relative energy profiles for self-assembly processes of the absence of anion for $\mathbf{L^1}$H and $\mathbf{L^2}$H computed at the B3LYP/6-31G(d).

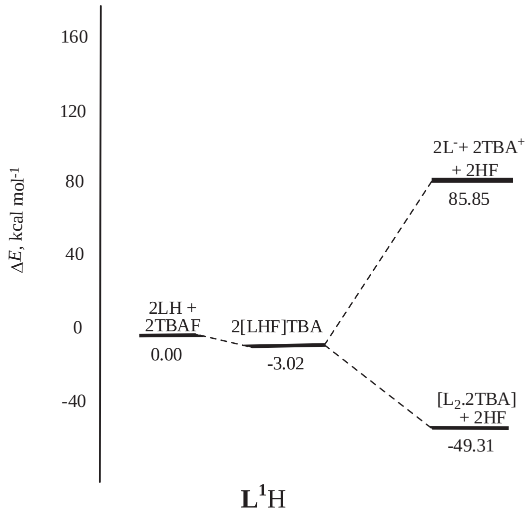

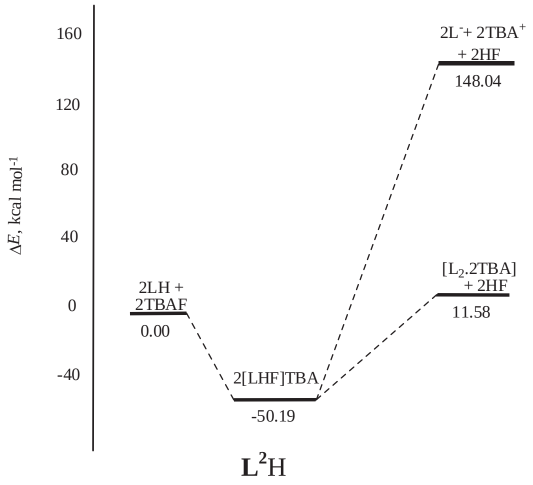

Figure 5. The relative energy profiles for self-assembly processes for $\mathbf{L}^1$H and $\mathbf{L}^2$H in the presence of fluoride ion computed at the B3LYP/6-31G(d).

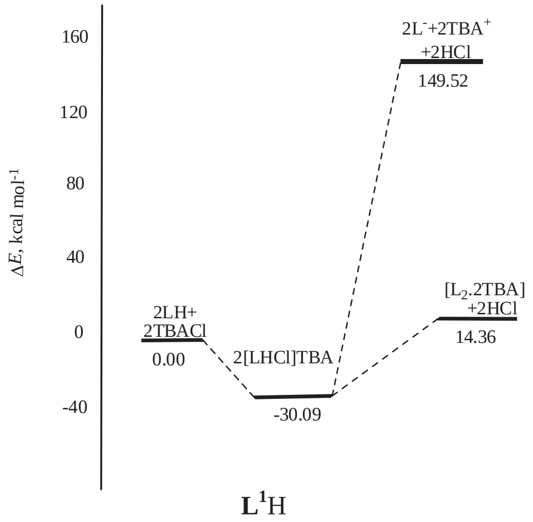

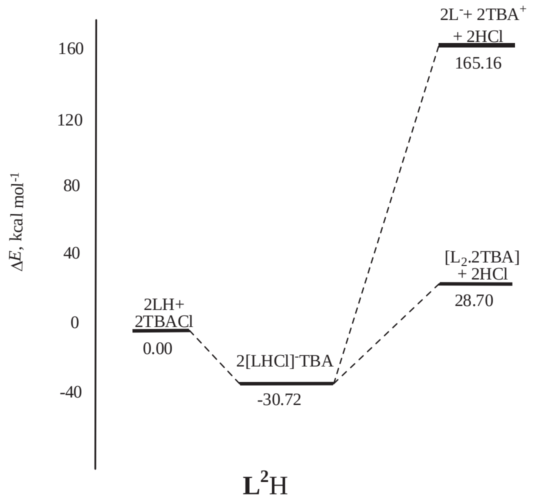

Figure 6. The relative energy profiles for self-assembly processes for $\mathbf{L}^1$H and $\mathbf{L}^2$H in the presence of chloride ion computed at the B3LYP/6-31G(d).

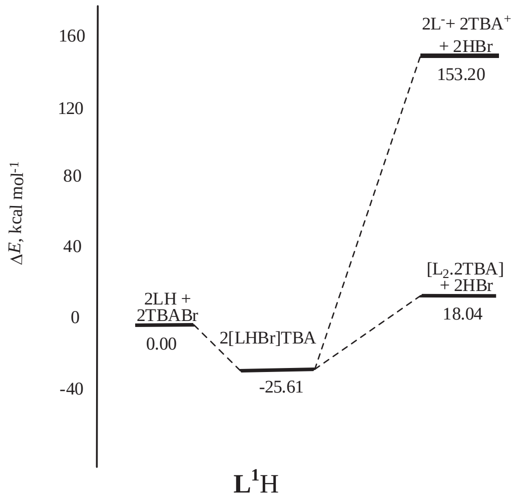

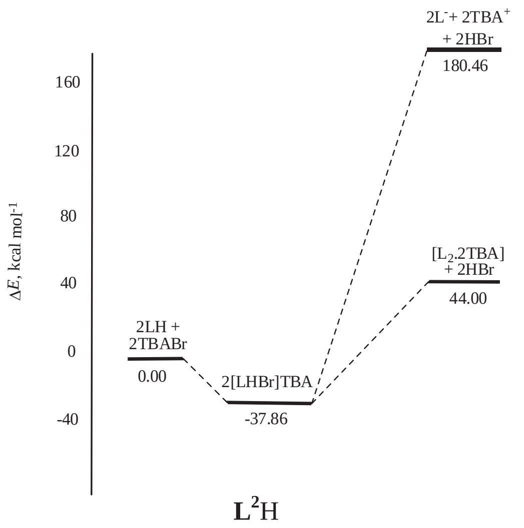

Figure 7. The relative energy profiles for self-assembly processes for $\mathbf{L}^1$H and $\mathbf{L}^2$H in the presence of bromide ion computed at the B3LYP/6-31G(d).

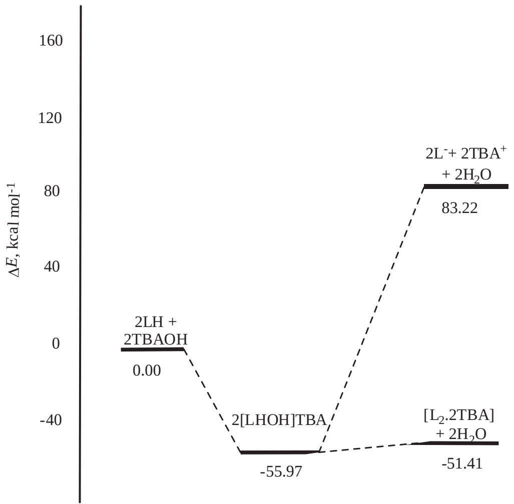

L^1H

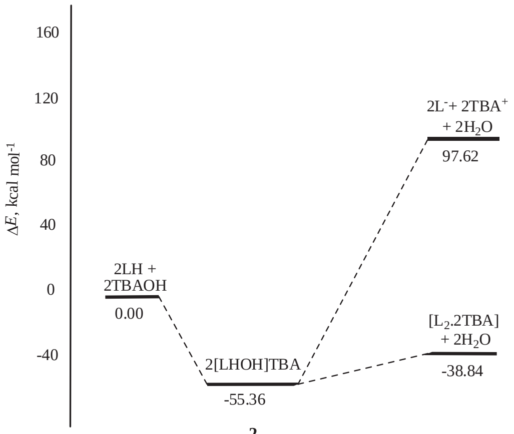

L^2H

Figure 8. The relative energy profiles for self-assembly processes for **L**^{1}H and **L**^{2}H in the presence of hydroxide ion computed at the B3LYP/6-31G(d).

The results show that the self-assembly mechanisms of both compounds as Eq. **(1)** were not occurred due to the high energy in deprotonation step at NH pyrrole. The anion complexation processes as Eq. **(2)** can be used to explain the systems of **L**^{1}H containing chloride and bromide ions and all systems of **L**^{2}H due to [**L**HX]TBA species are more stable than [**L**$_2$2TBA] species. Meanwhile, The self-assembly processes as Eq. **(3)** can be used to explain the systems of **L**^{1}H containing fluoride and hydroxide ions due to [**L**$_2$2TBA] species are more stable than [**L**HX]TBA species.

.

4. Conclusions

Two amidopyrrolic anion receptors, 3,4-dichloro-diphenyl-1*H*-pyrrole-2,5-dicarboxamide (**L**^{1}H) and 3,4-tetraphenyl-1*H*-pyrrole-2,5-dicarboxamide (**L**^{2}H), have been studied their anionic self-assembly properties using DFT computational techniques at B3LYP/6-31G(d) level of theory. The models have been calculated in the systems with fluoride, chloride, bromide and hydroxide ions. It has been found that anionic induced self-assembly dimerization processes via $NH_{amide}\cdots N^{-}_{pyrrole}$ interactions (Eq. **(3)**) were obtained in the **L**^{1}H systems with fluoride and hydroxide ions. However, in the **L**^{1}H systems with chloride and bromide ions, anion complexation processes were obtained (Eq. **(2)**). In the other hand, anion complexation processes (Eq. **(2)**) were obtained in all **L**^{2}H systems with these anions.

Acknowledgements

This research is supported by Commission on Higher Education (CHE), Ministry of Education. The Thailand Research Fund (TRF), Center of Excellence for Innovation in Chemistry (PERCH-CIC) and High Performence Computer Center, Ramkhamhaeng University are gratefully acknowledged.

References

[1] S. Camiolo; P. A. Gale; M. B. Hursthouse; M. E. Light; A. J. Shi, Chem. Commun. (2002) 758-760.
[2] P. A. Gale; K. Navakhun; S. Camiolo; M. E. Light; M. B. Hursthouse, J. Am. Chem. Soc. **124** (2002) 11228-11229.
[3] M. E. Light, P. A. Gale, K. Navakhun, M. Maynard-Smith, Acta. Cryst. **E61** (2005), o1302-o1303.
[4] M. E. Light, P. A. Gale, K. Navakhun, Acta. Cryst. **E61** (2005), o1300-o1301.
[5] K. Navakhun, V. Ruangpornvisuti, J. Mol. Struct. (Theochem) **772** (2006) 23-30.
[6] K. Navakhun, V. Ruangpornvisuti, J. Mol. Struct. (Theochem) **806** (2007) 145-153.
[7] K. Navakhun, V. Ruangpornvisuti, J. Mol. Struct. (Theochem) **864** (2008) 26-30.
[8] K. Navakhun, V. Ruangpornvisuti, J. Mol. Struct. (Theochem) **907** (2009) 131-134.

CHEMICALLY FUNCTIONALIZED MULTI-WALLED CARBON NANOTUBES

Thiyaporn Pansong[1], Kullatat Suwatpipat[1]*, Warut Thammawichai[2]

[1]Department of Chemistry, Faculty of Science, Silpakorn University, Maung, Nakorn pathom, 73000 Thailand
[2]Department of Chemistry, Royal Thai Air Force Academy, Don Maung, Bangkok 10220 Thailand

*E-Mail : kullatat@su.ac.th, Tel. +66 34255797, Fax. +66 34271356

Abstract: The multi-walled carbon nanotubes (MWCNTs) with different surface polarities were prepared by wet chemical method. The as-received MWCNTs were treated with concentrated HNO_3, a mixture of concentrated H_2SO_4/HNO_3 (3:1 v/v), and 0.1M $KMnO_4$. In case of $KMnO_4$, the produced MnO_2 was removed from the obtained MWCNTs by washing with concentrated HCl or 0.34 M $NaHSO_3$. FTIR spectroscopy was used to reveal the functional groups generated on the MWCNTs surface. In addition, KCN was added as an internal standard for functional groups' quantitation. The spectra of all treated MWCNTs showed a broad peak of O-H stretching at 3100-3300 cm^{-1} and a small peak at 1730-1750 cm^{-1} which is assigned as carboxylic group (C=O) vibration,while the carboxylic group (C=O) vibration was not found in the as-received MWCNTs. Normalized with the peak of KCN, the highest intensity of the C=O peak and O-H peaks were found in the MWCNTs treated with H_2SO_4/HNO_3 HNO_3, and $KMnO_4$, respectively. Furthermore, the dispersion behaviors of the treated MWCNTs in various liquid media were examined to determine their surface polarities. The suspended duration of the MWCNTs are varied depending on the treatment. For example, the MWCNTs treated with HNO_3 were dispersed well and floated longer in ethanol and acetone than other liquids, whereas the MWCNTs treated with $KMnO_4$ were suspended in acetone. It indicates the difference in surface polarities of the treated MWCNTs, and the results agree with the numbers and types of the functional groups on their surfaces.

1. Introduction

Carbon nanotubes (CNTs) were discovered in 1991 by Iijima [1] and have attracted great interest because of their unique structure and superior properties such as high strength, high thermal endurance, high chemical stability, low density and high surface area [2,3,4]. Two main types of CNTs are single-walled carbon nanotubes (SWCNTs) and multi-walled carbon nanotubes (MWCNTs). The MWCNTs are stronger than SWCNTs because their structure consists of two or more layers of grapheme-like wall and much larger compared to SWCNTs. Furthermore, MWCNTs can be produced in large quantities and low cost [5]. MWCNTs are widely used in many applications such as nanoreinforement fillers[6], chemical sensors [7] and nanoelectronic devices [1]. However, the applications of MWCNTs are limited due to bundle together and agglomeration of intrinsic van der Waals attraction between the individual tubes. These cause poor dispersion stability and weak interfacial bonding with other compounds.

In recent years, the surface of MWCNTs has attracted great attention to disentangle by efforts to modify their chemical and physical properties. The various routes of surface modification of MWCNTs have been considered. One is non-covalent functionalization based on weak Van der Waals forces [5] such as hydrophobic, π-stacking and adsorption. The advantage of non-covalent functionalization is that the prior structure of the nanotubes is not altered. On the other hand, covalent functionalization requires functional groups grafted to the surface of MWCNTs by forming covalent bonds.[8] The covalent attachment can greatly improve the dispersion of MWCNTs; however, it usually introduces structural defects on the nanotubes'surface. The most common procedure used for covalent attachment of reactive groups is the treatment with strong oxidizing agents due to the high chemical stability of MWCNTs. Many oxidizing agents have been used to functionalize MWCNTs, such as $H_2SO_4+HNO_3$[7,9], HNO_3[2,10], $KMnO_4$[11,12] and H_2O_2[12]. These oxidative treatments usually result in shortening of the MWCNTs' length and forming of surface reactive groups such as hydroxyl, carbonyl and carboxylic acid.

The quantity of functional groups on modified surface of MWCNTs depends on oxidation potentials and concentrations of oxidizing agents and also treatment conditions, such as reaction duration, reaction temperature and repeating time. It is important to know types and amounts of the functional groups grafted on the surface for further usages or modification. The functional groups on MWCNTs surface can be quantitatively determined using a few methods. X-ray photoelectron spectroscopy (XPS), for example, identifies types and numbers of atoms on the surface by measuring kinetic energies of ejected electrons, but this instrument is expensive and not easy to access.[13] On the other hand, Fourier transformed infrared spectrometry (FTIR) is a common instrument available in many laboratories, and its operation cost is rather affordable. One major problem of the use of FTIR is the difficulty in obtaining spectra quantitatively. In this case, the addition of an internal standard will be used for comparing the intensities of the functional group peaks.

In addition, many attempts have related the number of the functional groups to the dispersion ability of the treated MWCNTs in various liquid media.[14] It was found that the more functional group attached on the MWCNTs surface, the higher the dispersion of the treated MWCNTs in polar solvents, such as water. Thus, the MWCNTs dispersion can be used as an indicator to roughly determine the functional groups in term of types and numbers.

The aim of this work is to identify functional groups on MWCNTs surface quantitatively using FTIR with potassium cyanide (KCN) as an internal standard. The MWCNTs were introduced functional groups through the treatments with a) conc. H_2SO_4 + conc. HNO_3 (3:1 v/v), b) conc.HNO_3, and c) $KMnO_4$. Furthermore, the dispersion of the MWCNTs in various liquid media was performed, and the results were compared with the results from the FTIR measurement.

2. Experimental

2.1 Materials

Multiwalled carbon nanotubes (MWCNTs) were obtained from the Nanomaterial Research Unit (Chiang Mai University, Thailand). The strong oxidizing agents are nitric acid (HNO_3, 69.0-70.0%, J.T.Baker), sulfuric acid (H_2SO_4, 95.0-98.0%, J.T.Baker) and potassium permanganate ($KMnO_4$, AR grade, Aldrich). The liquid media for MWCNTs's dispersion were deionized water, ethanol, hexane, 2-butanol, 2-propanol, acetone, and dichloromethane and were used as received. The other chemicals are hydrochloric acid (HCl, 36.5-38.0%, J.T.Baker), sodium hydrogensulfide ($NaHSO_3$, AR grade, Merck), potassium bromide (KBr, Analytical grade, Aldrich) and potassium cyanide (KCN, Analytical grade, Aldrich).

2.2 Functionalization of the carbon nanotubes

The as-received MWCNTs were first dispersed in ethanol with the aid of ultrasonication for 5 h to reduce the agglomeration of MWCNTs. The dispersed MWCNTs were filtered and dried in an oven at 80°C overnight.

Three strong oxidants were used to treat the dispersed MWCNTs in different conditions as followed:

Method 1: a mixture of 40 mL concentrated HNO_3 and 0.1 g of the MWCNTs was heated at 80°C for 48 h in an oil bath with continuously stirring. After the treatment, the treated MWCNTs were washed using deionized water until the filtrate became neutral. Then, they were dried under vacuum at 600 mmHg, 80°C for 24 h. (named as CNTs-N)

Method 2 : a mixture of 40 mL conc.H_2SO_4 and conc.HNO_3 (3:1 v/v) and 0.1 g of the MWCNTs were heated at 80°C for 24 h in an oil bath with continuously stirring. After that the treated MWCNTs were recovered by the procedure identical to those used in Method 1. (named as CNTs-S+N)

Method 3: a mixture of 40 mL of 0.10 M $KMnO_4$ solution and 0.1 g of the MWCNTs was heated at 40°C for 24 h in an oil bath with continuously stirring. After the treatment, the treated MWCNTs and MnO_2 solid products were washed using deionize water until the filtrate became colorless. The solids were divided to two portions for removing the produced MnO_2 from the treated MWCNTs. One portion was added with concentrated HCl (named as CNTs-K/HCl) and the other portion with 0.34 M $NaHSO_3$ (named as CNTs-K/$NaHSO_3$) until the green MnO_2 was dissolved completely. After that, the black treated MWCNTs in both portions were recovered by the procedure stated in Method 1.

2.3 Characterization

FTIR spectroscopic analysis

The functional groups' quantitation of the as-received MWCNTs and the treated MWCNTs were characterized using Fourier Transform infrared spectroscopy (FTIR, Perkin Elmer model spectrum 100). The sample pellets were prepared by grinding dried MWCNTs samples together with potassium bromide (KBr) and potassium cyanide (KCN). FTIR was used to observe the functional groups on the MWCNTs surface in the frequency range of 4000–450 cm^{-1} and 16 scans at a resolution of 4 cm^{-1}.

Dispersion stability test

The dispersion stability of the MWCNTs samples was carried out in seven liquid media: deionized water, ethanol (EtOH), hexane (C_6H_{14}), 2-butanol ($C_4H_{10}O$), 2-propanol (C_3H_8O), acetone (C_3H_6O), and dichloromethane (CH_2Cl_2). Twenty-five milligrams of the MWCNTs were added into 5 mL of each liquid medium and sonicated for 20 min. These suspensions were placed steady and observed daily.

3. Result and discussion

3.1 FT-IR spectroscopy

The functional groups on the MWCNTs samples were analyzed using FTIR spectroscopy, and their spectra were shown in Figure 1. It is important to note that all spectra were adjusted so that the C≡N peaks (2080 cm^{-1}), which was the internal standard, were resemble. The peaks in the spectra can be attributed as followed: O−H stretching of carboxylic or alcohol groups at 3100-3200 cm^{-1}[15], C=O vibration of carboxylic groups at 1730-1750 cm^{-1}[16,17], C=O vibration of ketone groups at 1631 cm^{-1}[3,11,17,18], C−O stretching of phenol and ether groups at 1272 and 1125 cm^{-1}[10,11]. It was found that the shape and the number of peaks in all spectra were similar, even in the as-received MWCNTs' spectrum. The reason for the untreated MWCNTs containing the functional groups could be a result of the remaining from the synthesis process where ethanol was used as a carbon source.[19] The as-received MWCNTs does not have carboxylic groups on its structure as seen from the absence of the 1730-1750 cm^{-1} peak, while this peak presents in the spectra of all treated MWCNTs samples. It confirms the oxidation of the MWCNTs surface by the strong oxidants. On the other hand, the

C−O stretching of phenol at 1272 cm^{-1} does not appear in the spectra of the treated MWCNTs, except the CNTs-K/$NaHSO_3$ and the as-received MWCNTs. The slightly difference in the spectra indicates the difference in the number and types of functional groups on the treated MWCNTs samples.

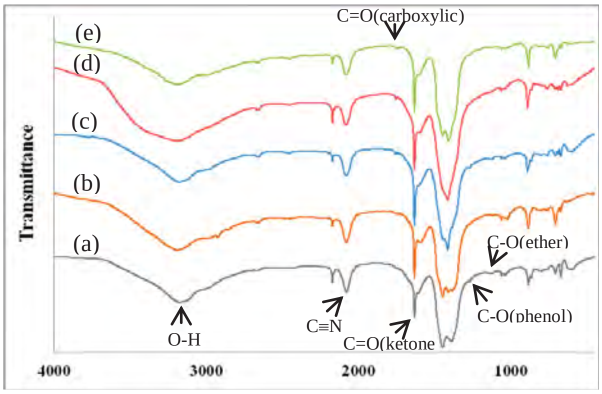

Figure 1. FTIR spectra of (a) as-received MWCNTs, (b) CNTs-K/HCl (c) CNTs-K/$NaHSO_3$ (d) CNTs-N and (e) CNTs-S+N.

To compare the functional groups on the MWCNTs samples quantitatively, the peak intensities of each vibration were normalized by the peak intensity of C≡N at 2080 cm^{-1} as shown in equation (1).

$$\text{Normalized intensity} = \frac{\text{Peak height of the functional group}}{\text{Peak height of the C≡N}} \quad (1)$$

The normalized intensities of the functional groups were displayed in Table 1. It is more obvious to consider the different quantity between the functional groups on the as-received and treated MWCNTs surfaces, as well as among the treated MWCNTs samples. The as-received MWCNTs have the highest intensity of C−O peaks, but the lowest intensity of C=O and O−H peaks. It is well known that the C−O in ether is almost non-polar, and the carboxylic and hydroxyl groups are polar. Thus, the as-received MWCNTs should have lowest polarity on their surface.

In contrast, all treated MWCNTs, except CNTs-K/$NaHSO_3$, presents the decrease of the C−O peak intensities, but the increase of the C=O and O−H intensities. This indicates the treatment of the as-received MWCNTs with the strong oxidizing agents causes the changes in the C−O bond to the carboxylic acid. In case of CNTs-K/$NaHSO_3$, the MWCNTs were oxidized by $KMnO_4$ and washed the MnO_2 byproduct with $NaHSO_3$ reducing insoluble MnO_2 to soluble Mn^{2+}. The excess $NaHSO_3$ causes the reduction of the carboxylic acid to the C−O. As a result, the intensities of C=O and O−H in the CNTs-K/$NaHSO_3$ decrease, and those of C−O increase, compared to those intensities in the CNTs-K/HCl (Table 1).

Table 1. Normalized intensities of the functional groups on the MWCNTs samples

Sample	Normalized intensity of the functional groups				
	O-H (3100-3200 cm^{-1})	C=O (1750-1730 cm^{-1})	C=O (1631 cm^{-1})	C-O (1272 cm^{-1})	C-O (1125 cm^{-1})
as-received MWCNTs	1.5261	-	1.7981	0.0705	0.0732
CNTs-K/HCl	1.8502	0.1232	2.3557	-	0.0265
CNTs-K/$NaHSO_3$	1.7748	0.1059	2.8975	0.0639	0.0941
CNTs-N	2.7097	0.1398	2.9470	-	0.0572
CNTs-S+N	1.7581	0.1969	2.8467	-	0.0253

Based on the normalized intensities in Table 1, we propose that both CNTs-N and CNTs-S+N are high in polarity, followed by CNTs-K/HCl, CNTs-K/$NaHSO_3$, and the as-received MWCNTs, respectively. It is worth mentioning that the O−H intensity might be interfered by the adsorbed water inside the opened MWCNTs or between the tubes, as well as the hygroscopic KBr and KCN.

3.2 Dispersion property

The dispersion stability of the MWCNTs samples was observed in the liquid media which have different in polarity to confirm the difference in surface polarities. The dried solid MWCNTs samples were dispersed in the liquid media in test tubes using an ultrasonicator for 20 min. In some portions, the MWCNTs samples were not dispersed, while some were still floating well even after 14 days. Figure 2 showed the MWCNTs samples in the liquid media. The images were taken on the 14th day after the sonication. Importantly, the observation must be continuously performed since the beginning of the sonication because it was found that the dispersion and the precipitation of the samples were varied. For example, the dispersions of all MWCNTs samples were very poor in CH_2Cl_2 and hexane, resulting from the non-polarity of the liquids, especially in CH_2Cl_2. Conversely, in high-polar water, the as-received MWCNTs were dispersed gradually after sonication, but they began precipitating 30 min after that and most of them were at the bottom of the tubes within 14 days as shown in Figure 2. Similarly, CNTs-K/$NaHSO_3$ and CNTs-K/HCl partially precipitated after 18 h, while CNTs-S+N were still dispersed after 14 days.

It is interesting that the dispersion stability of the treated MWCNTs was varied depended on the treatment methods. The CNTs-S+N and CNTs-N which are rich in hydroxyl and carboxylic groups (Table 1) have dispersion stability from very high to high in ethanol, 2-propanol, and 2-butanol, respectively. One should realize that these liquids posses an ability to form hydrogen bonds which may be the reason for the high dispersion stability of the CNTs-S+N and CNTs-N. Conversely, the CNTs-K/$NaHSO_3$ and CNTs-K/HCl samples were not well dispersed in the alcohol liquid media, but still dispersed well in acetone. Therefore, the dispersion degree in the alcohols can be used as a rough indicator to determine the number of carboxylic and hydroxyl groups on the MWCNTs. Furthermore, the difference in the amount of the C−O groups as seen in the CNTs-K/$NaHSO_3$ and CNTs-K/HCl samples did not affect the dispersion behavior because the polarity of these C−O groups is small.

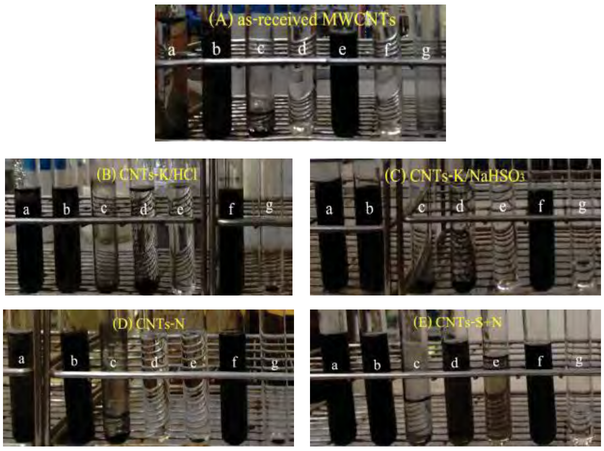

Figure 2. The dispersion of as-received MWCNTs **(A)**, CNTs-K/HCl **(B)**, CNTs-K/$NaHSO_3$ **(C)**, CNTs-N **(D)**, and CNTs-S+N **(E)** after 14 days. The liquid media from the left to right test tubes are water (a), ethanol (b), hexane (c), 2-butanol (d), 2-propanol (e), acetone (f), and dichloromethane (g), respectively.

4. Conclusion

The types and amounts of the functional groups on the MWCNTs are depended on the strong oxidants, and their characters could be identified using the quantitative FTIR spectroscopy and the dispersion stability in various liquid media. The results obtained from FTIR spectroscopy indicated the introduction of the polar functional groups, carboxyl hydroxyl, and carbonyl groups on the MWCNTs surface. The amounts of the functional groups became more comparable quantitatively by normalizing the functional group peaks' intensities with the C≡N peak's intensity of the internal standard KCN.

The dispersion stability in the liquid media can be reasonably related to the types and amounts of the functional groups obtained from the FTIR analysis. The oxidation treatment increases the functional groups on the MWCNTs observed from the FTIR spectra. It agreed with the dispersion stability that the more the number of the functional groups, especially carboxylic and hydroxyl, the higher the dispersion in the polar liquids.

Acknowledgements

The authors wish to thank the Faculty of Science, Silpakorn University for gratefully acknowledged and the Royal Thai Air Force Academy for research funds.

References

[1] J.A. Kim, D.G. Seong, T.J. Kang and J.R. Youn, *Carbon*. **44** (2006) 1898–1905.
[2] S. Lee, T. Oda, P.-K. Shin and B.-J. Lee, *Microelectron. Eng.* **86** (2009) 2110–2113.
[3] C.-C. Li, J.-L. Lin, S.-J. Huang, J.-T. Lee and C.-H. Chena, *Colloid. Surface. A*. **297** (2007) 275–281.
[4] S.-M. Yuen, C.-C.M. Ma, Y.-Y. Lin and H.-C. Kuan, *Compos. Sci. Technol*. **67** (2007) 2564–2573.
[5] D. Bikiaris, A. Vassiliou, K. Chrissafis, K.M. Paraskevopoulos, A. Jannakoudakis and A. Docoslis, *Polym. Degrad. Stabil.* **93** (2008) 952-967.
[6] J.Y. Kim, D.K. Kim and S.H. Kim, *Eur. Polym. J*. **45** (2009) 316–324.
[7] S.H. Jin, Y.-B. Park and K.H. Yoon, *Compos. Sci. Technol*. **67** (2007) 3434–3441.
[8] W. Li, Y. Bai, Y. Zhang, M. Sun, R. Cheng, X. Xu, Y. Chen and Y. Mo, *Synthetic. Met.* **155** (2005) 509–515.
[9] J.H. Lee, K.Y. Rhee and S.J. Park, *Mater. Sci. Eng. A*. **7** (2010) 6838–6843.
[10] T.A. Issam, A.-A. Adnan, T.P. Selvin, A.-H. Mamdouh and A.G. Salihu,S. Rachid and A.A. Muataz, *Compos. Part. B*. **42** (2011) 1554–1561.
[11] J. Chena, Q. Chena, Q. Mab, Y. Li and Z. Zhub, *J. Mol. Catal. A-Chem.* **356** (2012) 114– 120.
[12] K.A. Wepasnick , B.A. Smith, K.E. Schrote, H.K. Wilson, S.R. Diegelmann and D. H. Fairbrother , *Carbon*. **49** (2011) 24–36.
[13] http;//www.casaxps.com/help_manual/XPSinformation/XPSinstr.htm (Retrieved September 14, 2012).
[14] O.-K. Park, T. Jeevananda, N.H. Kim, S.-i. Kim and J. H. Lee, *Scripta. Mater.* **60** (2009) 551–554.
[15] C.Y. Kuo, *Desalination*. **249** (2009) 781–785.
[16] M.A.M. Motchelaho, H. Xiong, M. Moyo, L.L. Jewell and N.J. Coville, *J. Mol. Catal. A-Chem.* **335** (2011) 189–198.
[17] L. Stobinski, B. Lesiak, L. Kover, J. Toth, S. Biniak, G. Trykowski and J. Judek, *J. Alloy. Compd*. **501** (2010) 77–84.
[18] J. Wang, H. Xie, Z. Xin, Y. Li and L. Chen, *Sol. Energy*. **84** (2010) 339–344.
[19] P. Singjai, S. Changsarn and S. Thongtem, *Mater. Sci. Eng. A*. **443** (2007) 42–46.

SYNTHESES OF Cu_2O PHOTOCATALYSTS AND THEIR DECOLORIZATION OF ORGANIC DYES

Sasicha Jansu[1], Nattawan Decharin[1], Tarawipa Puangpetch[2], Cheewita Suwanchawalit[1*]

[1]Department of Chemistry, Faculty of Science, Silpakorn University, Sanam Chandra Palace Campus, Nakornpathom, 73000 Thailand
[2]Department of Chemical Engineering, Faculty of Engineering and Industrial Technology, Silpakorn University, Sanam Chandra Palace Campus, Nakornpathom, 73000 Thailand

*E-mail: cheewita@su.ac.th, Tel. +66 34255797, Fax. +66 34271356

Abstract: Microsphere cuprous oxide (Cu_2O) photocatalyst have been successfully prepared by reducing $CuSO_4.5H_2O$ using hydrazine hydrate under different pH conditions. The as-prepared products were easily separated and purified since no template or surfactant was introduced. The synthesized Cu_2O samples were characterized by X-ray powder diffractometry (XRD), scanning electron microscopy (SEM), Fourier transform infrared spectrometry (FTIR), diffuse reflectance spectroscopy (DRS) techniques. The photocatalytic efficiencies of the microsphere Cu_2O samples were evaluated by the degradation of methylene blue (MB) and Orange II (OII) dyes under visible light irradiation. In addition, the Cu_2O samples synthesized under different pH conditions showed different in their degradation activity which suggest the dissimilarity in their properties.

1. Introduction

Cuprous oxide (Cu_2O) is a p-type semiconductor with a direct band gap in the range of 2.0-2.2 eV, which makes it a promising material for many applications in gas sensors, solar energy, photocatalytic decgradation of organic pollutants. Cu_2O has been used as visible-light driven photocatalyst directly for splitting water and degradation of organic contaminations [1-4]. There are many advantages for Cu_2O to be used as photocatalyst such as low toxicity, good environmental acceptability, low cost, effectively utilize visible light and has a powerful adsorption for molecular which can scavenge photoelectrons to constrain the combination of electrons and holes [5-8].

In this work, microsphere cuprous oxide has been successfully prepared by reducing $CuSO_4.5H_2O$ using hydrazine hydrate, as reducing agent. In addition, the photocatalytic behaviours of as-prepared products were investigated.

2. Materials and Methods

2.1 Preparation of Cu_2O photocatalysts

All reagents used in this work were of analytical grade and were used without any further purification. A Cu_2O photocatalyst was prepared by precipitation method as following procedure, 0.025 mol $CuSO_4.5H_2O$ was dissolved in 100 mL deionized water. The solution was heat to 60 °C. Then 25 mL 2.58 *M* N_2H_4 was added into the solution. Then 0.3 *M* NaOH was added into the solution until pH equal to 7, 10 and 14. The precipitates were then separate from the suspension by filtered and washed with ethanol and distilled water for three times. The obtained products were dried at 60 °C under vacuum for 6 h and were collected for characterizations and photocatalytic degradation tests.

2.2 Characterization of Cu_2O photocatalysts

Crystal structure of the microsphere cuprous oxide was identified by a powder X-ray diffractometer (Rigaku, Miniflex II). During the XRD analysis, the samples were scanned from 20° to 80°. The morphology of the microsphere cuprous oxide was observed by scanning electron microscopy (SEM) obtained by using a Camscan (MX2000). The samples were coated with gold to help to improve the conductivity when they were observed with the microscope. The UV-vis diffuse reflection absorptive spectra (DRS) were recorded by an UV-vis spectrometer. The FT-IR spectrum of microsphere cuprous oxide with different pH was further characterized by Fourier Transform Infrared Spectrometer (FT-IR; Perkin Elmer, Spectrum 100).

2.3 Photocatalytic measurement

The adsorption and photocatalytic activity were perform as follow: 0.05 g of as-prepared product was dispersed in 50 mL solution of methylene blue (MB) and Orange II (OII) dyes. The suspension was magnetically stirred for 0.5 h in the dark then illuminated under visible light with constant stirring at room temperature. The residual concentration of methylene blue (MB) and Orange II (OII) solution was determined every 60 min using UV-vis spectrophotometer. For measurement the absorbance of MB and OII was observed the wavelength at 664 nm and 484 nm, respectively. The photocatalytic efficiency was calculated by follow formula:

$$\%\text{decolorization} = [(A_0 - A_t)/A_0] \times 100\%$$

where A_0: the original absorbency of dye solution; A_t: the absorbency of dye solution after irradiating for a certain time.

3. Results and Discussion

3.1. XRD patterns of the microsphere cuprous oxide samples

X-ray diffraction patterns of Cu_2O samples with different pH are shown in Figure 1. The peaks of Cu_2O from the XRD patterns match with standard data (JCPDS No. 78-2076). Only some impurity of $Cu(OH)_2$ match with standard data (JCPDS 35-0505) and CuO match with standard data (JCPDS 45-0937) [9] were also detected found in the as prepared Cu_2O samples. The crystalite size of prepared Cu_2O samples were shown in Table 1.

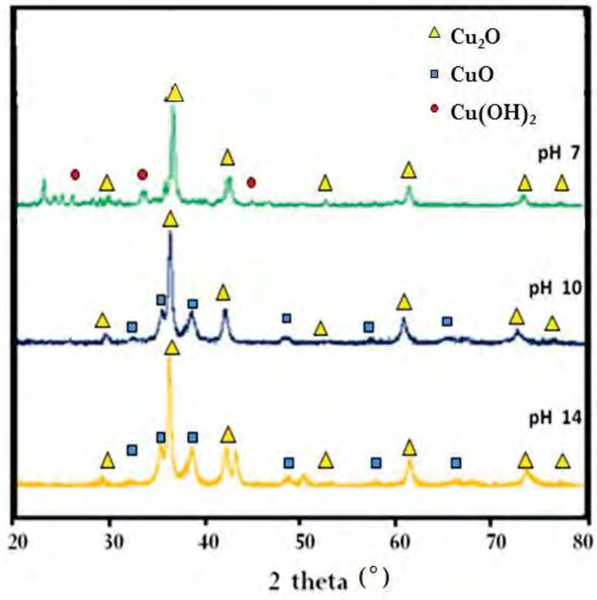

Figure 1. The XRD patterns of microsphere cuprous oxide samples with different pH.

3.2. SEM images of the microsphere cuprous oxide

Figure 2 give the SEM images of microsphere cuprous oxide with pH 7, pH 10 and pH 14 respectively. It can be seen that, varying the pH of solution during preparation process led to change in the size of the samples. When increasing the pH the sample have high agglomerated into larger microsphere, the color of the particle was changed from red brown to dark red brown when increase pH. It implied that the pH was an important factor that influences the size of the microsphere Cu_2O samples.

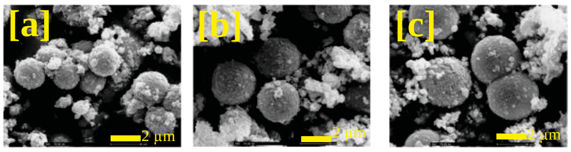

Figure 2. SEM images of microsphere cuprous oxide with [a] pH 7, [b] pH 10 and [c] pH 14

3.3. DRS of the microsphere cuprous oxide samples

The DRS spectra of different microsphere cuprous oxide samples are shown in Figure 3. The calculate band gap energy of samples was obtained according to the absorption onset and listed in Table 1. However, the optical absorption would be affected considerably by the morphology and crystallinity of Cu_2O crystals [10]. In the case of microsphere cuprous oxide with pH 10 and pH 14, whose band gap is hard to be estimated due to the lack of sharpness in the optical absorption feature [11]. In general, the DRS spectra indicate that the Cu_2O particles improve the visible light absorption ability, which accounts for the photocatalytic activity of Cu_2O powders under visible light irradiation.

3.4. The FT-IR spectrum of the microsphere cuprous oxide samples

The FT-IR spectrum shows a characteristic band at 624 and 1109 cm^{-1} which is attributed to the Cu-O vibration of the Cu_2O crystals (optically active lattice vibration in the oxide) [12-13]. The bands at 3321cm^{-1} and 1601 cm^{-1} which are the characteristic peaks attributed to the O–H stretching and O–H bending mode [14], respectively.

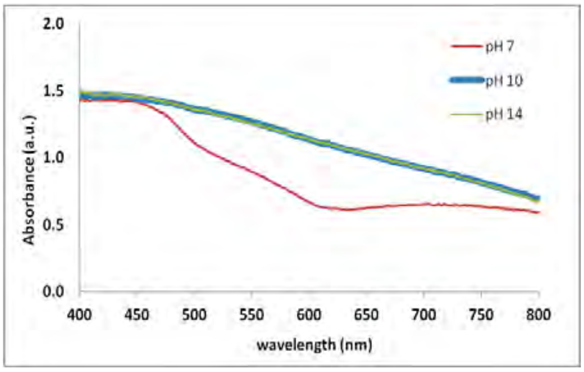

Figure 3. The DRS spectra of microsphere cuprous oxide with pH 7, pH 10, pH 14

Table 1: The crystal size, band energy, color, and surface area of the microsphere cuprous oxide samples

Samples	Crystal size (nm)	Band Gap* (eV)	Color
Cu_2O.pH7	22.40	2.03	Red brown
Cu_2O.pH10	18.85	-	Dark brown
Cu_2O.pH14	19.99	-	Dark brown

* The band gaps of the Cu_2O particles were calculated from equation $E_g = hc/\lambda$ by the linear extrapolation toward the baseline to give the onset of the optical absorption edges.

3.5. Photocatalytic degradation of dyes by as-prepared microsphere cuprous oxide samples

Photocatalytic activities of the as-prepared microsphere cuprous oxide samples were investigated towards the degradation of methylene blue (MO) and Orange II (OII) solution at room temperature. Figure 5 showed the photocatalytic degradation of MB and OII dyes under visible irradiation. It is well known that adsorption property plays a key role in most photocatalytic reactions. Therefore, the experiment with the photocatalytic system stirring in the dark was investigated. It can be seen that the after irradiation of 5 h the photocatalytic degradation ratio of OII reached to 85.06%, 86.44% and 93.16% for Cu_2O with pH7, pH10 and pH14, respectively. And the photocatalytic degradation ratio of MB reached to 93.64% for Cu_2O with pH7, while Cu_2O with pH10 and pH14 had no photocatalytic activity on MB. It was obviously seen that the Cu_2O with all pH has high adsorption capacity on OII that might be due to the size of particles of Cu_2O with all pH quite similarly and only Cu_2O with pH 7 has high adsorption capacity on MB. Therefore the synthesized Cu_2O with pH 7 is condition which showed excellent decolorized both MB and OII dye under visible catalyst.

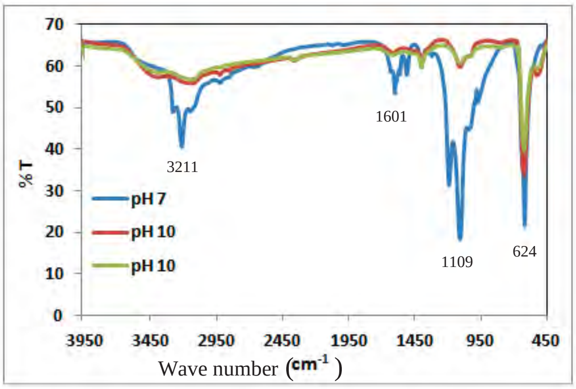

Figure 4. The FT-IR spectrum of microsphere cuprous oxide with pH 7, pH 10, pH 14

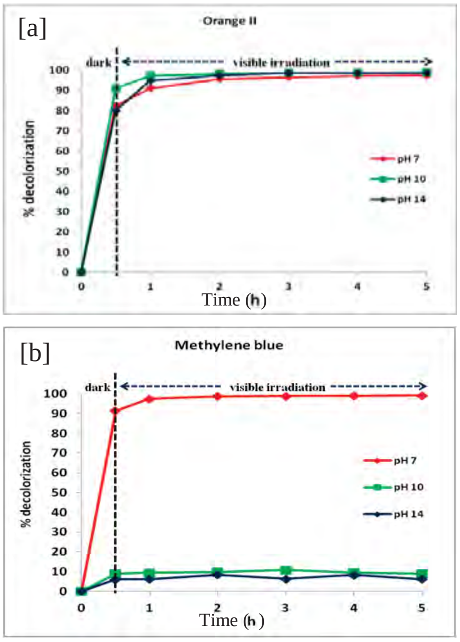

Figure 5. The efficiency of photocatalytic degradation of [a] OII and [b] MB by synthesized Cu_2O samples under visible irradiation for 5 h.

4. Conclusions

In summary, microsphere cuprous oxide has been successfully prepared by a simple wet chemical approach. Microsphere cuprous oxide with different pH showed different photocatalytic behaviours on degradation of methylene blue (MB) and Orange II (OII) dyes. The results show that microsphere cuprous oxide with pH 7 has highest degradation efficiency on both methylene blue (MB) and Orange II (OII) under visible irradiation.

Acknowledgements

This work was supported by Department of Chemistry, Faculty of Science, Silpakorn University, Sanam Chandra Palace Campus, Nakornpathom, Thailand.

References

[1] M. Hara, T. Kondo, M. Komoda, S. Ikeda, K. Shinohara, A. Tanaka, J.N. Kondo and K. Domen, *Chem. Commun.* (1998) 357-358.

[2] K. Domen, J.N. Kondo, M. Hara, T. Takata and Bull. *Chem. Soc. Jpn*. **73** (2000) 1307-1331.

[3] C.A.N. Fernando, T. Bandara and S.K. Wethasingha, *Sol. Energy Mater. Sol. Cells* **70** (2001) 121-129.

[4] M.K.I. Senevirathna, P.K.D.D.P. Pitigala and K. Tennakone, *J. Photochem. Photobiol*. **171** (2005) 257-259.

[5] W. Siripala, A. Ivanovskaya, T.F. Jaramillo, S.H. Baeck and E.W. McFarland, *Sol. Energy Mater. Sol. Cells* **77** (2003) 229-237.

[6] H.M. Yang, J. Ouyang, A.D. Tang, Y. Xiao, X.W. Li, X.D. Dong and Y.M. Yu, *Mater. Res. Bull*. **41** (2006) 1310-1318.

[7] B.J. Wood, H. Wise and R.S. Yolles, *J. Catal*. **15** (1969) 355-362.

[8] J.L. Li, L. Liu, Y. Yu, Y.W. Tang, H.L. Li and F.P. Du, *Electrochem. Commun*. **6** (2004) 940-943.

[9] G.H. Du and G. Van Tendeloo, *Chem. Phys. Letters* **393** (2004) 64–69.

[10] C.H. Lu, L.M. Qi, J.H. Yang, X.Y. Wang, D.Y. Zhang, J.L. Xie and J.M. Ma, *Adv. Mater*. **17** (2005) 2562-2567.

[11] L. Huang F. Peng, H. Yu and H. Wang,. *Solid State Sci.***11** (2009) 129-138.

[12] M. O'Keeffe, *J. Chem. Phys*. **39** (1963) 1789-1793.

[13] D. Persson and C. Leygraf, *J. Electrochem. Soc*. **140** (1993) 1256-1260.

[14] A. Asar, G. Namdeo S and J. Amish G. *Mater. Chem. and Phys*. **129** (2011) 740-745.

PREPARATION OF TiO_2-RUBBER SHEET AND ITS PHOTOCATALYTIC PROPERTY

Worakamol Nakpetpoon[1], Cheewita Suwanchawalit[1*], Sumpun Wongnawa[2]

[1]Department of Chemistry, Faculty of Science, Silpakorn University, Sanam Chandra Palace Campus, Nakornpathom, 73000 Thailand
[2] Department of Chemistry, Faculty of Science, Prince of Songkla University, Hat Yai, Songkhla 90110 Thailand

*E-mail: cheewita@su.ac.th, Tel. +66 34255797, Fax. +66 34271356

Abstract: The TiO_2-rubber sheet have been simply prepared by the mixing natural rubber latex (60% HA) and titanium dioxide particles suspended in ammonia solution followed by vacuum filtration through a sintered glass to form flexible TiO_2-rubber sheet. The effect of TiO_2 concentration was investigated in this work. The prepared TiO_2-rubber sheets were studied by X-ray diffractometer (XRD), scanning electron microscopy (SEM) and Fourier transform infrared spectrometry (FTIR) techniques. The photocatalytic activity was evaluated using methlyene blue (MB) as a model organic dye compound. These flexible TiO_2-rubber sheets could degrade methlyene blue molecules under UV-light irradiation. Furthermore, the effect of reusability was also investigated.

1. Introduction

Over the past decade, heterogeneous photocatalysis has attracted great attention for complete mineralization of various organic pollutants in wastewater treatment. Among of various semiconductor photocatalysts, titanium dioxide (TiO_2) has become the most promising photocalysts owing to its low cost, stability, non-toxicity and high efficiency in the photocatalysis process [1-2]. However, the TiO_2-based photocatalytic powders are difficultly in separating it from reaction system. To avoid the recyclability problem is to coat or immobilize TiO_2 powders on various supporting materials such as glass, plastics and polymer [3-5]. TiO_2 thin films have been prepared by various methods such as sol-gel dip coating, chemical vapour deporsition and spray pyrolysis deposition [6-8]. The above methods need expensive equipment and complex procedures. Therefore, a simple and low cost method for the preparation of immobilized TiO_2 powder in the rubber sheet was investigated in this work.

2. Materials and Methods

2.1 Chemicals and equipment

The natural rubber latex (60%HA) was purchased from Chana Latex Co. Ltd., Songkhla, Thailand. Methylene blue dye and titanium dioxide (anatase) were use as the main chemical substances. The surface morphologies of TiO_2-rubber sheet was characterized by using scanning electron microscopy (SEM, a Camscan MX2000). The crytalline phases of TiO_2 were identified by using X-ray diffraction technique (XRD) (Rigaku, Miniflex II). During the XRD analysis, the samples were scanned from 10° to 80°. The FT-IR spectrum was further studied for the functional group of the TiO_2-rubber sheet that obtained by Fourier Transform Infrared Spectrometer (FT-IR; Perkin Elmer, Spectrum 100).

2.2 Preparation of TiO_2- rubber sheet

The TiO_2 rubber sheet was prepared from ammonia solution mixed rubber latex and TiO_2 power mixed in ammonia solution. In a typical procedure to prepare the TiO_2 rubber sheet, 6.72 mL of natural rubber latex (60% HA) was mixed with 10.00 mL ammonia solution was added to the TiO_2 suspension, prepared by mixing 1.00g of TiO_2 powder (anatase) with 10.00 mL ammonia solution, and then stirred for 30 min until the homogenized mixture formed. After that, the mixture was subjected to vacuum suction through a sintered glass and dried in the oven at 60 °C for 6 hour for remove trace of water and ammonia gas. After drying, TiO_2-rubber sheet was taken out from the sintered glass and left to dryness at room temperature. The sheet obtained was designated as 1.00g TiO_2-rubber sheet. The TiO_2 1.50g and 2.00g TiO_2-rubber sheet were prepared likewise using the same procedure.

2.3 Photocatalytic studies

The TiO_2-rubber sheet was soaked in 100 mL of 1.0×10^{-5}M methylene blue (MB) dye which put into the photocatalytic compartment. The system was stirred for 30 min in the dark to reach the adsorption equilibrium in photocatalytic compartment. Then the system was illuminated under UV light at room temperature. At a given time interval (every 2h), 3 mL of MB solution was collected for measure the recidual concentration at 664 nm using a UV-vis spectrophotometer (Lamba 35, Perkin Elmer). The photocatalytic efficiency was calculated by Eq. (1):

$$\%\ \text{photocatalytic efficiency} = \frac{A_0 - A_t}{A_0} \times 100 \qquad (1)$$

where A_0 is the initial absorbance of MB dye and A_t is the absorbance at a specific time interval of the collected sample.

3. Results and Discussion

3.1 Characterization of TiO_2-rubber sheets

The XRD patterns of the pristine rubber sheet and TiO_2-rubber sheets with varied amount of titania were showed in Figure 1. The pristine rubber sheet shows a clean base line throughout the spectrum except a large broad peak near $2\theta=19^{\circ}$ [9-10]. This broad scattered peak also shows up in the patterns of both the impregnated sheets but at a much smaller intensity due to the inclusion of TiO_2 particles in the impregnated sheets. XRD results revealed the high crystallinity of anatase phase for the prepared TiO_2-rubber sheets and small broadening peak of rubber near $2\theta=19^{\circ}$.

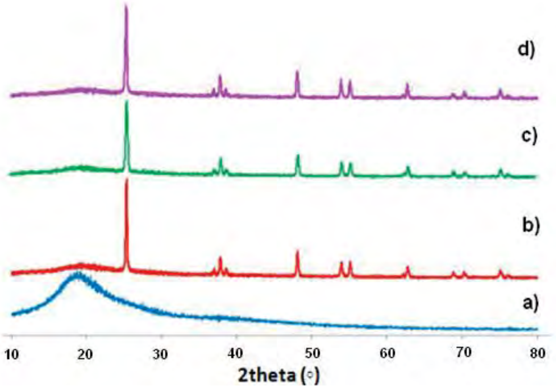

Figure 1. The XRD patterns of a) pristine rubber sheet, b) 1.0gTiO_2-rubber sheet, c) 1.5gTiO_2-rubber sheet, d) 2.0gTiO_2-rubber sheet.

The SEM images of the pristine rubber sheet and TiO_2-rubber sheets are comparatively shown in Figure 2. The surface morphology of TiO_2-rubber sheets demonstrated the increasing surface roughness when increased amount of TiO_2 powders compared with the smooth surface of the pristine rubber sheet.

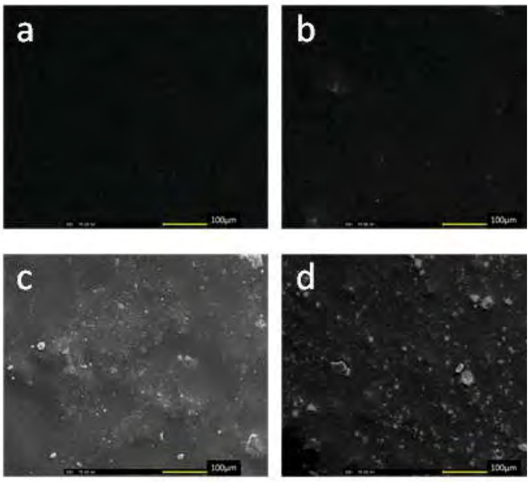

Figure 2. SEM images of a) pristine rubber sheet, b) 1.0gTiO_2-rubber sheet, c) 1.5gTiO_2-rubber sheet, d) 2.0gTiO_2-rubber sheet.

It has been known that the enhanced surface roughness structures are important factor for the photocatalytic activity of TiO_2 thin film [9-10].

The technique of attenuated total reflectance (ATR) used in conjunction with Fourier transform infrared spectrometry (FTIR) techniques which enables samples to be examined directly in the solid state without further preparation. The FTIR results revealed the characteristic peaks of pristine rubber sheet and Ti-O streching mode of TiO_2 powder impregnated inTiO_2-rubber sheets.

3.2 Photocatalytic degradation of dye by TiO_2-rubber sheets

The photocatalytic degradation of methylene blue (MB) by using the prepared TiO_2-rubber sheets under UV irradiation is shown in Figure 3. The photocatalytic results revealed that 2.0gTiO_2-rubber sheet showed higher photocatalytic efficiency than the 1.5gTiO_2-rubber, 1.0gTiO_2-rubber sheets and the pristine rubber sheet, respectively. The photocatalytic results corresponding with the surface roughness of TiO_2-rubber sheets from SEM technique.

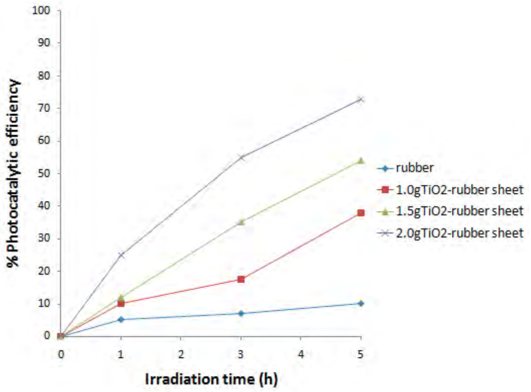

Figure 3. Photocatalytic degradation of methylene blue under UV irradiation using a) pristine rubber sheet, b) 1.0gTiO_2-rubber sheet, c) 1.5gTiO_2-rubber sheet, d) 2.0gTiO_2-rubber sheet.

In this work, TiO_2-rubber sheets can be repeatedly used for the photocatalytic degradation of methylene blue. The used TiO_2-rubber sheets have dye adsorbed on the surface after used therefore the photodegradation efficiency decreased when using in the next cycle.

4. Conclusion

In summary, the TiO_2-rubber sheet have been simply prepared by a simple mixing natural rubber latex (60% HA) and titanium dioxide particles suspended in ammonia solution followed by vacuum filtration through a sintered glass to form flexible TiO_2-rubber sheet. The prepared TiO_2-rubber sheets could be degrade methlyene blue molecules under UV-light irradiation. In addition, TiO_2-rubber sheets can be easily recovered after used and also can be reused.

Acknowledgements

This work was supported by Department of Chemistry, Faculty of Science, Silpakorn University.

References

[1] M.R. Hoffmann, S.T. Martin, W. Choi and D.W. Bahnemann, *Chem. Rev*. **95** (1995) 69-96.
[2] S. Senthilkumarr, K. Porkodi and R. Vidyalakshmi, *J. Photochem. Photobiol.* A. **170** (2005) 225-232.
[3] S.B. Sankapal, M.Ch. Steiner and A. Ennaoui, *Appl. Surf. Sci.* **239** (2005)165-170.
[4] C.H. Kwon, H. Shin, J.H. Kim, W.S. Choi and K.H. Yoon, *Mater. Chem. Phys*. **86** (2004) 78-82.
[5] J.H. Yang, Y.S. Han and J.H. Choy, *Thin Solid Films.* **495** (2006) 266-271.
[6] S. Sen, S. Mahanty, S. Roy, O. Heintz, S. Bourgeois, D. Chaumont, *Thin Solid Films.* **474** (2005) 245-249.
[7] Z. Ding, X. Hu, P.L. Yue, G.Q. Lu, P.F. Greenfield, *Catal. Today*. **68** (2001) 173-182.
[8] W. Weng, M. Ma, P. Du, G. Zhao, G. Shen, J. Wang, G. Han, *Surf. Coat.Technol*. **198** (2005) 340–344.
[9] C. Sriwong, S. Wongnawa, and O. Patarapaiboolchai, *Catal. Comm*. **9** (2008) 213–218.
[10] C. Sriwong, S. Wongnawa and O. Patarapaiboolchai, *Chem. Eng. J.* **191** (2012) 210–217.

NOVEL IMMOBILIZED JACK BEAN UREASE FOR INHIBITIVE DETECION OF AMINES AND OXIMES

Apichai Boonchaiming , Navarat KumKaew , Kornvalai Panpae *

Department of Chemistry, Faculty of Science, King Mongkut's University of Technology Thonburi, Tungkru, Bangkok, 10140
Thailand

*E-mail: kornvalai.pan@kmutt.ac.th, Tel. +66 24708855 , Fax. +66 24708843

Abstract: Ureases are enzymes highly desirable in immobilized form for a number of applications that exploit urea cleavage and an increase in pH, inherent to the reaction. Major among them are medical and analytical applications. We evaluated the potential of free and immobilized Jack bean urease for assaying toxicity of some organic toxidants, amines and oximes. Competitive inhibition of urease by two amines (N,N-dimethylaniline (NDMA) and tris(hydroxymethyl)methylamine (TMA)) and two oximes (dimethylglyoxime (DMG) and diacetylmonoxime (DAM)) has been studied at the optimum pH (7.3) in aqueous solution. Among these compounds high inhibitory activities, exhibited good in vitro activity, were observed in NDMA, DMG and DMG with IC_{50} = 0.018mM, 27.0mM and 0.002mM, respectively. By determination of the enzyme kinetic data, a contribution to detailed information on the inhibitor mechanism of all amines and oximes can be made with these results.

1. Introduction

Environmental pollution has an impact on human health and can therefore be considered being connected to life quality. Depending on the purpose, sensitive and selective methods are needed for both quatitative and qualitative determination of target analytes. Numerous such techniques are already available. However, the requirements for low cost, short time of analysis, sensitivity, simplicity, selectivity, stability and reliability can still not be met by a single analytical method. Biorecognition-based techniques are potential candidates to fulfill many of the above requirements, due to the general high selectivity, sensitivity and speed of interaction between the biological component and the analyte itself. Many different biosensors types have been developed for the determination of compounds with environmental relevance, like phenols[1-3], aromatic and aliphatic amines[4-5], oximes[6], pesticides[7-9], metals, etc. One of the most promising strategies to achieve the above goals is the utilization of enzymes. Enzymes exhibit a number of features that make their use advantageous as compared to conventional chemical catalysts. In addition, enzymes generally operate at mild conditions of temperature, pressure and pHwith reaction rates of the order of those achieved by chemical catalysts at more extreme conditions. This makes for substantial process energy savings and reduced manufacturing costs. In addition to the unquestionable advantages, there exists a number of practical problems in the use of enzymes. To these belong: the high cost of isolation and purification of enzymes, the instability of their structures once they are isolated from their natural environments. this is the result of short operational lifetimes. Several methods have been proposed to overcome these limitations, one of the most successful being enzyme immobilization [10].Enzymes may be immobilized by a variety of methods, which may be broadly classified as physical, where weak interactions between support and enzyme exist, and chemical, where covalent bonds are formed with enzyme. In analytical applications immobilized enzymes are used chiefly in biosensors[11] and to a lesser extent, in diagnostic test strips. For medical applications, immobilized enzymes include diagnosis and treatment of diseases[10], among those enzyme replacement therapies, as well as artificial cells and organs, and coating of artificial materials for better biocompatibility.

Urease (urea amidohydrolase; E.C.3.5.1.5) is widely distributed in a variety of bacteria such as *Helicobacter pylori* and *Proteus mirabilis. H. pylori* is a Gram-negative microaerophilic bacterium that infects up to 50% of the worl's human population[5,12]. Investigations revealed that the bacterium could cause many gastroduodenal diseases such as gastritis, gastric and duodenal ulcers, and even gastric cancer[13], as well as some other various extraintestinal pathologies. Structural studies of the enzymes have revealed a dinuclear Ni active site with a carbamylated lysine residue that bridges the deeply buried metal atoms[14-15]. One nickel ion (Ni-1) binds and activates urea with one resonance structure stabilized by a nearby carboxylate, while the second (Ni-2) binds a hydroxide. The latter molecule is actived for attack on theurea carbon by a protein residue acting as a general base. The tetrahedral intermediat collapses, eliminating ammonia with the help of an active site thiol, which was proposed to act as a general acid[5]. In addition, jack bean urease, the cysteine-rich enzyme, was proven by disulfide titration in non-denaturating conditions to contain five other cysteine residues per subunit that are more reactive[19]. With additional nine cysteine residues disclosed only in denaturating conditions, the overall number of cysteines per jack bean urease subunit amounts to 15, hence 90 cysteines per molecule.

Many urease inhibitors have been described in the past decades, as fliorofamide, hydroxyureas, and acetohydroxamic acids[14], but part of them were prevented from using in vivo because of their toxicity or instability. Hence, there are unmet medical needs for novel and efficacious urease inhibitors with low toxicity. Many compounds with amine or oxime group indicated potent biological activities and low toxicity. Some of them have been used as clinical medical agents[16]. The goal of this work was a comparative kinetic study of immobilized jack bean urease inhibition by organic chelators of nickel, two amines:N,N-dimethylaniline (NDMA) and tris(hydroxymethyl)methylamine (TMA) and two oximes dimethylglyoxime (DMG) and diacetylmonoxime (DAM). All have chemical structures presented below.

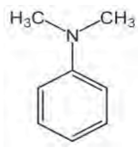
NDMA

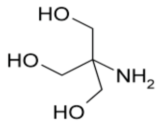
TMA

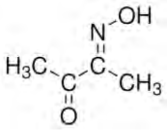
DMG

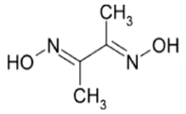
DAM

2. Materials and Methods

2.1 Chemicals and reagents

Urease type III (35,000 units/mg of protein), Tris-acetate salt, and phenol reagent were obtained from Fluka Chemical Co. Urea (enzyme grade), potassium sodium tartrate ($KNaC_4H_4O_6 \cdot 4H_2O$,AR), glutaraldehyde (25%$OHCC_3H_6CHO$, AR), calcium chloride ($CaCl_2$,AR), sodium carbonate (Na_2CO_3, AR), ammonium sulfate, NDMA, TMA and DMG were purchased from Ajax Chemical Co. Albumin (albumin bovine serum,BSA), DAM and other chemicals (sodium alginate, potassium iodide, sodium nitroprusside, sodium hypochlorite reagent) were obtained from Sigma Chemical Co. All chemical used are analytical reagent grade and all standard and reagent solutions were prepared without further purification and were prepared in double distilled water from an all-glass assembly.

A stock solution of 50 μg/L ammonium solution was prepared by solubilization of 0.33 g $(NH_4)_2SO_4$ in 1000 mL of H_2O. The series of 0.50 to 20.0 μM of standard ammonium solution was prepared by appropriate dilution of the stock solution.

2.2 Measurement of urease activity

For routine measurement of soluble urease activity, the amount of ammonia liberated during a fixed time period at a saturating concentration of urea was determined. To start the reaction 0.1 M urea was added to the enzyme, which was suitably diluted in 50 mM Tris acetate buffer (pH 7.3). Following incubation for 10 min the reaction was terminated by the addition of 10% (w/v) trichloroacetic acid. Color was developed in the supernatant using the indophenol method as described by Weatherburn[17]. The phenol-hypochlorite reaction was shown by the routes outlined in Scheme 1. An enzyme unit is defined as the amount of enzyme required to liberate 1 μmol of ammonia/ min under our test conditions (0.05 M Tris acetate buffer, pH 7.3 containing 0.1 M urea, at 37˚C). the main novelty of your work and suggested reviewers.

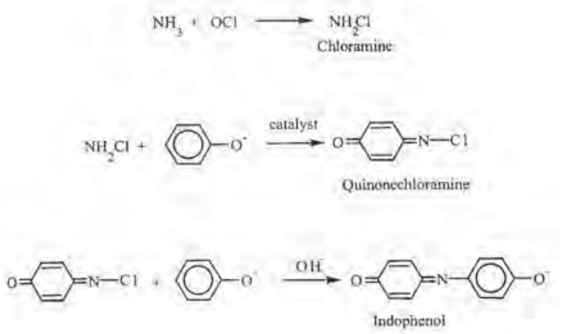

Scheme 1. Synthetic routes of indophenols reagent by Weatherburn's method[17].

2.3 Immobilization of urease

A 5%stock solution of sodium alginate is prepared by slowly adding alginate in 0.1M Tris acetate buffer (pH 7.3) at 37˚C. After the alginate has dissolved, bubbles are removed by cooling the solution. Enzyme is then added and the volume made up in buffer so that the final concentration of the alginate gel is 4%. Enzyme must be added at *ca* 0.1 mg/ml alginate for both optimum immobilization as well as blood urea assay. This is loaded in a 20 ml syringe and alginate enzyme mixture is dropped into 500 ml of chilled 8% calcium chloride in 0.1 M Tris acetate buffer (pH 7.3) with constant swirling on a magnetic stirrer. Drops are counted (to get the total number of alginate beads), while they are falling into the calcium chloride solution. As soon as the drop falls the free enzyme is entrapped in a cage of calcium alginate in the shape of a bead. After stirring for 4-5 h at 4˚C, beads of calcium alginate with entrapped enzyme are collected. Beads are washed with buffer to remove any calcium chloride solution and are stored suspended in buffer at 4˚C.

Protein was assayed by the method of Lowry et al [17] using the Folin-Ciocalteu reagent, and BSA as the standard. The amount of protein immobilized was estimated by subtracting the amount of protein determined in the supernatant following immobilization from the total amount of protein used for the immobilization.

2.4 Determination of urease catalytic activity in the presence and absence of inhibitors

Urea hydrolysis in the presence and absence inhibitors was performed at 36 ^{o}C. The total volume of the mixture was 50.0 mL to 32.0 mL of the original substrate mixture solution, 1.0 mL of urease aqueous solution (50 units) was added (its pH was adjusted to the required value) , 1.0 mL of inhibitor solution, 0.1 M urea, 1.0 mL of 10% (w/v) trichloroacetic acid and 5.0 mL of indophenol reagent. Final concentrations of each amine and oxime inhibitor ranged within 10-100µM. During the hydrolysis of urea in the presence and absence of the inhibitors, changes in absorbance were monitored at 640 nm. All measurements were performed on a T-60 spectrophotometer. Zero absorbance was adjusted by monitoring light absorption by the substrate mixture without inhibitors.

2.5 Kinetic parameters of inhibition effect

Initial reaction rate, $\surd_o$, was expressed in arbitrary units of absorbance changes per second and taken as 100% in the absence of inhibitors. Inhibition constants, K_i, were determined according to Dixon [18]. The rates $\surd_o$ and $\surd_s$ which are the reaction initial and steady-state rates, respectively, are given by the Michaelis-Menten equation describing competitive reaction. Kinetic curves were plotted and followed by the reversible competitive inhibition:

$$\surd_o = \frac{\surd_{max}\, S}{K_m\,(1+I/K_i) + S} \qquad (2)$$

$$\surd_s = \frac{\surd_{max}\, S}{K_m\,(1+I/K_i^{\,*}) + S} \qquad (3)$$

where S and I are substrate and inhibitor concentrations, respectively. K_m is the Michaelis constant and $\surd_{max}$ the maximum reaction rate of the uninhibited reaction, and Ki and KI* are the inhibition constants corresponding to the two steps of the reaction. The reciprocals of $\surd_o$ and $\surd_s$ were used to plot the kinetic curves of inhibitors. In this experiment, the enzyme was incubated with the inhibitor prior to the reaction, and the reaction is initiated by adding the substrate. These provided that there is no significant enzyme inactivation, substrat depletion, nor other enzyme-product secondary reactions.

3. Results and Discussion

3.1 Urease immobilization and storage stability of alginate beads

The alginate- immobilized urease had the following activity assay :The protein content of the immobilized urease is 238±10 mg/dL (average of three determinations with standard deviation) ; which means that the immobilized urease retain 77.17% of the activity of the free urease (the protein content is 310±10 mg/dL). The results also show that reticulation of the adsorbed enzyme significantly improves its stability as shown by the protein content and the reproducibility of response (storage stability) and lifetime of alginate-urease ($t_{1/2}$ = 38 days) at the optimal conditions : 50 mg/ml alginate, 0.1 mg/ml urease, 8%(w/v) $CaCl_2$, 4˚C and pH 7.3.

3.2 Sensitivity of immobilized and free urease assay to amines and oximes

In this study the concentration of all amines and oximes which giving 50% inhibition of enzyme activity, or the half- maximal inhibitory concentration (IC_{50}), was determined (Table 1). The free urease assay was most sensitive to all types of inhibitors.

Table 1: Inhibition of immobilized and free ureases by amine and oxime compounds.

Inhibitor	IC_{50}(mM)	
	Immobilized urease	Free Urease
NDMA	0.020±0.002	0.012±0.002
TMA	ND	ND
DMG	27.0±0.06	22.4±0.06
DAM	0.002±0.013	0.0011± 0.001

* Values obtained are presented as the means from 3 repeats for each concentration.

Among these compounds, NDMA and DAM exhibited good in vitro activities for alginate-immobilized urease. The results revealed that NH groups of amine and N=OH groups of oxime compete in the first stage of the reaction with urea in binding with one or two nickel atoms, partially or completely blocking urea hydrolysis.

3.3 Kinetic parameters of urease inhibition reaction by amines and oximes

The kinetic results obtained for the immobilized urease are presented in Figure 1. The linear nature of the plots proves that in the ranges of urea concentration examined the enzyme follows the Michaelis-Menten kinetics represented by the equations (2) and (3). For low concentrations of substrate the reaction is of the first order, for high concentrations it changes into zero order when the reaction rate is independent of substrate concentration (the results not shown). This range of concentration was used for enzyme activity determinations. Ureases typically exhibit simple Michaelis-Menten behavior. Figure 1 shows that the 1/√ versus 1/[urea] relationship at constant urea concentration appeared to be linear and strongly dependent on the initial urea concentration. This is clearly observed in the case of classical competitive inhibition. The calculated values of the kinetic parameters which are K_m (Michaelis constants) and $\surd_{max}$ (the maximum reaction rates) are summarized in Table 2.

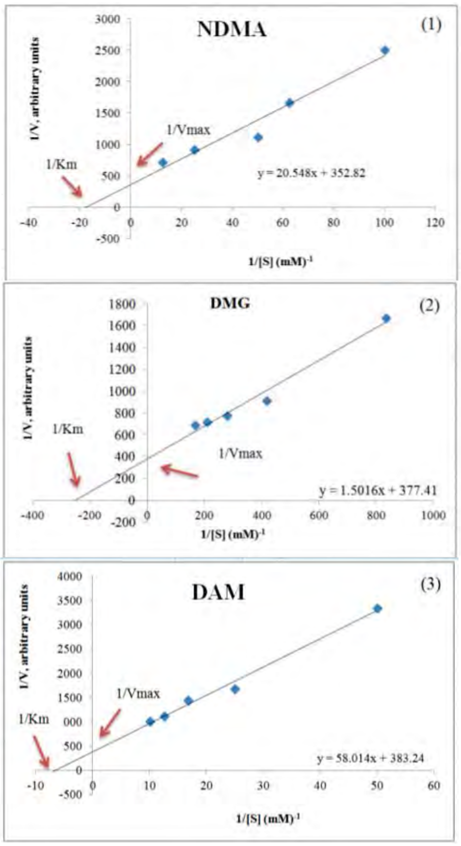

Figure 1. Lineweaver-Burk plots for immobilized urease inhibited by amine and oxime inhibitors : NDMA (1); DMG (2) and DAM (3) in aqueous solution (pH 7.3, 37 °C urease 50.02 units).

Table2: Kinetic parameters for inhibition of urea hydrolysis by amines and oximes (aqueous solution, pH 7.3, 37 °C urease 50.02 units)

Inhibitor	K_m (mM)	$\surd_{max}$ (mM/min)
NDMA	0.0582	0.0028
TMA	ND	ND
DMG	0.0040	0.0027
DAM	140.9	2.70

4. Conclusions

This study shows that urease can be successfully immobilized on calcium alginate beads. The obtained urease has a comparatively high enzymatic activity. The activity retention of urease after immobilization of 77.17% is good and somewhat higher than others previously reported. An important tool for the investigation of the catalytic mechanism of urease is enzymatic inhibition with potential inhibitors such as chemical compounds imitating urease substrate (urea) or compounds which are blocking nickel atoms in the active site of the enzyme. Four amines and oximes were used and evaluated for their inhibitory activity against immobilized jack bean urease compared with the native enzyme. The sensitivity of the immobilized urease to the various organic inhibitors was tested. Among these compounds, diacetylmonoxime (DAM) exhibited the best activity for the inhibition reaction (IC_{50}= 0.002mM). The kinetic plots confirm the observation that the immobilization of urease on alginate beads has a pronounced reducing effect on the inhibition by low toxic amines and oximes as compared to the soluble urease. In view of the presented results, it can be summarized that the observed kinetic behavior of alginate-immobilized urease in the inhibitions by some amine and oxime compounds results the competitive inhibition reactions.

References

[1] C. Nistor and J. Emneus, *Wastt Management.* **19** (1999) 147-170.
[2] H. Kotte, B. Gruendig, K-D. Vorlop, B. Strehlitz and U. Stottmeister, *Anal. Chem.* **67** (1995) 65-70.
[3] M. Hedenmo, A. Narvaez, E. Dominguez, J.J. Fenandez, V. Pavlov and I. Katakis, *Anal. Chim. Acta* **425** (1997) 1-11.
[4] F.D. Munteanu, A. Lindgren, J. Emneus, L. Gorton, T. Ruzgas, E. CaÖregi, A. Ciucu, R.B. Van Huystee, I.G. Gazaryan and L.M. Lagrimini, *Anal. Chem.* **70** (1998) 2596-2600.
[5] H.Q. Li, Z.P. Xiao, Y. Luo, T. Yan, P. C. Lv and H.-L. Zhu, *Euro. Med. Chem.* **44** (2009) (2246-2251.
[6] E.I. Tarun, D.B. Rubinov and D.I. Metelitza, *Biochemistry (Moscow)* **69** (2004) 1344–1352.
[7] J.L. Marty, N. Mionetto, T. Noguer, F. Ortega and C. Roux, *Biosens. Bioelectron.* **8** (1993) 273-280.
[8] P. Skladal, M. Fiala and J. Krejei, *J. Environ. Anal. Chem.* **65** (1996) 139-148.
[9] J. Wang, V.B. Nascimento, S.A. Kane, K. R.ogers, M.R. Snyth and L. Agnes, *Talanta* **43** 91996) 1903-1907.
[10] B. Krajewska, *Enzyme Microb. Tech.* **35** (2004) 126-139.
[11] J. Davis, DH. Vaughan and MF. Cardosi, *Enzyme Microb. Tech.* **17** (1995) 1030-1035.
[12] A. Covacci, J.L. Telford, G.D. Giudice, J. Parsonnet and R. Rappuoh, *Science* **284** (1999) 1328-1333.
[13] Y. Katsura, S. Nishimo, M. Ohno, K. Sakane, Y. Matsumoto, C. Morinaga, H. Ishikawa and H. Takasugi, *J. Med. Chem.* **41** (1998) 1777-1788.
[14] E. Jabri, M.B. Carr, R.P. Hausinger and P.A. Karplus, *Science* **268** (1995) 998-1004.
[15] N.C. Ha, S.T. Oh, J.Y. Sung, K.A. Cha, M.H. Lee and B.H. Oh, *Nat. Struct. Biol.* **8** (2001) 505-509.
[16] Z.P. Xiao, D.H. Shi, H.Q. Li, L.-N Zhang, C. Xu and H-L. Zhu, *Bioor. Med. Chem.* **15** (2007) 3703-3710.
[17] M.W. Weatherburn, *Anal. Chem.* **39** (1967) 971-974.
[18] N.E. Dixon, R.L. Blakeley and B. Zerner, *Can. J. Biochem.* **58** (1980) 481-488.
[19] P.W. Riddles, R.K. Andrews, R.L. Blakeley and B. Zener, *Biochim. Biophys. Acta.* **743** (1983) 115-120.

A NOVEL EXCIMER “ON-OFF” PYRENYLACETAMIDE-BASED FLUORESCENT PROBE FOR SELECTIVE Cu^{2+}-SENSING

Krit Setthakarn[1], Monchai Siriprumpoonthum[1], Chantana Wainiphithapong[1],
Vannajan Sanghiran Lee[2], Nantanit Wanichacheva[1]*

1 Department of Chemistry, Faculty of Science, Silpakorn University, Nakorn Pathom 73000, Thailand
2 Department of Chemistry, Faculty of Science, University of Malaya, Kuala Lumpur 50603, Malaysia

* Author for correspondence; E-Mail: nantanit@su.ac.th

Abstract: A novel fluorescent probe, two pyrenylacetamide moieties covalently attached to 2-[3-(2-aminoethylsulfanyl)propylsulfanyl]ethanamine, was designed and synthesized by using a conventional three-step synthesis for the selective detection to Cu^{2+} ions. The sensing behaviors were investigated by UV/Vis and fluorescence spectroscopy. The sensor exhibited a selective ON-OFF type sensing of excimer band of pyrene fluorophores toward Cu^{2+} ions at 481 nm. The detection limit of the sensor was examined to be 1.4 ppb for Cu^{2+}.

1. Introduction

The various heavy metals play the crucial roles in various fields including biological and environmental systems. Copper is an important factor in human body since it is the third abundant of essential element after Zn^{2+} and Fe^{3+} [1]. However, the excessive exposure of copper toward human causes the damage of neurotic system in the body, including Wilson’s disease [2-3], Alzheimer’s disease[4-5] and Prion’s disease[5]. Accordingly, continuous monitorring and simple, rapid and prompt detections for Cu^{2+} ions are of great importance.

Current techniques for Cu^{2+} determination, including atomic absorption spectroscopy [6], inductively coupled plasma mass spectroscopy (ICP-MS) [7], inductively coupled plasma atomic emission (ICP-AES) [8], inductively coupled plasma-optical emission spectrometry(ICP-OES) [9] and spectrophotometry [10] often require a large amount of samples, expensive and sophisticated instrumentations which pose serious limitations for determination of Cu^{2+} in biological samples.

Recently, the fluorescent sensors for the selective detection of the toxic heavy metals, including Cu^{2+}, have been considerable developing since they provide high sensitivity, prompt detection and serve as an inexpensive method. Although many fluorescent sensors have been designed for Cu^{2+}-sensing, many lack the suitability for practical uses due to multi-step syntheses, high costs of starting materials or lack of selectivity for Cu^{2+} [11-13].

Therefore, the major motivation of this work is the design and synthesis of Cu^{2+} sensor with high sensitivity and selectivity but with a significantly reduced synthetic effort using inexpensive starting materials. In this work, pyrene was chosen as an fluorophore since it is known as a high efficient signaling unit in the view of monomer and excimer emissions. Herein, we have focused on the excimer emission of pyrene moieties which occurs from intramolecular π-π* staking type that can be emissive in the visible region.

In the present work, we report the synthesis of a new “turn-off” Cu^{2+}-fluorescence chemosensor which provides high sensitivity and selectivity towards interfering ions, but with a significantly reduced synthetic cost and efforts. The sensor is fabricated from a sulfur and nitrogen containing ionophore based on a 2-(3-(2-aminoethylsulfanyl)propylsulfanyl)ethanamine ligand covalently bound to two pyrene fluorophores. We propose that the sensor will exhibit high sensitivity and selectivity to Cu^{2+} over other foreign ions due to the well-known interaction of Cu^{2+} with sulfur and nitrogen atoms. [14-16].

2. Materials and Methods

2.1 General Setting

All reagents and solvents were purchased from Fluka Chemical Corporation were used as received. All of the metal salts used in this study were acetate salts. Cadmium acetate was purchased from Merck and cobalt acetate was purchased from Prolabo. Tetrahydrofuran, dichloromethane and methanol were dried according to the standard methods prior to use. Aqueous solutions were freshly prepared using high-purity Millipore deionized water (18 MΩ.cm).

NMR spectra were obtained with a Bruker Avance 300 spectrometer operating at 300 MHz for ^1H and 75 MHz for ^{13}C. All NMR spectra were obtained in $CDCl_3$ solutions with TMS as internal standard. Mass spectra were performed by a ThermoElectron LCQ-DECA-XP, electrospray ionization ion trap mass spectrometer.

Fluorescence measurements were performed on a Perkin Elmer Luminescence spectrometer LS 50B. The excitation and emission slit widths were 5.0 nm.

2.2 Syntheses

Synthesis of compound **2:** In a 50 mL round bottom flask, 1-aminopyrene (0.20 g, 1.00 mmol) and triethylamine (0.2 ml, 1.45 mmol) were stirred in 20 mL dry dichloromethane under an argon atmosphere. Bromoacetyl bromide (0.12 ml, 1.45 mmol) was added to the solution mixture, and it was stirred for 12 hours at room temperature. The insoluble compound was filtered off and carefully washed with dichloromethane. The compound was allowed to dry under vacuum and yielded 387 mg of a white solid, 78 % yield. The compound was used without further purification.; ^{1}H NMR (300 MHz, $CDCl_3$) δ 4.30 (s, 2H), 8.03-8.11 (m, 4H), 8.16-8.25 (m, 4H), 8.44 (d, J = 8.1 Hz, H), 8.96 (s, H); ^{13}C NMR (75 MHz, $CDCl_3$) δ 30.0 (CH_2), 119.7 (CH), 121.8 (CH), 123.7 (C), 124.7 (C), 125.2 (CH), 125.2 (C), 125.3 (CH), 125.8 (CH), 126.3 (CH), 127.3 (2CH), 128.5 (CH), 129.2 (C), 129.6 (C),130.7 (C),131.3 (C), 164.1 (C). HR-ESI MS calcd for $C_{18}H_{12}BrNNaO$ $(M+Na)^+$ 360.0000 m/z, found 360.0034 m/z.

Synthesis of **3**: In a 10 mL round bottom flask, 2-(3-(2-aminoethylsulfanyl)propylsulfanyl)ethanamine (0.035 g, 0.18 mmol) and K_2CO_3 (0.032 g, 0.23 mmol) were stirred in 3 mL dry tetrahydrofuran under an argon atmosphere. **2** (0.12 g, 0.35 mmol) was added and the mixture was refluxed 12 h. The insoluble compound was removed by filtration, and the solution mixture was removed under vacuum. The crude product was purified on preparative thin-layer chromatography plates, run in the dark (5% methanol in dichloromethane), to yield 69 mg of a brown solid, yield 54 %. $R_f = 0.5$ (5% methanol in dichlorometane); ^{1}H NMR (300 MHz, $CDCl_3$) δ 1.65-1.90 (m, 6H), 2.40-2.65 (m, 8H), 2.83 (t, J = 5.7 Hz, 4H), 3.50 (s, 4H), 7.75-8.22 (m, 16H), 8.69 (d, J = 8.4 Hz , 2H); ^{13}C NMR (75 MHz, $CDCl_3$) δ 29.1 (CH_2), 30.9 ($2CH_2$), 32.8 ($2CH_2$), 48.8 ($2CH_2$), 52.9 ($2CH_2$), 120.0 (2CH), 120.1 (2CH), 120.5 (2C), 122.0 (2C), 124.8 (2CH), 125.3 (2CH), 125.5 (2CH), 126.1 (2CH), 126.5 (2CH), 126.8 (2C), 127.4 (2CH), 127.7 (2CH), 128.4 (2C), 130.6 (2C), 130.8 (2C), 131.4 (2C), 170.0 (2C). HR-ESI MS calcd for $C_{43}H_{41}N_4O_2S_2^+$ $(MH)^+$ 709.2671 m/z, found 709.2628 m/z.

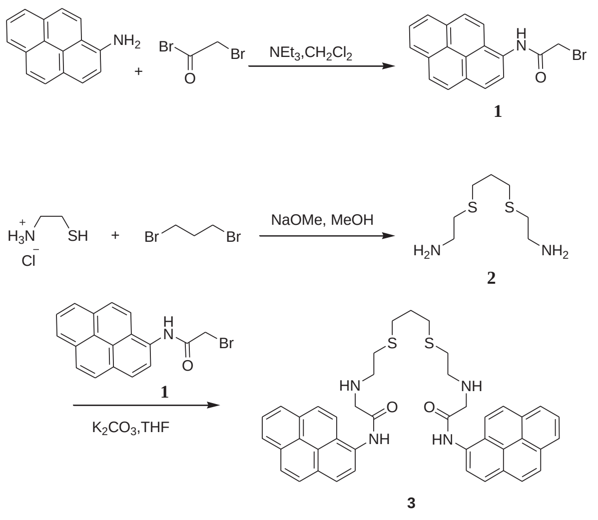

Figure 1. Synthesis of **3**

3. Results and Discussion

The synthesis of **3** was performed according to the synthetic steps outlined in Figure 1. 2-[3-(2-aminoethylsulfanyl)propylsulfanyl]ethanamine was prepared by alkylation of cysteamine hydrochloride with 1,3-dibromopropane. 2-bromo-*N*-pyren-1-yl-acetamide, **1,** was obtained by alkylation of 1-aminopyrene with bromoacetyl bromide in high yield (78 %). The alkylation of **2** with **1** was carried out and achieved **3** (54 % yield).

3 is based on a flexible podant structure containing two sulfur atoms and four nitrogen atoms which are covalently bound to the pyrene fluorophores. In this study, the design concept for the sensor is based on the fundamental requirements for the selective host-guest interactions in supramolecular chemistry. We expect that the selective ion recognition can originate from self-assembly of the sensor and Cu^{2+} by favorable electrostatic interactions of Cu^{2+} coordinated with sulfur and nitrogen atoms resulting in the change of excimer emissions of pyrene fluorophores.

The signaling behaviors of **3** were investigated by fluorescence measurements in common organic solvents and aqueous-miscible organic solvent systems. Figure 2. illustrates that the fluorescence behaviors of **3** are strongly dependent upon the employed solvent systems. In the dioxane and tetrahydrofuran solutions, the fluorescence spectra of **3** show the characteristic monomer emission bands of pyrene moieties at around 387 and 408 nm along with a small band around 481 nm which is typical of the pyrene excimer. In dichloromethane, methanol and acetonitrile solutions, however, the excimer emission of **3** becomes prominent compared to typical monomer emission bands of pyrene.

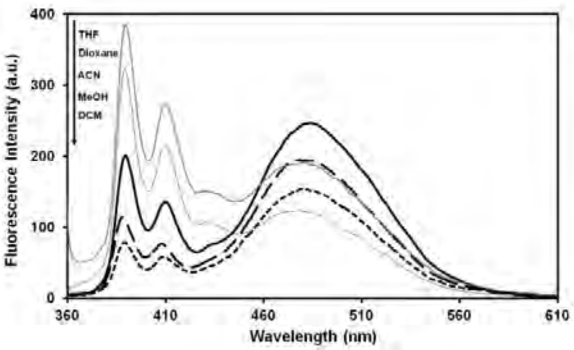

Figure 2. Fluorescence spectra of **3** in tetrahydrofuran, dioxane, acetonitrile, methanol and dichloromethane, λ_{ex} = 347 nm.

After a preliminary survey by titration Cu^{2+} with various solvent systems, **3** showed poor responses in dichloromethane, dioxane and tetrahydrofuran solutions, and exhibited high sensitivity in methanol, acetonitrile and aqueous-acetonitrile solutions. Based on these observations, we therefore focused on the fluorescence behavior of **3** in response to various metal ions in 80:20 acetonitrile:water.

To elucidate the quantitative binding affinity of **3**, fluorescence titrations of **3** with Cu^{2+} were carried out. Figure 3. illustrates the fluorescence responses obtained for **3** in the presence and absence of Cu^{2+} in

80:20 acetonitrile:water. In the absence of Cu^{2+} ions, the excimer response is at a maximum and the response decreases as Cu^{2+} concentration is increased. When the added copper acetate attained approximately 0.5 equiv of concentration of **3**, the excimer emission band around 481 nm reaches a minimum point and more than 50% quenching was observed. The association constant, K_{assoc}, of **3**-Cu^{2+} was determined by Benesi-Hildebrand plot of the signal changes in the fluorescence titration results. It was found to be 1.18 x 10^7 M^{-1} and 1:1 complex formation of **3**-Cu^{2+} was suggested.

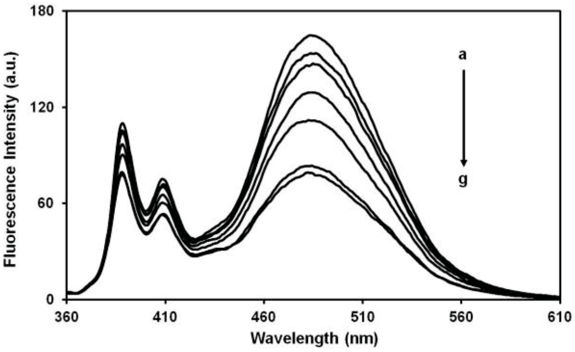

Figure 3. Fluorescence emission spectra (λ_{ex} = 347 nm) of **3** (0.46 μM) in 80:20 $CH_3CN:H_2O$ as a function of [Cu^{2+}]. a: 0 μM, b: 0.02 μM, c: 0.03 μM, d: 0.07 μM, e: 0.10 μM, f: 0.17 μM, g: 0.23 μM.

The selectivity studies of **3** were obtained in 80:20 acetronitrile:water solutions by recording the fluorescence spectra of the solution of **3** before and after the addition of each representative alkali, alkaline earth and transition metal ions (Figure 4.). The acetate salts of Cu^{2+}, Ag^+, Ca^{2+}, Cd^{2+}, Co^{2+}, Fe^{3+}, K^+, Mn^{2+}, Na^+, Ni^{2+}, Pb^{2+} and Zn^{2+} ions were used to investigate the metal binding affinities of **3**.

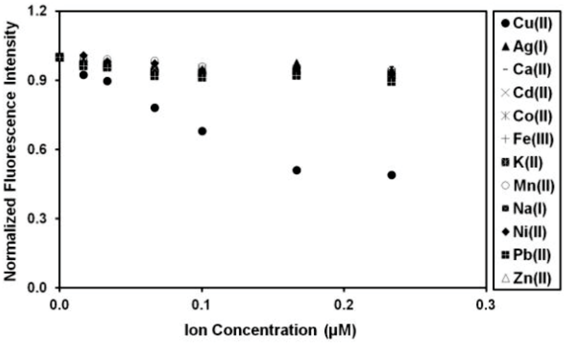

Figure 4. Normalized emission intensity (481 nm) of **3** (0.46 μM) in 80:20 $CH_3CN:H_2O$ versus the concentration of various metal ions**:** Cu^{2+}, Ag^+, Ca^{2+}, Cd^{2+}, Co^{2+}, Fe^{3+}, K^+, Mn^{2+}, Na^+, Ni^{2+}, Pb^{2+} and Zn^{2+} ions

As shown in Figure 4., the sensitivity studies were represented in the normalized fluorescence intensity of **3** and the changes of fluorescence intensity at 481 nm were observed. The results show that **3** offers highly selective detection toward Cu^{2+} in comparison with the various cations. The studies showed that the significant fluorescence intensity decreases as a function of addition of Cu^{2+} when it was compared with the addition of relevant foreign ions that the changes of fluorescence intensity was slightly observed. Especially, sensor **3** exhibited the highly selectivity for Cu^{2+} over Zn^{2+} and Fe^{3+} which are found in higher quantity than Cu^{2+} in environmental sources [1]. The detection limit of **3** as a fluorescent sensor for the analysis of Cu^{2+} was determined from the plot of the fluorescence intensity changes (481 nm) as a function of Cu^{2+} concentration. It was found to be 2.2 x 10^{-8} M or 1.4 ppb for detection of Cu^{2+} which are sufficient for the detection of sub-micromolar concentrations of Cu^{2+} ions found in environment and biota.

4. Conclusions

We have prepared and introduced a new copper fluoroionophore, **3**, that exhibits strong excimer emission in organic solution and aqueous-organic solution. The designed compound exhibited highly selective and sensitive fluoroionophoric behavior toward Cu^{2+} over a wide range of foreign ions, but with a significantly reduced synthetic effort and in good yield. The sensor is fabricated from two units of pyrenylacetamide covalently bound to 2-(3-(2-aminoethylsulfanyl)propylsulfanyl)ethanamine and prepared by a conventional three-step synthesis. The detection limit of **3** was observed to be approximately 1.4 ppb for Cu^{2+}.

Acknowledgements

This work was supported by a grant SCH-NR2009-16-05 from National Science and Technology Development Agency (NSTDA), Thailand.

References

[1] D. G. Barceloux, *J. Toxicol., Clin. Toxicol.* **37** (1999**)** 217–230.
[2] R. A, Løvstad, *BioMetals* **17** (2004) 111-113.
[3] P. C. Bull, G. R. Thomas, J. M. Rommens, J. R. Forbes and D. W. Cox, *nature genetic* **5** (1993) 327-337.
[4] Y. H. Hung, A. I. Bush, R. A. Cherny, *J Biol Inorg Chem* **15** (2010) 61–76.
[5] D. R. Brown, H. Kozlowski, *Dalton Trans.* (2004) 1907–1917.
[6] A. P. S. Gonzales, M. A. Firmino, C. S. Nomura, F. R. P. Rocha, P. V. Oliveira, I. Gaubeur, *Anal. Chim. Acta* **636** (2009) 198–204.
[7] J. S. Becker, A. Matusch, C. Depboylu, J. Dobrowolska, M. V. Zoriy, *Anal. Chem.* **79** (2007) 6074–6080.
[8] Y. Liu, P. Liang, L. Guo, *Talanta* **68** (2005) 25–30.
[9] C. Cui, M. He, B. Hu, *Journal of Hazardous Materials* **187** (2011) 379–385.

[10] J. J. Pinto, C. Moreno, M. Garcia-Vargas, *Talanta* **64** (2004) 562–565.
[11] D. Y. Lee, N. Singh, D. O. Jang, *Tetrahedron Letters* **51** (2010) 1103–1106.
[12] J.-M. Liu, Q.-Y. Zheng, J.-L. Yang, C.-F. Chen, Z.-T. Huang, *Tetrahedron Letters* **43** (2002) 9209–9212.
[13] Z. Jiang, R. Deng, L. Tang, P. Lu, *Sensors and Actuators B* **135** (2008) 128–132.
[14] D.T. Minkel, L. A. Saryan, D.H. Petering, *Cancer Res.* **38** (1978) 124-129.
[15] D.A. Winkelmann, Y. Bermke, D.H. Petering, *Bioinorg. Chem.* **3** (1974) 261-277
[16] P. K. Dhara, S. Pramanik, T.-H. Lu, M. G. B. Drew, P. Chattopadhyay, *Polyhedron* **23** (2004) 2457-2464.

MICROFLUIDIC CHEMILUMINESCENCE ASAAY FOR QUANTITATIVE ANALYSIS OF OXALIC ACID AFTER PHOTOCATALYSIS BY TITANIUM DIOXIDE NANOPARTICLES

Sakchai Satienperakul* and Jutimaporn Tangjit

Department of Chemistry, Faculty of Science, MaejoUniversity, Chiang Mai 50290Thailand
* Author for correspondence; E-Mail: sakchais@mju.ac.th, Tel. +66 53 873530, Fax. +66 53 878225

Abstract: The determination of oxalic acids was developed utilizing microfluidic chemiluminescence system (µFI-CL), after photo-oxidation reaction catalysts by titanium dioxide nanoparticle. In this research, a 'sandwich type' microfluidic device was made from small pieces of polymethylmethacrylate (PMMA) and polydimethylsiloxane (PDMS). The blue chemiluminescence light generated by the oxidation reaction between luminol and H_2O_2 in the presence of degraded free radical dicarboxylic was detected by a photomutiplier tube (PMT) at the wavelength of 425 nm. Some physical and chemical micro-flow parameters were thoroughly studied. Nanoparticles of titanium dioxide powder were employed to enhance the photo-oxidation rate of oxalic acid under UV–irradiation. At the optimum values, linear calibration range of oxalic acid can be determined in the concentration range of 7×10^{-4}-1.0×10^{-3} M, with the detection limit (3σ) of 5.0×10^{-5} M. The results from µFI-CL experiment were compared with standard HPLC method. Results from urine and some vegetable samples were agreed well at 95% confidence interval.

1. Introduction

Oxalic acid/oxalates are abundantly present in several plants [1]. Oxalate acts as a chelator of various positively charged metal ions, such as Fe^{2+}, Fe^{3+}, Cu^{2+}, Al^{3+} and Cr^{3+}, among others. It also forms strong chelates with dietary calcium, thus rendering the complex unavailable for absorption and assimilation. In humans, precipitation of calcium oxalate may lead to the formation of kidney stone [2]. Therefore, the determination of oxalic acid in some biological materials has attracted much attention.

Methods mostly reported for oxalic acid determination are based on fluorimetry [3], isotope dilution mass spectrometry [4], gas chromatography [5], High-performance liquid chromatography [6-8] and ion-exclusion chromatography [9] are also used for oxalate determination, but special instrumentation and relatively high costs of analysis are required. There is still a need for a sensitive, inexpensive, simple and rapid method for the analysis of oxalic acid.

The photo-oxidation of oxalic acid is occurred via photo-irradiation with visible or UV light. The emission of CO_2.and the formation of other oxidation products, then quantified by measuring the CL intensity in a luminol/H_2O_2 system in the absence of added oxidant [6], In this present work, microfluidic flow injection chemiluminescence was investigated for determination of oxalic acid in biological samples, such as blood serum, urine and selected vegetables, after the photo-catalytic oxidation of oxalic acid, when TiO_2 was added as nanaocatalyst [10] which then enhanced of sensitivity of CL reaction.

2. Materials and Methods

2.1 Reagent

All chemicals were of analytical reagent grade. Solutions were made in ultra-pure water (18.2 MΩ, Millipore, France).

Stock standard solution of oxalic acid (0.1000 M) was prepared by dissolving 1.267 g of oxalic acid (Merck, Germany) in water and diluting to 100 ml volumetric flask. Working standard solution of oxalic acid (2.5×10^{-4}–5.0×10^{-3} M) were obtained by appropriately diluting the stock solution and added 0.050 g TiO_2 (Ajax, Australia) which subject for photo-oxidation, shaking and filtering through cellulose acetate (0.45 µm) prior to injection.

EDTA stock solution (1×10^{-2} M) was prepared by dissolving 0.360 g of EDTA (Ajax, Australia) in 6×10^{-3} M KOH and diluting to 100 ml volumetric flask.

KOH stock solution (1 M) was prepared by dissolving 0.165 g of KOH (Merck, Germany) and diluting to 25 mL.

Luminol stock solution (1×10^{-2} M) was prepared by dissolving 0.0456 g of luminol (Sigma, USA) in 1 M NaOH and diluting to 25 ml. Luminol reagent solution (6×10^{-4} M) was prepared by diluting 6 ml of luminol stock solution and diluting to 100 mL with 0.15 M HCO_3^-/CO_3^- buffer solution to adjust the pH to 11.0.

H_2O_2 stock solution (1×10^{-2} M) was prepared by added to 1mL of 30% H_2O^2 (Merck, Germany) and diluted to 10 mL with water.

2.2 Microfluidic device design

The microchips channel were design by Corel Draw PC suite 5 as illustrate in Fig.1(a). The microchips were engraved by CO_2 laser which used to abate channel in polymethyl methacrylate (PMMA) following by the pattern. The microfluidic device composed the cover plate was made from polydimethylsiloxane (PDMS) sheet, the size of both microchip and cover plate was 35 × 35 × 35 mm. The cover plate made from mixture of 10:1 prepolymer and curing agent (Sylgard 184, Dow Corning, USA) by stirred thoroughly and degasses in a vacuum for 15 min. Then the prepolymer mixture was poured onto the glass slide template and cured at 70 °C for 1 h.

After curing, the PDMS replica was peeled from the template and cut to respectively sheet size. The completed set up microfluidic device was declared as sandwich type as illustrated in Fig. 1(b). After that the device was sealed by tightening the PMMA sandwich sheets with screws.

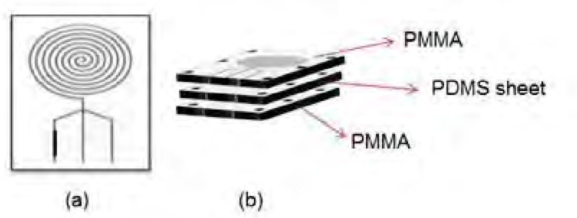

Figure 1 Illustration of the laser-engraved flow lines of the microfluidic platform (a); a sandwich type microfluidic device (b).

2.3 Apparatus and Procedure

Apparatus: The flow assembly used in oxalic acid determination is presented in Fig.2. The experimental setup consisted of a four-channel peristaltic pump with rate selector (Minipuls 3, Gilson, France), a sample injection valve (V-450, Upchurch Scientific, USA) and PTFE connection tubing (0.5 mm i.d., Agilent, USA). The CL signal was monitored in custom built flow-through luminometer, which consisted of a microfluidic device mounted flush against a red sensitive photomultiplier tube (PMT, Electron Tubes, UK). The operational potential for the PMT was provided by stable power supply (Thorn- EMI model PM20, Electron tubes Ltd., UK) at a voltage of 900 V. CL signal was detected via a digital multimeter (Uni-Trend, UT60D, Hong Kong) and the UNI-T® UT60D AC/DC software was used to determination the peak maximum.

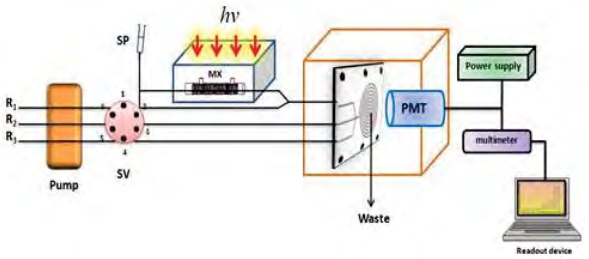

Figure 2 Schematic diagram of the µFI-CL system.

R1 = 2×10^{-3} M EDTA in 6×10^{-3} M KOH, R2 = 6×10^{-4} M luminol in 0.15 M carbonate buffer pH 11.0, R3 = 6×10^{-4} M H_2O_2, SP = Injector, SV = six-port valve , MX = mixing coils.

Procedure : The µFI-CL system procedure is also shown in Fig.2.The solutions of luminol, EDTA and H_2O_2 were pumped continuously at 0.4 mL min^{-1} by peristaltic pump R1, R2 and R3 at 0.6 $ml.min^{-1}$.The EDTA carrier stream solution was put in a photo-reactor box with a mixing reactor coils (length 230 cm), and UV irradiation was performed for 60 s. The combined reaction mixture was passed through the microfluidic cell, where CL signal was detected by PMT and correspondence to peak maximum.

3. Results and discussion

The primary photochemical reaction is assumed to be an intramolecular oxidation–reduction caused by an electron transfer from the organic acid with OH radicals produced by the reaction of photogenerated holes with adsorbed water molecules over titanium dioxide suspended in oxygenated aqueous solution. According to previous work by Kosanić [11], the oxalic acid reacts with OH radicals mechanism may be proposed for the photo-oxidation of oxalic acid at the surface of TiO_2 catalyst:

$$HC_2O_4^- + {}^{\cdot}OH \rightarrow OH^- + {}^{\cdot}COOH + CO_2$$

Then mechanism proposed for CL systems is:

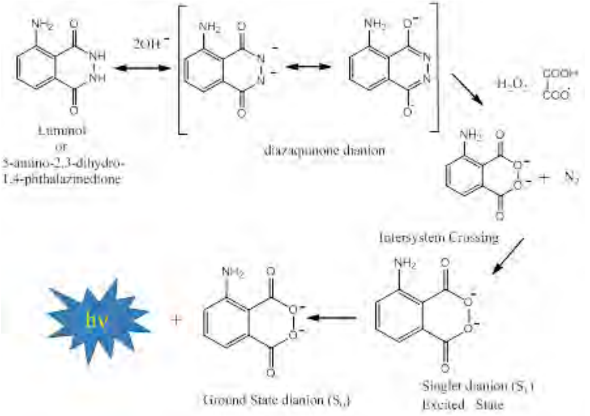

The variables affecting the photochemical and CL reactions were then studied with an FI system

3.1 Optimization of the Parameters

The µFI-CL system's parameters optimized in this study were the: (i) PMT voltage; (ii) concentration of H_2O_2; (iii) concentration of luminol; (iv) concentration of buffer; (v) pH value; (vi) concentration of KOH; (vii) concentration of EDTA; (viii) quantity of TiO_2 (ix); irradiation time of photo-catalytic reaction; (x) sample injection volume; (xi) flow rates of the carrier and reagent stream. The summary of their optimal value are show in Table 1. Under the optimal condition the linear calibration curve 2.5×10^{-4} –5.0×10^{-3} M was observed and illustrated in Figure 3, while the coefficient of correlation was 0.993. The limit of detection (s/n>3) was found to be 5.0×10^{-6} M.

Table 1 Optimization microfluidic-CL system parameter

Parameters	Studied range	Optimal value
PMT voltage (kV)	800-1000	0.90
H_2O_2concentration (M)	5.0×10^{-4}-1.0×10^{-3}	6.0×10^{-4}
luminol concentration (M)	1.0×10^{-4}-1.0×10^{-3}	6.0×10^{-4}
buffer concentration (M)	0.05-0.30	0.15
pH value	9.5–12.0	11.0
EDTA concentration (M)	1.0×10^{-3}-8.0×10^{-3}	2.0×10^{-3}
KOH concentration (M)	1.0×10^{-3}-1.0×10^{-2}	6.0×10^{-3}

Time of irradiation (s)	1-180	60
Injection volume (μL)	20-100	40
Total flow rate (mL)	0.2-3	1.4
Quantity of TiO_2(g)	0.001-0.05	0.05

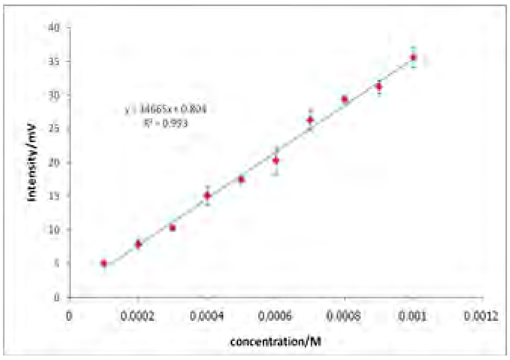

Figure 3 Calibration curve of oxalic acid by μFI-CL

3.2 The effect of photo-catalytic oxidation by TiO_2 nanoparticle

The influence of photo-catalytic reaction for determination of oxalic acid was studied by injection filtered solution of 2.5×10^{-3}M oxalic acid solution, TiO_2 solution (0.0125 g in 25 ml) and 2.5×10^{-3}M oxalic acid plus 0.0125 g TiO_2 to μFI-CL system. As can be seen from Fig 4, CL signal was increase surprisingly due to because TiO_2 powder enhanced the reaction rate of the photo-oxidation of oxalic acid with UV-irradiation [10].

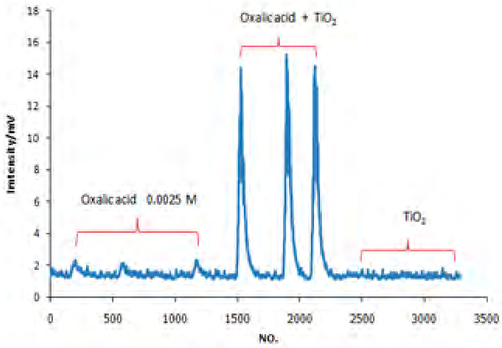

Figure 4 Effect of photo–oxidation reaction by TiO_2 nanoparticle

3.3 Interference studies

Interferences from common species, which may occur with desired samples, were investigated to studies for interferences in determination of 2.5×10^{-3} M oxalic acid using the propose method. The tolerance limit was taken as the amount of added species that caused error of ± 10 % in peak height. The maximum tolerance concentration for each co-existing are listed in Table 2. Serious interferences came from ascorbic and citric acids where react similarly with TiO_2 in the reagent stream.

Table 2 Interfering studies

Tolerance ratio	Interfering species
1:1	Ascorbic acid, Citric acid
1:10	Glycine
1:100	Salicylic acid
>1000	Glucose

3.4 Application to real samples

The analytical usefulness of the proposed reaction detection system was tested by determining these analytes in selected vegetables and urine samples.

The data of Table 3 show that the content of the oxalic acid, as measured by the proposed method, was in excellent agreement with that obtained by AOAC method (HPLC with absorbance detection at 210 nm). There is no significant difference between the mean values obtained by both methods at 95 % confidence (*t*-test). The accuracy of the proposed method was obtained by spiking three levels concentrated of oxalic acid in vegetable sample. The recovery was in the range of 90-102 %.

Table 3 Determination of oxalic acid in vegetable and urine samples

Samples	Oxalic acid concentration (mg kg^{-1})		
	μFI-CL	HPLC	*t* – value
V_1	2.64±0.43	2.01±0.03	2.52
V_2	1.55±0.49	1.42±0.01	1.76
U	4.45±0.28	4.61±0.02	1.75

However, amount of oxalic acid in some vegetable samples are significant different (with the standard method) which mean the investigation for a proper sample preparation process and further interfering species may require.

4. Conclusions

This research presented the utilizing of microfluidic system with chemiluminescence detection coupled with photo-catalytic oxidation by titanium dioxide nanocatalyst for the determination of oxalic acids. CL intensity was enhanced by titanium dioxide nanoparticle acceleration, where the chemi-luminescence detection was performed and enhanced by free radical decomposed products. The proposed procedure will be applied to the determination of oxalic acid in blood serum, urine and some selected vegetables.

Acknowledgements

The authors wish to thank Faculty of Science, Maejo University for partial financial support

References

[1] A. Hodgkinson, *Chin. Chem.*, **16** (1970) 547-557.
[2] A. Safavi, A.R. Banazadeh, *Food Chem.*, **105** (2007) 1106–1111.

[3] P.M. Zarembski and A. Hodgkinson, *J. Biochem*., **96** (1965)717-721.

[4] A.J. Zara, L.O. de, S. Bulhonoes, *Anal. Lett.* 20 (1987) 213. i, *Thai J. Phytopharm.*, **11** (2004) 21-32.

[5] N.C. France, P.T. Holland, T.K. McGhie, *J. Chromatogr*., **456** (1988) 1.

[6] T.Pérez-Ruiz,C.Mart´ınez-Lozano,V. Tomás, J. Mart´ın, *J. Chromatogr A*., **1026** (2004) 57–64

[7] L.-Ch. Li, T.-R. Li, P. Wang, Bull. *Anal. Testing*, **8** (3) (1989) 21.

[8] A. Brega, A. Quadri, *J. Liq. Chromatogr.* **15** (1992) 501.

[9] L. Yang a, L. Liu b, B.A. Olsen a, M.A. Nussbaum, *J. Pharm. Biomed. Anal.*, **22** (2000) 487–493

[11] A. Fujishima_, T.N. Rao, D. A. Tryk, *J. Photochem and Photobio C: Photochem* , **1** (2000) 1–21.

[10] M. M. Kosanić, *J. Photochem & Photobio. A*: *Chem.* 119 (1998) 119–122.

COPPER (I) IODIDE COMPLEXES OF 2,2'-BIPYRIDINE AND *N*-METHYLTHIOUREA

Chanokchon Chanasongkram[1]*, Weena A. Tapachai[1], Jittikarn Petwong[1], Chaveng Pakawatchai[2] and Ruthairat Nimthong[2]

[1]Department of Chemistry, Faculty of Science, Prince of Songkla University, Hat Yai, Songkhla, 90112, Thialand
[2]Department of Chemistry and Center for Innovation in Chemistry, Faculty of Science, Prince of Songkla University, Hat Yai, Songkhla, 90112, Thialand

* Author for correspondence; E-Mail: palm_kn@hotmail.com, Tel. +66 87 4447035, Fax. +66 74 212918

Abstract: Two new complexes, $[(bipy)(H_2O)Cu(OH)_2Cu(SO_4)]\cdot4H_2O$ (1) and $[Cu(bipy)_2I]I_3$ (2) (bipy = 2,2'-bipyridine) have been synthesized by reactions of copper(I) iodide with 2,2'-bipyridine and *N*-methylthiourea and characterized by Fourier transform infrared spectroscopy and single crystal X-ray diffraction. Complex (1) crystallize in monoclinic system, space group *P*2$_1$/c with cell parameters *a* = 9.6803(4), *b* = 34.5365(14), *c* = 7.8279(3) Å, *β* = 103.4980(10)° and *Z* = 4. Complex (2) crystallizes in monoclinic system, space group *C*2/c with cell parameters *a* = 26.3803(18), *b* = 7.3728(5), *c* = 14.8424(10) Å, *β* = 120.1390(10)° and *Z* = 8. The geometry of complex (1) is dinuclear in which the Cu^I ions adopt distorted tetragonal planar. In dinuclear unit the two copper centers are bridged by two O atoms of two OH$^-$ molecules to forms a four-membered Cu-O-Cu-O ring. There are two types of coordination environment around the copper centers. In one of the Cu center is bound to two N atoms of one bipy ligand and three O atoms of two OH$^-$ molecules and one sulphate ion while in other center the Cu center is coordinated with two N atoms of one bipy ligand and three O atoms of two OH$^-$ molecules and one water molecule. The structure of complex (2) features distorted tetragonal pyramid, copper(I) center coordinated to four nitrogen atoms from two 2,2'-bipyridine molecules and one iodide atom. Moreover, H-bondings and π-π stacking interactions of both complexes display a three-dimensional networks.

1. Introduction

The copper complexes have been widely surveyed due to their applications in catalyst [1-2], biological properties [3], photophysical properties [4], luminescent [5] and anti-microbial agents [6-7]. Copper(I) salts, soft acids, are known to from coordination complexes with soft base ligands containing S, P or N donor atom. The chosen mixed ligands substituted thiourea and 2,2'-bipyridine are used because nitrogen atoms and sulfur atom can coordinate to copper atom. An investigation of adduct formation of copper(I) iodide with the chosen mixed ligands has been carried out, we report reaction of copper(I) iodide with the chosen mixed ligands 2,2'-bipyridine and *N*-methylthiourea in acetonitrile have been synthesized and structurally characterized.

2. Experimental

2.1 Materials and methods

Copper iodide was obtained from Fluka Chemical, Buchs, Switzerland. 2,2'-Bipyridine was a product of Sigma Aldrich Co., India. *N*-methylthiourea was a product of Fluka Chemical, Buchs, Switzerland. Acetonitrile was purchased from Labscan asia Co., Thailand.

Melting point of the complexes was measured on capillary melting point apparatus hoover, Unimelt 0-360 °C. The IR spectrum of the complex was recorded on a Perkin Elmer 783 infrared spectrophotometer using KBr pellets over the range 4000-400 cm^{-1}.

2.2 Synthesis of the complex

CuI (0.10 g, 0.52 mmol) was added to a stirred solution of 2,2'-bipyridine (0.08 g, 0.52 mmol) in 15 cm^3 of acetonitrile. The mixture was warmed at 60°C for 2 hours. Then *N*-methylthiourea (0.05 g, 0.52 mmol) was added and stirring for 3 hours. This resulted in a precipitate and afterward the solvent was evaporated. After two weeks, the black crystalline and the green crystalline products were dried *in vacuo*. The melting point of the complexes are 210°C and 130°C. Complex 1; FTIR (KBr; cm^{-1}): *v*(N-H)3051.43(s), *v*(C-N) 1252.04(m), *v*(C=N)1597.87(s). Complex 2; FTIR (KBr; cm^{-1}): *v*(N-H)3051.65(s), *v*(C-N)1251.87(m), *v*(C=N)1597.66(s).

2.3 X-ray crystallography

The X-ray diffraction data of **$[(bipy)(H_2O)Cu(OH)_2Cu(SO_4)]\cdot4H_2O$** and **$[Cu(bipy)_2I]I_3$** were collected using SMART APEX CCD area detector with Bruker platform diffractometer at Prince of Sonkla University Crystallography Lab. The structure was solved by direct methods and refined by a fullmatrix least-squares on *F*^{2} using the SHELXTL program [8]. Molecular graphics were produced using MERCURY [9]. Crystal data and details of data collection are summarized in Table 1.

Table 1: Summary of crystal data and details of the structure determination for complexes of **$[(bipy)(H_2O)Cu(OH)_2Cu(SO_4)]·4H_2O$ (1)** and **$[Cu(bipy)_2I]I_3$ (2)**

Parameters	Complex 1	Complex 2
Crystal data		
Empirical formula	$C_{20}H_{28}Cu_2N_4O_{11}S$	$C_{10}H_8Cu_{0.50}I_2N_2$
Formula weight	650.60	441.75
Crystal system	Monoclinic	Monoclinic
Space group	$P2_1/c$	$C2/c$
a (A)	9.6803(4)	26.3803
b (A)	34.5365(14)	7.3728(5)
c (A)	7.8279(3)	14.8424(10)
α (°)	90	90
β (°)	103.4980(10)	120.1390(10)
γ (°)	90	90
V (A^3)	2544.76(18)	2496.5(3)
Z	4	8
ρ_{calc} (Mg/m^3)	1.722	2.351
Absorption coefficient(mm^{-1})	1.819	5.835
F(000)	1352	1620
Crystal size (mm^3)	0.32 x 0.181 x 0.036	0.307 x 0.15 x 0.015
Data collection		
Temperature (K)	293(2)	293(2)
λ Mo Kα (Å)	0.71073	0.71073
Θ Min-Max (°)	1.18-24.99	1.79- 24.98
h limits	-11:11	-31:31
k limits	-41:41	-8:8
l limits	9:9	-17:17
R_{int}		
Reflections collected	27585	13006
Refinement		
Final R indices [$I>2\sigma(I)$]	$R1$ = 0.0375	$R1$ = 0.0320
R indices (all data)	$R1$ = 0.0436	$R1$ = 0.0367

3. Results and Discussion

The treatment of copper(I) iodide, 2,2'-bipyridine and *N*-methylthiourea (1:1:1) in acetonitrile at 60°C provided **$[(bipy)(H_2O)Cu(OH)_2Cu(SO_4)]·4H_2O$ (1)** and **$[Cu(bipy)_2I]I_3$ (2)**. The research was set out to study the structure of complex by X-ray diffraction methods [10] and the crystal structure is depicted in Figure 2 and Figure 5.

3.1 Spectroscopic study

IR spectra vibration bands for the copper(I) complexes are given in Figure 1. The nitrogen atom of the 2,2'bipyridine ligand and the sulfur atom or nitrogen atom of the *N*-methylthiourea can coordinate to copper(I) atom. Complex 1, exhibits the wave numbers appear at 3051.43 cm^{-1} (ν(N-H)), 1597.87 cm^{-1} (ν(C=N) of the bipy), 1252.04 cm^{-1} (ν(C-N) of the bipy). Complex 2 exhibits the wave numbers appear at 3051.65 cm^{-1} (ν(N-H)), 1597.66 cm^{-1} (ν(C=N) of the bipy), 1251.87 cm^{-1} (ν(C-N) of the bipy).

The results from IR spectroscopy shows the shifts in peak positions of the ligands indicate that the 2,2'bipyridine ligand is coordinated to the copper ion in the coordination complexes.

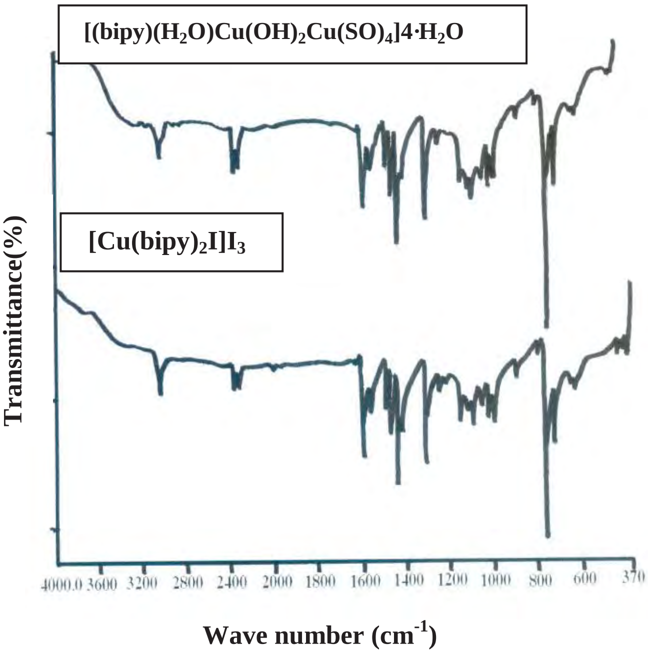

Figure 1. The IR spectra of **$[(bipy)(H_2O)Cu(OH)_2Cu(SO_4)]·4H_2O$** and **$[Cu(bipy)_2]I_3$**

3.2 Crystal structure description of complex **$[(bipy)(H_2O)Cu(OH)_2Cu(SO_4)]·4H_2O$ (1)**.

The dinuclear complex(1) is distorted tetragonal planar in geometry (Fig. 2). The Cu···Cu distance separation *via* two OH^- bridges is 2.897 Å. There are two kinds of coordination environment around the copper centers. In one of the Cu center is bound to two N atoms of one bipy ligand and three O atoms of two OH^- molecules and one sulphate ion while in other center the Cu center is coordinated with two N atoms of one bipy ligand and three O atoms of two OH^- molecules and one water molecule. In addition, four water molecules also observed. The Cu—N distances in the range 1.994(3)-2.219(2) Å is shorter than that found in 2.2278 Å for $[Cu(L^4)(2,2'\text{-bipy})]$ (H_2L = 2-hydroxyacetophenone*N*(4)-substituted thiosemicarbazones [6]. The Cu—O bond distances vary from 1.935(2)-2.219(2) Å, which is quite similar to those observed in related copper complexes [11-12]. In the crystal, the hydrogen bonds (Table 3) can be connected each molecule form layers parallel to (010). The copper(I) complex (1) exhibits intramolecular hydrogen bonding interactions (Fig. 4). Moreover, complex (1) forms the three-dimemtional network *via* π-π stacking interactions of bipy ligand with a centroid–centroid distance of 3.714 Å (Fig. 3).

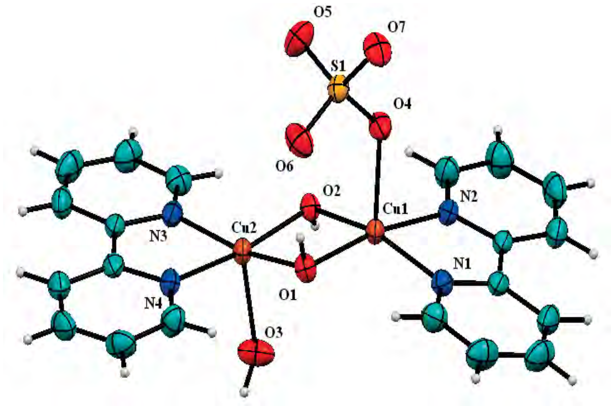

Figure 2. The structure of **[(bipy)(H_2O)Cu(OH)$_2$Cu(SO_4)]·4H_2O (1).** Ellipsoids are down at 50% probability level and water molecules omitted for clarity.

Table 2: Selected bond distances (Å) of **[(bipy)(H_2O)Cu(OH)$_2$Cu(SO_4)]·4H_2O**

Bond	Distances (Å)
Cu(1)-Cu(2)	2.897(5)
Cu(1)-O(1)	1.952(2)
Cu(1)-O(2)	1.955(2)
Cu(1)-N(1)	2.031(3)
Cu(1)-N(2)	1.994(3)
Cu(1)-O(4)	2.201(2)
Cu(2)-O(1)	1.956(2)
Cu(2)-O(2)	1.935(2)
Cu(2)-N(3)	2.019(3)
Cu(2)-N(4)	2.000(3)
Cu(2)-O(3)	2.219(2)

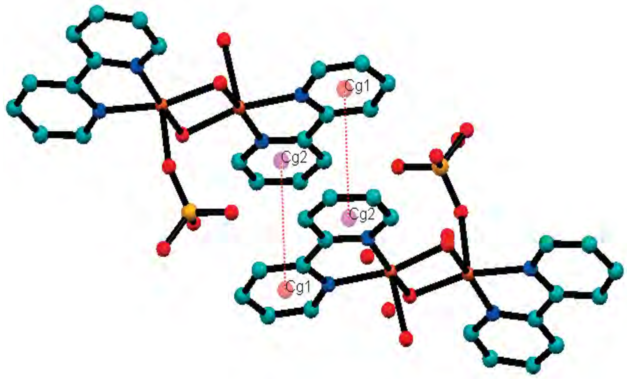

Figure 3. The π-π stacking interactions of **[(bipy)(H_2O)Cu(OH)$_2$Cu(SO_4)]·4H_2O**

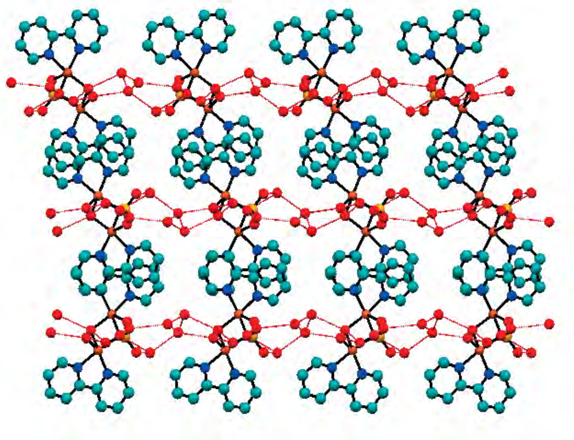

Figure 4.The intramolecular hydrogen bonding interactions of **[(bipy)(H_2O)Cu(OH)$_2$Cu(SO_4)]·4H_2O**

Table 3: Selected parameters for hydrogen bonding interaction in complex **[(bipy)(H_2O)Cu(OH)$_2$Cu(SO_4)]·4H_2O**

D-H...A	d(D-H)	d(H...A)	d(D...A)	<(DHA)
O(11)H(11B)...O(2)	0.804(19)	1.96(2)	2.755(3)	172(4)
O(11)H(11A)...O(5)	0.800(19)	2.01(2)	2.788(4)	164(4)
O(10)H(10A)...O(11)	0.809(19)	1.88(2)	2.686(4)	175(5)
O(9)-H(9B)...O(7)	0.811(19)	2.05(2)	2.864(4)	178(4)
O(9)-H(9A)...O(8)	0.802(19)	2.11(2)	2.891(5)	165(4)
O(1)-H(1A)...O(6)	0.800(19)	2.08(2)	2.856(3)	163(4)
O(10)H(10B)...O(9)#1	0.809(19)	1.99(2)	2.791(4)	172(5)
O(8)-H(8A)...O(1)#2	0.845(19)	2.02(2)	2.850(4)	167(4)
O(3)-H(3B)...O(10)#3	0.811(19)	1.90(2)	2.693(4)	168(4)
O(3)-H(3A)...O(6)#1	0.813(19)	1.91(2)	2.717(3)	174(4)
O(2)-H(2A)...O(7)#1	0.792(19)	1.96(2)	2.750(3)	172(4)

Symmetry transformation used to generate equivalent

atom: #1 x, y, z+1 #2 x+1, y, z #3 x-1, y, z

3.3 Crystal structure description of complex **[Cu(bipy)$_2$I]I$_3$ (2)**.

The structure of complex (2) features distorted tetragonal pyramid (Fig. 5), copper(I) center coordinated to four nitrogen atoms from two 2,2’-bipyridine molecules and one iodide atom. The Cu—N distances in the range 1.988(4)-2.088(4) Å this is quite similar the previous structure. In the crystal, π-π stacking interactions between the phenyl ring of bipy ligand with a centroid–centroid distance of 3.665 Å (Fig. 6) linked each molecule forming one dimentional chain. Moreover, C-H···I interactions also occurred which forming the three-dimentional networks (Fig. 7).

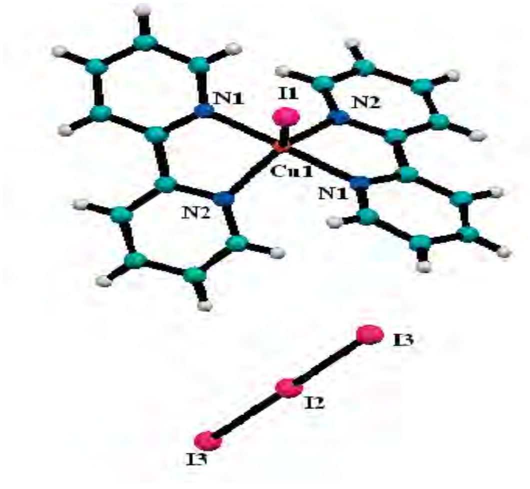

Figure 5. The structure of **[Cu(bipy)$_2$I]I$_3$**

Table 3: Selected bond distances (Å) of **[Cu(bipy)$_2$I]I$_3$**

Bond	Distances (Å)
Cu(1)-N(1)	1.988(4)
Cu(1)-N(2)	2.088(4)
Cu(1)-I(1)	2.6656(10)

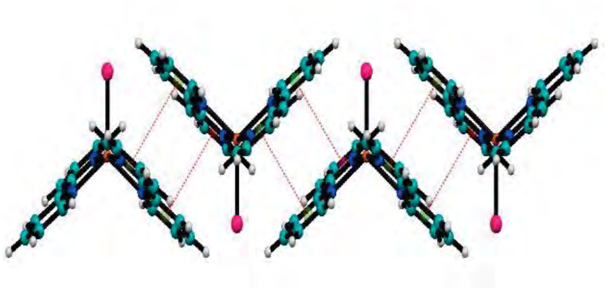

Figure 6. The π-π stacking interactions of **[Cu(bipy)$_2$I]I$_3$**

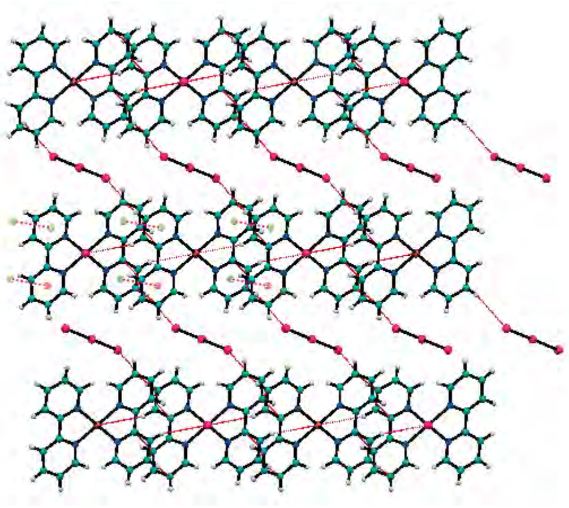

Figure 7. The C-H···I interactions of **[Cu(bipy)$_2$I]I$_3$**, unit cell content projected down the b-axis.

4. Conclusions

The aim of this work was to investigate the coordination of copper(I) iodide with the 2,2'-bipyridine and *N*-methylthiourea ligands. Minor products from the reactions have been identified. *N*-methylthiourea ligand not coordinated of the copper atom. Copper(I) complexes exhibit intramolecular hydrogen bonding interactions and π-π stacking interactions of both complexes display a three-dimensional networks.

Acknowledgements

We acknowledge with thanks the financial assistance from Science Achievement Scholarship of Thailand **(**SAST**)**, Department of Chemistry, Faculty of Science, Prince of Songkla University.

References

[1] M.P.A. Lyle, N.D. Draper and P.D. Wilson, *Organic Letter*. **7** (2005) 901-904.

[2] C. Ricardo and T. Pintaue, *Journal of Organometallic Chemistry*. **692** (2007) 5165–5172.

[3] E.K. Efthimiadou, H. Thomadaki, Y. Sanakis, C.P. RaptopoulouIn, N. Katsaros, A. Scorilas, A. Karaliota and G. Psomas, *Journal of Inorganic Biochemistry*. **101** (2007) 64-73.

[4] X. Gan, W.F. Fu, Y.Y. Lin, M. Yuan, C.M. Che, S.M. Chi, H.F. Jie Li, J.H. Chen, Y. Chen and Z.Y. Zhou, *Polyhedron*. **27** (2008) 2202-2208.

[5] J.L. Chen, X.F. Cao, W. Gu, B.T. Su, F. Zhang, H.R. Wen and R. Hong, *Inorganic Chemistry Communications*. **15** (2012) 65-68.

[6] R.P. John, A. Sreekanth, V. Rajakannan, T.A. Ajith, and M.R. Prathapachandra Kurup, *Polyhedron*. **23** (2004) 2549–2559.

[7] M. Geraghty, J.F. Cronin, M. Devereux and M. McCann, *2000 Kluwer Academic Publishers*. **13** (2000), 1-8.

[8] G. M Sheldrick, *Acta Crystallography*. **A64** (2008) 112-122.

[9] C.F. Macrea, I.J. Bruno, J.A. Chisholm, P.R. Edgington, P. McCabe, E. Pidcock, L. Rodriguez Monge, R. Tayler, J. van de Strec and P.A. Wood, *Journal of applied Crystallography*. **41** (2008) 466-470.

[10] B.E. Warren, *X-ray diffraction*. Addison-Wesley Pub. Co.,1969.

[11] K.L. Zhong, *Acta Crystallography*. **E67** (2011) m1215–m1216.

[12] C. Dietz, R.W. Seidel and I.M. Oppel, *New Crystal Structures*. **224** (2009) 509-511.

NON-PHENOLIC SUBSTANCES IN TEAS WITH POTENTIAL MEDICINAL PROPERTIES – PROBING THEIR COPPER COMPLEXING ABILITY

Klaus Stolze[1], Joyce Ferreira Severino[1] and Bernard A. Goodman[2]

[1] *Institute of Pharmacology and Toxicology, Department of. Biomedical Sciences, University of Veterinary Medicine, Veterinärplatz 1, A-1210 Vienna, Austria*
[2]*State Key Laboratory for Conservation and Utilization of Subtropical Agro-Bioresources, Guangxi University, Nanning, 530004 Guangxi, China*

[*] Author for correspondence; E-Mail: bernard_a_goodman@yahoo.com Tel. +86 771 3234439

Abstract: This paper describes the progress that is now being made in isolating and identifying some non-phenolic components of teas that are responsible for their copper complexing ability. Hot aqueous extracts of tea leaves were cooled, sequentially extracted with dichloromethane and 1-pentanol, and these extracts then investigated by HPLC along with the residue, and a 2-propanol extract of the wet tea leaves that remained after the initial water extraction. After drying, aqueous solutions of all samples were investigated by EPR spectroscopy over a wide range of pH values after reaction with Cu(II). HPLC gave traces consistent with the presence of caffeine and polyphenols, along with other as yet unidentified peaks from components that are not extractable by the organic solvents. EPR spectra showed the formation of several different types of Cu(II) complex, but the ability to form complexes at the lowest pH values was limited to the unidentified components that are not extracted into the organic solvents.

1. Introduction

Consumption of tea, *i.e*. beverages made by hot aqueous extraction of leaves of *Camellia sinensis*, has long been associated with a wide range of health benefits (e.g. [1]). These have been especially investigated for green tea, which has been associated with protection against heart disease [2,3], viral infections [4], and diabetes [5], as well as the possession of anticancer properties [6-8]. These beneficial effects are generally linked to the (poly)phenolic components [9], and the green tea polyphenols (GTP) in particular have received much scientific attention. Tea has also been shown to have the ability to stimulate brain activity [10,11], and to function in neuroprotection [12] and the treatment of neurodegenerative disorders [13]. There have even been proposals for medicinal uses of epigallocatechin gallate (EGCG), the major GTP, in the treatment of dementia [14,15]. Despite differences in composition of the polyphenolic components of different types of tea [16], epidemiological evidence suggests that their health benefits are comparable [6], and in addition, the antioxidant capacities of green and black teas are similar [17].

Metal chelation by polyphenols has been proposed as the mechanism through which green tea functions in the treatment of neurodegenerative disorders [13], but recent studies of the copper complexing ability of the GTP gallic acid (GA) and EGCG showed that they are relatively unreactive towards copper at low and neutral pH values [18,19], whereas both green and black teas can produce a range of mononuclear Cu(II) complexes under similar conditions [20,21]. Thus, at least some of the metal chelating properties of teas are derived from molecules other than polyphenols.

Although considerable efforts have been made to identify and understand the (bio)chemical reactions of the polyphenols in green tea, the non-phenolic compounds in the various types of tea have received less attention. Indeed, there is little information on the types of molecules that might be responsible for the metal chelating ability under acidic conditions, although Goodman et al. [21] provided tentative evidence for some being derived from amino acids, such as theanine. However, such molecules could not account for the observation of complex formation at very low pH values, and the present work was undertaken in order to investigate further the complexation of Cu(II) by green tea components under acidic conditions. Acidic conditions are relevant to reactions which occur in the stomach, and it is worthy of note that regular consumption of green tea is associated with a decreased risk of chronic gastritis and stomach cancer [22].

To gain further insight into the chemical species responsible for the Cu(II) chelating behaviour of green tea, sequential extractions of a conventional aqueous extract were made with dichloromethane (CH_2Cl_2) and 1-pentanol. Dichloromethane is commonly used to remove caffeine from coffee or tea, but might also be expected to extract other alkaloids, whereas 1-pentanol extracts the catechins and catechin gallates. Thus investigations of the Cu(II) complexing abilities of these extracts should show the contributions of these major tea components to the metal complexing activities of the tea. In addition to investigating the reactions of these extracts, reactions with Cu(II) of the aqueous residue that remained after the organic extractions and an additional 2-propanol extract of the tea leaves that remained after the initial aqueous extraction are also included in this study. Results from HPLC and EPR investigations are reported, the latter at acidic pH values after reaction with Cu(II).

2. Materials and Methods

The Chinese green tea used in these experiments was a commercial product of Shandong origin.

2.1 Preparation of the tea extracts

Green tea leaves were extracted twice with water (1g/50ml) at ~90°C for 10 min to yield Samples I and II. These extracts were cooled to room temperature (~22°C) and sequential extractions made with dichloromethane (3x) and 1-pentanol (4-5 x) to yield Samples III (66mg) and IV (391mg) respectively. Two additional samples were prepared; one consisted of the aqueous phase which remained after the sequential extractions (Sample V, 618mg), and the second sample was obtained by extracting the wet tea leaves (used in the aqueous extraction) with 100 ml of 2-propanol (Sample VI, 404mg). All extracts were dried (Rotavapor, Büchi), except for the first aqueous extract, which was prepared fresh, and the resulting products used in subsequent investigations.

2.2 HPLC measurements

For HPLC measurements, a Shimadzu prominence HPLC system was used equipped with a 20A UV detector (from 214-304 nm at 10 nm intervals) and a second detector (usually a BAS 254nm model). Alternatively, an electrochemical detector from ESA, model 5100A was used (300-800 mV at 100mV intervals). The aqueous extracts were diluted 1/5 with acetonitrile and centrifuged. 10 µl were injected and run at 35°C and 1ml/min on a Merck LiChrosphere C18 column 250 x 4mm/5µm particle size using the following gradient (always 1% H_3PO_4/187 mM, rest water): 0-15min: 10% acetonitrile (ACN); 15-30 min: 10-50% ACN; 30-35min: 50-99% ACN; 35-45min: 99%ACN; 45-60min: 10% ACN.

2.3 EPR spectroscopy

Reaction of the various extracts with Cu(II) were investigated over a wide range of pH values (1.4-13) (but only those with pH <~6 are considered here) in an attempt to use the spectral parameters to identify the different types of complexes that can form in these solutions. The samples were prepared as follows: 5ml of aqueous extract (1g/50ml H_2O, 100°C, 10min) was mixed with 5ml water, the pH was measured (ca. pH 5.7) and the first EPR spectrum was recorded. Then consecutive EPR spectra were recorded after addition of 200µl of copper(II) sulfate solution (100mM), and after addition of increasing amounts of H_2SO_4 (1M). The pH was measured immediately before starting the EPR spectral acquisition (5 scans accumulated). EPR conditions were: field range 1500 gauss; microwave frequency 9.797 GHz; microwave power 20 mW; modulation frequency 100 kHz; modulation amplitude 10 G; receiver gain $1x10^4$, time constant 81.9 msec; correlation time 81.9 msec; 1024 data points.

3. Results and Discussion

3.1. HPLC

The HPLC trace for the initial green tea extract is shown in Fig. 1. The 1st peak with a retention time of about 3 minutes appeared only in samples, I, II and V, and thus corresponds to components that are not soluble in the organic solvents investigated.

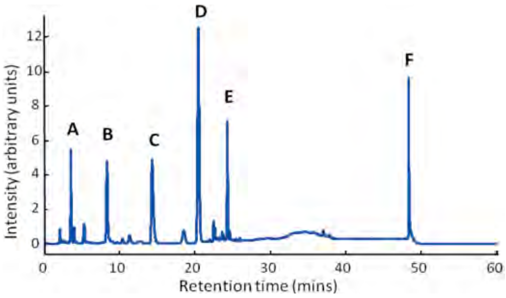

Figure 1. HPLC trace for the 1st hot aqueous extract from green tea (Sample I).

The 2nd significant peak with a retention time of about 8 minutes appears in the aqueous and 1-pentanol samples, I, II, IV, and V. The peak with a retention time of about 14 minutes was present in the initial aqueous extracts, I and II, but was completely extracted by dichloromethane (Sample III). It thus corresponds to caffeine, and its efficient extraction by this solvent is sometimes used as the basis for decaffeination of beverages, such as coffee. The components with the intense peaks in the original aqueous extracts (Samples I and II) with retention times of about 20 and 24 minutes are almost entirely extracted into 1-pentanol (Sample IV). Little remained in solution after the 1-pentanol extraction (Sample V), and none was extracted by CH_2Cl_2 (Sample III). However, additional amounts were removed from the leaf residues by 2-propanol (Sample VI). These peaks, therefore, probably correspond to the catechins and the catechin gallates. The final intense peak in the aqueous extracts (Samples I and II) with a retention time of about 48 minutes was only slightly extracted into CH_2Cl_2 and 1-pentanol (Samples II and IV), and remained largely in the aqueous phase (Sample V). However, appreciable amounts were still extracted by 2-propanol from the leaf residues (Sample VI). Because of the similarities between Samples I and II, Sample II was not investigated in the EPR experiments described in the following paragraphs.

3.2 EPR spectrum of the tea extract

The EPR spectrum of the aqueous extract of the tea before addition of Cu(II) is shown in Fig. 2. This spectrum consists of a sextet signal from the solvated Mn(II) ion.

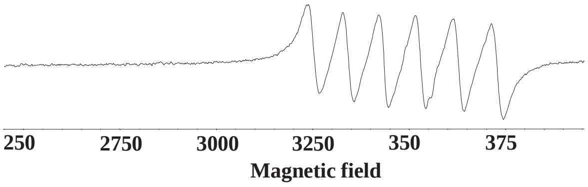

Figure 2 EPR spectrum of the aqueous extract of green tea

3.3 EPR spectra of the Cu(II) complexes

EPR spectra were recorded from the Cu(II) complexes of Samples I, III, IV, V and VI for a wide range of pH values similar to those reported in [21] for the aqueous tea extracts. The results obtained under acidic conditions are illustrated in Figs. 3-7 below.

The spectra from the aqueous tea extract (Sample I) after addition of Cu(II) are dominated by the Mn(II) signal (e.g. Fig. 3). Thus this signal was subtracted to produce results that correspond solely to the Cu(II) signal (Fig. 4). These results are similar to those published previously [21], and contain peaks from Cu(II) complexes at all pH values in addition to the broad single peak at low field from uncomplexed Cu(II).

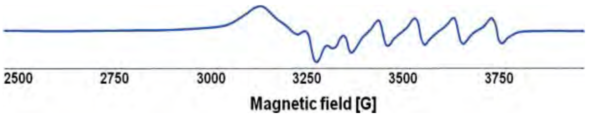

Figure 3. EPR spectrum of Sample I at pH 1.42 after reaction with Cu(II).

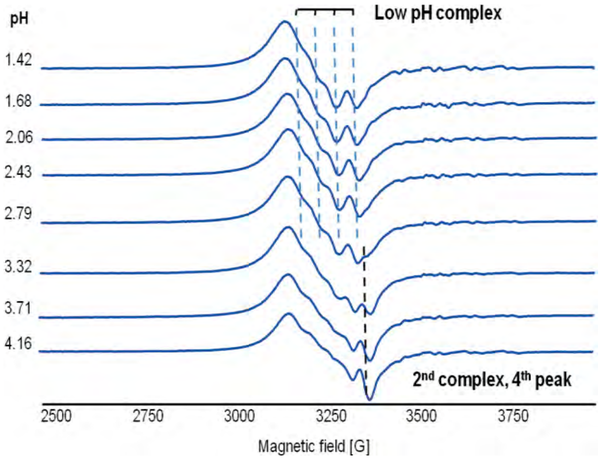

Figure 4. Dependence on pH of the Cu(II) EPR spectra of aqueous extracts of green tea (Sample I).

The EPR spectra obtained with the CH_2Cl_2 extract (Sample III) is completely dominated by the signal from the uncomplexed Cu(II) ion (Fig. 5), and there is just a small contribution from Cu(II) complexes at pH > 4.5. It should also be noted that the Mn component is absent from these spectra, and the results are consistent with this extract consisting mainly of caffeine.

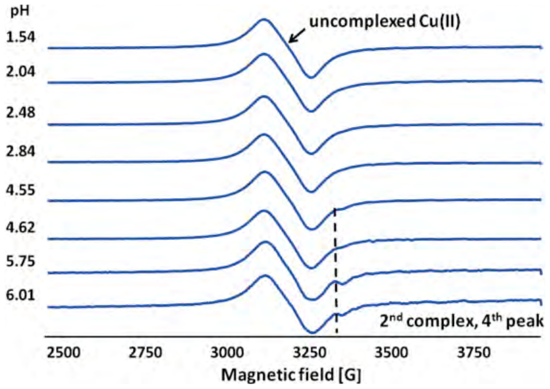

Figure 5. Dependence on pH of the Cu(II) EPR spectra of dichloromethane extracts of green tea (Sample III).

The 1-pentanol extract of the residue remaining after CH_2Cl_2 extraction (Sample IV) produced the spectra shown in Fig. 6. These are also dominated by the signal from the uncomplexed Cu(II) ion at pH < ~3.5, although there is evidence for substantial complex formation at higher pH values. Since many of the polyphenols would be expected to be extracted into this fraction, it is clear that they are not responsible for the formation of the Cu(II) complexes at very low pH.

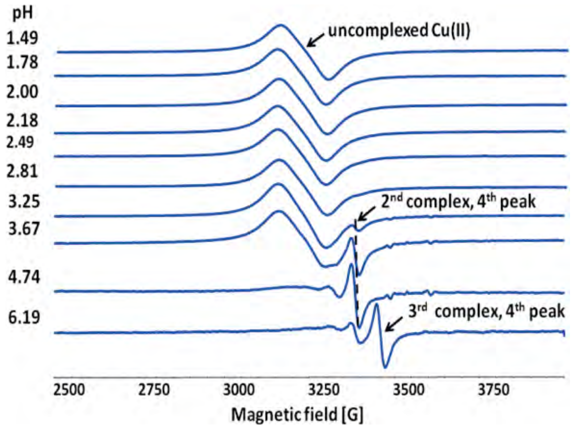

Figure 6. Dependence on pH of the Cu(II) EPR spectra of 1-pentanol extracts of green tea previously extracted with dichloromethane (Sample IV) with added Cu(II).

The EPR spectra from the aqueous residue remaining after the organic solvent extractions (Sample V) produced spectra similar to those from Sample I (and are not shown here). Thus the ligands responsible for the formation of Cu(II) complexes at very low pH values remained in the aqueous solution.

The final sample examined was the 2-propanol extract of the "spent" tea leaves that remained after the original aqueous extraction (Sample VI). The EPR spectra as a function of pH after reaction with Cu(II) are shown in Fig. 7. These are actually quite similar to the spectra obtained with Sample IV, and are consistent with the extraction of further quantities of polyphenols.

3.4 General Discussion

This paper has developed the measurements aimed at understanding the Cu(II) complexing ability of aqueous green tea extracts reported by [21] by investigating the complexing ability of various fractions of the original extract. The spectra from the unfractionated aqueous extract are similar to those reported originally, and show evidence for the formation of Cu(II) complexes at very low pH. However, the component(s) responsible for the spectra from the original aqueous extract under strongly acidic conditions (i.e. at pH values <2) was/were not extracted into either dichloromethane or 1-pentanol and remained in the aqueous phase after these extractions. Furthermore, this/these component(s) was/were not extracted by 2-propanol from the leaf residues remaining after the initial hot aqueous extraction.

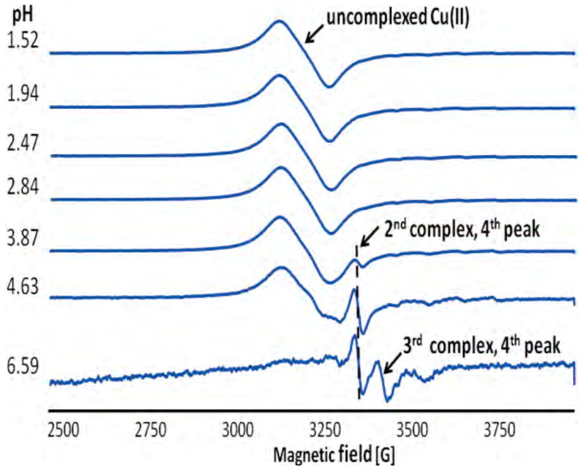

Figure 7. Dependence on pH of the Cu(II) EPR spectra of aqueous solutions of green tea after extraction of the wet tea leaves with 2-propanol (Sample VI) with added Cu(II).

By relating the EPR spectra to the HPLC traces, it is apparent that the component responsible for the complexing ability at low pH corresponds to the 1st HPLC peak with a retention time of about 4 minutes in these measurements. Attempts are now underway to isolate this component(s) in sufficient quantities for characterization by conventional analytical techniques, such as IR spectroscopy, mass spectrometry, and NMR spectroscopy, and investigation of its chemical and biological properties.

4. Conclusions

The present work shows that the water-soluble components in green tea with ability to complex Cu(II) at low pH, are not extractable into the organic solvents CH_2Cl_2 and 1-pentanol. Furthermore they exhibit a very short retention time in the HPLC measurements, and their isotropic EPR spectra shows that they must also have a quite low molecular mass. However, at the present time they have not been identified, although experiments aimed at achieving this are currently in progress.

References

[1] Y. Hara. Green Tea: health benefits and applications. Marcel Dekker Inc., New York (2004).
[2] J.A. Vinson, K. Teufel, N. Wu. *J Agric Food Chem.* **52** (2004) 3661-3665.
[3] J.M. Hodgson. *Asia Pac. J. Clin. Nutr.* **17** (2008) 288-290.
[4] H. Yamada, N. Takuma, T. Daimon, Y. Hara. *J. Alt. Comp. Med*. **12** (2006) 669-672.
[5] Y. Jing, G. Han, Y. Hu, Y. Bi, L. Li, D. Zhu. *J. Gen. Intern. Med.* **24** (2009) 557-562.
[6] S.K. Katiyar, H. Mukhtar. *Int. J. Oncol*. **8** 1996. 221-238.
[7] L. Kohlmeier, K.G.C. Weterings, S. Steck, F.J. Kok. *Nutr. Cancer* **27** (1997) 1-13.
[8] C.S. Yang. *Nature* **389** (1997) 134-135.
[9] H. Mukhtar and N. Ahmad. *Am. J. Clin. Nutr*. **71** (2000) 1698S-1702S.
[10] I. Hindmarch, U. Rigney, N. Stanley, P. Quinlan, J. Rycroft and J. Lane. *Psychopharmacology* **149** (2000) 203-216.
[11] H. Kim, M. Kim, S. Kim and J. Chong. *Biosci. Biotechnol. Biochem*. **68** (2004) 1977-1979.
[12] S.A. Mandel, Y. Avramovich-Tirosh, L. Reznichenko, H. Zheng, O. Weinreb, T. Amit and M.B. Youdim. *Neurosignals* **14** (2005) 46-60.
[13] S. Mandel, T. Amit, L. Reznichenko, O.Weinreb and M.B.H. Youdim. *Mol. Nutr. Food Res.* **50** (2006) 229-234.
[14] R.-R. Hou, J.-Z. Chen, H. Chen, X.-G. Kang, M.-G. Li and B.-R. Wang. *Cell Biol. Int.* **32** (2008) 22-30.
[15] S.A. Mandel, T. Amit, L. Kalfon, L. Reznichenko and M.B.H. Youdim *J. Nutr*. **138** (2008) 1578S-1583S.
[16] C.-T. Ho, N. Zhu. In: *Caffeinated Beverages, Health Benefits, Physiological Effects, and Chemistry* (T.H. Parliament, C.-T. Ho, P. Schieberle, editors), ACS Symposium Series 754, ACS Washington DC (2000). pp. 316-326.
[17] L. K. Leung, Y. Su, R. Chen, Z. Zhang, Y. Huang and Z.-Y. Chen. *J. Nutr*. **131** (2001) 2248-2251.
[18] J. Ferreira Severino, B.A. Goodman, T.G. Reichenauer and K.F. Pirker. *Free Rad. Res*. **45** (2011) 123-132.
[19] K.F. Pirker, M.C. Baratto, R. Basosi, and B.A. Goodman. *J. Inorg. Biochem.* **112** (2012) 10-16.
[20] B.A. Goodman, J. Ferreira Severino, T.G. Reichenauer and K.F. Pirker In: *Tea Production and Tea Products* (Eds. P. Winyayong, J.K. Syers & T. Theppakorn), Mae Fah Luang University, Thailand (2009) pp. 101-117.
[21] B.A. Goodman, J. Ferreira Severino and K.F. Pirker. *Food & Function* **3** (2012) 399-409.
[22] V.W. Setiawan, Z.-F. Zhang, G.-P. Yu, Q.-Y. Lu, Y.-L. Li, M.-L. Lu, M.-R. Wang, C.H. Guo, S.-Z. Yu, R.C. Kurtz and C.-C. Hsieh. *Int. J. Cancer* **92** (2001) 600–604.
[23] J. Ferreira Severino, B.A. Goodman, C.W.M. Kay, K. Stolze, D. Tunega, T.G. Reichenauer,and K.F. Pirker. *Free Radical Biol. Med.* **46** (2009) 1076-1088.

Material Sciences and Nanotechnology

PREPARATION AND PROPERTIES OF CARBON NANOTUBES-REINFORCED PHENOLIC COMPOSITES FOR BIPOLAR PLATE APPLICATIONS

Pattarakamon Chaiwan[1], Thapanee Sarakonsri[2], Jantrawan Pumchusak[1*]

[1] Department of Industrial Chemistry, Faculty of Science, Chiang Mai University, Muang, Chiang Mai, 50200 Thailand
[2] Department of Chemistry, Faculty of Science, Chiang Mai University, Muang, Chiang Mai, 50200 Thailand

[*] Author for correspondence; E-Mail: jantrawan@gmail.com, Tel. +66-53-9434011-5 Ext. 123, Fax. +66-53-892262

Abstract: This study aims to prepare the phenolic composites reinforced with the multiwalled carbon nanotubes (MWCNTs) for use as bipolar plates in a proton exchange membrane fuel cell. The polymer composites composed of 20 wt% of phenolic resin and 80 wt% of graphite powders. 0-2 wt% of MWCNTs was added into the phenolic composites in order to reinforce them. Two different methods as wet and dry mixing were applied for the composite preparation. For wet preparation method, firstly, the MWCNTs were dispersed in 2-propanol via ultrasonication and then mixed with other contents by dry ball milling. For dry preparation method, all components were mixed only by dry ball milling. After mixing, the polymer composites were fabricated into sheets by compression molding. Moreover, the effect of the oxidized MWCNTs (O-MWCNTs) on the properties of the polymer composites was studied. The results showed that the unmodified MWCNTs (U-MWCNTs) loading improved the electrical and mechanical properties of the polymer composites that were prepared by both preparation methods. For wet preparation method, the electrical conductivity, flexural strength and tensile strength of the polymer composites with 1 wt% of the U-MWCNTs increased by 37%, 29% and 19%, respectively. For dry preparation method, the electrical conductivity, flexural strength and tensile strength of the polymer composites with 1 wt% of the U-MWCNTs increased by 11%, 14% and 24%, respectively, compared to the no-MWCNTs composites. Thus the electrical conductivity and flexural strength already met the DOE requirement for the composite bipolar plates. However, the addition of the O-MWCNTs did not improve the properties of the polymer composites due to the agglomeration of the MWCNTs.

1. Introduction

Carbon nanotubes are being the excellent fillers with high aspect ratio, low density, and high mechanical thermal and electrical properties. So carbon nanotubes have been attracted for high performance polymer composite applications [1].

Several studies have reported that the use of the polymer composites incorporated with the carbon nanotubes shows the excellent electrical and mechanical properties for bipolar plates. However, the carbon nanotubes are strongly affected by van der Waals forces because of their small size and large surface area. So the carbon nanotubes commonly aggregated into the bundles, limiting their usefulness in the polymer composites [2]. Moreover, the interfacial bonding between the carbon nanotubes and the polymer matrix is weak. Therefore, the ability to disperse the carbon nanotubes in the polymer matrix and the interfacial interaction between them will be the challenges in order to get the full advantage of the extraordinary properties of the carbon nanotubes [1].

The chemical functionalization is known as an effective dispersion technique used to enhance the interfacial adhesion between the carbon nanotubes and the polymer matrix. One of these is the oxidation process with strong acid to create the carboxylic acid or hydroxyl groups on the surface of the carbon nanotubes [3].

This research aims to prepare the phenolic composites reinforced with the MWCNTs. Graphite powders and phenolic resin were used as the major conducting fillers and the polymer matrix, respectively. Moreover, the effect of the chemical functionalization of the MWCNTs on the properties of the phenolic composites was studied.

2. Materials and Methods

2.1 Materials

Novolac type phenolic resin was supplied by Thai GCI Resitop Co. Ltd., Thailand. The synthetic graphite of purity > 95% and particle size < 180 μm was purchased from TIMCAL Ltd., Switzerland. MWCNTs were purchased from Research Laboratory for Excellence Nano and Smart Materials of Chiang Mai University, Thailand. The MWCNTs were synthesized by an infusion chemical vapour deposition method, had a diameter range of 20-50 nm and the length greater than 10 μm [4]. The carbon nanotubes were burned in air at 480°C for 4 h to remove the amorphous carbon particles absorbing on the external wall of the carbon nanotubes.

2.2 Oxidation of the MWCNTs

The burned MWCNTs (which is labelled as U-MWCNTs or the unmodified MWCNTs) were oxidized with concentrated nitric acid via refluxing process at 120°C for 40 min. After that this mixture was filtered through nylon membrane and washed with deionized water and acetone until pH reached 6-7. The oxidized MWCNTs (O-MWCNTs) were dried in vacuum oven at 80°C for 24 h.

2.3 Fabrication of the polymer composites

The polymer composites composed of 20 wt% of phenolic resin and 80 wt% of graphite powders. 0-2 wt% of MWCNTs was added into the phenolic composites in order to reinforce them. Two different methods as wet and dry mixing were applied for the composite preparation. For wet preparation method, firstly, the MWCNTs were dispersed in 2-propanol via ultrasonication and then mixed with other contents by dry ball milling. For dry preparation method, all components were mixed only by dry ball milling. After mixing, the polymer composites were fabricated into sheets by compression molding at a temperature of 150°C and a pressure of 1500 psi. Finally, the polymer composites were cut into suitable dimensions for measurement of the various properties.

3. Results and Discussion

3.1 FTIR analysis

Fig. 1 showed the FTIR spectrum of the MWCNTs before and after oxidation. For the U-MWCNTs (Fig. 1a), the peaks at 3422 cm^{-1} and 1023 cm^{-1} indicated that the hydroxyl groups (-OH) on the surface of the MWCNTs could be formed by either oxidation during purification of the material or by the presence of atmospheric moisture on the surface of the MWCNTs [3]. The O-MWCNTs (Fig. 1b) shows carboxylic groups (-COOH) vibrations, C=O stretching at 1720 cm^{-1} and C-O stretching at 1158 cm^{-1}. The peak at 3422 cm^{-1} revealed the -OH groups on the surface and the peak at 1375 cm^{-1} was due to the -OH bending deformation in –COOH [5]. Therefore, the MWCNTs were oxidized and created the –OH and –COOH groups on the surfaces.

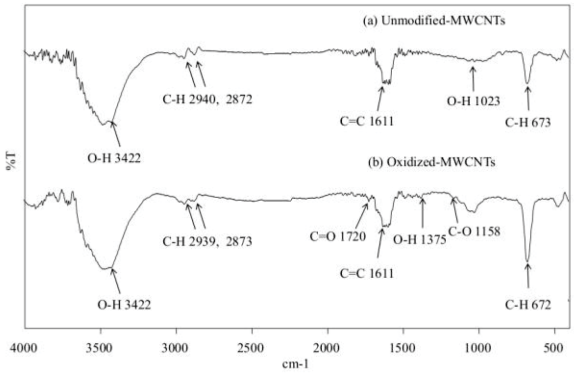

Fig. 1. FTIR spectrum of (a) unmodified-MWCNTs and (b) oxidized-MWCNTs.

3.2 Surface morphology of the MWCNTs

The surface morphology of the MWCNTs was observed using SEM. Fig. 2 shows SEM micrograph of U-MWCNTs and O-MWCNTs. It was observed that after the oxidation process, the structure of the MWCNTs was not destroyed or was not observed on the SEM micrograph.

3.3 The dispersion of the MWCNTs

The U-MWCNTs and O-MWCNTs were dispersed in 2-propanol for 30 min via the ultrasonication. After that the dispersion stability were observed. Fig. 3 showed the dispersion states of the U-MWCNTs and O-MWCNTs at interval of times. It was noticed that after 30 min of the ultrasonication, both MWCNTs showed good dispersion in 2-propanol and after 2 h, the U-MWCNTs almost completely settled while the O-MWCNTs still dispersed in the solvent. However, after 24 h, both MWCNTs completely settled. It can be conclude that the O-MWCNTs showed better dispersion stability in 2-propanol than the U-MWCNTs because of their hydrogen bonding ability enhancement due to the functionalized effect of their surface [3].

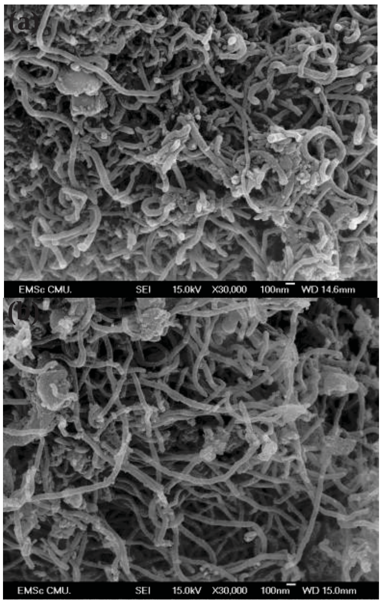

Fig. 2. SEM micrographs of (a) unmodified-MWCNTs and (b) oxidized-MWCNTs.

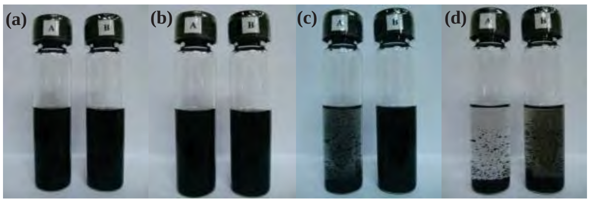

Fig. 3. The dispersion of the (A) U-MWCNTs and (B) O-MWCNTs at (a) just dispersed (b) 30 min (c) 2 h and (d) 24 h, respectively.

3.4 Surface morphology of the MWCNTs /phenolic composite

The SEM micrograph of the polymer composites that reinforced with the U-MWCNTs and O-MWCNTs which prepared by both wet and dry preparation method were shown in Fig. 4 and Fig. 5, respectively. It was observed that in the case of wet preparation method, it is clearly seen that the MWCNTs were dispersed and adhered on the surface of the graphite layers. Furthermore, the use of 1 wt% of the MWCNTs to reinforced the polymer composites showed a good dispersion (pointed by arrows) but the use of 2 wt% of the MWCNTs caused the agglomeration (circle areas). In the dry preparation method, it is hard to see the MWCNTs on the graphite surfaces and the agglomeration could be observed even with 1 wt% of the MWCNTs.

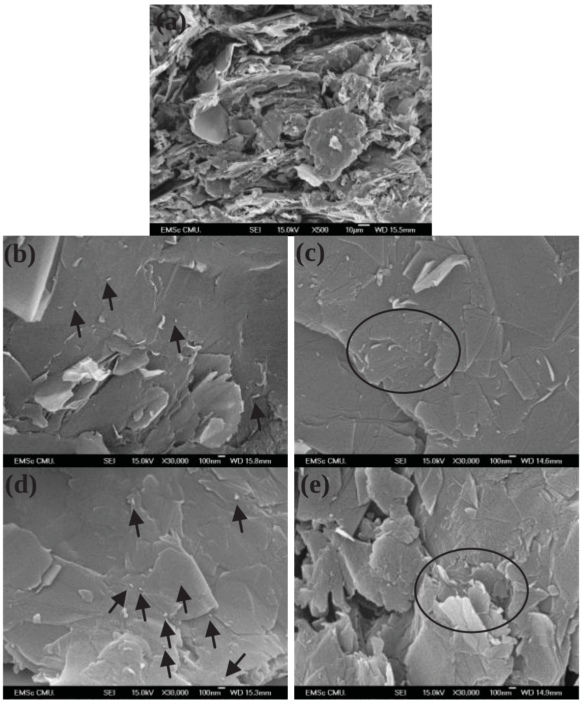

Fig. 4. SEM micrographs of the polymer composites with (a) 0 wt%, (b) 1 wt%, (c) 2 wt% of the U-MWCNTs, (d) 1 wt% and (e) 2 wt% of O-MWCNTs by wet preparation method.

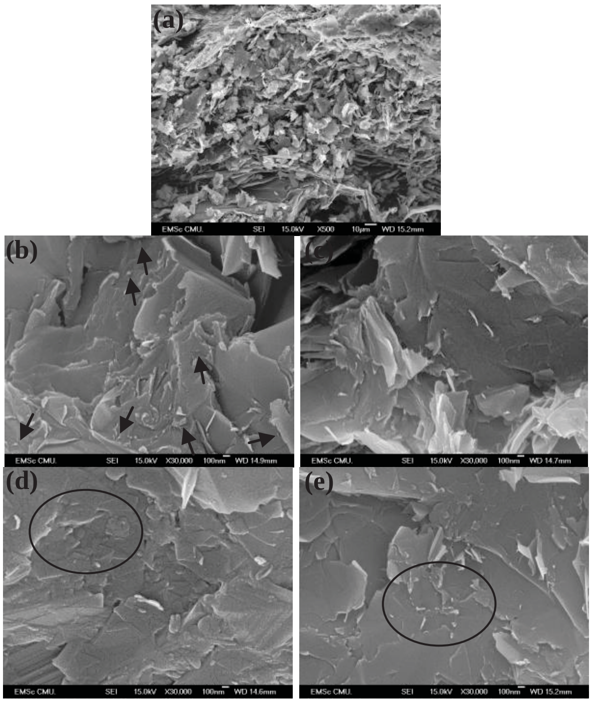

Fig. 5. SEM micrographs of the polymer composites with (a) 0 wt%, (b) 1 wt%, (c) 2 wt% of the U-MWCNTs, (d) 1 wt% and (e) 2 wt% of O-MWCNTs by dry preparation method.

3.5 The density and porosity of the composites

The density and porosity of the polymer composites of the U-MWCNTs and O-MWCNTs were shown in Fig. 6. It was found that the density of the polymer composites decreased when both U-MWCNTs and O-MWCNTs loading increased due to the density of the MWCNTs was lower than the graphite particles [6]. Moreover, for the polymer composites that reinforced with the U-MWCNTs, the porosity of the composites that prepared by wet preparation method were higher than the one that prepared by dry preparation method.

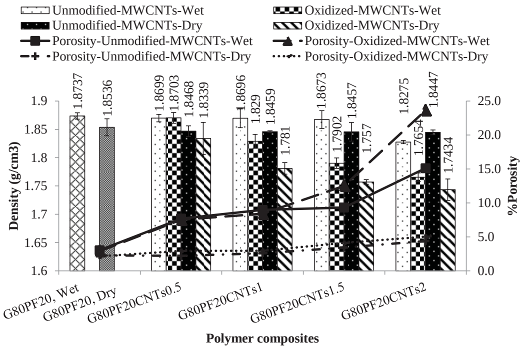

Fig. 6. The density and porosity of the polymer composites.

3.6 The electrical conductivity of the composites

The electrical conductivity of the polymer composites were shown in Fig. 7. By using the wet and dry preparation methods on phenolic-graphite composite, it was observed that the dry method provided higher electrical conductivity. This could be explained by the lower porosity in the composite which prepared by the dry method. The addition of both U-MWCNTs and O-MWCNTs in the wet preparation method enhanced the electrical conductivity significantly; however, this property improvement in the dry preparation method was insignificant. This is due to the MWCNTs in between the graphite particles acted as a bridge for electron mobility in all directions. So there is the formation of more efficient electron networks in the composites [7].

Using the unmodified and oxidized MWCNTs in the composites in the wet method did not make an obvious difference in electrical conductivity. However, in the dry method the oxidized MWCNTs showed a large deviation and lower in electrical conductivity value. This may be attributed to the destruction of the conductive shells of the MWCNTs as a result of strong surface oxidation [8]. The polymer composites reinforced with 1 wt% of U-MWCNTs and prepared by dry preparation method provided the highest electrical conductivity of 196.7 S/cm.

3.7 The flexural and tensile strengths of the composites

The flexural and tensile strengths of the polymer composites without MWCNTs, and with the U-MWCNTs and O-MWCNTs were shown in Fig. 8 and Fig. 9, respectively. The dry preparation method provided higher flexural strength than that of the wet method. However, the different methods did not affect the tensile strength.

It was found that both U-MWCNTs and O-MWCNTs loading improved the flexural and tensile strengths of the polymer composites which prepared by both wet and dry preparation methods. The U-MWCNTs and O-MWCNTs did not show the difference in reinforcement. The polymer composite with 1 wt% of U-MWCNTs using dry preparation method provided the highest flexural strength and tensile strength of 57.5 MPa and 32.0 MPa, respectively.

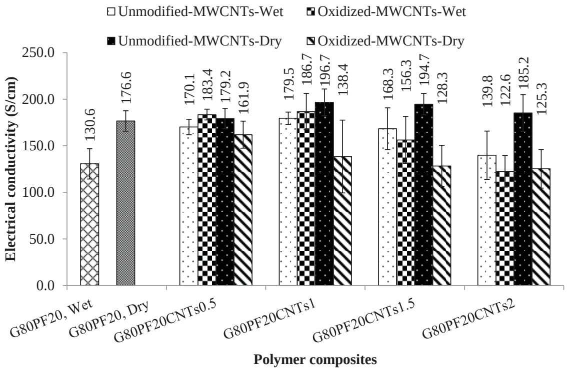

Fig. 7. The effect of MWCNTs on the electrical conductivity of the polymer composites.

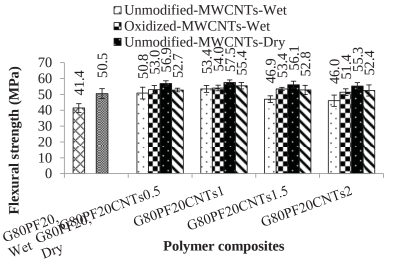

Fig. 8. The effect of MWCNTs on the flexural strength of the polymer composites.

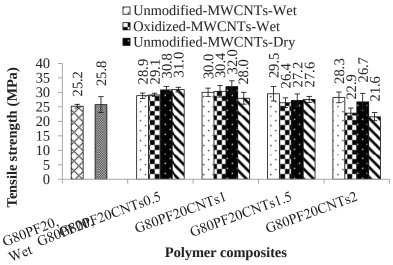

Fig. 9. The effect of MWCNTs on the tensile strength of the polymer composites.

4. Conclusions

Table : 1 The properties of the polymer composites of this study compared to DOE requirement for composite bipolar plates.

The properties of composites	**DOE requirements**	**This study**
Electrical conductivity (S/cm)	> 100	196.7
Flexural strength (MPa)	> 30	57.5
Tensile strength (MPa)	> 41(plug power requirement)	32.0
Density (g/cm^3)	< 5	1.8432

1. The dry preparation method was a proper method for the dispersion of the MWCNTs. The less porosity was observed via this method.
2. The composites with 1 wt% of U-MWCNTs which prepared by dry method provided the highest electrical conductivity of 196.7 S/cm.
3. The flexural and tensile properties of the polymer composites were improved by adding both U-MWCNTs and O-MWCNTs. The composites with 1 wt% of U-MWCNTs which prepared by dry method provided the highest flexural and tensile strength of 57.5 MPa and 32.0 MPa, respectively.
4. The oxidation treatment of the MWCNTs with strong acid did not improve the properties of the composites.
5. The electrical conductivity and flexural strength of the composites with 1 wt% of U-MWCNTs and prepared by dry preparation method that showed in Table 1 already met the DOE requirement for the composite bipolar plates.

Acknowledgements

The authors are grateful to the National Nanotechnology Center and the Graduate School Chiang Mai University for financial support.

References

[1] S.H. Liao, M.C. Hsiao, C.Y. Yen, C.C.M. Ma, S.J. Lee, A. Su, M.C. Tsai, M.Y. Yen and P.L. Liu, *J. Power Sources*, **195** (2010) 7808–7817.
[2] S.H. Liao, C.H. Hung, C.C.M. Ma, C.Y. Yen, Y.F. Lin and C.C. Weng, *J. Power sources*, **176** (2008) 175–182.
[3] J. Kathi, K.Y. Rhee and J.H. Lee, *Composites: Part A*, **40** (2009) 800–809.
[4] P. Singjai, S. Changsarn and S. Thongtem, *Mater. Sci. Eng., A*, **443** (2007) 42–46.
[5] M. Amornsit et al., *Principles and Techniques of Instumental Analysis Spectroscopy*, Chuan Pim 50, Bangkok, (2009), pp. 185-187.
[6] P. C. Ma, N. A. Siddiqui, G. Marom and J. K. Kim *Composites: Part A*,**41** (2010) 1345–1367.

[7] S.R. Dhakate, S. Sharma N. Chauhan, R.K. Seth and R.B. Mathur, *Int. J. Hydrogen Energy*,**35** (2010) 4195–4200.

[8] Z. Spitalsky, C.A. Krontiras, S.N. Georga and C. Galiotis, *Composites: Part A*,**40** (2009) 778–783.

TIME-TEMPERATURE PAPER INDICATOR FROM POLYDIACETYLENE

Natdanai Suta[1], Sumrit Wacharasindhu[2] and Mongkol Sukwattanasinitt[2]*

[1] Program of Petrochemistry and Polymer Science, Faculty of Science, Chulalongkorn University, Bangkok 10330, Thailand
[2] Center for Petroleum, Petrochemicals and Advanced Materials, Department of Chemistry, Faculty of Science, Chulalongkorn University, Bangkok 10330, Thailand

*E-mail: smongkol@chula.ac.th

Abstract: **Time-temperature indicator (TTI) is a single-use device for monitoring thermal history by changing its color. Their color change profile relates with the quality of perishable products such as food, drink and medicine. In this work, commercial 10,12-tricosadiynoic acid (TCDA) were investigated as a colorimetric active agent in TTI. A formulated mixture of the diacetylene compound, aliphatic alcohol and cationic surfactant was fabricated by dip coating onto filter paper stripes. The coated paper was irradiated by UV light at 254 nm under controlled temperature to convert the white diacetylene to its corresponding blue polydiacetylene. The color transition from blue to red of the blue indicator is monitored at a controlled temperature as a function of time by commercial webcam and the color is evaluated using RGB system by an image processing program. The plots of %Red and %Blue against time at each temperature provided two curves with an intersection which was assigned as a color transition time. The color transition time at each temperature of the indicator can be systematically tuned by the type and amount of aliphatic alcohol and cationic surfactant incorporated. For examples, the indicators prepared from the combination of TCDA, 1-dodecanol and Dodecyltrimethylammonium bromide (DTAB) changed their color from blue to red at 28 °C within 2 to 4 days depending on the content of DTAB.**

1. Introduction

Time and temperature are important parameters needed to be controlled in quality assurance of perishable products such as foods, beverages, pharmaceuticals and chemicals. There are a large number of devices have been developed for monitoring or recording the thermal history of the products. Time-temperature indicator (TTI) is a single-use device which can indicate if the product has been stored in proper temperature by their color appearance. A TTI needs to be irreversibly changes the color within the designated time of exposure to unsuitable environmental temperature.

Polydiacetylene (PDA) is a conjugated polymer, consisting of alternate double/single/triple bonds, prepared from polymerization of self-assembly diacetylene monomers by UV-irradiation at 254 nm. PDAs have received significant attention due to their unique optical properties, especially for the blue to red color change upon their exposure to external stimuli including heat, organic solvents, mechanical stress, molecular recognition and UV light [1]. Amphiphilic molecule such as aliphatic alcohol, surfactants and alkylamine can also induce the blue-to-red color transition of PDA [2]. PDA based TTIs have been prepared in the form of vesicle solutions of diacetylene lipids and amphiphilic polymers that showed promising time-temperature dependent color change of PDA but the vesicle solutions are rather impractical for TTI applications [3]. Besides vesicle solution, self-assembled PDAs may be prepared in other forms such as, thin films or electrospun fiber [4,5]. However, the preparations of these PDA forms are time-consuming and require additives and fancy equipment set up. In addition, these PDA forms are not suitable to be used as a label on every individual product.

White paper has been demonstrated as a practical supporting material for fabrication of portable multi-sensing single-used device [6]. The polymerization of diacetylene monomers can be readily performed on filter paper by UV irradiation. The PDA coated papers has been used as sensing arrays for identification of VOC vapors [7], solvents[8] and anionic surfactants [9]. Moreover, the new method for determination of the blue-to-red color transition point of PDA paper-based thermal and UV sensor using the intersection between %R and %B in the RGB color system has been devised [10]. In this work, a fabrication and evaluation of PDA paper-based TTI have been investigated. The indicators were formulated from a commercially available diacetylene lipid i.e. 10,12-tricosadiynoic acid (TCDA) in combination with 1-dodecanol and a cationic surfactant i.e. Hexadecyltrimethylammonium bromide (HTAB), Tetradecyltrimethylammonium bromide (TTAB) and Dodecyltrimethylammonium bromide (DTAB).

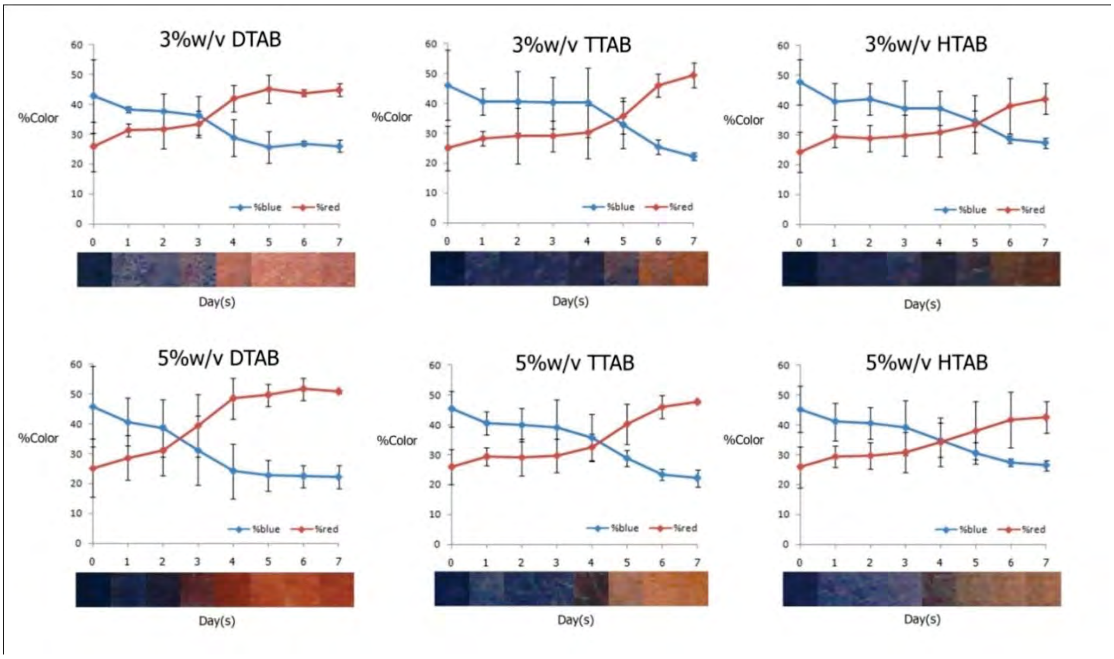

Figure 1. The plot of %color of PDA-TTI prepared from TCDA/1-dodecanol/cationic surfactants against time at room temperature (28°C).

2. Materials and Methods

2.1 Chemicals

TCDA were purchased from GFS Chemicals (USA). HTAB and TTAB were purchased from Fluka. DTAB and 1-dodecanol were purchased from Sigma-Aldrich. Chloroform analytical grade ($CHCl_3$) was used without further purification.

2.2 Preparation of paper-based PDA TTI

The diacetylene monomers were dissolved in $CHCl_3$ to obtain a 2%(w/v)stock solution, then filtered by using PTFE syringe filter (0.45µm) to remove inadvertently polymerized lipid before use. 1-dodecanol was dissolved in $CHCl_3$ to provide a 25% (w/v)stock solution. The diacetylene monomer, aliphatic alcohol solution and cationic surfactant were mixed in various ratios. A piece of filter paper (0.5×3 cm^2) was dipped in the solution mixture and allowed for air dry in a dark room at ambient temperature for 2 h. The resultant paper strips were attached to the outside of a 600 mL beaker filled with 450 mL of ice-water. The paper strips were covered with a sheet of clear LDPE plastic wrap film for moisture protection. The filter papers were irradiated by 254 nm UV light while keeping the inner beaker temperature at ~5°C for 1 min to generate blue indicator. After irradiation, the ice-water was replaced by room temperature water. The color appearance of the indicators were captured and recorded at designated time intervals by a commercial webcam (OKER177, 16M pixels). The photo images were cropped and converted to RGB values by an image-processing program.

2.3 Colorimetric measurements

The percentages of the red (%R), green (%G) and blue (%B) colors were calculated from the following equations:

$$\%R = \frac{R}{R+G+B} \times 100 \qquad (1)$$

$$\%G = \frac{G}{R+G+B} \times 100 \qquad (2)$$

$$\%B = \frac{B}{R+G+B} \times 100 \qquad (3)$$

The %B and %R were plotted as a function of time for each controlled temperature. The time required for the %B and %R curves to cross was assigned as a color transition time that used to evaluate the TTI sensitivity.

3. Results and discussion

3.1 Polymerization of diacetylene monomer on filter paper

The diacetylene monomers were fabricated on filter paper by dipping process then irradiated with UV light (254 nm) under controlled temperature (~5°C) for 1 min to give the blue indicator. The coated paper that contain DA monomers, 1-dodecanol and cationic surfactants were turned from colorless to blue indicator. The result suggested that diacetylene monomer appropriately self-assembled on filter paper provided ene-yne conjugated polydiacetylene.

3.2 Colorimetric response of paper based PDA-TTI

After the temperature of polymerized PDA-TTI was allowed to room temperature (28°C), its color were monitored by webcam for 7 days. From the results shown in Figure 1, PDA-TTI prepared from the combination of TCDA, 1-dodecanol and cationic surfactants can change from blue to red at different time. Moreover, the amount of cationic surfactants effects on the color transition time, the transition time of PDA-TTI were decreased with increasing amount cationic surfactant.

In order to determine the transition time, we assigned the intersection point between %Red and %Blue as the color transition time. The calculated transition time were shown in table 1.

Table 1. Calculated transition time

Cationic surfactant	**Transition time (Days)**
3%w/v DTAB	3.2
5%w/v DTAB	2.5
3%w/v TTAB	4.8
5%w/v TTAB	4.2
3%w/v HTAB	5.1
5%w/v HTAB	4.1

4.Conclusions

We have successfully fabricated PDA-TTI on the paper by dipping process. Moreover, the color transition time of the indicators were determined by intersection point between the plots of %Red and %Blue related with visual color. The color transition time at room temperature of the indicator can be tuned by the type and amount of 1-dodecanol and cationic surfactant incorporated.

References

[1] S. Okada, S. Peng, W. Spevak, D. Charych, *Acc. Chem. Res.*,(1998), *31*, 229-239.

[2] Y.L. Su, J.R. Li and L. Jiang, *Colloids Surf. B.*, (2004) ,39, 113–118.

[3] M. Gou, G. Guo, J. Zhang, K. Men, J. Song, F. Luo, X. Zhao, Z. Qian, and Y. Wei, *Sens. Actuator. B-Chem.* (2010),*150*, 406–411.

[4] T. Champaiboon, G. Tumcharern, A. Potisatityuenyong, S. Wacharasindhu, M. Sukwattanasinitt, *Sens. Actuator. B-Chem.*, (2009), *139*, 532–537.

[5] J. Yoon, S.K. Chae, J.M. Kim, *J. Am. Chem. Soc. 19* (2007) pp. 3038-3039.

[6] Martinez, A. W., Phillips, S. T., Carrilho, E., Thomas, S. W. 3rd, Sindi, H. and Whitesides, G. M., *Anal. Chem.*, (2008), 80, 3699-3707.

[7] T. Eaidkong, R. Mungkarndee, C. Phollookin, G. Tumcharern, M. Sukwattanasinitt, and S. Wacharasindhu, *J. Mater. Chem.*, (2012), 22, 5970-5977.

[8] S. Pumtang, W. Siripornnoppakhun, M. Sukwattanasinitt and A. Ajavakom, *Colloid interface Sci.*, (2011), 364, 366-372.

[9] W. Thongmalai, T. Eaidkong , S. Ampornpun , R. Mungkarndee, G. Tumcharern, M. Sukwattanasinitt and S. Wacharasindhu, *J. Mater. Chem.*, (2011), 21, 16391-16397

[10] W. Ngampeungpis, Doctoral's thesis, Chulalongkorn university.

EFFECTS OF CARBON BLACK AND SODIUM LIGNOSULFONATE IN EXPANDER ON CAPACITY OF LEAD ELECTRODE

Somsak Meenakorn[1*], Preecha Termsuksawad[1], Sorraya Phiboonkulsumrit[2]

[1] Integrated Product Design and Manufacturing Program, School of Energy, Environment and Materials, King Mongkut's University of Technology Thonburi, Bangkok, Thailand
[2] National Metal and Materials Technology Center, Pathum Thani, Thailand

[*] Author for correspondence; E-Mail: somsak_me@hotmail.com, Tel. +66 898150933

Abstract: Traction battery is a rechargeable battery, whose service life depends on its capacity and working environment. To increase its capacity, one approach is to modify active materials, which is used as negative electrode. One major constituent in the active material that affects performance of the battery is an expander: a mixture of barium sulfate, sodium lignosulfonate, and carbon black. In this study, effects of carbon black and sodium lignosulfonate in expander on capacity of lead electrode were investigated. Cyclic voltammetry (CV) and transmission electron microscope (TEM) were used to investigate the capacity of the electrode and to examine structure of the expander, respectively. The result showed that capacity of the electrode increases with amounts of carbon black and sodium lignosulfonate in the expander. In addition, capacity of the electrode was high when the amount of carbon black was equal to that of lignosulfonate. The reason for this phenomenon is related to the expander structure. The maximum capacity was obtained when the weight ratio of barium sulfate: sodium lignosulfonate: carbon black is 88:6:6.

1. Introduction

Traction battery is a rechargeable battery used in various types of vehicles such as forklifts, wheel chairs, ships, and subway trains. Its service life depends on its capacity and degradation during charge-discharge cycle. The capacity of each battery is related to the composition of active materials used as an electrode. An active material consists of lead oxide, dynel flock, sulfuric acid, water, vaseline, and expander. Function of the expander is to increase the apparent volume of the active material, which results in increasing discharge rates and cycle chargeability [1].

The expander comprises barium sulfate, sodium lignosulfonate, and carbon black. The function of sodium lignosulfonate is to increase surface area; thus reduce the effective current density during discharge. As a result, better utilization of active materials is obtained. Its effect is more pronounced at low temperature [2]. The role of carbon black is to improve electrical conductivity of the active materials during deep discharge. Typically, carbon black can be classified by its structure as low, medium, and high structure [3]. A low-structure carbon black refers to an aggregate of a relatively few primary carbon black particles. In contrast, high-structure carbon black is an aggregate consisting of many primary particles with considerable branching and chaining. The longer the carbon chain, the higher is the electrical conductivity [3]. In general, the recommended amount of carbon black in an expander is equal to that of lignosulfonate [4]. However, their roles on capacity of traction battery are still unclear. In addition, the proper ratio of these elements compared with barium sulfate is not known. This study, therefore, aims to study the effects of carbon black and sodium lignosulfonate in expander on capacity of lead electrode.

2. Methodology

2.1 Materials

Carbon black, namely XE2B (high-structure carbon black), was employed. Expander preparation was accomplished by mixing barium sulfate, sodium lignosulfonate, and carbon black by a bench-top high speed mixer at mixing speed of 500 rpm for 2 min. The designation and the composition of all samples were shown in Table 1. A commercial expander, HE115, was also used in this study as a reference. HE115, analyzed by thermogravimetry (TGA), consists of barium sulfate, sodium lignosulfonate, and type-unidentified carbon black at the weight ratio of 88:6:6.

Table 1: The designation of the prepared expander

Batch Name	Weight ratio		
	Barium sulfate	Sodium lignosulfonate	Carbon black
XE8844	88	4	4
XE8864	88	6	4
XE8846	88	4	6
XE8866	88	6	6
XE8886	88	8	6
XE8868	88	6	8
XE8888	88	8	8

2.2 Testing

Cyclic voltammetry was carried out using the Autolab PGSTAT30. High purity lead was used as a working electrode with an exposed area of 1 cm^2. Before testing, in order to get rid of lead oxide on the surface, the electrodes were mechanically polished by emery paper and then it was electrochemically cleaned using a constant potential of -0.90 V (versus Ag/AgCl electrode) until a steady current of 0.1 mA is reached.

The electrolyte is 1.25 g-cm^{-3} sulfuric acid. The prepared expander was added in sulfuric acid until the expander concentration is 20 ppm. Because expander is not directly dissolved in sulfuric acid, it was treated with a small amount of 0.1 M NaOH prior addition in sulfuric acid.

Cyclic voltammetry was conducted at the potential range of -0.90 to -0.30 V (versus Ag/AgCl electrode) with a scan-rate of 20 mV/s. Structures of carbon black in the prepared expander, and HE115 were investigated by JEOL JEM-2010 transmission electron microscope. TEM samples were prepared by dispersing 20 mg of sample in 50 ml of ethanol. During dispersion, the sample was sonicated in ultrasonic bath for 24 hours. Then, the dispersion was dripped on the sample grid and dried with air for at least one hour prior to examination.

3. Results and Discussion

An example of cyclic voltammogram of pure lead in 1.25 g-cm^{-3} density sulfuric acid containing the prepared expander was shown in Figure 1. In the figure, the expander is XE8866. The figure showed that the charge-discharge behaviour was observed in the voltage range of -0.9 to -0.3 V/V$_{\mathrm{Agcl}}$. A considerable broadening of the anodic peak is observed with a shift of the peak-potential towards higher values. The cyclic voltammetry experiments for other expanders were also conducted. The amount of charge was estimated from the area under the anodic peak,

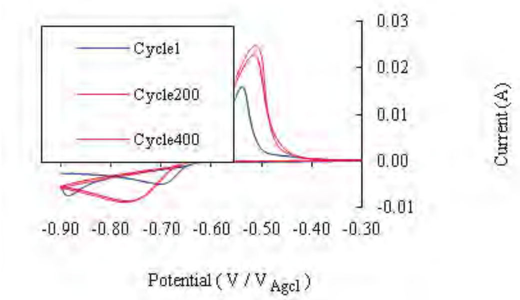

Figure 1. Cyclic voltammogram of a pure lead electrode in 1.25 g-cm^{-3} density sulfuric acid containing 20 ppm of XE8866.

Effect of sodium lignosulfonate on amount of charge was shown in Figure 2. For this series of experiment, the amount of barium sulfate and carbon black in expander was kept constant at the weight ratio of 88 and 6, respectively. Figure 2 shows that lignosulfonate improves cycle chargeability and increases discharge capacity of lead electrode. This result agrees with the studies by Boden [4] and Hirai, et al. [5]. This figure also indicates that the amount of charge when the weight ratio of lignosulfonate in the expander is at least 6 is higher than that when HE115 was used. To explain the effect of lignosulfonate on capacity, the function of each ion must be understood. When lignosulfonate is added in an expander, lignin (R+) anion may adsorb on the surface of the lead particles. The sulfonate cation, in addition, faces out to the aqueous electrolyte. This phenomenon causes an increase in the repulsion potential between lead particles. This potential prevents the particle coalescence and results in increasing the surface area of particles. Therefore, capacity of negative active materials increases. To clarify this explanation, transmission electron micrsope was used to investigate the structure of carbon black, lignosulfonate and barium sulfate in a prepared expander and in HE115 as shown in Figure 3. From the figure, the black aggregate, the gray cluster and the light-gray cluster are barium sulfate, carbon black and sodium lignosulfonate, respectively. Sodium lignosulfonate is chained by carbon black aggregate, calling lignosulfonate-carbon black cluster. Figure 3 showed that the branch of aggregate in XE8866 is longer than that found in HE115. The longer the branch, the higher is the surface area of the expander.

Although lignosulfonate increases surface area of lead particle, resulting in an increase of capacity, the effect of amount of lignosulfonate on increasing capacity is limited. From Figure 2, the maximum capacity was obtained when the weight ratio of lignosulfonate is 6. Further increasing lignosulfonate results in a small decrease of capacity. The capacity reduction may be explained by oversaturation. Excess lignin anions may increase the thickness of lignin layer on surface of lead particle and then hinder the charge transfer. Consequently, capacity decreases as well as electrical conductivity [6]. It should be noted that the maximum charge was obtained when the amount of carbon black is equal to that of lignosulfonate. This phenomenon agrees with the studies by Brodd and Kordesch [7], Hehner [8], Moseley et al. [9] and McNally, et al. [10].

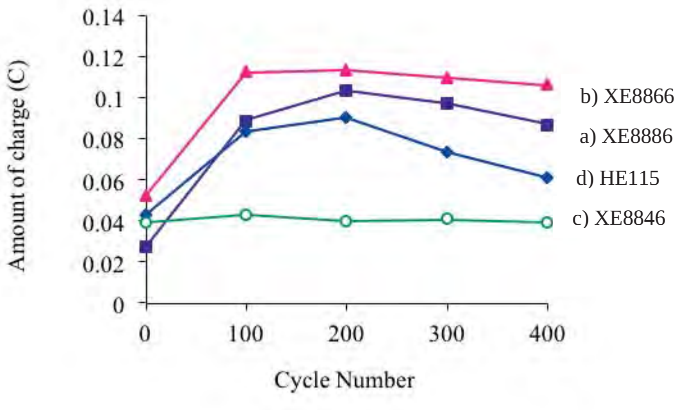

Figure 2. Amount of charge of the anodic peak and number of cycles for a pure lead electrode in 1.25 g-cm^{-3} density sulfuric acid containing 20 ppm of a) XE8886, b) XE8866, c) XE8846, and d) HE115 (commercial expander).

Not only increasing capacity, as shown in the Figure 2, lignosulfonate also preserves capacity after repeating several charge-discharge cycle. This result is consistent to that of Boden [11]. Capacity preservation is a result of a reduction of an amount of lead sulfate forming on the lead particle. Lead sulfate reaction is hindered by lignin anion adsorbing on the surface of lead particle. Therefore, the surface area of the lead particle is left free for further discharge [12].

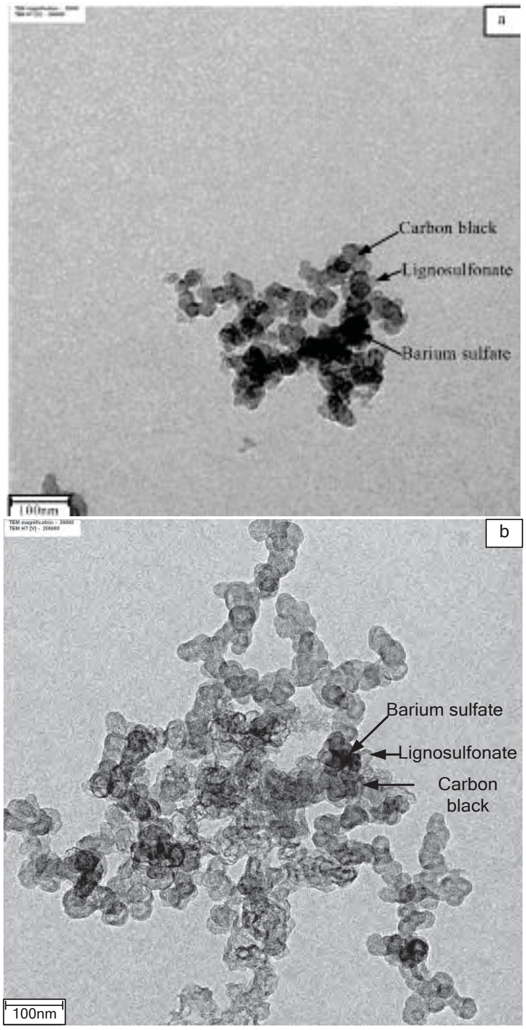

Figure 3. Images from transmission electron microscope (TEM) of (a) HE115 and (b) XE8866.

Figure 4 shows the effect of carbon black on amount of charge of the electrode when the amount of barium sulfate (weight ratio of 88) and sodium lignosulfonate (weight ratio of 6) in expander were kept constant. The figure indicates that the amount of charge increases as the amount of carbon black increases. In addition, the amount of charge when the weight ratio of carbon black is at least 6 is higher than that when HE115 was used. The function of carbon black is to improve electrical conductivity of the negative active material, which will assist the initial charging of the lead-acid battery [2]. It was also found that an increase of carbon black retards the lead sulfate formation on the surface of negative electrode [9, 13]. The accumulation of lead sulfate on the electrode surface decreases of electrical conductivity as well as capacity. Furthermore, an increase of carbon black enlarges a conductive network on lead electrode. This network prevents isolation of active materials by lead sulfate and facilitates charging of battery [13, 14]. Figure 4 also indicates that an increase of the amount of charge resulted by an increase of carbon black is limited at the weight ratio of carbon black is 6, which is equal to that of lignosulfonate. This result agrees with those of Pavlov et al. [15], Petkova and Pavlov [16], Nikolov et al. [17], Nikolov et al. [18] and Boden [19].

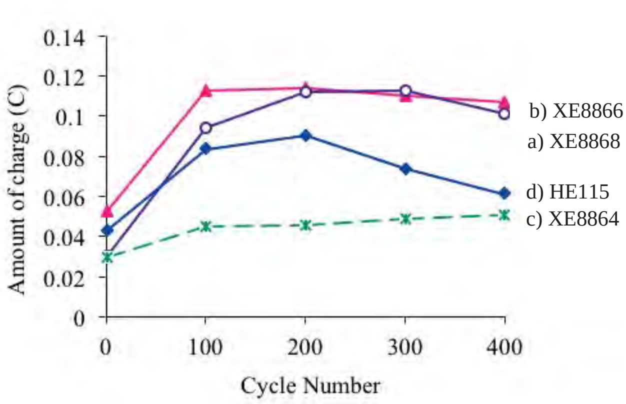

Figure 4. Amount of charge of the anodic peak and number of cycles for a pure lead electrode in 1.25 g-cm^{-3} density sulfuric acid containing 20 ppm of a) XE8868, b) XE8866, c) XE8864, and d) HE115 (commercial expander).

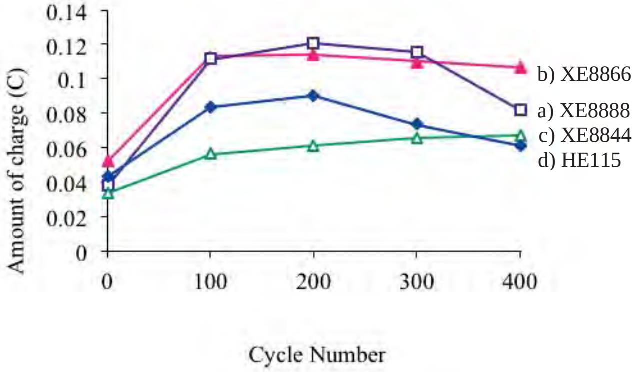

Figure 5. Amount of charge of the anodic peak and number of cycles for a pure lead electrode in 1.25 g-cm^{-3} density sulfuric acid containing 20 ppm of a) XE8888, b) XE8866, c) XE8844, and d) HE115 (commercial expander).

The comparison of amount of charge when the weight ratio of sodium lignosulfonate is equal to that of carbon black and the weight ratio of barium sulfate is 88 was shown in Figure 5. As shown in the figure, the increases of both lignosulfonate and carbon black increases amount of charge and the maximum charge was obtained after approximately 200 cycles. Then amount of charge decreases gradually after that. In addition, cycle chargeability of electrode for XE8866 case is better than that in case of XE8888 was applied after 300 cycles. Therefore, the appropriate weight ratio of barium sulfate: lignosulfonate: carbon black is 88:6:6.

4. Conclusions

In this study, effects of carbon black and sodium lignosulfonate in expander on charge capacity of lead electrode were investigated. The results showed that carbon black and sodium lignosulfonate enhanced capacity and cycle chargeability of the electrode. However, excessive amounts of both carbon black and lignosulfonate do not improve both capacity and cycle chargeability. The highest capacity was found when the amount of carbon black was equal to that of lignosulfonate. The reason for this phenomenon is related to the expander structure modified by carbon black and lignosulfonate. The maximum amount of charge and the best cycle chargeability were obtained when the weight ratio of barium sulfate to lignosulfonate to carbon black is 88:6:6.

Acknowledgements

This work is a project under the Memorandum of Understanding (MOU) between the Defense Industry and Energy Centre (Thailand), Office of the Permanent Secretary for Defense, Ministry of Defense and the King Mongkut's University of Technology Thonburi. The authors gratefully acknowledge the Metrohm Siam Ltd. and the National Metal and Materials Technology Center for their supports on the cyclic voltammetry testing and TEM characterization, respectively.

References

[1] C. Francia, M. Maja and P. Spinelli, J. Power Sources. Vol. 95 (2001), p. 119.
[2] D. P. Boden, J. Power Sources, Vol. 133 (2004), p. 47.
[3] J.K. Foster, Effects of Carbon Black Properties on Conductive Coatings, Presented in the 2nd international exhibition of paint industry suppliers, 1991.
[4] D. P. Boden, J. Power Sources, Vol. 73 (1998), p. 89.
[5] N. Hirai, D. Tabayashi, M. Shiota, T. Tanaka, J. Power Sources. Vol. 133 (2004), p. 32.
[6] G. Szava, Role of the organic expander in modern lead/acid batteries, J. Power Sources, vol. 23, (1988), p. 119-124.
[7] R. J. Brodd and K. V. Kordesch, Lead-acid batteries, 1977
[8] N. E. Hehner, Storage battery manufacturing manual, 1985.
[9] P. T. Moseley, R.F. Nelson, A.F. Hollenkamp, J. Power Sources, vol. 157, (2006), p. 3-10.
[10] McNally et al., Organic expander for lead-acid storage batteries, 2002.
[11] D. P. Boden, Organic Expander in Lead-Acid Batteries: Effects in NAM, 9th Asian battery Conference, 2001.
[12] E. Willihnganz, The nature of the action of expander in storage battery, Presented at the Fall Meeting of the Association of American Battery Manufactures, Inc, pp. 1-16, October 22-23, 1942.
[13] M. Shiomi, T. Funato, K. Nakamura, K. Takahashi, M. Tsubota, J. Power Sources, Vol. 64 (1997), p.147.
[14] K. Nakamura, M. Shiomi, K. Takahashi, M. Tsubota, J. Power Sources, Vol. 59 (1996), p.153.
[15] D. Pavlov, B.O. Myrvold, T. Rogachev, M. Matrakova, J. Power Sources, Vol. 85 (2000), p. 79.
[16] G. Petkova, D. Pavlov, J. Power Sources, Vol. 113 (2003), p. 355.
[17] P. Nikolov, G. Petkova, D. Pavlov, Influence of fluoropolymers on the performance of lead-acid battery negative plates, Presented at International Workshop "Portable and emergency energy sources – from materials to systems", September 16–22, 2005.
[18] P. Nikolov, G. Petkova, M. Matrakova, D. Pavlov, Study of the effect of PVP poly on the performance of lead-acid battery negative plates by electrochemical and physical investigation techniques, Presented at International Workshop "Advanced techniques for Energy Sources Investigation and Testing", September 4-9, 2004.
[19] D. P. Boden, Lead-acid battery expanders with improved life at high temperatures, 2008.

ADSORPTION EFFICIENCY OF MIXED WATER-BASED PAINT WITH NANO WHITE CHARCOAL ON VOLATILE TOLUENE AND XYLENE

Winyu Chitsamphandhvej[1]*, Panthira Ketkeaw[1], Manussawee Tadtai[1]
and Pichprapa Sittisukpaisan[1]

[1] Department of Chemistry, Faculty of Science, King Mongkut's University of Technology Thonburi,
Bangkok, 10140 Thailand

* Author for correspondence; E-mail: winyu.chi@kmutt.ac.th

Abstract: Indoor air pollutants become more concerning health hazard because they can cause chronic and acute health effects at high concentration. This work aims to study the efficiency of activated carbon to adsorb indoor air pollutants by mixing activated carbon into paint. Standard formula water-based paint mixed with various amount of nanosize white charcoal was prepared and coated onto the vinyl plates as a thin film. The adsorption experiment was performed inside a small headspace vial containing gaseous toluene and xylene. The remaining concentration of toluene and xylene were quantified using headspace/ gas chromatograph (HS/GC) with flame ionization detector (FID). Effects of white charcoal contents on paint's properties and stability were studied. It was found that the addition of 6 % (w/w) of white charcoal into paint formula resulted in the most effective adsorption ability on gaseous toluene and xylene, while the other paint characteristics were still acceptable. The corresponding HS/GC analysis results showed the significant decrease of toluene and xylene concentration from 211 mg/m^3 and 184 mg/m^3 to 44 mg/m^3 and 28 mg/m^3 respectively, after adsorption for 4 hours. The compared adsorption results using standard paint formula without activated charcoal coated film showed the remaining concentration of toluene and xylene of 141 mg/m^3 and 86 mg/m^3 respectively. Therefore, it can be concluded that the film containing activated carbon has higher adsorption efficiency on toluene and xylene than the film without activated carbon.

1. Introduction

Paint is any liquid or mastic composition which is converted to a solid film after being applied on a substrate to a thin layer. It is most commonly used to protect, colour, or provide texture to objects. Three main categories of paint ingredients are binder, diluent, and pigments/fillers. Binder is the film-forming component. It imparts an adhesion and strongly influences on properties such as durability, flexibility, toughness and gloss. The diluent are used to dissolve the polymer and adjust the viscosity of the paint. Water is the main diluent for water-based paints. Pigments are granular solids incorporated in the paint to contribute colour. Fillers are granular solids incorporate to impart toughness, texture, give the paint special properties, or to reduce the cost of the paint. Natural pigments include various clays, calcium carbonate, mica, silica, and talc. Synthetic pigments may include engineered molecules, precipitated calcium carbonate, calcined clays, blanc fixe, and synthetic pyrogenic silicas. Hiding pigments include titanium dioxide, phthalo blue, red iron oxide, and many others. Fillers are a special type of pigments that serve to thicken the film, support its structure and increase the volume of the paint. Fillers are usually cheap and inert materials, such as diatomaceous earth, talc, lime, barytes, clay, etc. Besides the three main categories of ingredients, paints can have a wide variety of miscellaneous additives, which are usually added in small amounts, to provide a significant effect on the product. Some examples include additives to modify surface tension, impart antifreeze properties, control foaming and skinning, increase wet edge and improve flow properties, the finished appearance and pigment stability, etc. Other types of additives include catalysts, adhesion promoters, thickeners, stabilizers, UV stabilizers, emulsifiers, texturizers and flatteners.[1] Water-based paints are most commonly applied on indoor and outdoor substrates due to low amount of organic solvents. Base on the advantage of activated carbon, it has been historically used for removal of odour and the applications can be classified into two categories: gas phase and liquid phase.[2] The present study develops the formulation of water-based interior paint by adding activated carbon into paint formulation in order to reduce the indoor air pollutants that may can cause health hazards. Sources of pollutants may come from furniture, appliances, as well as pollution from outdoor activities etc.[3] This research includes the preparation of water-based paint formulations containing various ratio of activated carbon, the experimental test on adsorption of toluene and xylene which are represented as the air pollutants and the standard characteristics of paints are also investigated. The appropriated formulation obtained from this study will give benefit to the paint industry in the term of clean indoor environment enhancement.

2. Materials and Methods

2.1 Apparatus and reagents

Toluene and xylene were determined by HP-7964 headspace sampler (Hewlett Packard, USA) coupled with an HP-6890 gas chromatograph with flame ionization detector (Hewlett Packard, USA) by connecting the heated transfer line of headspace sampler into a volatile interface inlet of GC. A CP-

SIL 5 CB column (Varian: 25 m x 0.25 mm, 0.25 µm film thickness) was used.

Toluene (99.0 %) and xylene (99.0 %) were obtained from Fluka (Steinheim, Germany). Methanol (99.9 %, HPLC grade) was employed as solvent in the standard preparation.

Microsize white charcoal, nonosize white charcoal, rutile TiO_2 powder, calcined kaolin clay, calcined clay, calcium carbonate and the water-based interior paint used in these tests were provided by a famous paint manufacturing company in Thailand. The preparation of water-based interior paint formulations with various amount of white charcoal, the coating films and basic tests of paint properties were studied in laboratory of this paint manufacturing company.

2.2 General procedure

Adsorption of toluene and xylene by activated carbons, pigment and filler: Six of 20 mL headspace vials contain 0.30 g of nanosize white charcoal, microsize white charcoal, rutile TiO_2 powder, calcined kaolin clay, calcined clay and calcium carbonate were placed in a 2 L closed glass container to adsorb gaseous toluene and xylene for 4 hours. (0.50 mL of both toluene and xylene standard in a small vial was placed at the bottom of a glass container). After adsorption process, toluene and xylenes were desorbed by adding 2.00 mL of CS_2 into each vial and 50.00 µL of these solutions were determined by GC–FID.

Adsorption of coated film: In order to test the ability of the coated films (with various amounts of nanosize white charcoal) to adsorb toluene and xylenes compounds in air, a coated film was rolled, placed inside 20 mL headspace vial containing 5 µL of 4,350 mgL^{-1} toluene and xylene standard solution which resulted in 1,087 mg m^{-3} of toluene and xylene after evaporation. The vial was capped hermetically, and stored for exposure time of 4 hours at 25±3 °C. Then, the vial was loaded into a headspace sampler and the remaining concentration of toluene and xylenes compounds were determined by GC–FID.

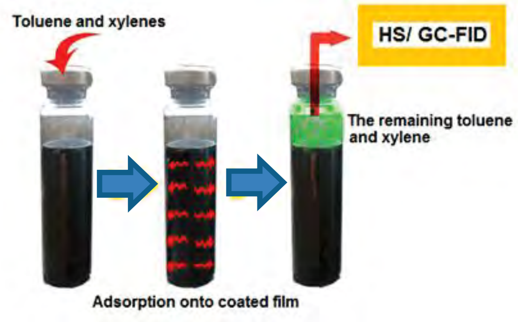

Figure 1. Diagram of the experimental setup for the adsorption and the measurement of toluene and xylene.

HS-GC/FID determination: The vial was heated at 70 °C for 0.1 minutes in oven of headspace sampler, toluene and xylenes gases were transferred via a heated transfer line to a volatile interface of GC in split mode (split ratio 1:10) at 150 °C and employing helium as carrier gas. The temperature of GC oven was 70 °C where they were separated in a GC column and detected with a flame ionization detector, the FID temperature was 150 °C.

3. Results and Discussion

The GC/FID chromatogram of toluene and xylene was shown in Figure 2.

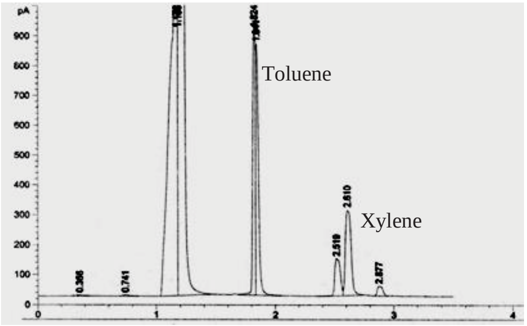

Figure 2 Chromatogram of standard toluene and xylene (4,350 mgL^{-1}).

Because the standard formulation of a water-based paint used in this study contained rutile TiO_2 powder, calcined kaolin clay, calcined clay and calcium carbonate as pigment/fillers. Therefore the adsorption efficiency of each component on toluene and xylene was studied. It was found that toluene and xylene were slightly adsorbed on those components in comparison with microsize white charcoal and nanosize white charcoal as shown in Table 1.

Table 1: % Adsorption of toluene and xylene

Material	**% Adsorption**	
	Toluene	**Xylene**
Nanosize white charcoal	100	100
Microsize white charcoal	9.07	19.69
Rutile TiO_2	0.24	3.93
Calcined Clay	0.37	0.80
Calcined Kaolin Clay	0.25	0.37
$CaCO_3$	0.06	0

The results from Table 1 confirmed that nanosize white charcoal can adsorbed large amount of toluene and xylenes. Therefore, the water-based interior paint formulations with various amount of nanosize white charcoal were prepared. The adsorption experiment was designed and carried out in a small headspace vial. The paints were coated as thin films in the headspace vials by two different procedures. The first one was to coat paint directly onto the inner surface of vial by rolling and we found that it was very difficult to control film thickness. Therefore, we changed the coating procedure by coating the paint on a vinyl plate (using coating device in laboratory of paint manufacturing company) that we can control the film thickness. An appropriate size of a coated vinyl plate was placed into the vial. The standard solution of toluene and xylene were added into the headspace vials containing thin film of paints from both procedures for adsorption studies. The remaining gaseous toluene and xylene in the vials were easily determined using headspace/gas chromatograph. The peak area of remaining toluene and xylene after being adsorbed from a direct coating thin films (A) and coating on vinyl plates (B) showed in Figure 3. It can be concluded that coating films on vinyl plate were suitable because they can be controlled the thickness of films and they gave smooth curves.

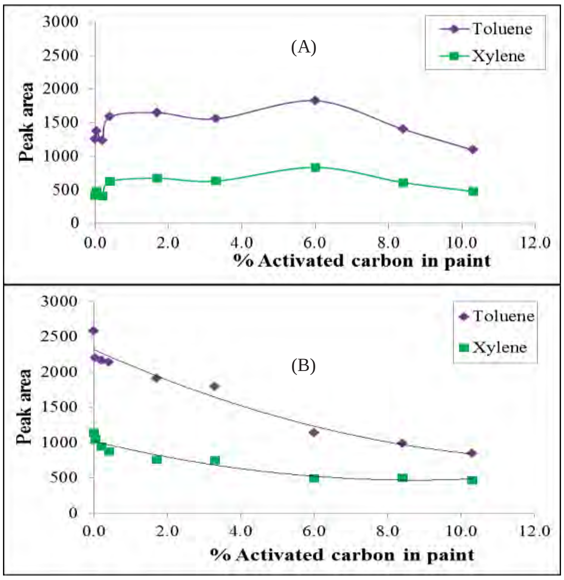

Figure 3. Peak area of the remaining toluene and xylene after adsorption from direct coating film (A) and from thin films coating on vinyl plate (B).

The effect of film thickness on adsorption of toluene and xylene were studied, the coating films on vinyl plates were prepared with two thickness sizes, 50 and 100 microns. The adsorption results were shown as in Figure 4. It was indicated that the adsorption efficiency increased as the amounts of white charcoal in the formulations increased and increasing of films thickness could not improve the adsorption efficiency of toluene and xylene.

Although the formulation of paints with higher % activated carbon had higher adsorption efficiency of toluene and xylene than the formulation with lower % activated carbon but the amount of white charcoal in paints formula can affect the color of paints. The standard formulation of paint in this study was a white color when white charcoal was added into paint formulations, the color of paint were gray tone and the color of gray tone change to dark gray when the % white charcoal increased. Therefore, the color shades of all formulations were measured and the results were shown in Figure 5.

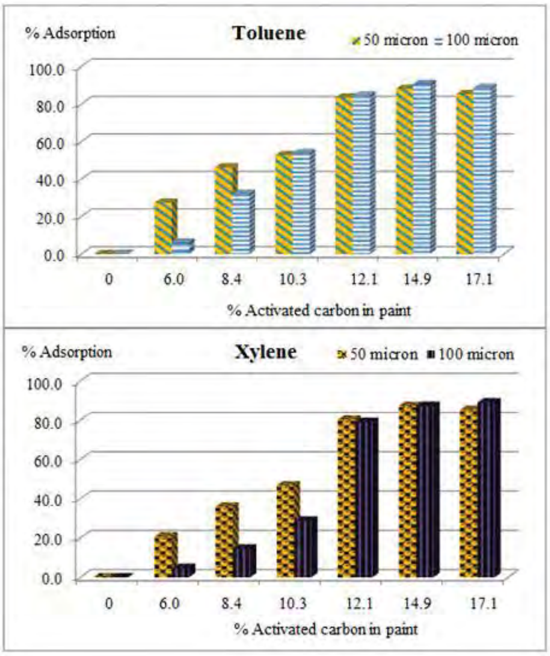

Figure 4. %Adsorption of toluene and xylene from thin films of paint (50 microns and 100 microns).

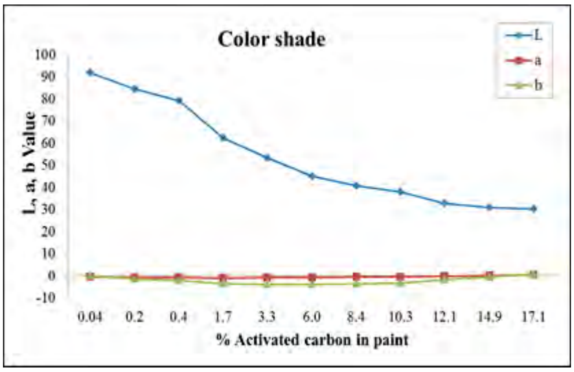

Figure 5. Color shades of paints with various amount of white charcoal in formulations.

The other basic paint properties were also checked and the results were shown in Figure 5. After the basic properties of all paints with various amount of white charcoal from 0.04% to 17.1% were checked, it was indicated that 6% white charcoal in paint formulation was the best formulation due to most effective adsorption ability on gaseous toluene and xylene while the other paint characteristics were still acceptable.

In the previous experiment presented in this study, the white charcoal was firstly prepared as slurry. This slurry was then added during the preparation process to make various formulations containing various amount of white charcoal due to its convenience and fast process.

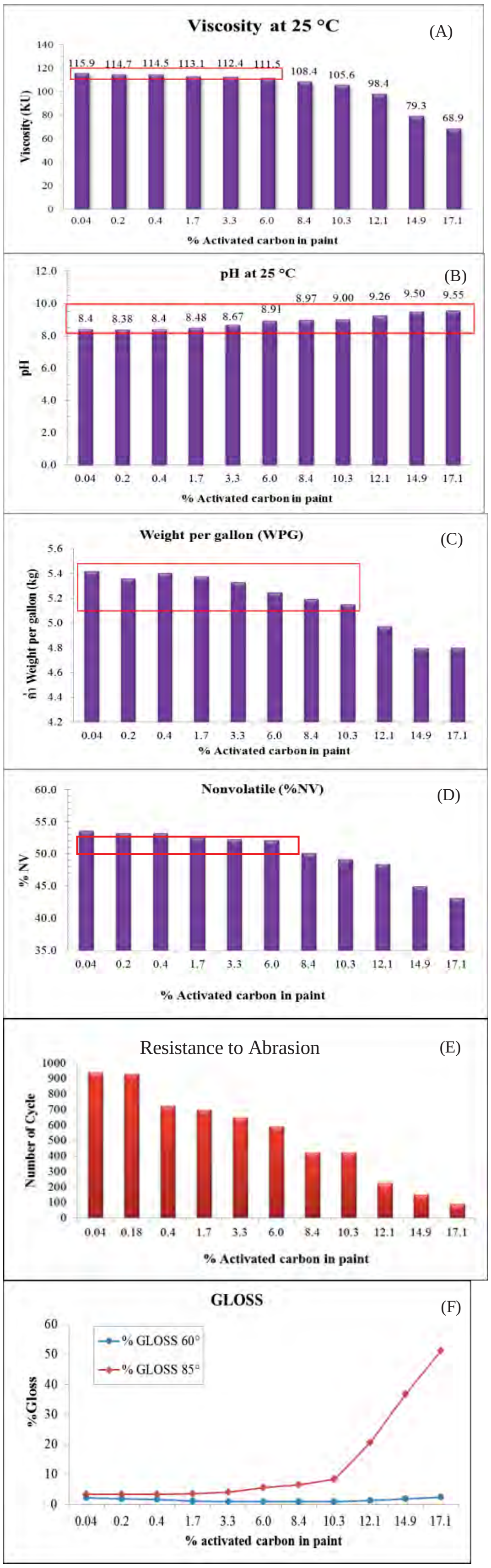

Figure 5. The basic properties of paints: viscosity (A), pH at 25°C (B), weight per gallon (WPG) (C), non-volatile (%NV) (D), resistance to abrasion (E) and gloss (F).
Note: boxes represent the acceptable values.

But when we found that it gave an excellent formulation, the preparation of paint was changed by adding white charcoal powder directly into paint without slurry preparation process. The adsorption experiments were done again in the vials containing gaseous toluene and xylene. The initial concentration and the remaining concentration of toluene and xylene were determined and the results were shown in Table 2 and Figure 6. It was found that the paint formulated with white charcoal in powder form has the highest adsorption efficiency. It might be caused nanosize white charcoal in slurry adsorbed some chemicals containing in slurry prior to the adsorption of toluene and xylene.

Table 2: The initial concentration and the remaining concentration of toluene and xylene after adsorption.

Concentration (mg/m^3)	**Toluene**	**Xylene**
Initial concentration	211.29	184.89
Remaining concentration		
Standard formula	185.40	144.06
+ AC Slurry	141.20	86.08
+ AC Powder	44.21	27.68

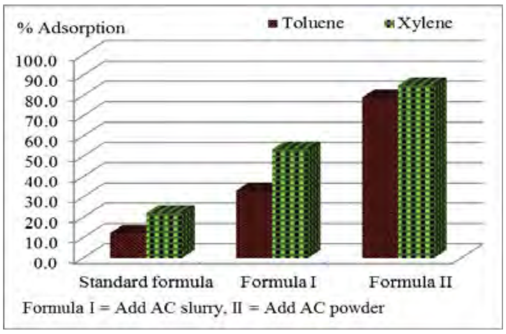

Figure 6. %Adsorption of toluene and xylene by various formulations of paint.

4. Conclusions

We designed to study adsorption ability to adsorb toluene and xylene by using thin film of paint which was put in small headspace vials. Toluene and xylene concentration in the vials were determined using GC technique without any sample preparation steps which made it is easy and convenience. The results showed that the water-based interior paint formulation containing nanosize white charcoal can adsorb toluene and xylene in indoor air. So, it can be developed to be commercial production in the future.

References

[1] http://en.wikipedia.org/ (Retrieved December 6, 2012).
[2] http://www.kuraraychemical.com/(Retrieved December 6, 2012)
[3] D. Saraga, A. Papadopoulos, Ch.Vasilakos, S. Pateraki, and Th. Maggos, Journal of Building and Environment. 46 (2011) 2333-2341.

FABRICATION OF ASPIRIN-LOADED POLYVINYLPYRROLIDONE ULTRAFINE FIBERS BY ELECTROSPINNING TECHNIQUE

Thammasit Vongsetskul*, Phatcharee Chuaymuang, Pattra Pornprompirak, Chutima Siatakul, Dul Boriboon

Department of Chemistry, Faculty of Science, Mahidol University, Rama VI Road, Ratchathewee, Bangkok, 10400, Thailand

* Author for correspondence; E-Mail: thammasit.von@mahidol.ac.th, Tel. +66 2201-5110, Fax. +66 2354-7151

Abstract: Electrospun aspirin-loaded polyvinylpyrrolidone (PVP) (MW ~ 1.3 x 10^6 g/mol) fibers with diameters from 386 to 1,170 nm were successfully fabricated from the 8% w/v ethanolic PVP mixtures. The effect of the applied voltages (8, 10, 12, 14, and 16 kV) on their diameters and morphology was investigated. Scanning electron micrographs revealed that the optimum applied voltage for fabricating fibers was 14 kV.

1. Introduction

Electrospinning is one of the simplest methods for fabricating ultra-fine fiber from either polymer solution or polymer melt. In this process, a continuous strand of a polymer fluid is drawn through a spinneret by a high electrostatic force. The obtained fibers are deposited randomly on a grounded collector as a non-woven mat. The interesting characteristics of ultra-fine fiber are high surface area to mass or volume ratio, and the mats have high porosity. Since their surface is easy to functionalize, ultra-fine fibers are suited for a wide variety of applications such as bioengineering, biotechnology, energy, electronics, environmental engineering, and security [1]. For example, the ultra-fine fibers have recently been applied for the inclusion of bioactive constituents for pharmaceutical applications [2]. In addition, this technique also possesses several advantages such as repeatability and controlling on nanofiber dimension [2-3].

Polyvinylpyrrolidone (PVP), a vinyl-based polymer in which the pendant group is the five-membered amide ring, possesses good adhesion, good complexation, low toxicity, biocompatibility, and good solubility in water and several organic solvents. Because of its excellent biomedical properties, it has also been used as drug carriers [4].

Aspirin, a pain killer and anti-inflammatory agent, is normally administered orally. The chemical structure of aspirin is shown in Figure 1.

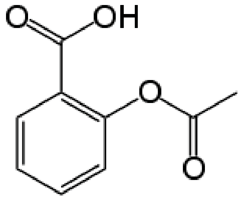

Figure 1. Chemical structure of aspirin.

However, there are some publications reporting on the use of aspirin as a transdermal/topical drug. Benedittis et al. studied the topical aspirin/diethyl either mixtures for treating an acute herpatic neuralgia and a post herpetic neuralgia [5]. In addition, the designation of transdermal aspirin was proposed for antithrombotic drugs [6].

Even though there are reports on the use of aspirin as a transdermal drug, aspirin has never been incorporated into any drug-controlled release media. Therefore, this study aims to incorporate aspirin into ultrafine fibers, one of various drug delivery systems. Mats of aspirin-loaded PVP ultrafine fibers were fabricated by the electrospinning technique, which is the first time that aspirin was added into ultrafine fiber mats. The effect of applied electrical voltages and aspirin concentrations on the prepared fibers was also studied.

2. Materials and Methods

2.1 Materials

PVP with MW of 1.3 x 10^6 g/mol from Sigma-Aldrich (USA), absolute ethanol from LabScan (Thailand), acetylsalicylic acid (aspirin) from Sigma-Aldrich (China) were used without further purification.

2.2 Preparation and characterization of the spinning mixture

The appropriate amount of aspirin and PVP powders were dissolved in 10 ml of absolute ethanol under magnetic stirring for 1 h at room temperature to achieve the 8% w/v PVP and 2.0% w/v aspirin.

2.3 Fabrication of electrospun aspirin-loaded fiber mats

Electrospinning of the as-prepared PVP solutions was carried out in room conditions (25 ± 1 °C; relative humidity of 71 ± 3%) by connecting the emitting electrode of positive polarity from a Gamma High-Voltage Research ORMOND BEACH power supply (D-ES50PN-20W/QAM, FL, USA). Each solution was filled in a standard 25-ml syringe, and the open end of which was attached to a blunt guage-20 stainless steel needle (OD = 0.91 mm), used as the nozzle. The grounding electrode and fiber collector were an aluminium foil. The applied voltages were varied from 8, 10, 12, 14, to 16 kV. A distance between the tip of the nozzle and the ground collector was 10 cm. The feed rate of the solutions was 1.5 ml h^{-1}. The collection time was 15 min for observing the morphology of the as-spun products. The electrospinning set-up used in this work is shown in Figure 2.

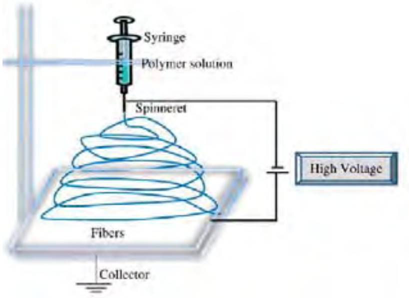

Figure 2. Electrospinning setup used in this work.

2.4 Characterization of electrospun aspirin-loaded fiber mats

The morphology of the electrospun fibers was investigated under scanning electron microscope (SEM; S-2500, Hitachi, Japan). The fibers were dried on an aluminum foil in a dust-free environment before being stuck on the sample holder with a double-coated carbon conductive tape and sputter-coated under vacuum by using a sputter coater (E-102, Hitachi, Japan). An average diameter of the electrospun fiber mats was measured directly from SEM (at 15 kV) using a Photoshop 5.0 (n ≥ 50).

3. Results and Discussion

SEM images of the aspirin-loaded fibers prepared from the spinning mixtures are shown in Figure 3.

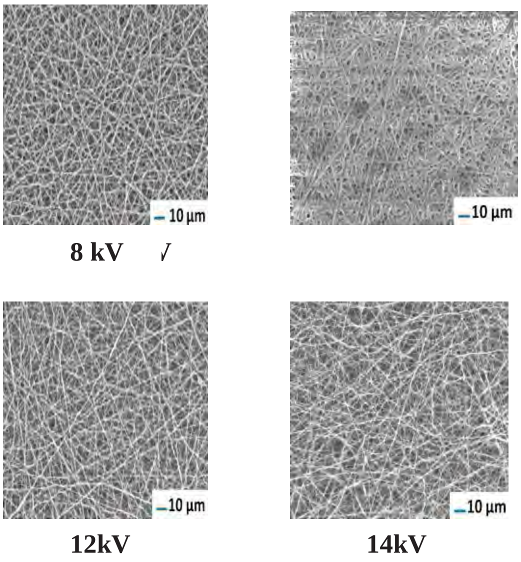

Figure 3. SEM images of aspirin-loaded electrospun PVP fibers prepared from 8 wt % PVP and 2 %w/v aspirin.

It was observed that the surface of the obtained composite fibers were smooth. From the SEM micrographs, the average diameters of the composite fibers were 812, 799, 788, 780, and 1,170 nm when the applied electrical voltages were 8, 10, 12, 14, and 16 kV, respectively. Therefore, the diameter of the composite fibers decreased with increasing the applied electrical voltages except when the applied voltage was 16 kV because a higher voltage led to a greater amount of charges, which accerelated the jet faster. Hence, a greater stretching of the solution due to the greater columbic forces in the jet as well as the stronger electric field was obtained [1]. Moreover, a high voltage favors the formation of secondary jets during electrospinning. This also contributed the reduction in the fiber diameter [7].

When the applied voltage was 16 kV, the travelling time of the charged polymer jet was so short that the jet could be not solidified in time. Therefore, the fibers were stickled to the others, and, hence, the fiber diameter was extraordinary large. When all the fiber diameter results are compared, the optimal applied voltage for fabricating fibers was 14 kV for obtaining the thinnest uniform fibers.

4. Conclusions

SEM images confirmed the success of the preparation of electrospun aspirin-loaded PVP fibers with diameters of 386 – 1,170 nm. The best applied electrical voltage providing the smallest uniform fibers was 14 kV. The fabricated fibers have potentials to be used in biomedical applications.

References

[1] S. Ramakrishna, K. Fujihara, W. Teo, T. Lim, and Z. Ma, *An introduction to electrospinning and nanofibers*, World Scientific Publishing, Singapore, Singapore (2005).

[2] K. N. Kontogiannopoulos, A. N. Assimopoulou, I. Tsivintzelis, C. Panayiotou, and V. P. Papageorgiou, *Int. J. Pharmaceutics* **409** (2011) 216-228.

[3] B. L. Fletcher, T. E. McKnight, J. D. Fowlkes, D. P. Allison, M. L. Simpson, and M. J. Doktycz, *Synth. Met.* **157** (2007) 282-289.

[4] F. Fischer and S. Bauer, *Chem. unserer Zeit.* **43** (2009) 376-383.

[5] J. G. Benedittis and A. Lorenzetti, *Pain* **65** (1996) 45-51.

[6] H. O. Ammar, M. Ghorab, S.A. El-Nahhas, and R. Kamel, *Int. J. Pharmaceutics* **327** (2006) 81–88.

[7] M. M. Demir, I. Yilgor, E. Yilgor, and B. Eman, *Polymer* **43** (2002) 3303-3309.

THE DEVELOPMENT OF Pt/C ELECTROCATALYST IMPREGNATED BY PHOSPHOMOLYBDIC ACID FOR CO TOLERANCE IN PROTON EXCHANGE MEMBRANE FUEL CELLS

Patiwat Onbhuddha, Somsak Supasitmongkol, Korakot Sombatmankhong*

National Metal and Materials Technology Center, 114 Thailand Science Park, Phahonyothin Rd., Khlong Nueng, Khlong Luang,
Pathum Thani, 12120, Thailand

* Author for correspondence; E-Mail: Korakots@mtec.or.th, Tel. +66 2564 6500 ext.4706, Fax. +66 2564 6403

Abstract: Proton exchange membrane fuel cells (PEMFCs) are seriously poisoned by H_2 gas containing even small amount of CO. The strong adsorption of CO on platinum (Pt) catalyst causes a decrease in the number of active sites, leading to a poor performance and durability of PEMFCs. Consequently, Pt-based carbon supported (Pt/C) catalyst was impregnated with heteropoly acids of polyoxometalate (PMA), which are oxidising agents for CO desorption. In this study, phosphomolybdic acid ($H_3PMo_{12}O_{40}$) was selected due to its ease of synthesis, good proton conductivity and durability. The effect of PMA loading (from 0-40%wt) on improving CO tolerance as well as the corresponding current was investigated through the following diagnostics. First of all, the catalyst morphology was examined by scanning electron microscopy together with energy dispersive x-ray spectroscopy to verify the PMA content. It was found that the introduction of PMA into Pt/C catalysts had no significant effect on their physical structure. Pt nanoparticles were highly dispersed in all samples as determined by transmission electron microscopy. Next, a screening method to identify electrocatalytic activity and CO-stripping efficiency was carried out via cyclic voltammetry. Among various PMA/Pt compositions, 40%wt PMA on Pt/C catalyst exhibited a 1.5-fold increase in the peak current in comparison with pure Pt/C. Hence, the 40%wt PMA-Pt/C would be utilised as an alternative electrocatalytic material that significantly improves the cell performance and CO tolerance.

1. Introduction

Proton exchange membrane fuel cells or PEMFCs have been extensively developed for transportation and portable applications due to their low operating temperature, quick response time and high power density. In a typical PEMFC, hydrogen is commonly used as a fuel which mostly contains certain amount of carbon monoxide as it is produced from steam reforming or partial oxidation of hydrocarbons. The presence of carbon monoxide in hydrogen gas can cause a serious deterioration of platinum-based electrocatalysts as a result of strong CO-Pt adsorption; hence, the cell performance and durability greatly decrease.

Several works have been undertaken to overcome this problem, for example, development of CO tolerant Pt-based alloys [1-6], modified electrode configuration [7], polymer electrolyte membranes for high temperature PEMFCs [8-10], and introduction of hetero polyacids [11-15] such as polyoxometalates (PMAs). Among various methods, the incorporation of PMAs to Pt-based electrocatalysts has been increasingly studied due to its simple synthesis, great ability for CO electrooxidation, and improved durability. Even though it has been reported that cell performance was improved with the amount of PMAs existed in the Pt-based electrocatalysts, the PMA loading has been investigated only up to 16.7 % wt [16]. In this study, Pt-based electrocatalysts containing a wide range of PMA loadings (from 0 to 40 %wt) has been investigated to verify the effect of PMA loading on improving the electrocatalytic activity as well as CO tolerance using several diagnostics: electrochemical techniques, transmission electron microscopy (TEM) and scanning electron microscopy (SEM).

2. Materials and Methods

2.1 Preparation of PMA impregnated on Pt/C electrocatalyst

The procedure for PMA impregnated on Pt/C electrocatalyst (denoted as PMA-Pt/C) synthesis was carried out according to Choi and co-workers [16]. A certain amount of 20 %wt Pt/C (purchased from fuelcellstore) was vigorously stirred for 30 minutes in distilled water to obtain 0.6 g Pt/C. Next, the Pt/C suspension was mixed with different quantities of phosphomolybdic acid hydrates (Sigma Aldrich) in 20 ml of distilled water to provide three different PMA loadings of 10, 20 and 40 %wt in Pt/C catalysts (denoted as 10PMA-Pt/C, 20PMA-Pt/C and 40PMA-Pt/C respectively). After that, the mixture was stirred and sonicated for 12 hours. The PMA-Pt/C was separated using a high-speed centrifuge and then dried in a vacuum oven at 40^{o} C for 48 hours.

2.2 Characterisation of PMA-Pt/C

The CO tolerance of various PMA-Pt/C compositions was examined through electrochemical techniques. This work employed CO stripping measurement based on a three-electrode system consisted of a glassy carbon working electrode coated with different PMA-Pt/C compositions, a Pt rod as a counter electrode, and Ag/AgCl as a reference electrode. The working electrode was made of a glassy carbon paper coated with a PMA-Pt/C layer by drop casting method. The PMA-Pt/C catalyst ink was prepared from 5 mg PMA-Pt/C powder, 50 µl Nafion 117 solution (Sigma Aldrich), and 1 ml of 5 M ethanol solution. A sonication for at least 30 minutes was required to ensure a well-mixed suspension of the catalyst ink. Subsequently, 75 µl of the catalyst ink was dropped onto glassy carbon paper and then dried at 60 °C for 1 hour in a vacuum oven. Prior to the CO-stripping measurement, 0.5 M H_2SO_4 (Sigma Aldrich) electrolyte solution was purged with N_2 gas for 1 hour to remove dissolved oxygen in the solution, followed by CO gas (1000 ppm in N_2 gas) at a flow rate of 200 ml/min for 15 minutes. Two voltammetry methods were sequentially employed as follows. Firstly, the CO pre-adsorption was performed at a potential range of 100-300 mV for various adsorption periods (300-1200 seconds). Before starting the second voltammetry technique, N_2 gas was continuously supplied to the solution to entirely remove dissolved and physically adsorbed CO. The CO stripping test was then carried out using cyclic voltammetry, scanning the potential from -0.2 to 1.2 V at a scan rate of 100 mV/s.

The morphology and topography of PMA-Pt/C containing various Pt contents were also investigated using SEM and TEM, respectively. PMA contents were also verified using energy-dispersive X-ray spectroscopy (EDX).

3. Results and Discussion

3.1 Physical properties of PMA-Pt/C

The representative TEM images of the Pt/C catalysts containing 0, 20 and 40 %wt PMA are demonstrated in Figure 1. The TEM images show the structural properties of all PMA-Pt/C samples which had uniformly dispersed Pt nanoparticles with similar particle size of approximately 3 nm. This implied that structural properties of Pt was not affected by the presence of PMA which could be supported by the FTIR spectrum; the basic structure of Pt/C is intact and preserved as compared Figure 2b to Figure 2c. When the PMA was introduced to the Pt/C catalyst (Figure 2c), the additional characteristic peaks of the $[PW_{12}O_{40}]^{3-}$ Keggin unit were obtained at 804 cm^{-1} (W-O_c-W), 898 cm^{-1} (W-O_b-W), 977 cm^{-1} (W=O_d) indicating the existence of PMA in the Pt/C catalyst.

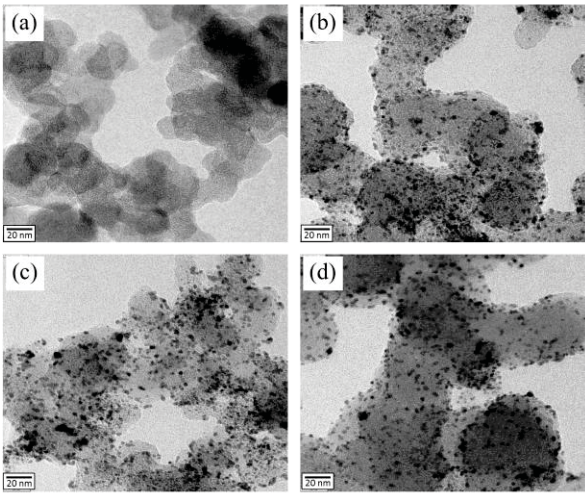

Figure 1 Representative TEM images of (a) carbon black and Pt/C with (b) 0, (c) 20 and (d) 40 %wt PMA

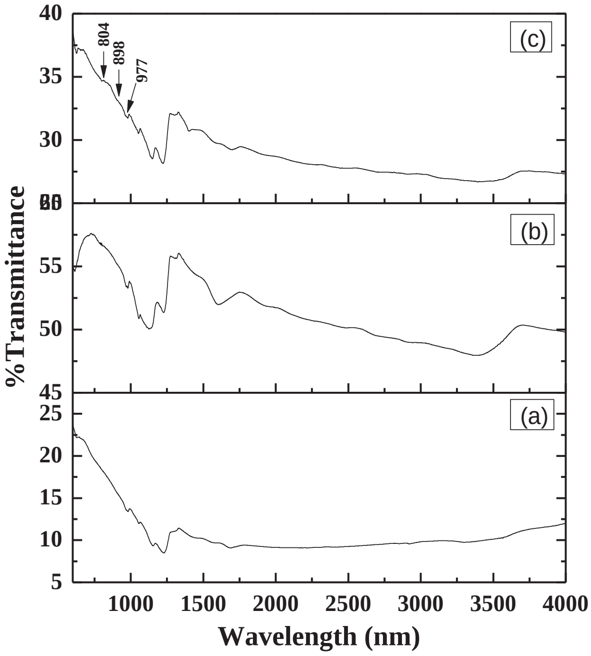

Figure 2 FTIR spectrum of (a) carbon black and Pt/C with (b) 0 and (c) 20 %wt PMA

3.2 Synthesis and Morphology of PMA

Figure 3 illustrates SEM images and EDX spectrum of Pt/C containing different quantities of PMA. All samples exhibit Pt/C agglomerates uniformly dispersed on the carbon support (Pt nanoparticles can be clearly observed using TEM). The representative EDX spectrum revealed the main compositions of each sample which were subsequently used to determine the quantity of PMA within each PMA-Pt/C sample according to the Mo concentration. Table 1 shows the compositions of PMA-Pt/C and it was found that the percentage of Mo in PMA-Pt/C samples agreed very nearly to the desired PMA concentration despite relatively smaller.

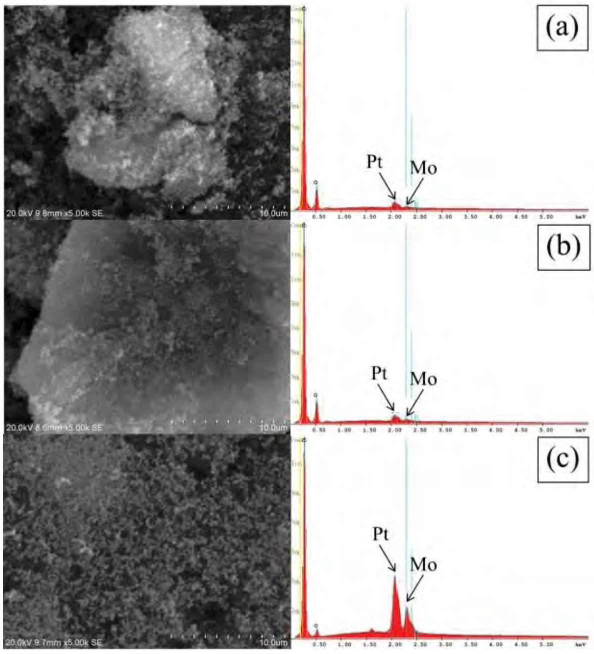

Figure 3 SEM images and EDX analysis of (a) 10% (b) 20% and (c) 40 %wt PMA-Pt/C

Table 1 The compositions of PMA-Pt/C calculated from EDX results

Samples	% concentration (wt)		
	C	Pt	Mo
Pt/C	80.40	19.60	0
10PMA-Pt/C	70.65	21.05	8.30
20PMA-Pt/C	61.06	19.02	19.92
40PMA-Pt/C	44.45	19.87	35.68

3.3 Electrochemical properties of PMA-Pt/C

A CO-stripping test was carried out using cyclic voltammetry technique as described in experimental section. In order to understand the CO-stripping mechanism, the effects of adsorption potential and time on the corresponding stripping current were evaluated as demonstrated in Figure 4 and 5, respectively.

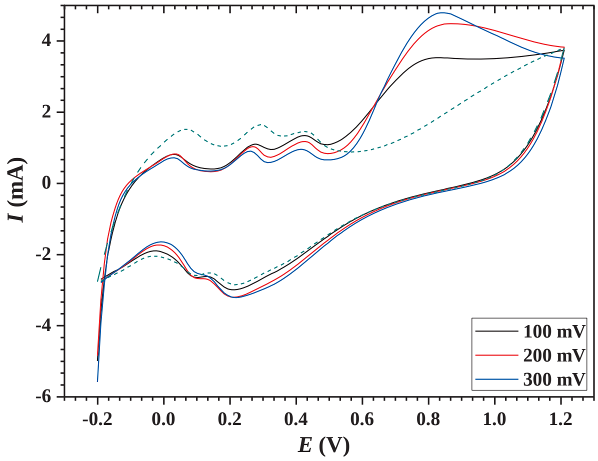

Figure 4 CO stripping voltammograms of 10PMA-Pt/C catalyst using different CO-adsorption potential of 100, 200, and 300 mV. The CO adsorption time was 300 s. The dashed line represents the second-scanned voltammogram.

All the CO stripping voltammograms shown here were obtained from the first cycle since they contained the characteristic peaks of CO oxidation. After the first potential scan, the adsorbed CO molecules were completely oxidised and no CO-stripping peaks could be found in the second-scanned voltammogram (dashed line). In general, the voltammograms of the Pt/C without PMA exhibits characteristics of polycrystalline Pt on both the reductive adsorption region of protons and the oxidative desorption region of atomic hydrogen at the potential range of -0.2 to 0.4 V [16]. However, the peak current for hydrogen adsorption on bare surface of Pt could not be observed from the cyclic voltammogram (red line) in Figure 6. On the other hand, the presence of PMA in Pt/C catalysts was found to promote the hydrogen desorption and adsorption mechanisms, revealing two dominant characteristic regions. The first region was located in a potential range of -0.1 to 0.4 V which was driven by three different reactions: (i) hydrogen adsorption and desorption on Pt sites, (ii) the reaction of CO molecules on Pt sites, and (iii) the reaction of oxygenated species on Mo Sites [17]. These three different reactions occasionally occurred on different Pt and/or Mo sites, resulting in three different oxidative and reductive peaks located in this low potential range. The second peak current was found at around 0.8 V corresponding to the oxidation of pre-adsorped CO and OH over Pt sites in the PMA-Pt/C catalysts.

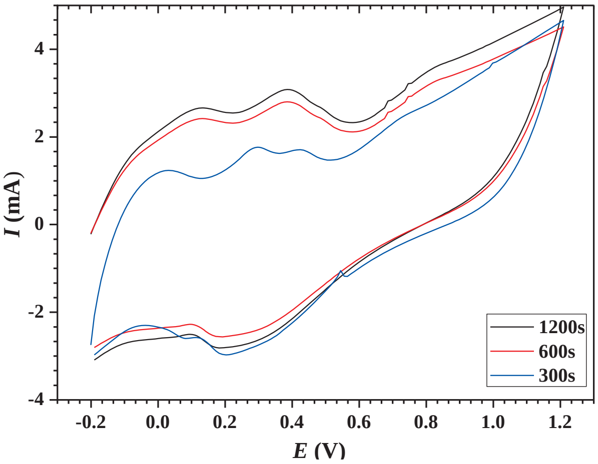

Figure 5 CO stripping voltammograms of 40PMA-Pt/C catalyst using different CO-adsorption time of 300, 600 and 1200 seconds. The CO adsorption potential was 100 mV.

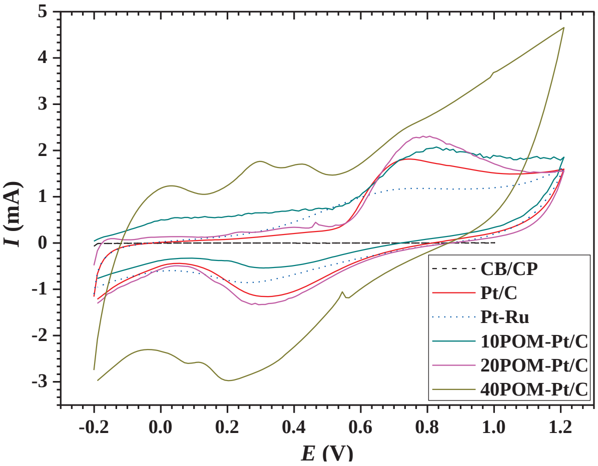

Figure 6 CO stripping voltammograms of various Pt/C catalysts containing different PMA loadings of 0, 10, 20 and 40 %wt (denoted as Pt/C, 10PMA-Pt/C, 20PMA-Pt/C and 40PMA-Pt/C, respectively). The dashed and dotted lines represent carbon paper coated with carbon black (denoted as CB/CP) and Pt-Ru alloy, respectively.

The CO adsorption potential and time significantly influenced the electrocatalytic activity for CO oxidation. The characteristic peak current for CO oxidation was found to increase with the adsorption potential and time. The increase in the adsorption potential during CO adsorption process enhanced the electrical energy necessary to drive the electrode reaction; hence, larger amount of CO was pre-adsorbed and subsequently oxidised during CO stripping process. Similarly, the longer CO pre-adsorption time also led to an enhanced CO quantity available for CO adsorption as well as effective pre-conditioning process for the electrochemical system. Interestingly, the broad oxidation current peak is observed with the PMA loading of 40%wt which is possibly caused by a very week interaction between Pt surface and CO with the presence of excessive PMA loading.

Figure 6 shows CO stripping voltammograms of various Pt/C catalysts containing different PMA contents compared with other electrode materials. It was found that an increase in the PMA loading to Pt/C catalysts enhanced the electrical double layer which was attributed to a proton transfer redox reaction (O/OH ligands) on the Mo atoms [18]. Similar to the CO-adsorption time and potential, the larger quantity of PMA presence in Pt/C catalysts dramatically improved the CO-oxidation peak current. The maximum peak current was obtained with 40PMA-Pt/C catalyst with a shift of the second CO-oxidation peak current from 0.8 to 0.7 V. At this lower CO-oxidative potential, it can be implied that the pre-adsorbed CO on Pt sites in the 40PMA-Pt/C catalyst would be easily oxidised when compared to that of the Pt/C catalyst without PMA loading. In addition to the excellent CO-tolerance property, the 1.5-fold increase in peak current was obtained from 40PMA-Pt/C in comparison with the Pt/C which was a result of the existence of Mo co-catalyst; this indicates that the 40PMA-Pt/C catalyst is a promising electrocatalyst that significantly improves the cell performance and CO tolerance.

4. Conclusions

The effect of PMA loading (from 0-40%wt) on improving CO tolerance together with the CO-oxidative current was investigated in this work. The catalyst morphology and topography were examined by SEM and TEM, respectively. The structural properties of all PMA-Pt/C samples had uniformly dispersed Pt nanoparticles with similar particle size of approximately 3 nm, implying that structural properties of Pt was not affected by the presence of PMA. A screening method to identify electrocatalytic activity and CO-stripping efficiency was carried out via cyclic voltammetry. It was found that the CO adsorption potential and time significantly influenced the electrocatalytic activity for CO oxidation. Furthermore, the characteristic peak current for CO oxidation increased with the adsorption potential and time, indicating that larger amount of CO was adsorbed and oxidised with increasing either adsorption potential or time. When compared various PMA/Pt compositions, 40%wt PMA on Pt/C exhibited a 1.5-fold increase in the peak current (at the potential of ~0.8 V) in comparison with pure Pt/C due to the existence of Mo co-catalyst. As a result, the 40%wt PMA/Pt would be utilised as an alternative electrocatalytic material that significantly improves the cell performance and CO tolerance.

Acknowledgements

This work was financially supported by National Metal and Materials Technology Center, under National Science and Technology Development Agency in Thailand.

References

[1] D.C. Papageorgopoulos, M. Keijzer and F.A. de Bruijn, *Electrochim Acta*. **48** (2002) 197-204.

[2] C. He, H.R. Kunz and J.M. Fenton, *J Electrochem Soc*. **150** (2003) 1017-1024.

[3] Y. Liang, H. Zhang, H. Zhong, X. Zhu, Z. Tian and D. Xu, *J Catal*. **238** (2006) 468-476.

[4] Y. Liang, H. Zhang, Z. Tian, X. Zhu, X. Wang and B. Yi, *J Phys Chem B*. **110** (2006) 7828-7834.

[5] L. Ma, H. Zhang, Y. Liang, D. Xu, W. Ye and J. Zhang, *Catal Commun*. **8** (2007) 921-925.

[6] L.G.S Pereira, V.A. Paganin and E.A. Ticianelli, *Electrochim Acta*. **54** (2009) 1992-1998.

[7] C. Wan and Q.H. Zhuang, *Int J Hydrogen Energy*. **32** (2007) 4402-4411.

[8] T.J. Schmidt and J. Baurmeister, *Electrochemical Soc Trans*. **16** (2008) 263-270.

[9] Q. Li, R. He, J.O. Jensen and N.J. Bjerrum, *Fuel Cells*. **4** (2004) 147-159.

[10] Q.F. Li, H.C. Rudbeck, A. Chromik, J.O. Jensen, C. Pan and T. Steenberg, *J Memb Sci*. **347** (2010) 260-270.

[11] M.H. Seo, S.M. Choi, H.J. Kim, J.H. Kim, B.K. Cho and W.B. Kim, *J Power Sources*. **179** (2008) 81-86.

[12] J.R. Ferrell, M-C. Kuo, J.A. Turner and A.M. Herring, *Electrochim Acta*. **53** (2008) 4927-4933.

[13] L.G.S. Pereira, F.R. Santos, M.E. Pereira, V.A. Paganin and E.A. Ticianelli, *Electrochim Acta*. **51** (2006) 4061-4066.

[14] I. Gatto, A. Sacca, A. Carbone, R. Pedicini, F. Urbani and E. Passalacqua, *J Power Sources*. **171** (2007) 540-545.

[15] Z. Cui, W. Xing, C. Liu, D. Tian and H. Zhang, *J Power Sources*. **195** (2010) 1619-1623.

[16] M.C. Sung, H.S. Min, J.K. Hyung, J.L. Eun and B.K. Won, *INT J Hydrogen Energ*. **35** (2010) 6853-6862.

[17] M.H. Seo, S.M. Choi, H.J. Kim, J.H. Kim, B.K. Cho and W.B. Kim, *J Power Sources*. **179** (2008) 81-86.

[18] B.N. Grgur, N.M. Markovic and P.N. Ross, *Electrochim Acta*. **43** (1998) 3631-3635.

POLYANILINE/MONTMORILLONITE NANOCOMPOSITES FOR CORROSION PROTECTION STEEL

Pattama Piromruen[1], Suwadee Kongparakul[2], Pattarapan Prasassarakich[3*]

[1] Program in Petrochemistry and Polymer Science, Faculty of Science, Chulalongkorn University, Pathumwan, Bangkok, 10330 Thailand
[2] Department of Chemistry, Faculty of Science and Technology, Thammasat University, Klong Luang, Pathum Thani, 12120 Thailand
[3] Department of Chemical Technology, Faculty of Science, Chulalongkorn University, Pathumwan, Bangkok, 10330 Thailand

*E-mail: ppattara@chula.ac.th, Tel. +66 2187517, Fax. +66 2255831

Abstract: Polyaniline/organophilic montmorillonite (PANI/MMT) nanocomposite was synthesized by in situ chemical oxidative polymerization for improving the anticorrosive properties. The polymer clay nanocomposites (PCN) were prepared by varying the MMT content (1, 3, 5 and 7 %wt based on monomer content). The results showed that the maximum monomer conversion was 75.8% at MMT content of 1 %wt. PANI/MMT nanocomposites were characterized by Fourier-transform infrared spectroscopy (FT-IR) and X-ray diffraction (XRD). The surface morphology of nanocomposites was observed by scanning electron microscopy (SEM). Thermal property of the PANI/MMT nanocomposites was examined by thermogravimetric analysis (TGA). The thermal stability of PANI/MMT nanocomposites was enhanced by increasing MMT content.

1. Introduction

Polyaniline (PANI) is one of the widely studied conducting polymers due to its good conductivity, environmental stability and optical properties. One of the important applications of conducting polyaniline is the corrosion protection [1-3]. Polyaniline has both barrier and electrochemical protection effects. The electrochemical protection is caused by the increase in the corrosion potential and formation of a protective passive layer on metal surface due to redox catalytic properties [4-6]. However the increase in barrier effect of polyaniline coating is needed to enhance its efficiency in corrosion protection.

Layered materials such as montmorillonite (MMT) have attracted much interest for the preparation of polymer/clay nanocomposites (PCN). The PCN was found to have enhanced gas barrier, thermal stability, mechanical strength, fire retardant and anticorrosive properties [7-8]. The montmorillonite can enhance the anticorrosive properties of polyaniline coating due to the improved barrier property of polyaniline [9-10].

In this work, polyaniline/montmorillonite (PANI/MMT) nanocomposites were synthesized by in situ chemical oxidative polymerization. The anticorrosive properties of nanocomposite coating were investigated.

2. Materials and Methods

2.1 Materials

Aniline (Loba Chemie), ammonium persulphate (APS, Ajax Finechem), hydrochloric acid (HCl, QRec, 37%), ammonia solution (NH_4OH, QRec, 25%), methanol (QRec) and N-Methylpyrrolidone (NMP, QRec) were used as received. Closite15A (OC15A, natural montmorillonite modified with 30%wt of quaternary ammonium salt with a cation exchange capacity of 125 meq/100 g clay) was supplied by Southern Clay Products.

2.2 Experimental

Polyaniline/montmorillonite nanocomposites were prepared by in situ chemical oxidative polymerization. In this work aniline polymerization was performed in 1M HCl solution by using ammonium persulphate as oxidant/initiator in the presence of clay nanoparticles. The reaction mixture was vigorously stirred at 0° C to 5°C for 6 h. The emeraldine salt nanocomposite precipitate was obtained by filtration followed by washing with 80/20 water/methanol solution and drying in vacuum oven at 50°C for 48 h. The emeraldine salt form of polyaniline in nanocomposite was dedoped with 1M ammonia solution for 4 h followed by washing with 80/20 water/methanol solution and drying in vacuum oven at 50°C for 48 h. The polyaniline was prepared by similar procedure without montmorillonite addition.

2.3 Characterization

Fourier transform infrared (FT-IR) spectra were recorded using a Spectrum GX Perkin Elmer with the sample pressed into a KBR disk. X-ray diffraction (XRD) patterns were recorded using a Bruker AXS Model D8 Discover with Cu Kα radiation at 40 kV and 40 mA. The samples were scanned in the 2θ range from 1º to 35º, with a step time of 0.3 s and a step size of 0.02º. Thermogravimetric analysis (TGA) was performed using a Perkin Elmer, Pyris diamond model. The samples were heated from room temperature to 700ºC at a heating rate of 10ºC/min under 50 mL/min nitrogen flow rate. The morphology of nanocomposites was investigated by scanning electron microscope (SEM), a JEOL JSM-5410.

2.4 Corrosion studies

The electrochemical Tafel slope analysis was used to evaluate the anticorrosive performance of PANI/MMT nanocomposite coating on iron samples. Tafel plots for polyaniline and PANI/MMT coated iron samples were recorded by sweeping the potential from equilibrium potential toward negative and positive potentials against Ag/AgCl reference electrode in 1M H_2SO_4 electrolyte.

3. Results and Discussion

3.1 Synthesis of PANI/MMT : Effect of montmorillonite loading

The effect of montmorillonite loading on monomer conversion is presented in Table 1. The monomer conversion decreased with increasing montmorillonite loading due to the aggregation of montmorillonite particles. The maximum monomer conversion of 75.8% was achieved at montmorillonite content of 1 %wt.

The monomer conversion was determined by gravimetric method and calculated using following equations:

$$\text{Monomer conversion } (\%) = (M_0 - M_1/M_2) \times 100$$

Where; M_0 = Mass of the resulting composite particles
M_1 = Mass of the charged MMT particles
M_2 = Mass of the charged aniline monomer

Table 1: Effect of montmorillonite content on monomer conversion.

Samples	MMT Content (%wt)*	Conversion (%)
PANI	0	78.5
PANI/MMT(1%wt)	1	75.8
PANI/MMT(3%wt)	3	74.0
PANI/MMT(5%wt)	5	73.3
PANI/MMT(7%wt)	7	73.4

*MMT content based on monomer

3.2 Characterization

FT-IR spectra of (a) montmorillonite (MMT), (b) PANI/MMT nanocomposite and (c) polyaniline (PANI) are illustrated in Figure 1. For FT-IR spectrum of polyaniline, the peaks at 1561.82, 1478.49, 1295.32, 1107.48 and 793.01 cm^{-1} are assigned as the benzenic quinonic nitrogen, C=C aromatic, C-N-C stretching of aromatic amine, vibration mode of quinoid ring and C-H out of plane, respectively. FT-IR spectrum of PANI/MMT nanocomposite shows band characteristic of polyaniline as well as of montmorillonite which confirms the presence of both components in the nanocomposite.

Figure 2 (a) and (b) show the TGA and DTG curves of the polyaniline (PANI), montmorillonite (MMT) and PANI/MMT nanocomposites. The initial decomposition temperature of polyaniline (200ºC) is lower than that of montmorillonite (400ºC) and PANI/MMT nanocomposites (240ºC). Moreover, the initial decomposition temperature of PANI/MMT nanocomposites increased with increasing montmorillonite loading. This confirms that the thermal stability of PANI/MMT nanocomposites could be improved and these can be attributed to the MMT nanosheets acting as barriers for the degradation of polyaniline [5].

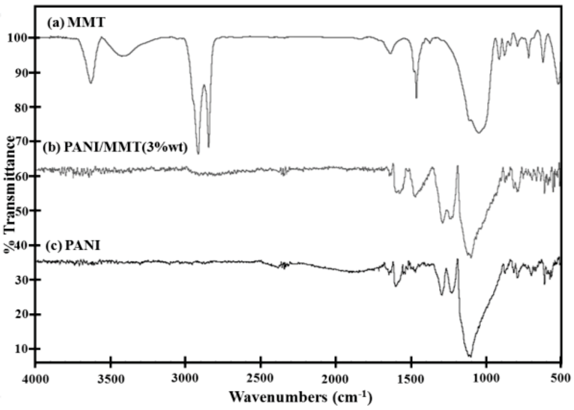

Figure 1. FT-IR spectra of (a) MMT, (b) PANI/MMT (3%wt) and (c) PANI.

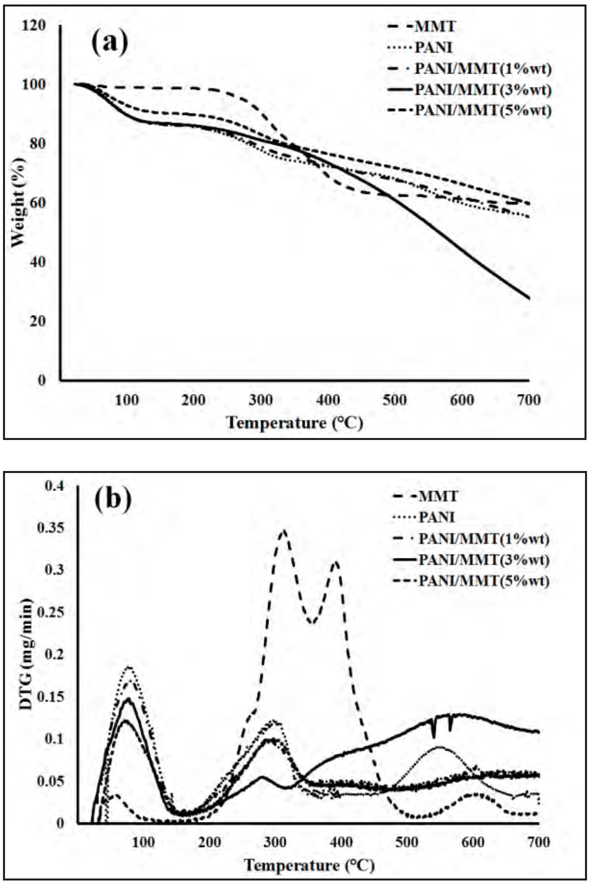

Figure 2. (a) TGA and (b) DTG curves of polyaniline and PANI/MMT nanocomposites.

3.3 Morphology of nanocomposites

From XRD pattern (Figure 3), the characteristic peaks of montmorillonite are observed at 2θ of 2.81 corresponding to the basal space of 3.14 mm. XRD pattern of polyaniline show the sharp peaks at 2θ of 25.45. The characteristic peaks for PANI/MMT at 1 %wt and 3 %wt of montmorillonite loading shifted at 2θ of 3.79 and 2θ of 3.95. The peaks intensity increased with increasing montmorillonite loading. These peaks in the XRD pattern of PANI/MM confirm the presence of polyaniline and montmorillonite in the nanocomposite.

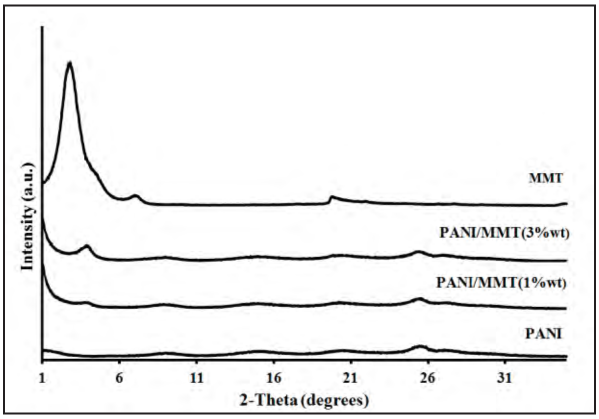

Figure 3. XRD pattern of montmorillonite, polyaniline and PANI/MMT nanocomposites.

SEM micrograph of montmorillonite (Figure 4a) shows the layered structure. The SEM micrograph of polyaniline show of agglomerated spheres (Figure 4b). For the PANI/MMT at 3 %wt MMT (Figure 4c), the montmorillonite layer and the agglomerated spheres of polyaniline dispersed in the nanocomposite structure was observed.

3.4 Corrosion studies of PANI/MMT nanocomposites

The electrochemical Tafel slope analysis was used to evaluate the anticorrosive performance of polyaniline and PANI/MMT coating. The steel samples were coated with 40 and 50 µm thickness of polyaniline and PANI/MMT. Table 2 shows the results of corrosion current (I_{corr}), corrosion potential (E_{corr}) and corrosion rate (C_R) of polyaniline and PANI/MMT at 1 %wt of montmorillonite. The results showed that the anticorrosive properties of PANI/MMT nanocomposite coating at 1 %wt was improved compared with polyaniline coated samples due to the barrier property of MMT in nanocomposites [9].

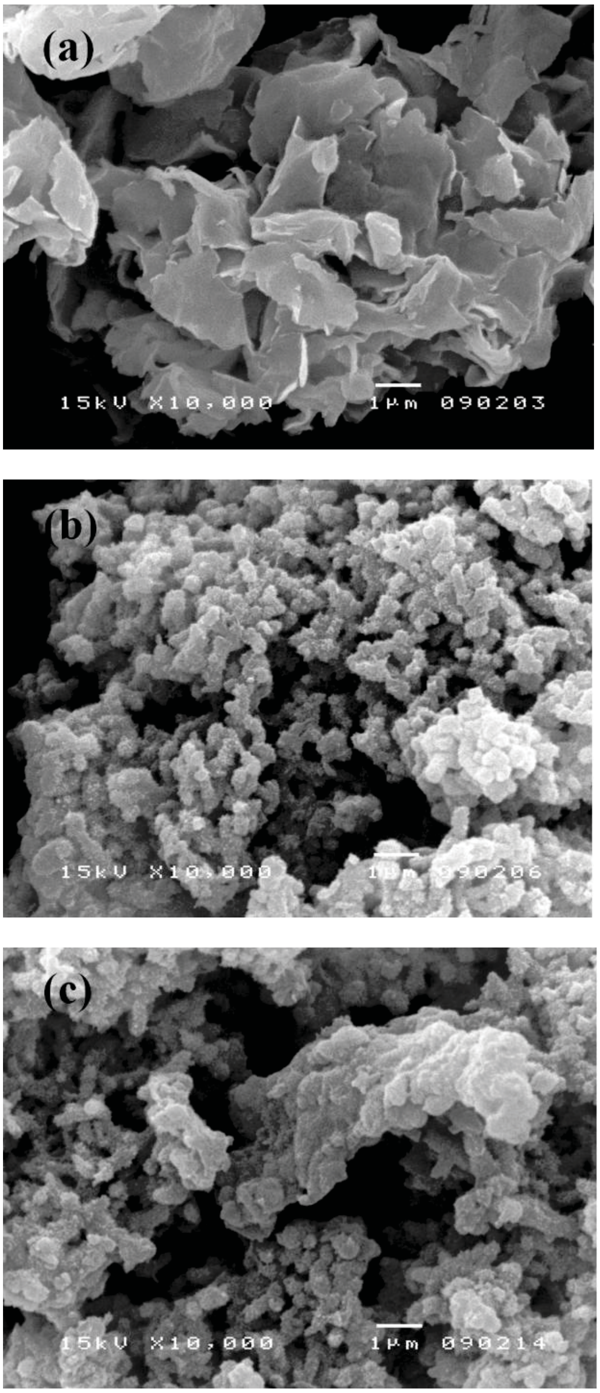

Figure 4. SEM images of (a) MMT, (b) PANI and (c) PANI/MMT (3 %wt).

Table 2. Corrosion current (I_{corr}), corrosion potential (E_{corr}) and corrosion rate (C_R) of polyaniline and PANI/MMT nanocomposites 1 %wt of MMT.

Sample	**Thickness of layer (µm)**	**E_{Corr} (V)**	**I_{Corr} (Acm^{-2})**	**CR (mm/year)**
Steel	-	-0.459	8.769×10^{-4}	10.17
PANI	40	-0.343	1.69×10^{-4}	1.959
PANI	50	-0.326	9.129×10^{-5}	1.058
PANI/MMT(1%wt)	40	-0.307	1.039×10^{-4}	1.204
PANI/MMT(1%wt)	50	-0.361	2.182×10^{-5}	0.253

4. Conclusions

Polyaniline/montmorillonite nanocomposites were prepared by in situ chemical oxidative polymerization. The maximum monomer conversion of 75.8% was achieved at montmorillonite content of 1 %wt. The functionality, surface morphology and phase identification of crystalline material for polyaniline, montmorillonite and PANI/MMT nanocomposites were confirmed by FTIR, SEM and XRD results. The anticorrosive property of coated iron samples with PANI/MMT nanocomposite was improved.

Acknowledgements

The authors are gratefully acknowledged the support from the Thai Government Stimulus Package 2 (TKK2555) under the Project for Establishment of Comprehensive Center for Innovative Food, Health Products and Agriculture and the National Research University Project of CHE and Ratchadaphiseksomphot Endowment Fund (AM1024I).

References

[1] S. Bhadra, D. Khastgir, N.K. Singha and J. H. Lee, *Prog. Polym. Sci*. **34** (2009) 783-810.
[2] P. Liu, *Curr. Opin. Solid. State. Mater. Sci.* **12** (2008) 9-13.
[3] S. Radhakrishnan, C.R. Siju, D. Mahanta, S. Patil and G. Madras, *Electrochim. Acta* **54** (2009) 1249-1254.
[4] J. Fang, K. Xu, L. Zhu, Z. Zhou and H. Tang, *Corros. Sci*. **49** (2007) 4232-4242.
[5] S. Sathiyanarayanan, S. Muthkrishnan and G. Venkatachari, *Electrochim. Acta* **51** (2006) 6313-6319.
[6] C. Saravanan, S. Palaniappan and F. Chandezon, *Mater. Lett*. **62** (2008) 882-885.
[7] B.N. Narayanan, R. Koodathil, T. Gangadharan, Z. Yaakkob, F.K. Saidu and S. Chandralayam, *Mater. Sci. Eng.B*. **168** (2010) 242-244.
[8] Q.Y. Soundararajah, B.S.B. Karunaratne and R.M.G. Rajapakse, *Mater. Chem. Phys*. **113** (2009) 850-855.
[9] A. Olad and A. Rashidzadeh, *Prog. Org. Coat*. **62** (2008) 293-298.
[10] J.M. Yeh and K.C. Chang, *J. Ind. Eng. Chem*. **14** (2008) 275-291.

ACETYLATION OF THE PITHS OF JOINTED GRASS AND KAPOK FOR OIL SPILL CLEAN UP

Thitima Tanosawan[1], Supawan Tantayanon[2, 3]*

[1]Program of Petrochemistry and Polymer Science, Faculty of Science, Chulalongkorn University, Bangkok, 10330 Thailand
[2]Green Chemistry research laboratory, Department of Chemistry, Faculty of Science, Chulalongkorn University, Bangkok, 10330 Thailand
[3]Center of Petroleum and Advanced Material, Chulalongkorn University, Bangkok, 10330 Thailand

* E-Mail: supawan.t@chula.ac.th, Tel. +662 218 7641, Fax. +662 218 7641

Abstract: Acetylated of Jointed Grass piths and kapok was performed used acetic anhydride as the acetylation agents. The extent of acetylation was quantitatively determined using the degree of substitution, which varied volume of acetic anhydride, reaction temperature, reaction time, types and the amounts of catalyst used. The results demonstrated that acetylated of Jointed Grass piths and acetylated kapok with high degree of substitution (DS=2.87 and 2.09) was achieved at 40 and 80 ml of acetic anhydride at 80˚C under 2.0 hours of reaction time using 1.5% *N*-Bromosuccinimide (NBS) in acetic anhydride as a catalyst. The morphology of the fibers was evaluated by SEM. FT-IR and ^{13}C-NMR studies showed the evidence of a successful acetylation. The oil sorption capacity of the Acetylated of Jointed Grass piths and acetylated kapok was 7.46 and 76.72 times higher than the non-acetylated ones. As the results, they can be used as the potential materials for oil spills cleaning up.

1. Introduction

Oil is the most important energy source in the world. During production, transportation, storage and usage of oil there is always a risk of oil spillage [1]. Oil spills into land, river or ocean can cause environmental problems. Synthetic sorbents such as polypropylene (PP) are the most popular oil sorbent materials . A disadvantage of these materials is that they are non-degradable [2]. Organic natural products such as Jointed Grass and kapok are of our interest to use as oil sorbents. The hydrophobic properties of these materials could be modified by replacing their cell wall hydroxyl groups with acetyl using acetic anhydride. The acetylated products are biodegradable, in addition, they show a higher oil absorptivity and lower water adsorption when compared to the unmodified natural products.

2. Materials and Methods

2.1 Material and reagents

Jointed Grass and kapok used in this study were weed and agricultural product of Thailand. Before use, Jointed Grass were cut into piths part, all dust and lumps in raw kapok fiber had been removed and then dried in an oven at 65˚C for 22 h. The reagents used for synthesis were purchased from Merck and Carlo Erba**.**

2.2 Instruments and Equipments

The FT-IR spectra were recorded on a Nicolet 6700 spectrophotometer. The solid-state ^{13}C-NMR spectra were recorded using a Varian INOVA spectrometer at 500 MHz with magic-angle spinning and cross-polarisation (CP-MAS). About 250 mg of sample was packed into zirconia rotors for MAS at approximately 500 rpm. The CP contact time was 3 s, acquisition time 0.02, and total acquisition time 1.5 h [3]. SEM micrographs were examined using JEOL JSM-5410LV scanning electron microscope. Before SEM observation, all samples were fixed on aluminum stubs and coated with gold.

2.3 Acetylation reaction

The dried sample (1 g) was mixed with acetic anhydride and catalysts in round bottom flask and refluxed at 70-100˚C for 1-3 h with stirring. The volume of acetic anhydride was varied from 20-120 ml and the concentrations of catalysts were 0.5-1.0% sulfuric acid (H_2SO_4) and 1.0–3.0% NBS. When the reaction was completed, the liquid phase was removed and the acetylated products were washed with ethanol and acetone and dried in an oven at 65 ˚C for 22 h.

2.4 Degree of substitution (DS)

The degree of substitution of the acetylated products was obtained from the FT-IR spectra. The ratio of absorbance values of C=O stretching (1750 cm^{-1}) : O-H stretching (3400 cm^{-1}) was calculated for cellulose acetylated products [4].

2.5 Oil absorptivity

The oil absorptivity of the acetylated products was determining by mixing 0.5 g of sample with 20 ml of machine oil and allowing the sample to absorb oil for 15 min at room temperature. The remained oil was drained out for 30 s and the acetylated products was weighed.

3. Results and Discussion

3.1 Characterization of the piths of jointed grass and kapok fiber

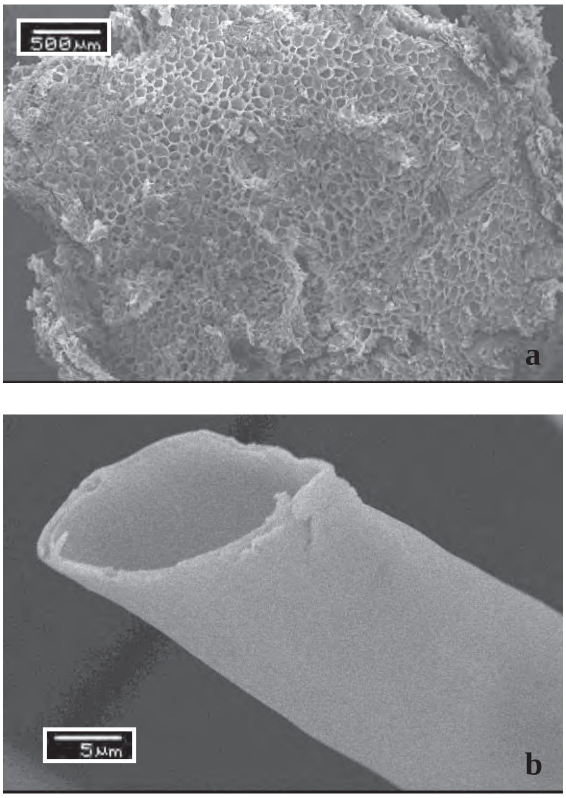

Figure 1. SEM images of the Jointed Grass piths (a), and kapok fiber (b).

The natural products, Jointed Grass piths and kapok fiber, were charactized using SEM.

Fig. 1 shows the SEM images of Jointed Grass piths and kapok fiber. The Jointed Grass piths exhibit porous structures like sponge as shown in Fig. 1 (a). Kapok fiber exhibit hollow tubular structure (or lumen) as shown in Fig. 1 (b), with an average external diameter of 16.5±2.4 μm, average internal diameter of 14.5±2.4 μm and average length of 25±5 mm. This indicates that 77% of the fiber volume is lumen [5,6]. The large porous structures of Jointed grass piths and pore volume in the kapok assembly are suitable for oil sorption.

3.2 Effect of reaction conditions

Table 1: Acetylation conditions for modification of Joints grass piths and kapok.

Catalyst	Volume of Acetic anhydride (ml)	Acetylated of Jointed Grass piths		Acetylated kapok	
		DS	OA[a]	DS	OA.
1.5% NBS	20	2.13	6.23	1.26	49.74
1.5% NBS	40	2.87	7.46	1.88	64.78
1.5% NBS	60	-	-	1.90	69.09
1.5% NBS	80	2.38	7.22	2.09	76.72
1.5% NBS	100	2.98	7.62	1.91	69.69
1.5% NBS	120	-	-	2.03	73.20
no cat.	40,80[b]	1.22	4.48	1.05	48.01
0.5% H_2SO_4	40,80	-	-	no	45.25
1.0% H_2SO_4	40,80	no[c]	1.15	-	-
1.0% NBS	40,80	2.20	6.45	1.83	62.21
2.0% NBS	40,80	1.91	5.95	1.87	62.74
3.0% NBS	40,80	1.74	5.40	1.86	62.32
1.5% NBS	40,80[d]	1.43	4.53	1.45	53.50
1.5% NBS	40,80[e]	1.53	4.81	1.59	56.04
1.5% NBS	40,80[g]	1.54	5.10	1.42	53.01
1.5% NBS	40,80[h]	1.59	5.32	1.69	57.09
1.5% NBS	40,80[i]	1.81	5.70	1.72	57.80
1.5% NBS	40,80[j]	1.44	4.65	1.54	55.02

reaction conditions : 80 °C for 2 h

[a] Oil absorptivity

[b] 40 and 80 ml for acetylation reaction of Jointed Grass piths and kapok.

[c] can not calculated

[d] reaction temperature 70 °C

[e] reaction temperature 90 °C

[g] reaction temperature 100 °C

[h] reaction time 1 h

[i] reaction time 2.5 h

[j] reaction time 3 h

The effects of the reaction conditions such as volume of acetic anhydride, type of catalysts, amounts of catalyst used, reaction temperature and reaction time on the DS value of the acetylated of Joints Grass piths and acetylated kapok were investigated, results shown in Table 1.

The volume of acetic anhydride was varied in the acetylation reaction of Jointed Grass piths and kapok from 20 to 120 ml. Under the condition of 1.5 % NBS, 80 °C and reaction time of 2 h, the obtained DS seemed to increase with increasing volume of acetic anhydride and reached the maximum at 100 and 80 ml for acetylated of Jointed Grass piths and acetylated kapok, respectively. Further increasing volume of acetic anhydride seemed to the fluctuated the DS. However, acetylation reaction of Jointed Grass piths at 40 ml of acetic anhydride obtained DS was not much different from the maximum value. Thus, volume of acetic anhydride for acetylated of Jointed Grass piths of 40 ml could be considered sufficient for acetylation reaction and high DS could be obtained.

In comparison of DS values among catalysts used, it is apparent that NBS is a suitable for acetylation reaction of Jointed Grass piths and kapok. The DS increased as the amount of catalyst increased. 1.5% of NBS in the reaction system at 80 °C for 2 h resulted in an increase in DS from 1.22 and 1.05 to 2.87 and 2.09, for acetylated of Jointed Grass piths and acetylated kapok, respectively, which was approximately two times higher than obtained under the same conditions without catalyst. When the amounts of NBS catalyst was higher than 1.5%, the DS decreased to 1.91 and 1.87 at 2.0% NBS and 1.74 and 1.86 at 3.0% NBS, for acetylated of Jointed Grass piths and acetylated kapok. This is probably limited rate of NBS diffusion into sample matrix [7].

The results also showed that DS increased with the reaction temperature and reaction time. At 80°C, the DS increased from 1.43 and 1.45 to 2.87 and 2.09, for acetylated of Jointed Grass piths and acetylated kapok, respectively. When temperature is higher than 80°C, the DS value was not increased anymore, indicating that the acetylation was more rapid at lower temperature [8]. Furthermore, at 2 h, the DS increased from 1.59 and 1.69 to 2.87 and 2.09, for acetylated of Jointed Grass piths and acetylated kapok, respectively.

3.3 FT-IR spectra

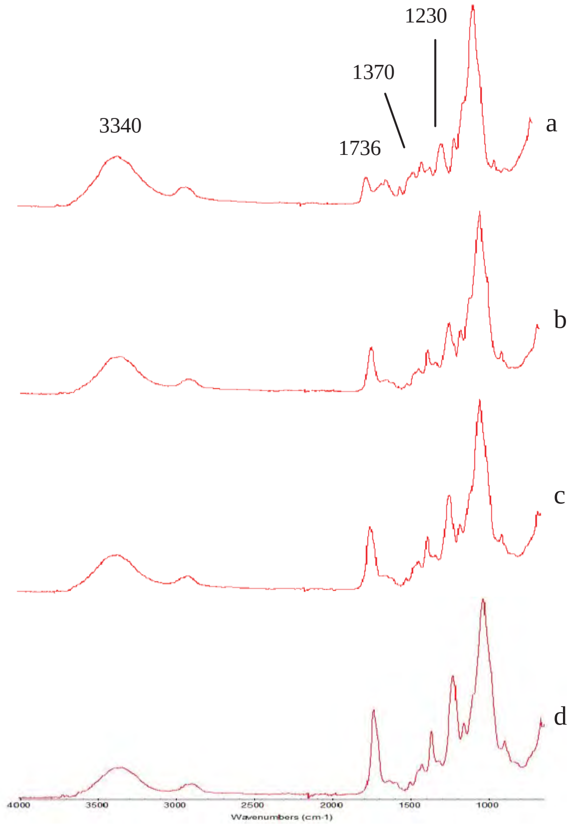

Figure 2. FT-IR spectra of unmodified Jointed Grass piths (spectrum a) and acetylated of Jointed Grass piths, DS=1.22 (spectrum b), DS=1.74 (spectrum c), DS=2.98 (spectrum d)

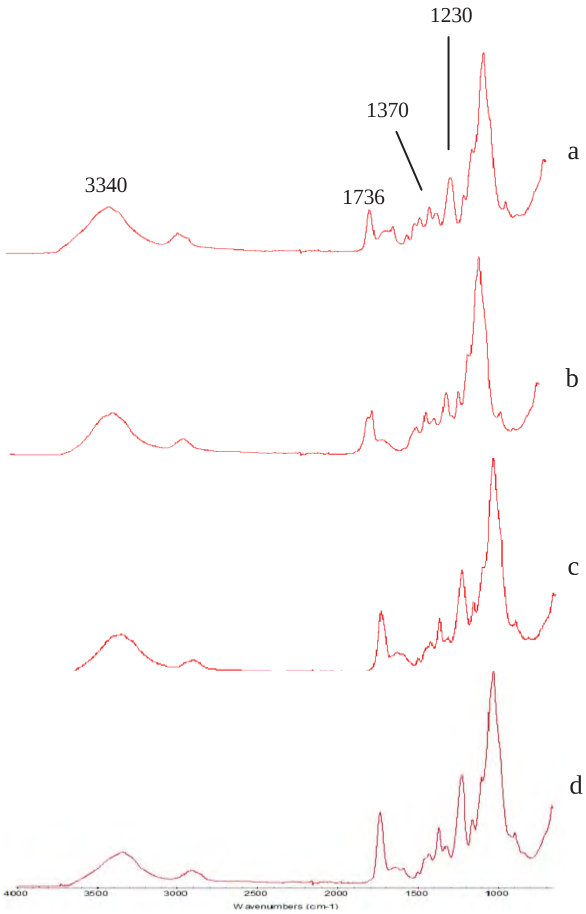

Figure 3. FT-IR spectra of unmodified kapok (spectrum a) and acetylated kapok, DS=1.05 (spectrum b), DS=1.54 (spectrum c), DS=2.09 (spectrum d)

FT-IR spectra of unmodified and acetylated products were show in Fig. 2 and 3**.** The spectra showed the differences between bands before and after acetylation**.** The main differences of acetylated in comparison to unmodified spectra are related to enhanced of three important ester bands at 1745, 1367 and 1242 cm^{-1}, these were attributed to absorption by carbonyl bonds (C=O ester), C-H stretching (-C-CH_3), and C-O stretching in esters (-O-C-CH_3), respectively. In contrast, the intensity of the hydroxyl stretching band (O-H) at 3430 cm^{-1} was decreased, indicating that the hydrogen of hydroxyl group was substituted by acetyl groups, confirming the formation of ester bonds [3,9]**.** The results indicated that Jointed Grass piths and kapok were successfully acetylated under conditions used in this study.

3.4 ^{13}C-NMR spectra

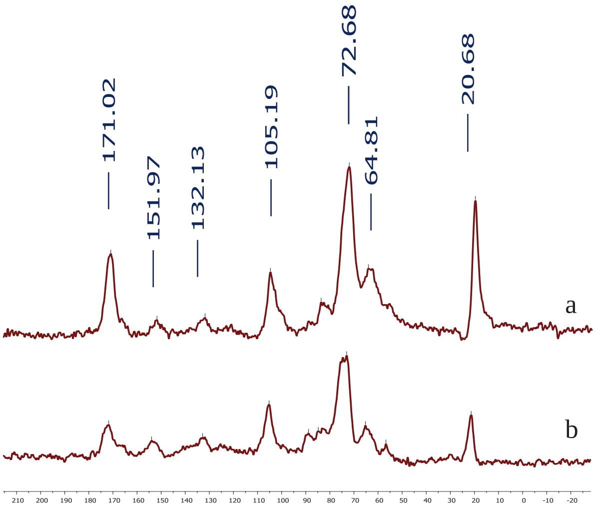

Figure 4. ^{13}C-NMR spectra of acetylated of Jointed Grass piths (spectrum a) and acetylated kapok (spectrum b).

^{13}C-NMR spectra of acetylated of Jointed Grass piths and acetylated kapok were show in Fig. 4. The spectrum showed the methyl band of the acetyl group (OCH_3) at 20.6 ppm and the carbonyl of the acetyl groups at 171.0 ppm, indicating the presence of acetyl groups and apparent of acetylation in products. Another region from 60 to 110 ppm is carbohydrate, namely C-1 (105.1 ppm), C-4 (88.8 ppm, crystal cellulose, and 84.7 ppm, amorphous cellulose or less ordered surface cellulose molecules), C-2, C-3 (74.0 ppm) and C-5 (72.6 ppm), and C-6 of cellulose and C-5 of xylan (64.8 ppm) [3,7,8].

3.5 Oil absorptivity

Acetylated of Jointed Grass piths and acetylated kapok were immediately absorbed machine oil. As shown in Table 1, oil absorptivity of acetylated of Jointed Grass piths and acetylated kapok were 7.62 and 76.72 g oil/g sorbent, increased with DS. The oil absorptivity of the acetylated kapok were higher than acetylated of Jointed Grass piths and polypropylene fiber (~10 g oil/g sorbent) [10]. Acetylated of both products can be reuse several times by squeezing operation.

4. Conclusions

The results obtained from this study indicated that changing hydrophobic properties of Jointed Grass piths and kapok could alter the oil absorptivity of these natural products. When the hydroxyl groups were replaced with acetyl, the DS values increased, suggesting that acetylated of Jointed Grass piths and acetylated kapok could be used as sorbents for cleanup oil spill. Both materials are inexpensive and biodegradible, in addition, they have quick uptake and high capacity for oil absorption.

Acknowledgements

This work was supported by Program in Petrochemistry and Polymer Science, Faculty of Science, Chulalongkorn University.

References

[1] R. S. Rengasamy, D. Das and P. Karan, *J. of Hazardous Materials.* **186 (**2011**)** 526-532.
[2] H. M. Chol and R.M. Cloud, *Environ. Sci.Technol.* 26 **(**1992**)** 772-776.
[3] X. F. Sun, R. C. Sun and J. X. Sun, *J.Materials sci.* **38 (**2003) 3915-3923.
[4] D. A. Cerqueria, G.R. Filho and C.S. Meireles, *Carbohydrate Polymers* **69 (**2007**)** 579-582.
[5] T.-T. Lim and X. Huang, *Chemosphere.* **66** (2007) 955–963.
[6] X. Huang and T.-T. Lim, *Desalination* **190 (**2006) 295-307**.**
[7] R. C. Sun, X. F. Sun, J. X. Sun and Q.K. Zhu, *C.R.Chimie*. **7** (2004**)** 125-134**.**
[8] C**.** Yan, Z**.** Jun, H**.** Jiasong, L**.** Huiquan and Z**.** Yi, *Chin.* ***J.*** *Chem***.** **18 (**2010**)** 515-522**.**
[9] S.M. Luz, J. Del Tio, G.J.M. Rocha, A.R. Goncalves and A.P. Del'Arco Jr., *Composites: Part A* **39** (2008**)** 1362-1369.
[10] H. M. Choi, *J. Environ. Sci. Health* A. **31** (1996) 1441-1457.
[11] E. Khan, W. VIrojnagud and T. Ratpukdi, *Chemosphere.* **57** (2004) 681-689.
[12] A. R. Bertoti, S.Luporini and M.C.A. Esperidiao, *Carbohydrate Polymers***.** **77** (2009) 20-24.
[13] T. M. Venas and A. Rinnan,. *Chemometrics and Intelligent Laboratory system.* **92** (2008) 125-130.
[14] C. I. K. Diop, H.L. Li, B.J. Xie and J. Shi, *Food Chemistry.* **126** (2011) 1662-1669.
[15] M. A. Abdullah, L.Chiang and M. Nadeem, *Chemical Engineering Journal*. **146** (2009) 370-376.
[16] T. R. Annunciado, T.H.D. Syndenstricker and S.C Amino, *Marine Pollution Bulletin.* **50** (2005) 1340-1346.
[17] M. Saito, N. Ishii, S. Ogura, S. Maemura and H. Suzuki, *Spill Science&Technology Bulletin.* **8** (2003) 475-482.
[18] W. Hu, S. Chen, Q. Xu, and H. Wang, *Carbohydrate Polymers.* **83** (2011) 1575-1581.

FABRICATION OF IBUPROFEN/MENTHOL-LOADED POLY(VINYL ACETATE) ULTRAFINE FIBERS AS A DRUG DELIVERY SYSTEM BY ELECTROSPINNING TECHNIQUE

Tharakorn Jamvitheelerd, Thammasit Vongsetskul*

Department of Chemistry, Faculty of Science, Mahidol University, Rama VI Road, Ratchathewi, Bangkok, 10400

* Author for correspondence; E-Mail: thammasit.von@mahidol.ac.th, Tel. +66 2201-5110, Fax. +66 2354-7151

Abstract: Electrospun ibuprofen (5 %w/v) /menthol (4 %w/v)-loaded poly(vinyl acetate) (PVAc) (MW ~ 1.4 x 10^5 g/mol) ultrafine fibers with diameters from 300 to 800 nm were successfully fabricated from 8% to 12% w/v PVAc in acetone:ethanol (6:4) solvent mixtures. The effects of PVAc concentrations and the applied voltages (8, 10, 12, 14, and 16 kV) on their diameters and morphology were investigated. Scanning electron micrographs revealed that the suitable condition for fabricating fibers was 8 %w/v PVAc and 14 kV. The toxicity of prepared fibers and behavior of drug release will be investigated further. These fibers are expected to be useful in pain relief in the future.

1. Introduction

Electrospinning is a drawing process of polymeric solution that uses an electric field to draw a polymer one-dimensional nanostructured material such as rod, tube, hollow tube and fiber [1]. This technique is simple, convenient to control the fiber dimension, and capable of producing ultrafine fibers in a continuous way. Ultrafine fiber possesses the special characteristics such as very high surface to volume ratio [2] that could be applied as a controlled release system.

Poly(vinyl acetate) (PVAc) is a homopolymer synthesized from vinyl acetate monomer via a free-radical polymerization technique [3]. There are several reports on applying PVAc as a media for controlled release system [4-7].

Ibuprofen is a non-steroidal anti-inflammatory drug (NSAID), frequently used in the treatment of osteoarthritis, rheumatoid arthritis and inflammation. It also has analgesic properties [8,9], Despite a wide variety of pharmacological properties, it has a short half-life time [10]. Therefore, the suitable drug control release system could help keeping the drug level in blood plasma constantly which could improve the treatment.

Menthol is an organic compound made synthetically or obtained from peppermint or other mint oils. It is a white waxy and crystalline substance, at room temperature and could melts slightly when temperature increases. The main form of menthol occurring in nature is (−)-menthol, which is assigned the (1R,2S,5R) configuration [11].

Menthol's analgesic properties are mediated through a selective activation of κ-opioid receptors [12]. It also blocks voltage-sensitive sodium channels, reducing neural activity that may stimulate muscles [11], and enhances the efficacy of ibuprofen in topical applications via vasodilation, which reduces skin barrier function [13,14,15].

Therefore, this study aimed to fabricate the (ibuprofen/menthol)-loaded PVAc ultrafine fibers. The effect of applied electrical voltages and PVAc concentrations on the prepared fibers was also studied to obtain the best conditions for preparing the ultrafine fibers.

2. Materials and Methods

2.1 Materials

PVAc with MW of 1.4 x 10^5 g/mol, ibuprofen, and menthol were purchased from Sigma-Aldrich (USA) and used as received. Absolute ethanol and acetone were obtained from RCI Labscan (Thailand) and used without further purification.

2.2 Preparation of electrospinning solution

The appropriate amount of PVAc, ibuprofen, and menthol were dissolved in 30 ml of 2:3 v/v (ethanol: acetone) mixed solvent to obtain the PVAc, ibuprofen, and menthol concentrations of 6-12% w/v, 4% w/v, and 5% w/v, respectively. The mixtures were stirred for 3 hours to obtain the homogeneous solutions.

2.3 Fabrication and characterization of PVAc ultrafine fibers

In this process, each of the spinning solutions was loaded into a glass syringe. The electrospinning set up used in this work is shown in Figure 1. A Gamma High Voltage Research ORMOND BEACH power supply (DES50PN-20w/QAM) was used to charge the spinning solution by connecting the emitting electrode of positive polarity to the nozzle and the roll collector, used as a collection device. The applied positive electrical potentials were varied between 8 and 16 kV. Fiber collection distance (TCD) and time were 10 cm and 4 h, respectively. The flow rate was 5 ml/h. The diameter of needle was 0.9 mm. The speed of fiber collector was 60 rpm. Morphology of the prepared ultrafine fibers was observed by scanning electron microscope (SEM, TM-1000, Hitachi, Japan).

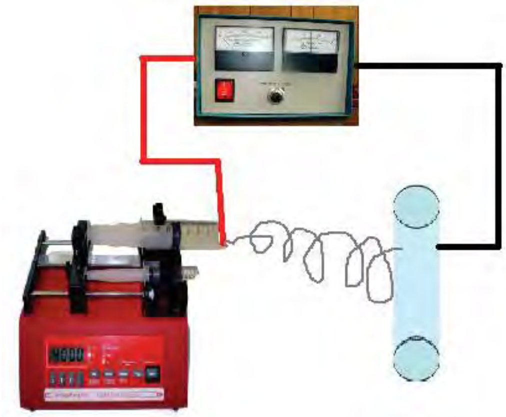

Figure 1. Electrospinning set-up used in this work

The fibers were dried on an aluminium foil in a dust-free environment before being stuck on the sample holder with a double-coated carbon conductive tape. An average diameter of the electrospun fiber mats was measured directly from SEM using a J software (n = 100).

3. Results and discussion

3.1 Effect of PVAc concentration

Table 1: The relation between of the average fiber diameter and PVAc concentration with the applied boltage of 15kV

[PVAc] (w/v%)	Average fiber diameter (nm)	Standard deviation
6	318.0	125.4
8	350.6	110.9
10	424.9	128.4
12	977.6	358.5

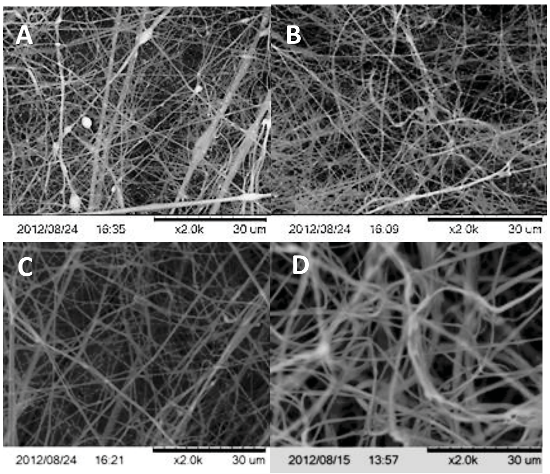

Figure 2 SEM images of (ibuprofen/menthol)-loaded PVAc fiber with the PVAc concentrations of (A) 6% wt, (B) 8% wt, (C) 10% wt, and (D) 12% wt with the applied voltage of 15 kV

The relation between the average fiber diameter and the PVAc concentration was shown in Table 1. The morphology of fabricated ultrafine fibers was shown in Figure 2. To illustrate the effect of PVAc concentration on the fiber morphology clearly, the applied voltage was fix at 15 kV. SEM images shown in figure 2 suggest that 8% PVAc was the most appropriate polymer concentration for spinning ultrafine fibers (no bead). It was found that if the PVAc concentration was too low, the charged jet would be broken when the electrostatic field was applied which resulted in bead formation. If the PVAc concentration was too high, the fiber diameter would increase.

Effect of polymer concentration could be explained by the conductivity results as shown in Table 2.

Table 2: The relation between the PVAc concentration and the conductivity of the spinning mixtures with 4% w/v ibuprofen and 5% w/v menthol

[PVAc] (w/v%)	Conductivity (uS)	Temp (°C)
6	563	23.8
8	515	23.4
10	478	23.6
12	450	23.4

The electrical conductivity of the spinning mixtures decreased when increasing in PVAc concentration, and the fiber diameter increased with increasing in the polymer concentration because the higher the solution conductivity, the stronger the more strong stretching forces associated with electrospinning [16].

3.2 Effect of applied electrical potentials

Table 3: Average fiber diameters of (ibuprofen/ menthol)-loaded PVAc fiber obtained from 8%wt/v PVAc spinning mixture

Applied voltage (kV)	Average fiber diameter (nm)	Standard deviation
8	282.9	65.7
10	298.9	109.1
12	432.2	130.5
14	271.4	77.3
16	310.6	310.6

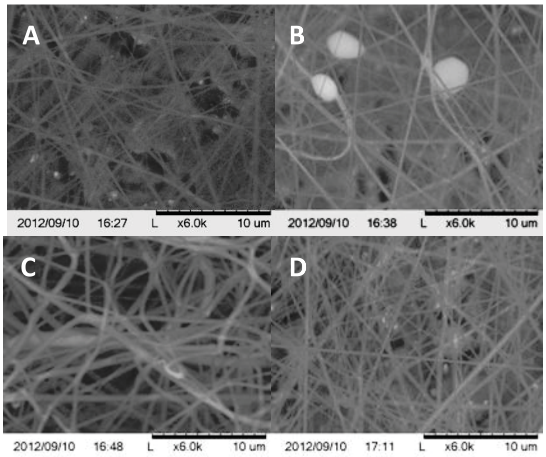

Figure 3 SEM images of (ibuprofen/menthol)-loaded PVAc fibers with the applied voltages of (A) 8kV, (B) 10kV, (C) 12kV, and (D) 14kV and the PVAc concentration of 8%w/v

When the applied potentials increased initially, the fiber diameters initially increased. It was because, with the high electrical voltages, the time of the polymer strand for travelling from the nozzle to the fiber collector was so short that the Coulombic repulsion could not stretch the charged jet fully. However, the fiber diameter suddenly dropped when the applied voltage was 14 kV. The fiber diameter increased once again when the applied voltage was 16 kV which resulted from the reason mentioned earlier. Thus, it can be concluded that the optimum applied voltage for fabricating PVAc fibers was 14 kV.

4. Conclusions

Electrospun ibuprofen (5 %w/v) /menthol (4 %w/v)-loaded PVAc ultrafine fibers with diameters from 300 to 800 nm were successfully fabricated. Optimum conditions were 8%w/v PVAc and 14 kV. These ultrafine fibers would be potentially used in biomedical applications such as patches for healing the muscle pain in the future.

References

[1] A. S. Nain, J. C. Wong, C. Amon, and M. Sitti, *Appl. Phys. Lett.* **89** (2006) 18105-18107.
[2] D. G. Yu, L. M. Zhu, K. White, and C. Branford-White, *Health* **1** (2009) 67-75.
[3] J. Y. Park, I. H. Lee, and G. N. Bea, *Ind. Eng.Chem. Res.* **14** (2008) 707-713.
[4] W. G. Schmidt, W. Mehnert, and H. Fromming, *Eur. J. Pharm. Biopharm.* **42** (1996) 348-350.
[5] F. Zhang and J. W. McGinity, *Drug Dev. Ind. Pharm.* **26** (2000) 931-942.
[6] A. Ali and S. N. Sharma, *India. Drugs* **33** (1996) 30-35.
[7] T. Niwa, H. Takeuchi, T. Hino, A. Itoh, Y. Kawashima, and K. Kiuchi, *Pharmacol. Res.* **11** (1994) 478-484.
[8] G. A. G. Novoa, J. Heinamaki, S. Mirza, O. Antikainen, A. I. Colarte, A. S. Paz, and J. Yliruusi, *Eur. J. Pharm. Biopharm.* **59** (2005) 343-350.
[9] M. Moreno, F. Villena, C. P. Sotomayor, A. M. Edwards, M. A. Munoz, P. Garidel and M. Suwalsky, *Biochim Biophys Acta*. **1808** (2011) 2656-2664.
[10] C. D. Brabander, C. Vervaet, L. V. Bortel and J. P. Remon, *int. J. Pharm*. **271** (2004) 77-84.
[11] N. Galeottia., L. D. C. Mannellia, G. Mazzantib, A. Bartolinia, and C. Ghelardini, *Neurosci. Lett* **322** (2002) 145–148.
[12] R. Eccles, *J. Pharm. Pharmacol.* **46** (1994) 618–630.
[13] K. R. Braina, D. M. Greena, P. J. Dykesb, R. Marksb, and T. S. Bola, *Skin Pharmacol. Physiol.* **19** (2006) 17-21.
[14] G. Haeseler, D. Maue, J. Grosskreutz, J. Bufler, B. Nentwig, S. Piepenbrock, R. Dengler and M. Leuwer, *Eur. J. Anaesthesiol.* **19** (2002) 571–579.
[15] C. S. Yong, Y. K. Oh, S. H. Jung, J. D. Rhee, C. K. Kim and H. G. Choi, *Eur J Pharm Sci*. **23** (2004) 347-353.
[16] Q. Z. Yu, MM. Shi, M. Deng, M. Wang and H. Z. Chen, *Mater. Sci. Eng., B.* **150** (2008) 70-76.

PROPERTIES OF NATURAL RUBBER AND STYRENE BUTADIENE RUBBER FILLED WITH CARBON NANOTUBE

Preeyanuch Junkong[1], Pattana Kueseng[1], Nittaya Rattanasom[1,2*]

[1]Department of Chemistry, Faculty of Science, Mahidol University, Bangkok, 10400 Thailand
[2]Centre for Rubber Research and Technology, Mahidol University, Salaya, Nakhon Pathom, 73170, Thailand

*E-mail: nittaya.rat@mahidol.ac.th

Abstract: In this work, various amounts of carbon nanotube (CNT) are incorporated into natural rubber (NR) and styrene butadiene rubber (SBR) matrices. The mechanical properties and, cut growth and abrasion behaviours of CNT-filled NR and SBR vulcanizates are studied. The results reveal that hardness, modulus, tear strength and compression set of both vulcanizates increase with increasing CNT content, while their elongation at break, abrasion loss of both vulcanizates decrease. Additionally, it is found that the increase of CNT content gives the reduction in tensile and relative cut tensile strength of NR while those of SBR increase. Besides, SEM images of both vulcanizates show better defined ridges on the abraded surface when CNT content is increased corresponding to the improvement in abrasion resistance. Moreover, the rupture of both vulcanizates occurs by a simple lateral cut growth at all CNT contents.

1. Introduction

Carbon nanotube (CNT) is one of the nanofillers that has been attracted by many researchers since the discovery by Iijima in 1991 [1]. CNT has high aspect ratio, high mechanical strength, and good electrical and thermal conductivity [2,3]. Compared with the other conventional fillers such as carbon black (CB) and silica, satisfied properties such as tensile strength, modulus and electrical property of the materials can be achieved by adding only small amount of CNT [4,5]. Recently, several researchers have reported the effects of CNT content on properties of elastomeric matrices. Zhou et al. reported that styrene butadiene rubber (SBR) composites filled with 20 phr of acid-treated CNT give nearly three times of tensile strength and twice of tear strength higher than those of the gum SBR [6]. Boonmahittisud and Chuayjuljit found that 80/20 NR/SBR blend containing 0.2 phr of CNT has similar tensile strength to that having 5 phr of CB. This is because CNT has large surface area for interacting with rubber matrix [4]. Although, various properties of several rubbers filled with CNT have been studied, their reports about abrasion and cut growth behaviours are found to be lacking. It is well-known that NR is crystallizable at high strain, while this phenomenon does not occur in SBR. Therefore, cut and normal tensile strength, and tear strength of gum NR are often higher than SBR [7]. However, abrasion resistance of gum NR is normally lower than gum SBR [8]. Hamed et al. found that the fracture in gum SBR, gum NR and CB-filled SBR takes place by simple lateral cut growth, but CB-filled NR exhibits auxiliary cracking prior to catastrophic fracture [7]. Since cut growth behaviour of NR and SBR filled with CB is considerably different, it is interesting to investigate their behaviour when containing CNT. In this research, various amounts of MWCNT are incorporated into NR and SBR. Then, morphology, mechanical properties and, abrasion and cut growth behaviors of NR and SBR vulcanizates are studied.

2. Materials and methods

2.1 Materials

NR and SBR used in this work were STR 5L grade and 1502 grade, respectively. Carbon nanotubes was MWCNT (type 7000) having average diameter of 9.5 nm and average length of 1.5 μm. Ethanol and a non-ionic surfactant (Nonidet P40) were used to prepare MWCNT suspension. Other compounding ingredients composed of zinc oxide, stearic acid, wax, N-(1,3-dimethyl)-N'-phenyl-p-phenylenediamine (6-PPD), N-tert-butyl-1,2-benzothiazole sulfenamide (TBBS), and sulfur were standard industrial grade.

2.2 Preparation of NR and SBR vulcanizates filled with MWCNT

The compound formulations of NR and SBR composites are shown in Table 1. NR or SBR was masticated in an open two-roll mill. Then, the MWCNT suspension was slowly mixed into the rubber at 80 °C. Thereafter, the other ingredients, except the curatives which were sulphur and accelerators, were added into the premixed MWCNT/rubber compounds. After the two-roll mill cooled down, the curatives were incorporated into the premixed compounds. Finally, 10 end-roll passes were made always in the same direction before sheeting off. Later, the rubber compounds were used to prepare the vulcanized sheets and test pieces by curing under pressure of 15 MPa at 150°C and using compression molding according to their respective t_{c95} as determined from Moving Die Rheometer (MDR).

Table 1 Compound formulations of NR and SBR filled with different amounts of MWCNT

Chemicals	Amounts (phr)	
	MWCNT/NR	MWCNT/SBR
NR	100	-
SBR	-	100
Stearic acid	2	2
ZnO	4	4
6-PPD	2	2
WAX	2	2
TBBS	1.6	1.6
S	1.4	1.4
MWCNT	0,2,4,6,8	0,2,4,6,8

2.3 Testing of rubber vulcanizates

Hardness of the vulcanizates was carried out following ASTM D2240, using a Wallace Shore A durometer. Tear and tensile properties were measured using a universal tester (Instron 5566 series) according to ASTM D624 and D412 respectively. The dumbbell and crescent specimens for tensile and tear tests were punched from the rubber vulcanized sheets along the milling direction. Cut tensile strength was determined by using edge-cut dumbbell specimens having a notch of 0.67 mm on one edge and perpendicular to the specimen length. The relative cut tensile strength was calculated by using equation (1) and the cracking pattern of edge-cut specimens after testing was examined using CCD camera.

$$\text{Relative cut tensile strength} = \frac{CTS}{TS} \qquad (1)$$

where CTS and TS are cut tensile strength and normal tensile strength, respectively. Static compression set was performed on standard test specimen according to ASTM D395. Din Abrader was used to determine the abrasion loss of the vulcanizates, conforming to ASTM D5963 and the abraded surfaces were observed by using scanning electron microscope (SEM, s-2500 Hitachi).

3. Results and discussion

Hardness and tensile properties of NR and SBR filled with various CNT loadings are shown in Figures 1-4. It can be observed that hardness of both vulcanizates increases with increasing CNT content corresponding to the increase in 300% modulus and reduction in elongation at break. This is because the presence of CNT reduces the mobility and flexibility of the rubber chains. Tensile strength of SBR vulcanizates depicted in figure 4 gradually increases with increasing CNT loading, while tensile strength of NR decreases when 4 phr CNT is added. This may be resulted from the formation of some CNT agglomerates which could act as failure points in NR. Also, it is possible that the extent of strain-induced crystallization is less when CNT content is increased. However, the tensile strength of NR is still higher than that of SBR at a specific loading. The relative cut tensile strength results for both rubbers are shown in figure 5. It is found that SBR shows slight increase in relative cut tensile strength with increasing CNT content, while that of NR decreases. At a given CNT content, relative cut tensile strength of SBR is higher than that of NR. These results are different from

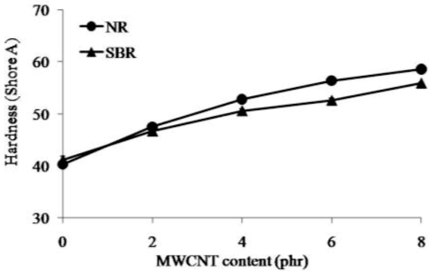

Figure 1. Hardness of NR and SBR filled with various CNT contents.

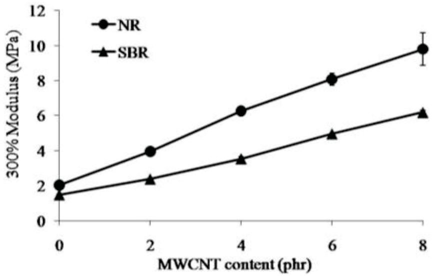

Figure 2. 300% Modulus of NR and SBR filled with various CNT contents.

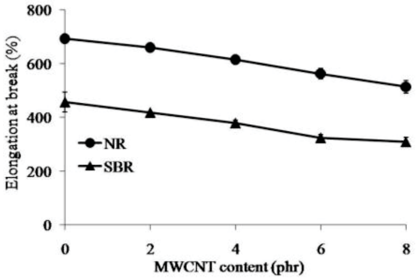

Figure 3. Elongation at break of NR and SBR filled with various CNT contents.

those observed in NR filled with reinforcing CB. Hamed et al. reported that normal and cut tensile strengths of CB-filled SBR were markedly lower when compared with those of CB-filled NR [7,9]. Moreover, the latter exhibited auxillary cracking prior to catastrophic fracture, while this behavior is not observed in all CNT-filled NR as presented in figure 6 (arrows indicate initial cut tip). Only a simple lateral cut growth occurs in all samples. This may be due to poor interaction between CNT and NR matrix.

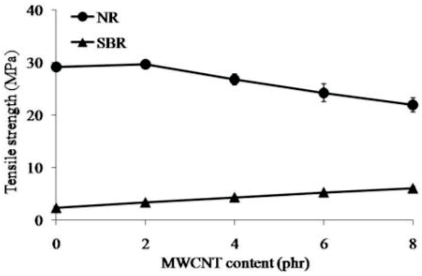

Figure 4. Tensile strength of NR and SBR filled with various CNT contents.

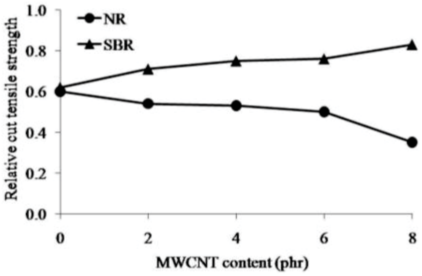

Figure 5. Relative cut tensile strength of NR and SBR filled with various CNT contents.

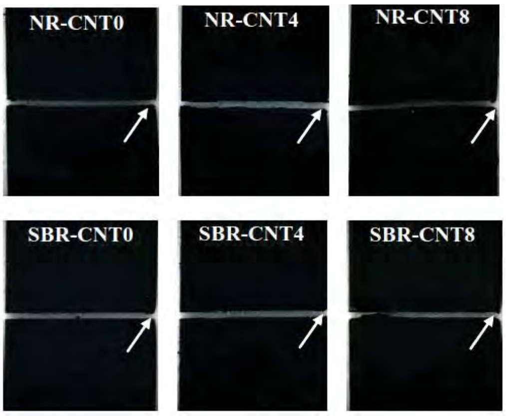

Figure 6. The cracking pattern of NR and SBR vulcanizates filled with various CNT contents.

Tear strength of CNT-filled NR and SBR vulcanizates increases with increasing CNT content as shown in figure 7. It is thought that the extent of stress concentration at crack tip of crescent specimen is less than that in edge-cut dumbbell specimen. Therefore, CNT can alter the tear path along its length, which leads to higher resistance to tear propagation [10].

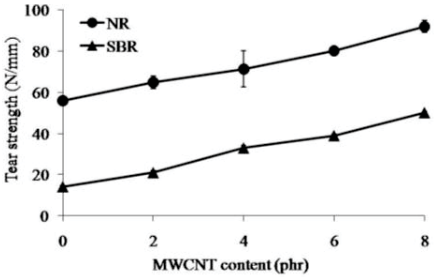

Figure 7. Tear strength of NR and SBR filled with various CNT contents

Figure 8 shows an increase in compression set of both NR and SBR vulcanizates when the amount of CNT is increased. This is because the addition of CNT results in the restriction of the flexibility of the rubber chains. At a specific CNT loading, NR gives higher compression set than SBR. The reason for the obtained result is not yet clarified.

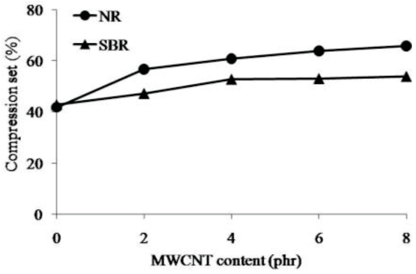

Figure 8. Compression set of NR and SBR filled with various CNT contents

Figures 9 and 10 respectively illustrate the abrasion loss and SEM images of abraded surface for both NR and SBR vulcanizates. Abrasion loss of both CNT-filled rubbers decreases with increasing CNT content. Additionally, the ridges on abraded surfaces of both unfilled NR and SBR are wide, but the ridges become narrower when the amount of CNT is increased. The narrower spacing of the ridges coincides with the improved abrasion resistance.

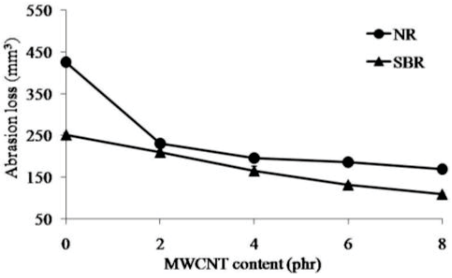

Figure 9. Abrasion loss of NR and SBR vulcanizates filled with CNT contents

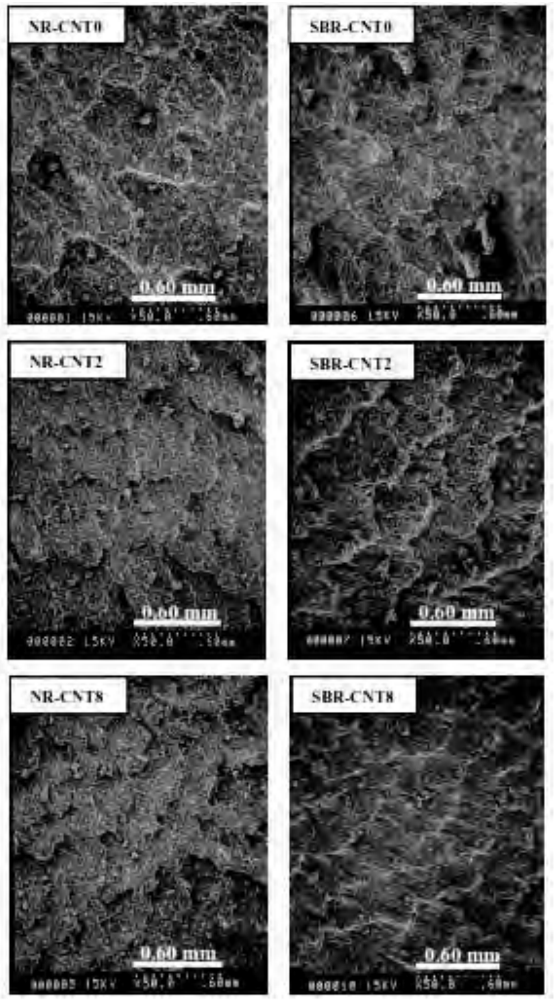

Figure 10. SEM images of abraded surface of NR and SBR vulcanizates filled with various CNT contents.

4. Conclusion

The addition of CNT into NR and SBR leads to the improvement of hardness and modulus, but their elongation at break and compression set resistance decrease. The slight increase in tensile strength, relative cut tensile strength and tear strength of SBR can be observed, while those of NR, except for tear strength, decrease with increasing the amount of CNT. In addition, the cracking pattern of edge-cut specimens of gum and, CNT-filled NR and SBR is not different. All vulcanizates show a simple lateral crack path at all CNT contents. NR and SBR vulcanizates show better defined ridges on the abraded surface when CNT content is increased corresponding to the improvement in their abrasion resistance.

5. Acknowledgement

The Research and Development Centre for Thai Rubber Industry (RDCTRI) and Mahidol University are gratefully acknowledged for supporting the instruments used in this research.

6. References

[1] S. Iijima, *Nature* **354** (1991) 56-58.
[2] E.T. Thostenson, Z Ren, T.W. Chou, *Compos.Sci.Technol.* **61** (2001) 1899-1912.
[3] J.N. Coleman, U. Khan, Y.K. Gun'ko, *Adv. Mater.* **18** (2006) 689-706.
[4] A. Boonmahitthisud, S. Chuayjuljit, *Mater. Sci. Forum* **654-656** (2012) 2783-2786.
[5] L. Bokobza, *Compos. Interfaces* **15** (2008) 9-17.
[6] X.W. Zhou, Y.F. Zhu, *Mater. Res. Bull.* **42** (2007) 456-464.
[7] G.R. Hamed, B.H. Park, *Rubber Chem. Technol.* **72** (1999) 946-959.
[8] C.K. Hong, H. Kim, *J. Mater. Sci.* **42** (2007) 8391-8399.
[9] G.R. Hamed, N. Rattanasom, *Rubber Chem. Technol.***75** (2002) 935-942.
[10] N. Tebsan, S.Wirasate, *Wear* **269** (2010) 394-404.

EFFECTS OF IR REFLECTIVE PIGMENTS ON THERMAL PERFORMANCE OF ACRYLIC POLYURETHANE COATING PAINT

Sasithorn Boonphao[1*], Sasithorn Kitchareon[1], Boonnak Sukhummek[1*]

[1] Department of Chemistry / Faculty of Science, King Mongkut's University of Technology Thonburi, Bangkok, Thailand

[*] Author for correspondence; E-Mail: boonnak.suk@kmutt.ac.th, Tel. +66 24 709557, Fax. +66 24 708843

Abstract: This work aimed to develop acrylic polyurethane coating paint in order to increase thermal performance by replacing standard pigments containing in conventional colored acrylic paint with infrared reflective pigments. Controllable factors that affected the abilities of solar reflectance and thermal performance in reducing surface temperature of the acrylic paint film were type of pigments and the volume concentration. Four different color paint shades of black, blue, green oxide and yellow oxide were studied. The result revealed that increasing in solar reflectance resulted in decreasing in the surface temperature of the paint film. Incorporation of the IR reflective pigments for a full shade system showed an increase in solar reflectance and also a decrease in surface temperature of paint film for all color shades, except only the blue shade which revealed higher surface temperature than that of the conventional one. As compared to the standard conventional pigments, incorporation of the black IR reflective pigment exhibited the highest reduction of the paint film surface temperature up to 17 °C. While incorporation of the IR pigments by volume concentrations showed a thermal reduction of the yellow shade only. It could lower the thermal reduction up to 19 °C compared to that of the standard conventional one.

1. Introduction

Due to the progression growth of Thai industry nowadays, the requirement of industrial paint rapidly increases. Industrial paints have been widely used in various industries, involving automotive parts, construction materials, industrial machines, metal products, for some specific objectives. The development of industrial paint aims to increase both an adhesion and the stability of the paint film against severe weather, scratching and chemical corrosion. Microorganism from the surrounding environment deposited on painted surfaces can lead to degradation, blistering and spilling of the coating, especially in the condition of high humidity or condensation along with raised temperatures [1-2]. Such bio-deterioration can cause a high economic loss [3] and a reduction in thermal performance of building. Thus, in a tropical climate region accompanying with a situation of global warming at the present, the necessity of heat reflective cool colored paint has arisen.

Paints have four major components: binder, solvents, additives and pigment. Besides, providing nice color to the films, pigment is a key factor that controls gloss, hiding power, strength and permeability. It normally absorbs and reflects different parts of the sun's wavelength spectrum due to its chemistry and mineralogy [4]. Generally, organic pigments have limited service life and more susceptible to the photochemical degradation, causing by sun light, as compared with inorganic pigments [5]. With the right pigment used, some researchers found that raising the solar reflectance of a roof from 0.1-0.2 to 0.6 can reduce the amount of energy needed to cool a building by more than 20% [6].

Scope of this work is to compare the ability of thermal reduction between standard (conventional) formulated acrylic polyurethane coating paint and new formulated ones both in part shade and full shade systems. An infrared reflective pigment (IR pigment) was chosen to replace over a standard pigment, traditionally containing in conventional paint, in order to increase thermal reduction and heat reflection of paint film on metal sheet. Thermal performance with various quantities of IR reflective pigments was also investigated.

2. Materials and Methods

2.1 Materials

The cool paints of dark colors studied included four color shades: black, blue, yellow oxide and green oxide. The standard pigments used were Black-S, Blue-S, G/Ox-S and Y/Ox-S, whereas IR pigments involving were Black-IR1, Blue-IR3, Blue-IR-4, G/Ox-IR1 and Y/Ox-IR1, respectively. All pigments and chemical reagents were used as received.

2.2 Paint preparation

To compare properties and ability in thermal performance of pigment types, two sets of equivalent acrylic polyurethane coating paints: one formulated with standard pigments and another one incorporated with infrared reflective pigments (IR pigments). Four color shades of conventional paints were formulated with standard pigments of Black-S, Blue-S, G/Ox-S and Y/Ox-S, whereas another set were adjusted the quantity of IR pigments of Black-IR1, Blue-IR3, G/Ox-IR1 and Y/Ox-IR1, respectively, as equivalent to a standard formulation by weight concentration for each color shade.

To study the effect of volume concentration of pigments, only three color shades were examined: black, blue and yellow oxide. Coating paints were adjusted the quantity of IR pigments of Black-IR1, Blue-IR3, and G/Ox-IR1, as equivalent to a standard formulation by volume concentration for each color shade. They were coded as Black-IR1/1, Blue-IR3/1 and Y/Ox-IR1/1. For IR pigment of G/OX-IR1, the amount of IR pigment adjusted as equivalent to the standard formulation by weight and by volume were equal, therefore it would not include in this study.

To study ability in thermal performance of IR color paints, prepared from the previous study, used to formulate new color shades, three new color shades: smoke grey, light blue and light green were prepared. The amount of IR formulated paints obtained in the previous study used in preparation the new color shades showed in Table 1. After that the abilities in thermal performance of the new three color shades were compared with coating paints formulated with standard pigments of smoke grey, light blue and light green of SG-S, LB-S and LG-S, respectively.

Table 1: Formulations of new three color shades: smoke grey, light blue and light green prepared from IR color paints.

Amount (%)	**Smoke gray**	**Light blue**	**Light green**
Top guard white	68.5	20.1	1.5
Y/OX-IR1	4.3	0.3	7.0
Blue-IR3	10.9	78.0	11.3
Black-IR1	16.3	1.6	40.1
G/Ox-IR1	0.0	0.0	40.1
Total	100	100	100

2.3 Paint characterisation

Acrylic polyurethane coating was performed on tin plate: unpainted specimen (blank) and painted specimen. To study the effect of formulation adjusted by weight and by volume, the painted specimens were applied on tin plates by using a spray gun with dry thickness of 120 μm as called part shade system. For full shade system, bottom rust-protective layer was first coated on the tin plate with a dry thickness of 100 μm. After drying, the liquid paint prepared was applied on top of the rust-protective layer with a dry thickness of 120 μm. The coated specimens were left to dry at ambient temperature for 7 days. All coating paints were analysed by the following parameters.

Surface temperature: Surface of the coated specimens was exposed to a source of radiation emitted by a 200 W infrared radiation lamp, placed 20 cm above the specimens. The surface temperatures of the specimens were measured with type T thermocouples which placed under the specimens. The device was made of wood with 4 sample slots. The blank plate, tin plate coated with standard coating paint and tin plate coated with IR coating paint were analysed at the same time in order to compare temperature profile of the coatings. The device was place in a room with fixed internal temperature at 27 °C to assure that the heat absorbed by the coated specimens was exclusively by only irradiation. Reading data were recorded every 5 minutes for 1-2 hours or until the measured temperature was constant. The temperature at a saturated state was recorded for each tested specimen.

UV-VIS-NIR reflectance: The solar reflectance of painted and unpainted specimens was measured using a UV-VIS-NIR spectrophotometer, Shimadzu, model UV 3100. Barium sulphate ($BaSO_4$) was used as a reference material giving a standard reflectance. The results were shown as plots of % reflectance versus wavelength in the range of 300 to 2500 nm.

3. Results and Discussion

3.1 Effect of formulations adjusted by weight and by volume concentration on thermal performance

Temperature profiles of specimens with various pigments are shown in Figure 1. The saturated temperatures and temperature changes for the specimens incorporating with various pigments are summarized in Table 2.

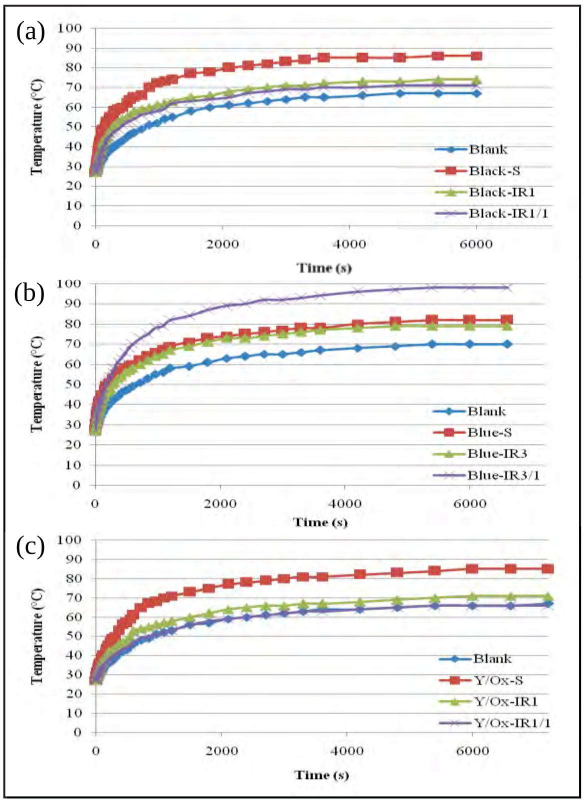

Figure 1. Temperature profile of unpainted specimen and those painted with standard paint and IR paints for a part shade system, a) Black color b) Blue color and c) Yellow oxide color.

Compared to the standard formulation with standard pigments, IR coating paints for all color shades revealed lower surface temperature, especially the yellow oxide color. It could lower down the surface temperature from 85 to 71 °C, approx. 19% reduction as compared to that of standard yellow color. Moreover, adjusting pigment quantity by volume concentration showed an increase in thermal performance for both black and yellow oxide shades. The Y/Ox-IR paint exhibited the most effective IR pigment. It reduced the surface temperature of tin plate up to 26% and 7% as compared with the standard pigment and that adjusted by weight concentration. On the contrary, adjusting pigment quantity by volume concentration decrease thermal performance of blue coating paints as seen in Figure 1 and Table 2. This finding was in accordance with the reflectance result shown in Table 3. The values of reflectance in the UV (300-400 nm), visible (400-700 nm) and NIR (720-2500 nm) regions were calculated from the integrated area of the reflectance curve within each wavelength region. The reflectance results clearly showed that the specimen formulated with Blue-IR3/1 exhibited lower reflectance than those of Black-IR1/1 and Y/Ox-IR1/1, especially, in IR region showing the lowest reflection. It is worth to note that because of high specific gravity of IR pigments, the weight of IR pigments used were high when being formulated by volume concentration. This brought to have good hiding properties.

Table 2: Surface temperatures of unpainted and painted specimens for a part shade system.

Color	Specimen	Surface temperature (°C)	Temp. change (°C)
Black	Blank	67	-
	Black-S	86	-
	Black-IR1	84	-2
	Black-IR1/1	81	-5
Blue	Blank	70	-
	Blue-S	82	-
	Blue-IR3	79	-4
	Blue-IR3/1	98	+16
Yellow	Blank	67	-
	Y/Ox-S	85	-
	Y/Ox-IR1	71	-14
	Y/Ox-IR1/1	66	-19

Table 3: Reflectance of specimens coated with paints formulated by volume concentration adjustment.

Specimen	% Reflectance			% Total solar reflectance
	UV	VIS	NIR	
Black-IR1/1	0.20	3.07	29.63	32.9
Blue-IR3/1	0.26	9.04	14.52	23.82
Y/OX-IR1/1	0.23	20.20	40.81	61.24

3.2 Effect of full shade system on thermal performance

The bottom rust-protective layer in full shade system affected thermal performance of coating paints. The color paints in the full shade system, significantly increased the surface temperature of convention coating paints, especially the black and blue color. In turn, the Black-IR1 and Blue-IR3 pigments revealed high efficiency in thermal reduction as seen in Table 4. In full shade system, Black-IR1 was the most effective in reducing surface temperature, showing a reduction of 17% as compared with the standard pigment.

Table 4: Surface temperatures of unpainted and painted specimens for a full shade system.

Color	Specimen	Surface temperature (°C)	Temp. change (°C)
Black	Blank	67	-
	Black-S	99	-
	Black-IR1	82	-17
Blue	Blank	69	-
	Blue-S	93	-
	Blue-IR3	92	-1
Green	Blank	68	-
	G/Ox-S	83	-
	G/Ox-IR1	80	-3
Yellow	Blank	66	-
	Y/Ox-S	84	-
	Y/Ox-IR1	76	-8

3.3 Effect of IR coating paints on thermal performance of the new color paints

The new color paints of smoke grey, light blue and light green were performed in a full shade system. The temperature profiles of the specimens coated with conventional paint formulated with standard pigments and those of coating paints prepared by using the IR coating paints were shown in Figure 2. The surface temperatures and temperature changes for uncoated specimens, specimens coated with standard paints and IR coating paints are summarized in Table 5.

Table 5: Surface temperatures of unpainted and painted specimens for new color shade.

Color	Specimen	Surface temperature (°C)	Temp. change (°C)
Smoke grey	Blank	65	-
	SG-S	85	-
	SG-IR	72	-13
Light blue	Blank	68	-
	LB-S	73	-
	LB-IR	89	+16
Light green	Blank	64	-
	LG-S	91	-
	LG-IR	90	-1

<u>Remark</u> SG represents smoke grey, LB represents light blue, LG represents light green.

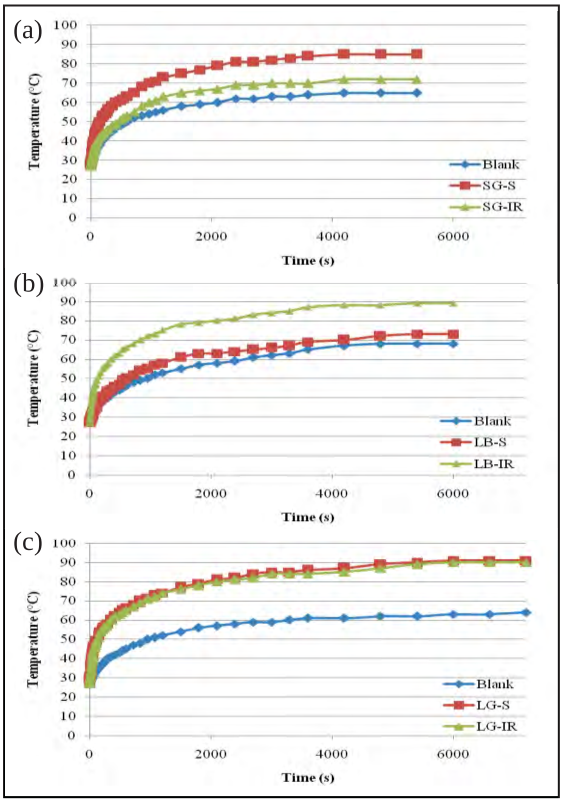

Figure 2. Temperature profile of unpainted specimen and those painted with standard paint and IR paints for a full shade system, a) Smoke grey b) Light blue and c) Light green.

Table 6: Reflectance of specimens coated with new color shade paints.

Specimen	**% Reflectance**			**% Total solar reflectance**
	UV	VIS	NIR	
SG-IR	0.37	28.24	34.12	62.73
LB-IR	0.29	15.21	17.21	32.71
LG-IR	0.20	5.85	17.40	23.45

The surface temperature of smoke grey color revealed the highest efficiency in thermal reduction. It could reduce the surface temperature down to 72 °C, corresponding to 15% reduction as compared to that of conventional paint. As expected, light blue formulated with IR paint showed higher surface temperature as compared with that formulated with standard pigment. The reason was the smoke grey color composed mainly of the Black-IR1 paint, the pigment which had the highest efficiency in thermal reduction as found in the previous study. While, the light blue color formulated with the most quantity of Blue-IR3, which exhibited the lowest thermal reduction efficiency as seen in Table 1. These results were corresponding to the reflectance spectra obtained from coated specimens shown in Table 6 and Figure 3. Only the smoke grey color showed high reflective value over all solar radiation wavelengths, especially, in the VIS and NIR regions.

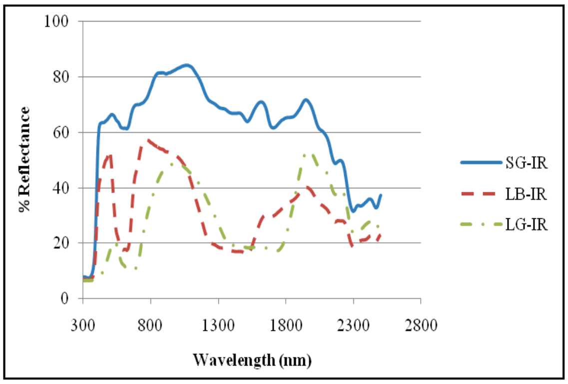

Figure 3. Reflectance spectra of specimens coated with smoke grey, light blue and light green formulated with IR coating paints.

4. Conclusions

In this work, the replacement of conventional pigments in commercial paint formulations by IR pigments of four color shades: black, blue, yellow oxide and green oxide was studied. The IR pigments which gave high reflection in solar radiation range, especially in NIR region, revealed high thermal reduction efficiency such as the Black-IR1 and Y/Ox-IR1. For new color shade formulated from IR coating paints, coating paint formulated with high weight ratio of the efficient IR pigment revealed lower surface temperature. The bottom rust-protective layer in a full shade system had some effects on thermal ability of coating paint. It dropped some thermal reduction abilities of IR coating paints.

Acknowledgements

The authors would like to thank TOA Paint (Thailand) Co., Ltd. for supplying all ingredients, operation support and some characterization instruments.

References

[1] C.C. Gaylarde, L.H.G. Morton, K. Loh and M.A. Shirakawa, *International Biodeterioration & Biodegradation* **65** (2011) 1189–1198.

[2] M.Y.L. Chew and I.P. Ping, *Staining of Facades*, Singpapore: World Scientific Publishing, Singapore (2003).

[3] H. Winter, *Microbial Biodeterioration*, Academic Press, Oxford, UK (1981).

[4] K.L. Uemoto, N.M.N. Sato and V.M. John, *Energy and Building* **42** (2010) 17–22.

[5] N.S. Allen, M.Edgea, A. Ortega. G. Sandovala, C.M. Liauwa and J. Verrana, *Polym.Degrad. Stabil.* **85** (2004) 927–946.

[6] H. Akbari, R. Levinson, W. Miller and P. Berdahl, *Cool colored roofs to save energy and improve air quality*, Passive and Low Energy Cooling for the Built Environment Conf. Proc., Santorini, Greece, (2005), pp. 238–242.

NOVEL PHOSPHORUS-NITROGEN CONTAINING FLAME RETARDANT: SYNTHESIS AND THERMAL DEGRADATION

Katahut Thanomwong[1*], Boonchoat Paosawatyanyong[2, 3], Worawan Bhanthumnavin[4]

[1] Program of Petrochemistry and Polymer Science, Faculty of Science, Chulalongkorn University, Bangkok 10330, Thailand
[2]Department of Physics, Faculty of Science, Chulalongkorn University, Bangkok 10330, Thailand
[3]ThEP Center, Commission on higher Education, Bangkok 10400, Thailand
[4]Department of Chemistry, Faculty of Science, Chulalongkorn University, Bangkok 10330, Thailand

[*] Author for correspondence; E-mail: Katahut.T@Student.chula.ac.th, Tel. +66 22187626

Abstract: In this research, 3-methylbut-3-enylphenyl 4-aminophenyl phosphoramidate (MPAP) was synthesized. MPAP was prepared by a reaction of phenyl dichlorophosphate with 3-methyl-3-butenol and *p*-phenylene diamine in tetrahydrofuran at 0◦C. The solution was filtered followed by evaporation to remove solvent. After a standard workup and column chromatography purification, the product was obtained as an orange solid powder in 30% yield. Fourier transform infrared (FT-IR) and ^{1}H nuclear magnetic resonance (^{1}H NMR) spectroscopy were used to confirm the functional groups and the chemical structure of MPAP. Thermal degradation of MPAP was investigated by thermo gravimetric analysis (TGA). A 2-step thermal degradation behavior was demonstrated. The final char weight of MPAP in air is higher than that in N_2. Morphological studies of the residual chars after burning were performed using scanning electron microscopy (SEM). The surface of char has a continuous and coherent structure that acts as heat resistance.

1. Introduction

Today, polymeric materials have replaced traditional materials such as metals and wood in many applications. However, one of the main problems of polymer its flammability [1]. Phosphorus flame retardant has been widely used in the flame retardation of polymers. Compared to other flame retardants, phosphorus flame retardant has several advantages including high efficiency, halogen-free, and small amount of smoke. Apart from phosphorus-based flame retardant, P-N containing flame retardant can offer a high efficiency because of synergistic effect between phosphorus and nitrogen [2-10]. For example, melamine salt of pentaerythritol phosphate (MPP) is a very effective intumescent flame retardant (IFR) that combines acid source, carbonization agent, and blowing agent that show the best synergism between the three components [10].

In this research, three components were combined into one molecule. 3-methylbut-3-enylphenyl 4-aminophenyl phosphoramidate (MPAP) was synthesized. The structure of MPAP is characterized by FT-IR, ^{1}HNMR. Thermal degradation behavior was investigated by thermo gravimetric analysis (TGA). The residues after combustion were investigated by scanning electronic microscopy (SEM).

2. Experimental

2.1 Materials

Phenyl dichlorophosphate (PDCP) was purchased from TCI. 3-Methyl-3-butenol was purchased from Aldrich. *p*-Phenylene diamine and triethylamine (TEA) were purchased from Merck. Tetrahydrofuran (THF) was dried by sodium metal which benzophenone as indicator. The mixture is refluxed under nitrogen atmosphere until the blue color. Ethyl acetate and *n*-hexanes were distilled before use.

2.2 Synthesis of 3-methylbut-3-enylphenyl 4-aminophenyl phosphoramidate (MPAP)

Phenyl dichlorophosphate (PDCP) (0.1 mol) was dissolved in dry tetrahydrofuran (THF) (120 mL) in a 500 mL three-necked round bottom flask equipped with mechanical stirred under N_2 atmosphere. Triethylamine (TEA) (0.2 mol) was added to the mixture and the mixture was cooled down in an ice bath and stirred for 20 minutes. The solution of 3-methyl-3-butenol (0.1 mol) in dry THF (40 mL) was added dropwise to the mixture and then, the mixture was stirred for 40 minutes. Next, the mixture was added dropwise to a solution of *p*-phenylene diamine (0.1 mol) in dry THF (200 mL) in a 1000 mL three-necked round bottom flask and the temperature was kept at 0°C for 4 hours. The reaction mixture was allowed to warm to room temperature and stirred overnight. After the reaction was complete, triethylamine hydrochloride salt was filtered off by suction filtration. The filtrate was performed by rotary evaporator to remove THF. Finally, the crude mixture was purified by using a flash silica gel chromatography column, and eluted with a mixture of *n*-hexanes and ethyl acetate.

2.3 Measurements and characterization

^{1}H NMR spectra were recorded on Mercury Varian 400 MHz nuclear magnetic resonance (NMR) spectrometer at 400 MHz with CDCl3 as the solvent. IR spectroscopy was recorded on attenuated total reflection Fourier transform infrared spectroscopy (ATR-FTIR) spectrometry in the 4000-600 cm^{-1} range. Thermogravimetric analysis was performed using thermo gravimetric analyzer (TGA) at a scanning rate of 10 ◦C/ min from 25 to 600 ◦C under N_2 and air.

Morphological studies of the residual chars after burning were performed using scanning electron microscopy (SEM).

3. Results and Discussion

3.1 Synthesis and characterization of MPAP

3-Methylbut-3-enylphenyl 4-aminophenyl phosphoramidate (MPAP) was synthesized by a reaction of phenyl dichlorophosphate (PDCP), 3-methyl-3-butenol and *p*-phenylene diamine in tetrahydrofuran (THF) at 0°C. After workup and column chromatography purification, the product was obtained as an orange solid in 30% yield. The synthetic route was shown in Scheme 1.

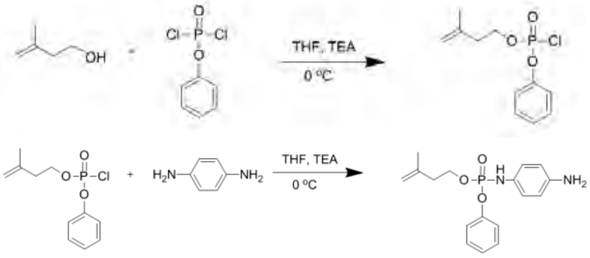

Scheme 1. The Synthesis of 3-methylbut-3-enylphenyl 4-aminophenyl phosphoramidate (MPAP)

The ^1H NMR spectrum of MPAP is shown in Fig. 1. The peaks of H: δ7.40-6.60 ppm (9H, aromatic protons), δ6.15 ppm (1H, -NH-), δ4.75 ppm (trans) and 4.65 ppm (cis)(1H, $CH_2=C(CH_3)$-), δ4.3-4.1 ppm (2H, $-CH_2-O$), δ3.30 ppm (2H, $-NH_2$), δ2.35 ppm (2H, $-CH_2-$) and δ 1.67 ppm (3H, CH_3-). Fig.2 shows FTIR spectra of MPAP. The absorption peak between 3500 and 3100 cm^{-1} can be ascribed to the stretching vibrations of N–H bond, meanwhile the bending vibration of N–H appears at 1590 cm^{-1}. The absorption peak of C=C stretching of vinyl was observed at 1629 $cm^{-1}$and the absorption peak of C=C of aromatic were observed at 1515 and 1487 cm^{-1}. The P=O and P-O stretching vibrations appeared at 1211 and 927 cm^{-1}, respectively. All the analysis above confirms the successful synthesis of MPAP.

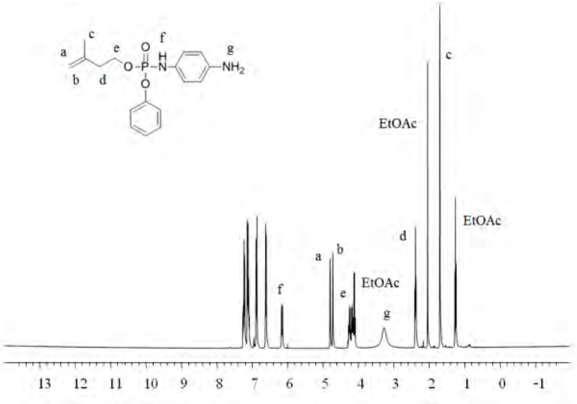

Fig. 1. ^1H NMR spectrum of MPAP.

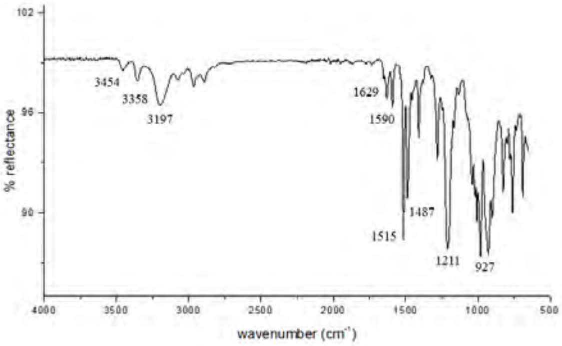

Fig. 2. FTIR spectra of MPAP.

3.2 Thermal degradation

The thermal degradation behavior of MPAP has a 2-step major degradation in both air and N_2 that were demonstrated in Fig. 3. The first step occurred at 200 ◦C that may be due to the decomposition of *p*-phenylenediamine which resulted in the release of NH_3. The second step is the major degradation step because it has high weight loss that may be due to the decomposition of aromatic structure and formation of poly (phosphoric acid) char between 250 and 500◦C [11]. Considering thermal degradation behavior in air and N_2, it can be seen that weight loss in air and N_2 occurred at the same time but the second step of degradation in air occurred before N_2. It may be caused by the existence of oxygen in air that leads to oxidation of MPAP [12]. Although the thermal stability of MPAP in air is lower than N_2, the final char weight in air (45%) is much more than N_2 (38%). This demonstrates oxygen can promote the char formation.

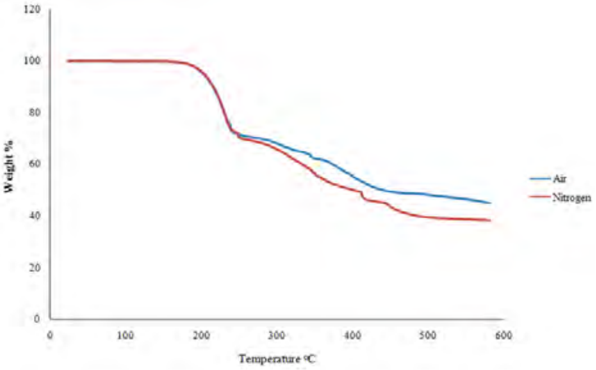

Fig. 3. TGA curves of MPAP in air and N_2.

3.3 Char formation

The swelling ability of IFR contributes to the enhancement of flame retardant because it generates effective char layer that acts as heat barrier between heat source and materials [9, 10]. Fig. 4 shows the morphology of MPAP before and after burning. MPAP was degraded and expanded to a certain extent. The micro scale of morphology was investigated by SEM and shown in Fig. 5. The char formation resulted in many bubbles on the char layer surface that show the swelling of the non-flammable gas emitted by the blowing agent during combustion. Furthermore, the char layer was continuous and coherent structure that can effectively prevent the heat and mass transfer between the heat source and materials.

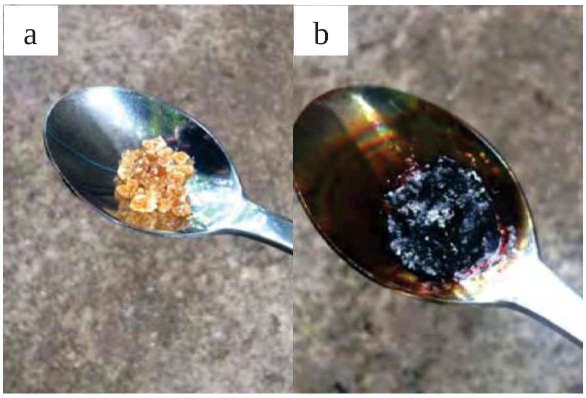

Fig.4. Morphologies of MPAP (a) before and (b) after burning.

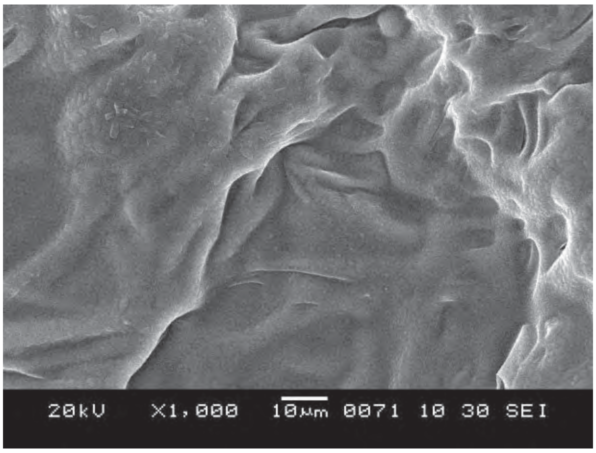

Fig. 5. SEM images of residue of MPAP after burning.

4. Conclusions

A novel phosphorus-nitrogen containing flame retardant, 3-methylbut-3-enylphenyl 4-aminophenyl phosphoramidate (MPAP) which combine an acid source, a carbonization agent, and a blowing agent was successfully synthesized and characterized. MPAP has a 2-step major degradation and the final char weight in air is much more than N_2 that indicated oxygen can be promoted the char formation that act as effective heat barrier to prevent the heat and mass transfer between the heat source and materials.

Acknowledgements

This research was gratefully supported by ThEP Center.

References

[1] Horrocks, A. R. and Price, D., *Fire Retardant Materials*, Woodhead Publishing Ltd, (2001).

[2] Wang, D. Y.; Liu, Y.; Wang, Y. Z.; Artiles, C. P. and Hull, T. R., *Polymer Degradation and Stability*, **92** (2007) 1592-1598.

[3] Li, L.; Chen, G.; Liu, W.; Li, J. and Zhang, S., *Polymer Degradation and Stability*, **94** (2009) 996–1000.

[4] Zhan, J.; Song, L.; Nie, S. and Hu, Y., *Polymer Degradation and Stability*, **94** (2009) 291-296.

[5] Li, Y. L.; Kuan, C. F.; Hsu, S.W.; Chen. C. H.; Kuan, H. C.; Lee, F. M.; Yip, M. C. and Chiang, C. L., *High Performance Polymers*, **24 (**2012) 478-487.

[6] Liu, H.; Xiong,Y.; Xu, W.; Zhang, Y. and Pan, S., *Journal of Applied Polymer Science*, **125** (2012) 1544–1551.

[7] Chen, M. J.; Shao, Z. B.; Wang, X. L.; Chen, L. and Wang, Y. Z., *Industrial & Engineering Chemistry Research*, **51** (2012) 9769−9776.

[8] Tai, Q.; Song,L.; Lv, X.; Lu, H. Hu, Y. and Yuen, K. K. R., *Journal of Applied Polymer Science*, **123** (2012) 770–778.

[9] Ma, H. and Fang, Z., *Thermochimica Acta*, **543** (2012) 130– 136.

[10] Chen, Y.; Wang, Q., *Polymers for advanced technologies*, **18** (2007) 587–600.

[11] Hua, X.; Guo, Y.; Chen, L.; Wang, X.; Li, L. and Wang, Y., *Polymer Degradation and Stability*, **97** (2012) 1772-1778.

[12] Song, L.; Xuan, S.; Wang, X. and Hu, Y., *Thermochimica Acta*, **527** (2012) 1– 7.

ELECTROSPUN TiO_2 FIBERS AS GAS SENSORS

Thanetpong Paisunthornsook[1*], Boonchoat Paosawatyanyong[2,3], Worawan Bhanthumnavin[4]

[1]Program of Petrochemistry and Polymer Science, Faculty of Science, Chulalongkorn University, Bangkok 10330, Thailand.
[2]Department of Physics, Faculty of Science, Chulalongkorn University, Bangkok 10330, Thailand.
[3]ThEP Center, Commission on Higher Education, Bangkok 10400, Thailand.
[4]Department of Chemistry, Faculty of Science, Chulalongkorn University, Bangkok 10330, Thailand.

[*] Author for correspondence; E-Mail: Thanetpong.P@Student.chula.ac.th, Tel. +66 2 2187626, Fax. +66 2 2187598

Abstract: TiO_2 fibers were fabricated via electrospinning process. Mixtures of titanium isopropoxide, polyvinyl pyrrolidone (PVP), butanone, ethanol, and dimethylformamide (DMF) at specific ratios were prepared as TiO_2 precursor solutions. Electrospun TiO_2 fibers were hot-pressed at 180 °C followed by a calcination at 600 °C. Polymeric and organic components were decomposed and electrospun TiO_2 fibers as sensing material were obtained. Morphology of TiO_2 fibers was characterized by scanning electron microscopy (SEM) to show that the diameter of TiO_2 fibers was in a micrometer to a nanometer range. X-ray diffraction analysis (XRD) showed that electrospun TiO_2 fibers largely consist of an anatase phase along with some rutile phase. Sensing property of TiO_2 fibers was investigated with some small molecule gases. Acetone detection of TiO_2 fibers has been investigated in 30-300 ppm at room temperature.

1. Introduction

Air pollution is an important problem. Many gases such as CO, H_2S, NO_2, and other volatile organic solvents are harmful to human and other bio organism. For example, inhalation of acetone at high concentrations in the air causes irritation of the throat in humans in as little as 5 minutes. Concentrations of H_2S over 1000 ppm cause immediate collapse with loss of breathing, even after inhalation of a single breath. CO as low as 667 ppm may cause up to 50% of the body's hemoglobin to convert to carboxyhemoglobin, which is ineffective for delivering oxygen to bodily tissues [1]. Therefore, it is necessary to detect these gases. Many metal oxide semiconductors such as ZnO, SnO_2, TiO_2, WO_3 have been reported as sensing material for gas detection [2]. Because of low cost, robustness, light weight, and quick response to target gas, metal oxide semiconductors are of great interest.

In general, most metal oxide semiconductors must be activated to be used as sensors. Conventionally, many research groups require heating to activate metal oxide semiconductors [3-6]. Alternatively, there have been reports that UV lights with proper wavelength can also activate such sensors which make it possible to operate the systems at room temperature.

Sensing performance of metal oxide semiconductors relies on the surface-to-volume ratio. Fan et al. reported that ZnO wide line with 100 nm particles exhibit the better sensitivity of gas detection than the higher particle size and thin film of ZnO [7]. Small grain size and high surface area indicated high sensing performance [7, 8]. One method that offered a large surface-to-volume ratio on sensing material is electrospinning. Electrospinning is a simple and versatile method to fabricate microfibers to nanofibers of various materials such as polymers, ceramics, and composites.

In this research, electrospun TiO_2 fibers were fabricated to be tested as sensing material for gas sensor application. Morphology of TiO_2 fibers was investigated. Sensing property of TiO_2 fibers to acetone at various concentrations was also determined.

2. Materials and Methods

2.1 Chemical reagents

Titanium isopropoxide and polyvinyl pyrrolidone (PVP) with average M_w ~ 1,300,000 g/mol were purchased from Sigma-Aldrich. 2-butanone was obtained from Carlo Erba. *N,N'*-dimethylformamide (DMF) and ethanol were purchased from Fluka and MERCK respectively. All of the chemical reagents were used without further purification.

2.2 Electrospinning

The titanium electrospinning solution was prepared by mixing of 6 g of titanium precursor with 0.4 g of PVP. Titanium precursor with titanium concentration of 0.74 mol/L consisted of titanium isopropoxide and 2-butanone. Thereafter, 0.1 mL DMF and 0.2 mL ethanol were added. The whole mixtures were stirred at 60 °C for 4 hours. The electrospinning solution was loaded into a 10 mL plastic syringe equipped with a stainless steel needle of 0.4 mm diameter. The needle tip and conductive collector plate were connected to high voltage power supply. The applied voltage was maintained at 18 kV. Feeding rate of solution was kept at 0.6 mL/h by using syringe pump. The distance between needle tip and collector was fixed at 20 cm. The collecting time was about 30 minutes.

2.3 Sensor fabrication

The obtained fibers were hot-pressed at 180 ^{o}C for 10 minutes. Hot-pressed fibers were then calcined at 600 ^{o}C to remove organic and polymeric components. TiO_2 fibers (as sensing material) were obtained. Commercial printed circuit board (PCB) was used as substrate. Substrate size was 2.54 × 1.27 cm^2. The gap between copper electrodes was about 0.5 mm. Calcined TiO_2 fibers were placed on the substrate by using silver paint to adhere between them. Sensor was heated at 100 ^{o}C to remove organic solvent.

2.4 Characterization

Scanning electron microscope (SEM) was used to characterize the morphology of TiO_2 fibers. The diameter of TiO_2 fibers were evaluated by using JMicro Vision V.1.27 software. The crystallinity of the TiO_2 fibers was analyzed with X-ray diffraction (XRD) crystallography. The sensing performance was investigated by measuring conductance change under air and acetone ambience. Electrical characterization was operated in an in-house assembled chamber which has a volume of about 2 L. UV lamp (4W) with dominant wavelength at 367 nm was placed 2 mm above the sensor. Agilent 4284A LCR meter and Labview program were used to monitor the sensing property of sensor by measuring conductance which was carried out at 25 Hz frequency and 2 V. The response change (%R) was defined as

$$\%R = 100 \times (G_a - G_g)/G_a$$

where G_g is conductance under target gas ambience and G_a is conductance under air ambience. Acetone sensing was performed under different concentrations at 85 ± 5% humidity and room temperature (28 ± 3 ^{o}C).

3. Results and Discussion

TiO_2 fibers were prepared via electrospinning method. TiO_2 fibers were then hot-pressed at 180 ^{o}C for 10 minutes followed by calcination at 600 ^{o}C for 1 hour. Morphology of electrospun TiO_2 fibers has been examined by SEM results of which are shown in figures 1(a-b). The diameter of electrospun fibers before calcination was approximately 0.8-1.4 μm while ~ 0.7-1.1 μm diameter was obtained after calcination at 600 ^{o}C. It can be seen that the diameter of TiO_2 fibers was decreased after calcination. Although organic and polymeric components were removed, TiO_2 fibers still retained their fiber morphology.

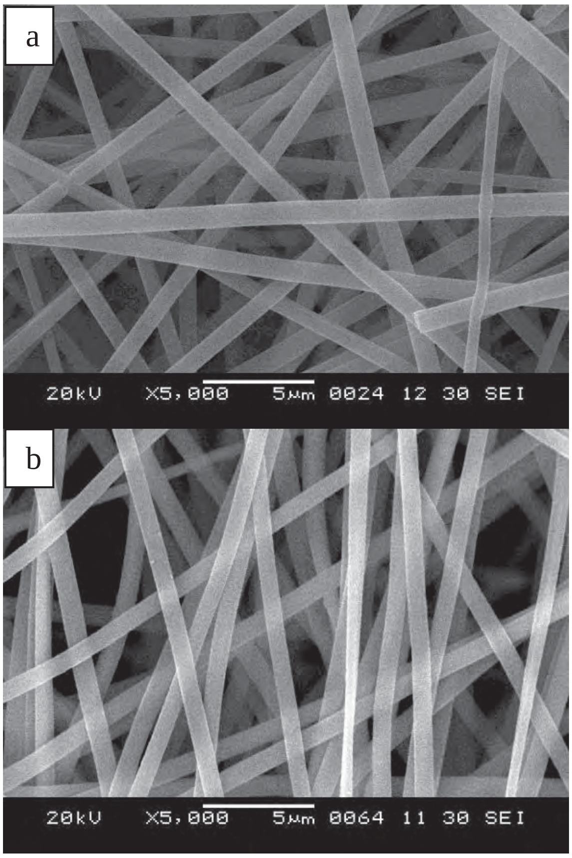

Fig 1. SEM image of a) electrospun TiO_2 fibers and b) calcined TiO_2 fibers

The XRD pattern of calcined TiO_2 fibers is shown in figure 2. The main peaks corresponding to the crystallographic planes of (101), (004), (200), (211), and (204) confirmed the anatase phase of TiO_2 structure. However, there is a small peak of (110) which showed some occurrence of TiO_2 in the rutile phase. The grain size of calcined TiO_2 fibers at main peak (101) was approximately 15 nm which indicated that TiO_2 fibers consist of nanocrystalline structure.

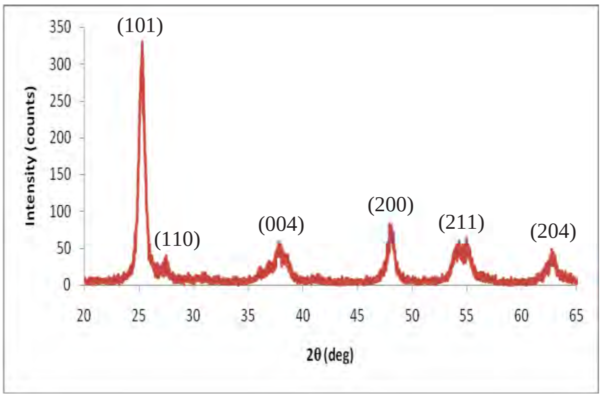

Fig 2. XRD pattern of TiO_2 fibers that has been calcined at 600 ^{o}C for 1 hour

To investigate the effect of UV light to gas sensing property of TiO_2 fibers, acetone detection at various concentrations was determined both with and without UV light. Figure 3 shows acetone detection of TiO_2 fibers without UV light. It can be seen that relatively unchanged response of acetone detection was obtained while there was an occurrence of the signal response of detection under UV light, shown in figure 4.

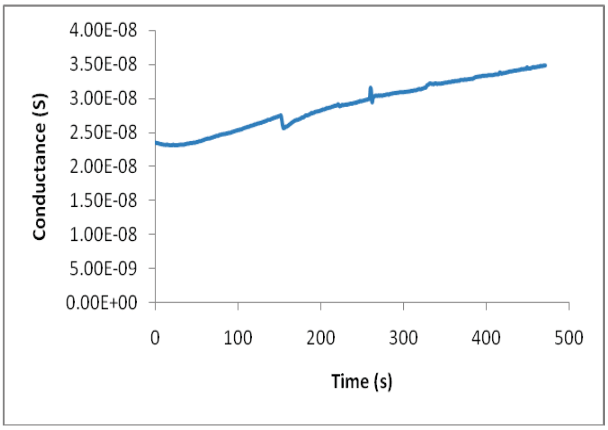

Fig 3. Acetone sensing of TiO_2 fibers without UV light

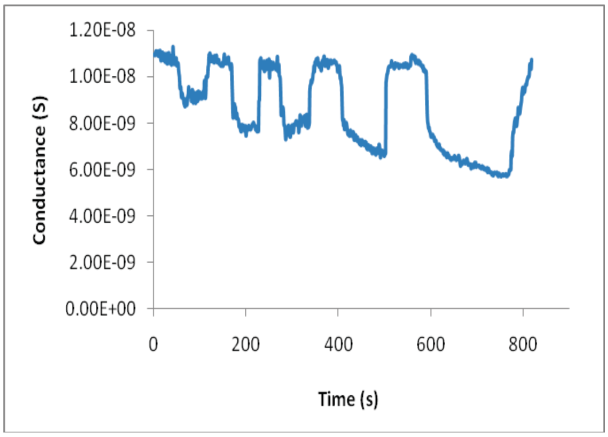

Fig 4. Acetone sensing of TiO_2 fibers under UV light

Many reports proposed that metal oxide can generate excited electrons and positive holes when exposed the UV light [8-11]. This confirms that UV light with appropriate wavelengths which give energy corresponding to the band gap of metal oxide semiconductors plays an important role to activate metal oxide semiconductors to be a sensor.

The behavior of acetone detection using TiO_2 fibers is indicated in figure 4. The cyclic response was observed when exposed to acetone concentrations between 39.55 and 316.40 ppm. Acetone injection was at 51, 167, 276, 406, and 591 s at which the decreasing of conductance was observed. This behavior conforms to de Lasy Costello and Gong works [10, 11].

Moreover, %response of acetone detection between 39.55 and 316.40 ppm has been shown in figure 5. At 39.55, 79.10, 118.65, 197.75, and 316.40 ppm of acetone concentrations, %response of acetone detection at various concentrations were approximately 20-80 %.

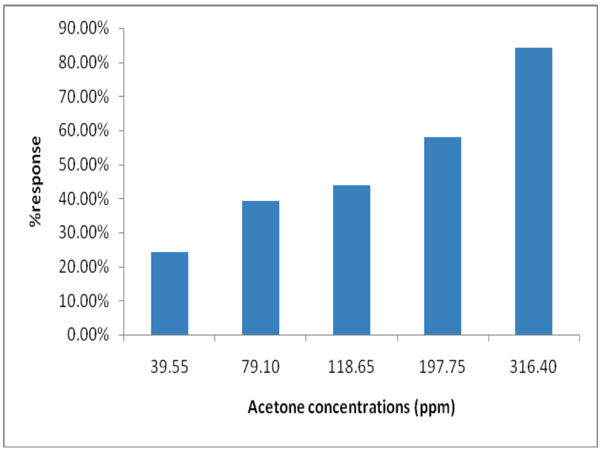

Fig 5. % response of acetone sensing at various concentrations (ppm).

It can be seen that the TiO_2 sensor is well responsive to the increased amount of acetone.

4. Conclusions

Gas sensor based on electrospun TiO_2 fibers was successfully fabricated. The diameter of TiO_2 fibers is 0.7-1.1 μm. From XRD result, TiO_2 fibers largely consist of anatase phase. The grain size of crystalline structure is approximately 15 nm. The maximum response of acetone detection is about 80% at 316.4 ppm.

Acknowledgements

This research was gratefully supported by ThEP Center.

References

[1] P. Patnaik, *A Comprehensive Guide to the Hazardous Properties of Chemical Substances*, 3rd edition, Wiley, USA (2007)

[2] G.F. Fine, L.M. Cavanagh, A. Afonja and R. Binions, *Sensors* **10** (2010) 5469-5502.

[3] J.Y. Leng, X.-J. Xu, N. Lv, H.-T. Fan and T. Zhang, *J. Colloid Interface Sci.* **356** (2011) 54–57.

[4] S. Wei, Y. Yu and M. Zhou, *Mater. Lett.* **64** (2010) 2284-2286.

[5] H. Gong, J.Q. Hu, J.H. Wang , C.H. Ong and F.R. Zhu, *Sens. Actuators, B* **115** *(2006) 247–251*.

[6] I. Alessandri, E. Comini, E. Bontempi, G. Faglia, L. E. Depero and G. Sberveglieri, *Sens. Actuators, B* **128** (2007) 312–319.

[7] S.-W. Fan, A.K. Srivastava and V.P. Dravid, *Sens. Actuators, B* **144** (2010) 159–163.

[8] J. Zhang, S.-W. Choi and S.S. Kim, *J. Solid State Chem.* **184** (2011) 3008–3013.

[9] H. Chen, Y. Liu, C. Xie, J. Wu, D. Zeng and Y. Liao, *Ceram. Int.* **38** (2012) 503–509.

[10] B.P.J. de Lacy Costello, R.J. Ewen, N.M. Ratcliffe and M. Richards, *Sens. Actuators, B* **134** (2008) 945–952.

[11] J. Gong, Y. Li, X. Chai, Z. Hu and Y. Deng, *J. Phys. Chem. C* **114** (2010) 1293–1298.

Cu(II) ADSORPTION BEHAVIOR OF PMMA/PEI CORE–SHELL NANOPARTICLES

Saysuree Seneeburaphathid[1], Nuttaporn Pimpha[2], Panya Sunintaboon[1]*

[1] Department of Chemistry, Faculty of Science, Mahidol University, Salaya, Nakhon Pathom 73170, Thailand
[2] National Nanotechnology Center, National Science and Technology Development Agency,
Thailand Science Park, Pathumthani 12120, Thailand

* E-mail: panya.sun@mahidol.ac.th, Tel. +66 840091330, Fax. +66 24410551

Abstract: This work illustrated the utilization of poly(methyl methacrylate)/polyethyleneimine (PMMA/PEI) core-shell nanoparticles for removal of copper(II) ions. The PMMA/PEI core-shell nanoparticles were chosen for removal of Cu(II) ions as a result of plentiful amine groups on the PEI chain that can be effective for chelation. First, the synthesis of core-shell nanoparticles was carried out *via* an emulsifier-free emulsion polymerization induced by *tert*-butyl hydroperoxide (TBHP). Then, the chemical structure and morphology of PMMA/PEI nanoparticles were investigated by Fourier transform infrared spectrometer (FT-IR) and transmission electron microscope (TEM), respectively. It was shown that the adsorption capacity (q_c) was increased according to pH of the medium (in range of 3 – 5). The adsorption of Cu(II) on the core-shell nanoparticles was found to correspond to Langmuir isotherm with the maximum adsorption capacity (q_m) of 55.55 mg/g that was close to the experimental q_m of 50.94 mg/g.

1. Introduction

Copper is a common metal that occurs naturally. It has a good heat and electricity conductor, easy to process and can blend with another metal such as zinc to get brass. Humans widely apply copper for industrial and agricultural uses, resulting to spreads of copper through the environment especially in water sources. High level of copper in living tissues can cause headache, vomiting and diarrhea, while long-term exposure can cause liver or kidney damage[1]. The common methods for removing heavy metal from wastewater such as chemical precipitation, ion exchange, and reverse osmosis[2-4]. Nevertheless, these methods are costly, inconvenient, and less effective. Beside, adsorption is the most widely used alternative method because the adsorption is using less time and the adsorbents can be regenerated by suitable desorption process and reused[5]. For instance, Guillermo J. Copello *et al*. prepared a synthetic polyampholyte as a sorbent bearing carboxylate and 2-methylimidazole (2MI) groups for the removal of Pb(II) and Cd(II) in solutions. This material has the benefits of synthetic polymers, such as high adsorption capacity and chemical stability. Langmuir model presented the best fitting to the isotherm equilibrium data, with a maximum adsorption capacity of 182 mg/g for Cd(II) and 202 mg/g for Pb(II)[6].

Polyethyleneimine (PEI) has also been utilized for removal of heavy metal since it has a plenty of amine groups on the chain. Therefore, it can form complexes with metal ions, and often be used to modify adsorbents surface to increase adsorption capacities. For instance, Deng *et al.* used the biomass of Penicillium chrysogenum, which was modified with polyethyleneimine (PEI) and then crosslinked with glutaraldehyde for adsorption of some metal ions. The results showed the maximum adsorption at 92 mg copper, 204 mg lead and 55 mg nickel per gram of biomass [7]. Bayramoğlu *et al.* developed the magnetic poly(glycidylmetharylate-ethyleneglycol dimethacrylate) (poly(GMA–EGDMA)) beads coated with PEI for the removal of Cr(VI) ions from aqueous solutions, showing that the maximum adsorption capacity of the magnetic beads was 137.7 mg/g[8].

In this work, the core-shell nanoparticles that possess poly(methyl methacrylate) (PMMA) as a core and polyethyleneimine (PEI) as a shell were prepared for removal of copper ions. The effect of pH on adsorption of Cu(II), adsorption capacity, and adsorption isotherm were investigated using flame-atomic adsorption spectrometer.

2. Materials and Methods

2.1 Materials

Polyethyleneimine (PEI) in a form of 50% aqueous solution with the average Mw ~ 750,000 and methyl methacrylate (MMA) were purchased from Sigma-Aldrich. MMA monomer was purified before use by washing with 5-10% sodium hydroxide for removing inhibitors and washing with water until pH of aqueous part was 7. Then, MMA was distilled under reduced pressure. *tert*-Butyl hydroperoxide (TBHP) 70% in water was supplied from Fluka. Copper nitrate trihydrate was obtained from Sigma-Aldrich. All other chemicals were of analytical grade and deionized water was used as the medium.

2.2 Synthesis of PMMA/PEI core-shell particles

The preparation of PMMA/PEI particles started with weighing 10 g of PEI (10wt%) and mixing it with a predetermined amount of deionized water. The total weight of the reaction mixture was adjusted to 50 g. The mixture was purged with N_2 for 30 minutes and the reaction temperature was raised to 80 °C. Then, purified MMA (monomer) 3 g was added, followed by the addition of TBHP (initiator), and the reaction was left for 2 hours under stirring and N_2 atmosphere. The resulting particles were cleaned to remove the free PEI by repeated centrifugation and re-dispersion. Particle size and zeta-potential values were obtained by using microelectrophoresis (Zetasizer 3000, Malvern Instrument, UK) in 1mM NaCl solution at room temperature. The chemical structure was characterized by Fourier transform infrared spectrometer (FT-IR). %Conversion of MMA and solid content of the nanoparticles were calculated by the following equations :

$$\%\text{Conversion of MMA} = \frac{\text{wt. of dried latex} - \text{wt. of PEI}}{\text{Initial wt. of MMA}} \times 100 \qquad (1)$$

$$\%\text{Solid content} = \frac{\text{wt. of dried latex}}{\text{wt. of latex}} \times 100 \qquad (2)$$

Then, TNBS assay was conducted for determining the percentage of grafted PEI on the particles. In general, this method has been used to determine a concentration of proteins or amino acids[9] through the reaction between free amine groups and 2,4,6-trinitrobenzene sulfonic acid (TNBS), which then generates an observable chromogenic product. This work used the TNBS assay to determine a concentration of free PEI in the supernatant obtained by centrifugation. The concentration of grafted PEI was calculated by comparing between a concentration of total PEI used and free PEI obtained.

2.3 Adsorption of Cu(II) on PMMA/PEI core-shell nanoparticles

Firstly, 0.5 g PMMA/PEI core-shell nanoparticles with a known concentration of PEI, was mixed with a certain amount of 15 mM Cu(II) solution. The pH value of medium was adjusted to 5 with 0.1 M NaOH. Then, the volume of mixture was adjusted to 10 ml. After 1 hour, the mixture was cleaned to remove the residue Cu(II) by centrifugation. The Cu(II) concentration in the supernatant was determined by atomic adsorption spectrometer (AAS) (PerkinElmer, AAnalyst 200). The equilibrium adsorption capacity (q_e) of Cu(II) was calculated by the following equation:

$$q_e = \frac{(C_0 - C_e)\, V_L}{M} \qquad (3)$$

where C_0 and C_e are the initial and the equilibrium concentrations of Cu(II) in the solution (mg/L), respectively. V_L is the volume of solution (L) and M is the mass of the adsorbent (g).

3. Results and discussion

3.1 Characterization of complexes of PEI with Cu(II)

Figure 1 showed the effect of adsorption time on the PEI, which was characterized by UV-Visible spectrometer. The absorbance of complex between PEI and Cu(II) was rapidly increased at the first 5 minutes due to the occurrence of strong chelation between PEI and Cu(II). So, the PEI would be a suitable material for removal of Cu(II) ions.

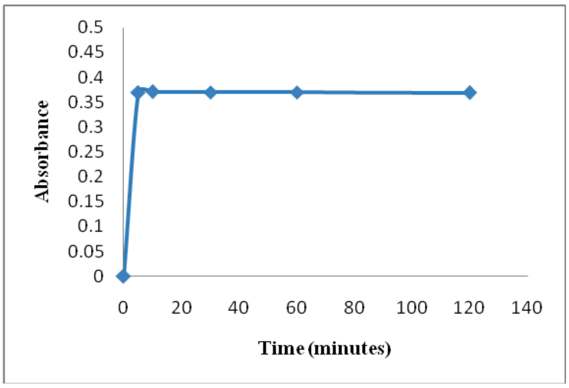

Figure 1. Relationship between absorbance of PEI formed complexes with Cu(II) at 650 nm and time.

3.2 Characterization of PMMA/PEI core-shell nanoparticles

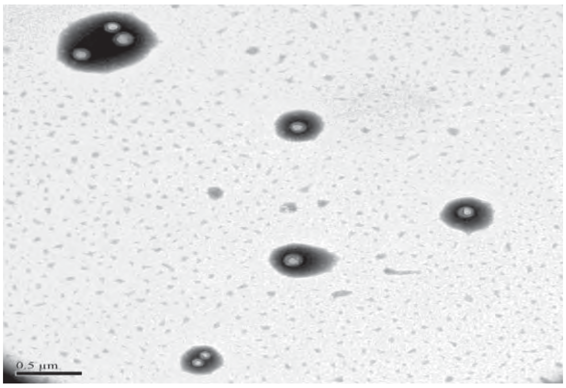

Figure 2. TEM image of PMMA/PEI core-shell nanoparticles.

PMMA/PEI core-shell nanoparticles were synthesized by a one-step emulsifier-free polymerization method reported by Li *et al.*[10]. %Conversion and solid content of PMMA/PEI core-shell nanoparticles were around 77% and 6.6%, respectively. The particles had a mean diameter of 254.6 nm and polydispersity index was 0.088. The zeta-potential, which is the surface charged of particles, was 39.7 mV at pH 6.5 and the content of grafted PEI on the core-shell particles determined by TNBS assay was 0.17 gram per gram of particles. The